Transcriptional Regulatory Dynamics Underlying Neuroinflammation-Associated States of Microglia

Doctoral Thesis

Presented by:

Carmen María Navarrón Izquierdo

Thesis Director:

Jose Pascual López-Atalaya Martínez

PhD Program in Neuroscience

Instituto de Neurociencias

Universidad Miguel Hernández

- 2021 -

CSIC UNIVERSITAS Miguel Hernández
INSTITUTO DE NEUROCIENCIAS

1999 - 2019 20 AÑOS
INSTITUTO DE NEUROCIENCIAS

EXCELENCIA SEVERO OCHOA

This Doctoral Thesis entitled "***Transcriptional Regulatory Dynamics Underlying Neuro-inflammation-associated States of Microglia***" is presented under the conventional thesis form with the following quality indicator:

Michal Lipinski , Rafael Muñoz-Viana , Beatriz Del Blanco, Angel Marquez-Galera, Juan Medrano-Relinque , José M Caramés, Andrzej A Szczepankiewicz, Jordi Fernandez-Albert , **Carmen M Navarrón** , Roman Olivares , Grzegorz M Wilczyński , Santiago Canals , **Jose P Lopez-Atalaya** , Angel Barco. KAT3-dependent acetylation of cell type-specific genes maintains neuronal identity in the adult mouse. *Nature Communications* 2020 May 22;11(1):2588. DOI 10.1038/s41467-020-16246-0"

Sant Joan d'Alacant, 30th of May 2021

Dr. Jose Pascual López-Atalaya Martínez, Director of the doctoral thesis entitled "***Transcriptional Regulatory Dynamics Underlying Neuroinflammation-associated States of Microglia***"

CERTIFIES:

That Mrs. Carmen María Navarrón Izquierdo has carried out under my supervision the work entitled "***Transcriptional Regulatory Dynamics Underlying Neuroinflammation-associated States of Microglia***" in accordance with the terms and conditions defined in her Research Plan and in accordance with the Code of Good Practice of the University Miguel Hernández of Elche, satisfactorily fulfilling the objectives foreseen for its public defence as a doctoral thesis.

I sign for appropriate purposes, in Sant Joan d'Alacant, 30th of May 2021

Thesis director,

Dr. Jose Pascual López-Atalaya Martínez

Sant Joan d'Alacant, 30th of May 2021

Ms. Elvira de la Peña García, Coordinator of the Neurosciences PhD programme at the Institute of Neurosciences in Alicante, a joint centre of the Miguel Hernández University (UMH) and the Spanish National Research Council (CSIC),

INFORMS:

That Mrs. Carmen María Navarrón Izquierdo has carried out under the supervision of our PhD program the work entitled "***Transcriptional Regulatory Dynamics Underlying Neuro-inflammation-associated States of Microglia***" in accordance with the terms and conditions defined in her Research Plan and in accordance with the Code of Good Practice of the University Miguel Hernández of Elche, fulfilling the objectives satisfactorily for its public defence as a doctoral thesis.

Which I sign for the appropriate purposes, in Sant Joan d'Alacant, 30th of May 2021

And for the record, for all purposes, I sign this certificate.

Dra. Elvira de la Peña García

Coordinator of the PhD Programme in Neurosciences

Av Ramón y Cajal s/n

E-mail : elvirap@umh.es | Tel: +34 965 919533 | CAMPUS DE SANT JOAN

www.in.umh.es | Fax: +34 965 919549 | 03550 SANT JOAN D'ALACANT– ESPAÑA

The present PhD thesis has been funded by the following research agencies:

Dña. Carmen María Navarrón Izquierdo is recipient of a FPI contract (BES-2016-076281) associated with the excellence program Severo Ochoa (SEV-2013-0317).

The present PhD thesis has been supported by the grants SAF2014-60233-JIN RYC-2015-18056, and RTI2018-102260-BI00, from MICINN co-financed by the European Regional Development Fund (ERDF).

INDEX

LIST OF ABBREVIATIONS

3D	3 Dimensional
Aβ	Amyloid β
ACSF	Artificial Cerebrospinal Fluid
AD	Alzheimer's Disease
ALS	Amyotrophic Lateral Sclerosis
ApoE	Apolipoprotein-E
AP-1	Activator Protein 1
APP	Amyloid Precursor Protein
ASC	Apoptosis-associated speck-like protein containing a CARD
ATAC-seq	Assay for Transposase-Accessible Chromatin Sequencing
ATP	Adenosine Triphosphate
BAMs	Border-Associated Macrophages
BBB	Blood Brain Barrier
BDNF	Brain-Derived Neurotrophic Factor
BrdU	Bromodeoxyuridine
cDNA	Complementary Deoxyribonucleic Acid
CLRs	C-Type Lectin Receptors
Cx3cr1	Chemokine (C-X3-C) Receptor 1
CE	Common Era
CSF-1	Colony Stimulating Factor 1
CNS	Central Nervous system
DAM	Disease-associated Microglia
DAMPs	Damage-Associated molecular patterns
DAP12	DNAX Activation Protein 12
DAPI	4',6-diamidino-2-fenilindol
DARs	Differentially Accessible Regions
DCI	Dendritic Complexity index
DEA	Differential Expression Analysis
DEG	Differential Expressed Genes
DeltaE9	Delta Exon 9
DEPC	Diethylpyrocarbonate
DG	Dentate Gyrus
DNA	Deoxyribonucleic Acid
DNase	Deoxyribonuclease

E	Embryonic Day
EDTA	*Ethylenediaminetetraacetic acid*
EOAD	Early-Onset Alzheimer's Disease
EYFP	Enhanced Yellow Fluorescent Protein
FACS	Fluorescent Activated Cell Sorting
FDR	False Discovery Rate
fEPSPs	Field Excitatory Postsynaptic Potentials
GFP	Green Fluorescent Protein
GO	Gene Ontology
GWAS	Genome-Wide Association Studies
H	Human
HBSS	Hanks' Balanced Salt Solution
HM	Homeostatic Microglia
HCL	HydroChloric Acid
Iba-1	Ionized Calcium Binding Adaptor Molecule 1
IGV	I*ntegrative Genomics Viewer*
iKB	Inhibitor of Nuclear Factor Kappa B
iKK	Inhibitor of Nuclear Factor Kappa B Kinase
IL	Interleukin
ImmGen	Immunological Genome
i.p.	Intraperitoneal
I.G.	Intragastric
IRES	Internal Ribosome Entry Site
IRF	Interferon
IRM	Interferon-Related Microglia
LXh	X Hour from Lipopolysaccharide
LPS	Lipopolysaccharide
LOAD	Late-Onset Alzheimer's Disease
LTD	Long-Term Depression
LTP	Long-Term Potentiation
M	Mouse
MD2	Myeloid Factor 2
MHC-II	Major Histocompatibility Complex Type II
MS	Multiple Sclerosis

MS4	Membrane Spanning 4
MyD88	*Myeloid* Differentiation Primary Response 88
NAMPs	Neurodegeneration-Associated Molecular Patterns
NcRNA	Non-Coding RiboNucleic Acid
NCS	Newborn Calf Serum
NF-κB	Nuclear Factor Kappa B
NGS	Next Generation Sequencing
NLRP3	NOD-, LRR- and pyrin domain-containing 3
NLRs	NOD-Like Receptors
NOD	Nucleotide-Binding Oligomerization Domain
NSAID	Non-Steroidal Anti-Inflammatory Drug
OAS	2'-5'-oligoadenylate synthetase
P	Postnatal
PAMPs	Pathogen-Associated Molecular Patterns
PBS	Phosphate Saline Buffer
PCA	Principal Component Analysis
PCR	Polymerase Chain Reaction
PDGF-β	Platelet-Derived Growth Factor Beta
PFA	Paraformaldehyde
PM	Proliferative Microglia
PPR	Paired-Pulse Ratio
PrP	Prion Protein
PRRs	Pattern-recognition receptors
PS1	Presenilin-1
PS2	Presenilin-2
PVM	Perivascular Macrophages
RIG	Retinoic Acid-Inducible Gene
RLRs	RIG-I-Like Receptors
RNA	RiboNucleic Acid
RNAse	Ribonuclease
RNA-seq	RiboNucleic Acid Sequencing
RT	Room Temperature
RT-qPCR	Real-Time Quantitative Polymerase Chain Reaction
scRNA-seq	Single-Cell RNA-sequencing

SIP	Isotonic Percoll Solution
TAM	Tyro-3, Axl and Mer
TLR	Toll-like Receptor
TMX	Tamoxifen
TNF	Tumor Necrosis Factor
TREM2	Triggering Receptor Expressed on Myeloid Cells
TRIF	TIR-domain-containing adapter-inducing interferon-β
UMAP	Uniform Manifold Approximation and Projection
UTP	Uridine Triphosphate
WT	Wild-Type

SUMMARY

Microglia heterogeneity has been shown in both healthy and chronic neurodegenerative conditions, however, very little is known about microglia chromatin accessibility and transcriptome landscape during acute neuroinflammation. We combined bulk RNA-sequencing and ATAC-sequencing on FACS-sorted microglia population with single molecule *in situ* hybridization (RNAscope), to reveal dynamic transitions across microglia functional states along the acute neuroinflammatory response. We identify an immediate-early cytokine-related (*Il1b*) and an immediate-sustained interferon response (*Oasl2*) microglia; a delayed response associated to heterogeneous proliferative microglia (*Ms4a4a*); and a delayed-sustained late stage of MHC-II-expressing (*Axl*) microglia; altogether with a transient loss of homeostatic genes (*P2ry12*, *Cx3cr1* among others). Meta-analysis of published DAM microglia marker genes and LPS-responsive microglia shows that late stage of acute inflammation-associated microglia shares DAM phenotype. We confirm the presence of DAM and IRM microglia by microglia single-cell RNA-sequencing of J20 mouse model of AD. Moreover, we identify *in situ* by RNAscope of common acute and chronic neuroinflammation marker genes, a specific upregulation of the interferon-related marker (*Oasl2*) in the proximity of diffuse Aβ plaques whereas the phagocytic-related marker (*Axl*) is expressed by microglia in the surrounding of both dense and diffuse Aβ plaques. We also revealed an increase in the expression of both *Oasl2* and *Axl* in human *post-mortem* brain tissue from AD patients. Finally, *in silico* transcription factor motif analysis shows the *RelA*/p65 subunit of the transcription factor NF-κB as a key regulator of microglia cytokine-related transcriptional program. Conditional depletion of *RelA* in microglia during adulthood (RelA-cKO mice) recapitulates the interferon-related (with upregulation of *Oas* family) and phagocytic microglia phenotypes (with an upregulation of *Axl*) that is sufficient to alter instrumental learning and memory, and LTP. Our findings reveal common microglia signatures in acute (LPS) and chronic (AD) inflammatory conditions both in mouse animal models and human AD. Depletion of *RelA* reprograms microglia towards a phenotype present in both the late state in acute LPS, and Aβ plaques-associated microglia in chronic disease. Our work deepens our knowledge of microglia heterogeneity in acute and chronic neuroinflammatory response, with major implications for our understanding of microglia contributions to disease.

RESUMEN

La heterogeneidad de la microglía ha sido demostrada tanto en el cerebro sano como en condiciones patológicas. Sin embargo, los cambios en la accesibilidad de la cromatina y el perfil transcripcional de la microglía durante una inflamación aguda son poco conocidos. La combinación de *RNA-sequencing* y *ATAC-sequencing* en microglía aislada por FACS junto con ensayos de hibridación *in situ* (*RNAscope*), muestran que la microglía lleva a cabo transiciones dinámicas entre distintos estados funcionales a lo largo de la respuesta inflamatoria aguda. Hemos identificado una respuesta temprana-corta compuesta por genes relacionados con la respuesta de las citoquinas (*Il1b*) y una respuesta temprana-sostenida compuesta por genes de la vía del interferón (*Oasl2*); una respuesta tardía y heterogénea asociada la función proliferativa de la microglía (*Ms4a4a*); y una respuesta tardía-sostenida relacionada con la expresión de MHC-II (*Axl*); al mismo tiempo, hay una disminución transitoria en la expresión de genes homeostáticos (*P2ry12, Cx3cr1,* entre otros). Tras meta-analizar datos publicados de marcadores de DAM microglía junto con los genes identificados en nuestro estudio con LPS, observamos que los marcadores que identifican a la microglía DAM son compartidos con los expresados por la microglía en los estadios tardíos de inflamación aguda. Confirmamos la presencia de DAM e IRM microglía en el modelo de AD J20 mediante *single-cell RNA-sequencing* de microglía aislada. Además, identificamos mediante *RNAscope* de marcadores comunes de neuroinflamación aguda y crónica un aumento en la expresión de *Oasl2* en la proximidad de las placas β-amiloideas difusas, mientras que el aumento observado en la expresión de *Axl* ocurre tanto en placas β-amiloideas difusas como compactas. También mostramos un aumento en la expresión de *Oasl2* y *Axl* en tejido *post-mortem* de pacientes con enfermedad de Alzheimer. Finalmente, hemos identificado, mediante un análisis *in silico* de motivos de unión de factores de transcripción, a la subunidad *RelA*/p65 del factor de transcripción NF-κB como un regulador clave en la microglía del programa transcripcional relacionado con la expresión de citoquinas. La depleción condicional de *RelA* en la microglía durante la etapa adulta recapitula la respuesta relacionada con el interferón (con un aumento en la expresión de la familia *Oas*) y la fagocitosis (con un aumento en la expresión de *Axl*) que es suficiente para alterar el aprendizaje instrumental y la LTP. Nuestros hallazgos muestran estados comunes de la microglía en condiciones inflamatorias agudas (LPS) y crónicas (AD) tanto en modelos animales como en humano. La depleción selectiva de *RelA* reprograma a la microglía hacia un fenotipo presente tanto en los estados tardíos en la respuesta aguda a LPS como en enfermedad crónica. Nuestro trabajo aumenta el conocimiento actual sobre la heterogeneidad de la microglía en situaciones neuroinflamatorias agudas y crónicas lo que supone grandes implicaciones para nuestro entendimiento sobre cómo el papel que juega la microglía en diferentes patologías del CNS.

INTRODUCTION

1. Inflammation in the central nervous system

The first description we find of inflammation goes back to the first century CE on the hand of Aulus Cornelius Celsius. He defines the tetrad of inflammation as “dolor, rubor, calor et tumor” referred to heat, pain, redness and swelling respectively (Talamonti et al., 2020), the four classical signs of inflammation. More than two millennia later, a complete field of research is focused on inflammation and its relevance in neurological diseases is exponentially increasing nowadays.

The inflammatory response is a very complex process coordinated by many different cell types in the body that comprise innate and adaptative immunity to cope with a wide variety of inflammatory scenarios.

The acute inflammatory response can be controlled and beneficial as it is finally resolved and, for that to be achieved, the neutralization and elimination of the triggering agent is crucial. Failure to achieve this will result in chronic inflammation with the aetiology of the insult dictating the outcome of the inflammatory process. Of note is that the other factor that greatly influences the immune response is the tissue/organ where it takes place, where the tissue-resident macrophages orchestrate the inflammatory response (Serhan, 2010). In particular, as will be further discussed in this PhD thesis, microglia are the brain-resident macrophages that mediate the innate immune response in the brain (Fig.1).

Inflammation is commonly referred to as the response of the immune system to bacterial and viral infections or as part of autoimmune diseases. Recently, the term neuroinflammation has been attributed to neurodegenerative diseases, like Alzheimer’s disease (AD), which are now considered neuroinflammatory diseases. Most neurodegenerative diseases present a well-established glial cells reaction signature together with the release of inflammatory mediators to the brain parenchyma (Ransohoff, 2016).

Besides, current inflammatory treatment approaches are very limited in the central nervous system (CNS). In general, the therapeutic approach is focused in the first place on the elimination of the aetiology or cause of the disease if it is known; for example, in an infection, antibiotic treatments are administered; or if it is driven by autoimmune responses, immunosuppressants are applied. Other drugs that are commonly used to relieve the pain associated with inflammation are corticosteroid therapy or non-steroid drugs (NSAIDs), but both of them have limited effects over inflammatory main cause directly (Serhan, 2010). Several clinical trials using NSAID therapy for AD have failed as well as other therapies targeting the innate immune system using antibodies against amyloid β (Aβ) (Heneka et al.,

2015). Given this, a better understanding of the inflammatory process is needed to develop more effective anti-inflammatory drugs that can be used safely on a long-term basis.

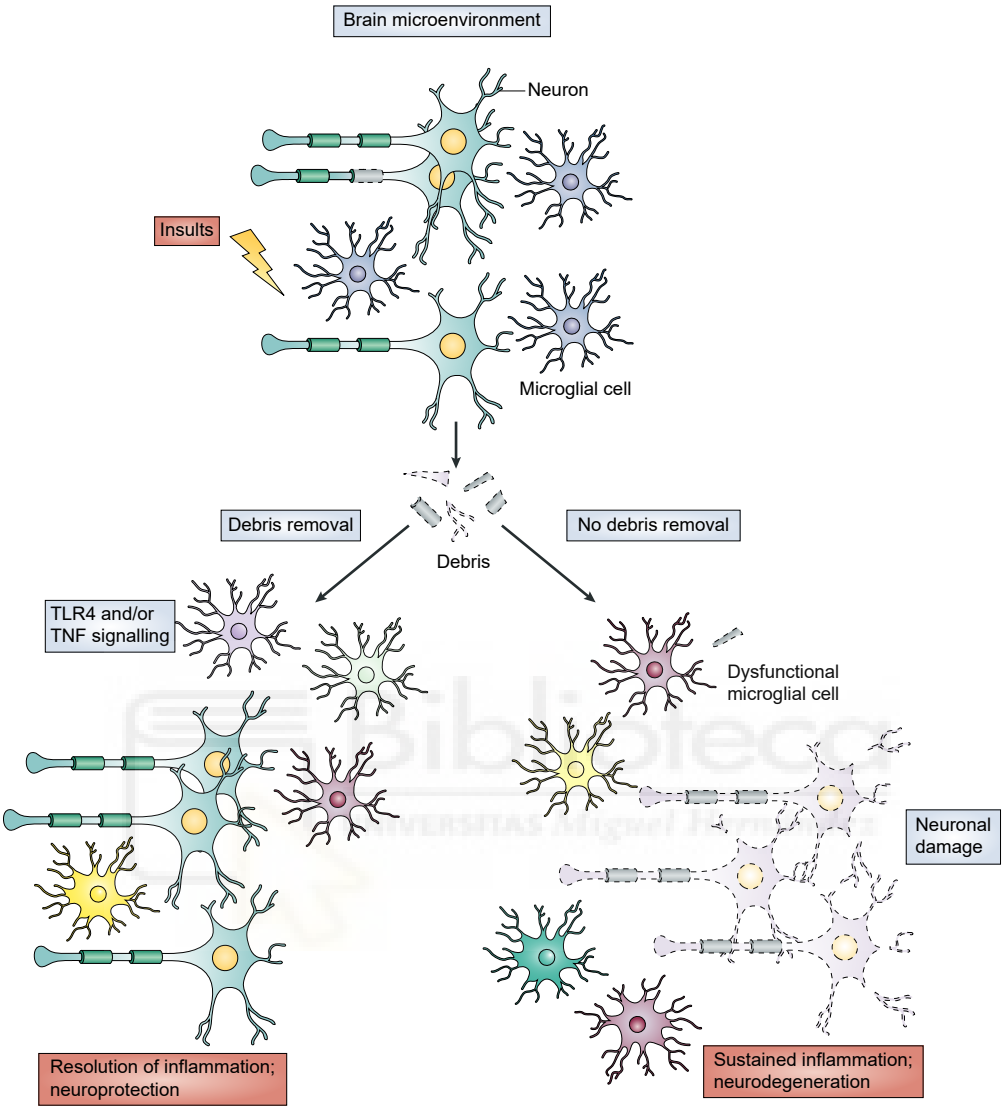

Fig.1. Innate immune response in the central nervous system. In the brain microenvironment, microglial cells respond to a wide variety triggering agents, both external like bacteria or viruses and internal like por-inflammatory cytokines, neuronal dysfunction, and cellular debris. Microglia present a big repertoire of receptors to couple with the inflammatory response. In particular, in response to LPS, toll-like receptor 4 (TLR4) signalling produce a rapid activation of microglial cells which adopt a continuum of multiple activation states to finally resolve the inflammation and promote neuroprotection. Without the rapid clearance of myelin debris or toxic elements from the brain, the inflammatory response is chronified and detrimental for neurons resulting in demyelination, synaptic dysfunction and ultimately neurodegeneration. Adapted from Rivest S, Nat Rev Immunol 2009.

1.1 Models to study inflammation *in vivo*

Inflammation is a common hallmark of most CNS diseases (Sarlus & Heneka, 2017). It is a process that can be triggered by many different factors. Depending on the trigger and its duration or presence, beneficial or detrimental outcomes are expected to occur.

To shed some light into such a complex process, in this PhD thesis, we are taking advantage of the following mouse models to study the neuroinflammatory response: intraperitoneal

administration of lipopolysaccharide (LPS), and the Alzheimer's disease mouse models J20 and APPswe/PS1dE9.

Lipopolysaccharide induced acute neuroinflammation

Lipopolysaccharide is a component of the surface of the gram-negative bacteria whose recognition by immune cells triggers a robust inflammatory response. In clinical settings, the presence of endotoxins is associated with septicaemia. One of the most used experimental models that mimic the acute-phase response to systemic infection is the systemic administration of LPS that recapitulates some symptoms like fever, cognitive impairment, release of glucocorticoids, reduction of the locomotor activity, thirst, appetite, and social interactions (Chakravarty & Herkenham, 2005; Zhao et al., 2019).

This model has been widely used to study the regulation of the immune system. Of note is that the response to LPS is entirely dependent upon microglia although other cell types like astrocytes participate as well (Holm et al., 2012). LPS administered intraperitoneally reaches the brain and produces a robust induction of proinflammatory cytokines and chemokines as well as proteins of the complement system by activation of toll-like receptor 4 (TLR4) directly in the circumventricular organs inducing the expression of tumor necrosis factor-α (TNF-α) that spreads the pro-inflammatory signal throughout the brain parenchyma (Rivest, 2009). One of the main advantages that present this model is that the activation of microglial cells occurs through the whole brain without external contributors (for example, as it occurs with intracerebroventricular administration) (Rivest, 2009).

AD as a paradigm of chronic neuroinflammation associated with neurodegeneration

One of the most prevalent neurodegenerative disease is Alzheimer's disease. AD is a complex, multifactorial disease characterized by the accumulation of intracellular neurofibrillary tangles of hyperphosphorylated microtubule-associated protein Tau and extracellular aggregates of β-amyloid peptide (Aβ) into β-pleated sheets. The main clinical feature is the loss of memory and cognition affecting around 40 million patients worldwide (Selkoe & Hardy, 2016). AD initiates around 10 to 20 years before the first clinical symptomatology appears (prodromal phase) which complicated the identification of the origin of the disease and the implementation of an effective treatment that may reverse or improve the progression of the disease.

Neuroinflammation associated with AD has been defined as "sterile". Although the same receptors as in the response to LPS are involved, there are not living pathogens that can be eliminated. In AD, several factors like the Aβ accumulation compromise the cessation

of inflammation establishing a chronic, non-resolving inflammation (Heneka et al., 2015). Besides, half of the genetic variants that have been shown to predispose to AD are expressed by microglial cells like TREM2, APOE, MS4A or CD33 (Villegas-Llerena et al., 2016). This shows the importance of microglia and inflammation in AD and points out the necessity of a better understanding of neuroinflammation in the CNS.

Sporadic late-onset AD (LOAD) accounts for the majority of the cases worldwide, being aging the primary risk factor (Campion et al., 1999). In contrast, early-onset AD (EOAD) is mainly caused by well-known familiar mutations that increase the predisposition to suffer Alzheimer's disease. The first described EOAD associated mutations are present in genes encoding for amyloid precursor protein (APP), presenilin-1 (PS1) and presenilin-2 (PS2) that directly affect the balance between the production and accumulation of Aβ, a central factor to AD pathogenesis (Selkoe & Hardy, 2016). The characterization of these mutations was also important for the development of some of the currently used animal models of AD.

One of the most classical animal models to study AD is the J20 mouse line. This model presents the Swedish (KM670/671NL) and the Indiana (V717F) mutations of human APP under the PDGF-β promoter (Mucke et al., 2000). The incorporation of these mutations increases the production of total Aβ from APP. These mice develop neuronal loss, changes in long-term potentiation and depression (LTD/LTP), synaptic loss and cognitive impairment between 3 and 4 months of age, even before amyloid deposition that occurs around 6 months together with gliosis. These mice do not develop one of the classical AD features that is the presence of mature neurofibrillary tangles.

APP transgenic mice recapitulate some features of AD pathology. To further model the remaining hallmarks of AD, APP mice were combined with mutations of PS1, a constituent of the γ-secretase complex essential for Aβ production. One of the most used animal models that combine both mutations is the APPswe/PS1dE9 mouse line. This model presents the Swedish mutation (KM670/671NL) of human APP and the DeltaE9 mutation of human PS1 transgenes inserted under control of the prion PrP promoter (Jankowsky et al., 2004). The combination of these mutations increases pathogenic Aβ production and accumulation, however these mice also recapitulate only a part of AD pathology, including the development of Aβ plaques, gliosis, and synapsis loss between 3 to 6 months of age. From 7 months old, memory impairment and alterations in long term potentiation can be observed. Neuronal loss is evident at later stages of the disease when the animals are around 17 months old but there is no production of neurofibrillary tangles in this model either. In summary, APP mutations alone or the combination of APP and PS1 mutations broadly recapitulate the same features of AD pathology with a different temporal distribution (Sasaguri et al., 2017).

2. Microglia in the healthy brain

Microglial cells are unique cells within the CNS due to its myeloid origin that is different to that of the cells in the brain that arise from brain neuroepithelial progenitors. Microglia are very active cells that have many different functions in the healthy brain, essential for the maintenance of brain homeostasis and function.

2.1 Microglia ontology

Since microglial cells were first described by Pío del Río-Hortega in 1919 (Río-Hortega, 1919), a big controversy has been associated with its ontology. Originally thought that monocytes and tissue macrophages were microglia progenitors both in health and disease (Butovsky & Weiner, 2018), it was proposed in 1999 that microglia derived from yolk-sac macrophages (Alliot et al., 1999). Conclusive evidence was provided by Ginhoux et al., in 2010 when they showed the unique myeloid microglia origin from hematopoietic precursor cells in the yolk sac at embryonic day E7.5 in mice (Ginhoux et al., 2010; Schulz et al., 2012). At this embryonic date, nucleated red blood cells and macrophages that will colonize the mouse embryo arise in what is known as the first hematopoietic wave. Brain-macrophage precursors will migrate through the blood vasculature to the brain until E13 when the blood-brain barrier is closed (Ginhoux et al., 2010). From this point, they proliferate and colonize the brain following a specific pattern and undergo different phases of differentiation with the exclusive contribution of signals from the brain microenvironment. Microglial cells colonize the brain parenchyma and acquire their mature identity without the contribution of circulating monocytes (as it occurs in most brain-resident macrophages outside the brain) meanwhile the macrophages that colonize meninges, choroid plexus, and vasculature (border-associated macrophages - BAMs) present specific signatures that depend on external cues as shown on choroid plexus macrophages population (Goldmann et al., 2016).

The recent discovery of microglia ontology is an example of the novelty of this field and the uniqueness of microglial cells within the brain and points out the importance of both, origin, and environment in the definition of microglial cells identity.

2.2 Microglia functions in the healthy brain

Microglia roles during development and in the postnatal brain

As previously described, microglia migrate to the brain early during development, being the only cell type that coexists and maturates together with neurons for a long time until the later appearance of astrocytes and oligodendrocytes, suggesting a possible role of microglia for correct neural circuit assembly and brain development (Thion & Garel, 2017).

In this sense microglia has shown to play an important role in the formation of axonal tracts during development like the outgrowth of dopaminergic axons and interneurons migration (Squarzoni et al., 2014) or the corpus callosum tracts (Pont-Lezica et al., 2014). The fractalkine receptor Cx3Cr1 and the DAP12 adaptor molecule have an important role in the previously mentioned functions which suggests that microglia sensing machinery is essential also during development.

Microglia phagocytic function is important during development for the phagocytosis of neural progenitors during embryonic neurogenesis (Cunningham et al., 2013). Besides, microglia secrete neurotrophic and growth factors that regulate the proliferation of oligodendrocytes, astrocytes, and neuronal progenitors, contributing to the maturation of neural circuits (Schafer & Stevens, 2015).

Postnatally, microglia phagocytosis of supernumerary synapses is necessary for the establishment of efficient neuronal networks (Paolicelli et al., 2011; Schafer et al., 2012). Microglia also promote the formation and remodelling of synapses (Weinhard et al., 2018) and regulate neuronal connectivity and synapse loss through a non-phagocytic mechanism (Cheadle et al., 2020) (Fig.2).

Microglia roles in adulthood

To maintain population levels, one of the main functions that microglia carry out is microglia population self-renewal coupling apoptosis and proliferation (Askew et al., 2017). Mouse microglia renewal rate has been recently calculated to be three times during a 2-year lifespan (Tay et al., 2017). In humans, microglia have shown to be long-lived cells that renew slow, with cells living for several decades (Reu et al., 2017). Human microglia turnover is estimated to be 30% of the population per year, each cell living on average 4.2 years (Butovsky & Weiner, 2018).

Phagocytosis is one of the main functions of microglial cells in the healthy brain. In adulthood, microglia play important roles in adult neurogenesis clearing the excess of new-born neurons (Sierra et al., 2010; Cunningham et al., 2013). Microglia can also promote neuronal death by phagocyting stressed but viable neurons through phagoptosis (Brown & Neher, 2014). Besides, the microglia population is essential to maintain brain homeostasis rapidly clearing the apoptotic cells. *In vivo*, it has been estimated that the clearance time of apoptotic cells in physiological conditions is around 70-90 minutes (Sierra et al., 2010).

Microglial cells are very active cells constantly surveilling the environment as shown by super-resolution imaging (Tonnesen et al., 2018). They are equipped with a set of receptors

in their membrane that allow them not only to respond to external damage agents but also to communicate with other cell types. Neuronal release of norepinephrine has been shown to modulate microglia surveillant state suggesting an important role for microglia in fine-tuning neuronal circuits in the healthy brain (Liu et al., 2019; Stowell et al., 2019). Besides, microglia promote learning-dependent synapse formation through BDNF signalling (Parkhurst et al., 2013).

Finally, microglial cells interact with other brain cell types contributing to normal brain function. Microglia interact with astrocytes regulating the blood brain barrier (BBB) permeability; with endothelial cells contributing to vasculogenesis; and with oligodendrocytes for axons myelination and remyelination (Sierra et al., 2019) (Fig.2).

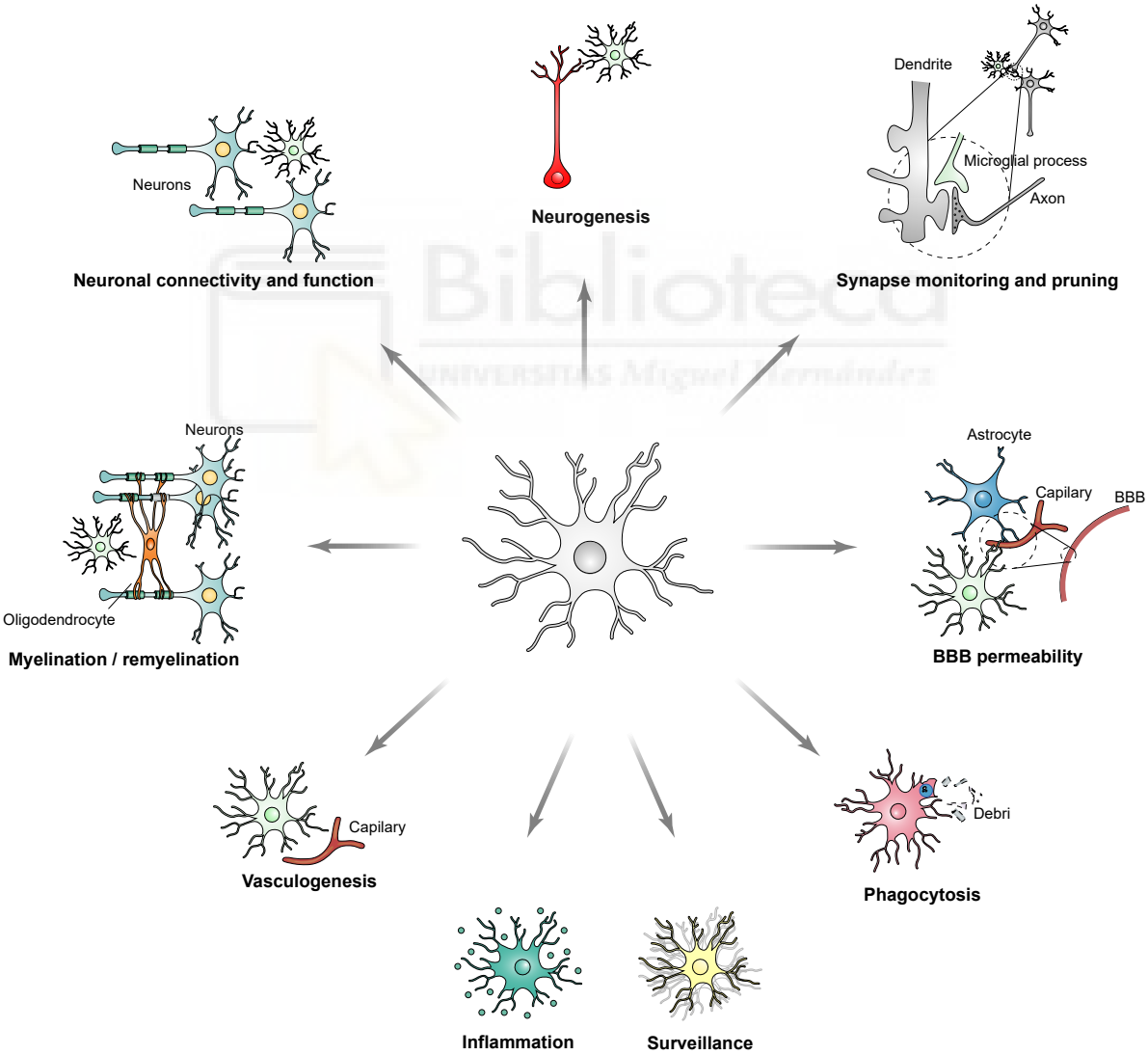

Fig.2. Microglia functions in the healthy brain. Many functions have been attributed to microglia in the healthy brain. Microglia are highly motile cells constantly surveilling the environment; coupled with a set of receptors, microglia recognize cell debri and apoptotic cells and phagocyte them to keep brain homeostasis. Microglia contribute to neuronal functions playing a key role in synapse monitoring and pruning and neurogenesis. Microglia also contribute to myelination and remyelination, blood brain barrier (BBB) permeability and vasculogenesis. In pathological conditions, microglia are the innate immune cells of the CNS and mediate the inflammatory response. Adapted from Sierra A, Paolicelli RC, and Kettenmann H, Trends in Neurosci 2019. Graphics adapted from Rivest S, Nat Rev Immunol 2009.

2.3 Methods to study microglia

The development of the first microglia culture in 1986 by Dana Giulian and Timothy Baker, together with the later generation of the BV2 cell line, supposed an important advance in the microglia research field (Giulian & Baker, 1986; Bocchini et al., 1992). It is also relevant that most of the studies in the microglia field until the year 2000 were performed *in vitro* (Sierra et al., 2019).

Despite the advantages of *in vitro* models in comparison with *in vivo* approaches, recent studies have shown that cultured microglia do not recapitulate *in vivo* microglia hallmarks in their immune-privilege neural environment. Novel *in vivo* transcriptomic studies have defined microglia identity in the adult healthy brain (Butovsky et al., 2014; Galatro et al., 2017; Gosselin et al., 2017; Olah et al., 2018; Zhang et al., 2014). On this context, Gosselin et al., show that human microglia transcriptome transferred to an *in vitro* environment downregulate key microglia identity genes like *Trem2*, *P2ry12* or *Sall1* compared with *ex vivo* acute-isolated microglia (Gosselin et al., 2017).

Besides, the majority of the tissue processing protocols, not only for *in vitro* culture but also for *in vivo* microglia purification, included, until very recently, enzymatic tissue dissociation, serum and incubation at 37ºC. Several groups have shown the importance of removing serum from tissue cultures (Bohlen et al., 2017) and enzymatic digestion at high temperatures (Bennett et al., 2016) for microglia *in vivo* purification protocols to mimic and preserve microglia *in vivo* transcriptome (Ayata et al., 2018; Hirbec et al., 2018).

Microglia are very plastic cells, and the environmental cues are essential for their correct identity and function. Despite the fact that a big effort is being made, an *in vitro* method that resembles microglia *in vivo* transcriptional profile is not available yet. Altogether, it reinforces the importance of performing *in vivo* studies with specific processing of the tissue at 4ºC to study microglial cells.

3. Microglia innate immune response

Microglial cells are the brain-resident macrophages. They mediate the innate immune response in the CNS through pattern-recognition receptors (PRRs) able to recognise damage or pathogen-associated molecular patterns (DAMPs and PAMPs respectively) (Presta et al., 2018). In the brain, the group of vessels that vascularize the CNS and the endothelial cells that recover them form the blood brain barrier (BBB) that acts as a physiological barrier maintaining the brain homeostasis tightly regulating the interchange of ions, molecules and cells between the blood and the brain. In this sense, the BBB is not only essential for

the delivery of oxygen and nutrients, removing carbon dioxide and metabolic waste from the brain, but it also presents a fundamental function in the interaction with the peripheral immune system (Daneman & Prat, 2015). Another important thing worth mentioning is that the circumventricular organs, the choroid plexus, and leptomeninges are highly vascularized areas of the brain where there are no BBB and the response to pathogens is similar to that found in the rest of the organs. Rapid immune responses are initiated at these regions which are highly colonized by brain associated macrophages followed by subsequent activation of resident microglial cells in the parenchyma (Rivest, 2009). This activation is mediated by PRRs. Currently, the 4 classes of PRRs that have been identified comprise toll-like receptors (TLRs), C-type lectin receptors (CLRs), as well as cytoplasmic proteins such as the Retinoic acid-inducible gene (RIG)-I-like receptors (RLRs) and NOD-like receptors (NLRs).

TLRs were the first receptors identified as PRRs by Bruce A Beutler and Jules A. Hoffmann, awarded for this discovery with the Nobel Prize in 2011 (Lemaitre et al., 1996; Medzhitov et al., 1997). 10 types of TLRs have been identified in humans and 12 types in mice. Through TLR2, microglia sense various components from bacteria, mycoplasma, fungi, and viruses inducing proinflammatory cytokines and interferon depending on the cells involved. TLR4 recognizes lipopolysaccharide (LPS), a component which is present on the surface of gram-negative bacteria known to be a cause of septic shock. It also recognises myeloid factor 2 (MD2) and viruses by binding to viral envelope proteins. TLR3, 7, 8, and 9 recognize nucleic acids derived from viruses and bacteria leading to the production of cytokines and interferon. While TLR2 and 4 are located in the plasmatic membrane, TLR 3, 7, 8, and 9 are mainly present on the endoplasmic reticulum membrane to avoid unwanted autoimmune activation

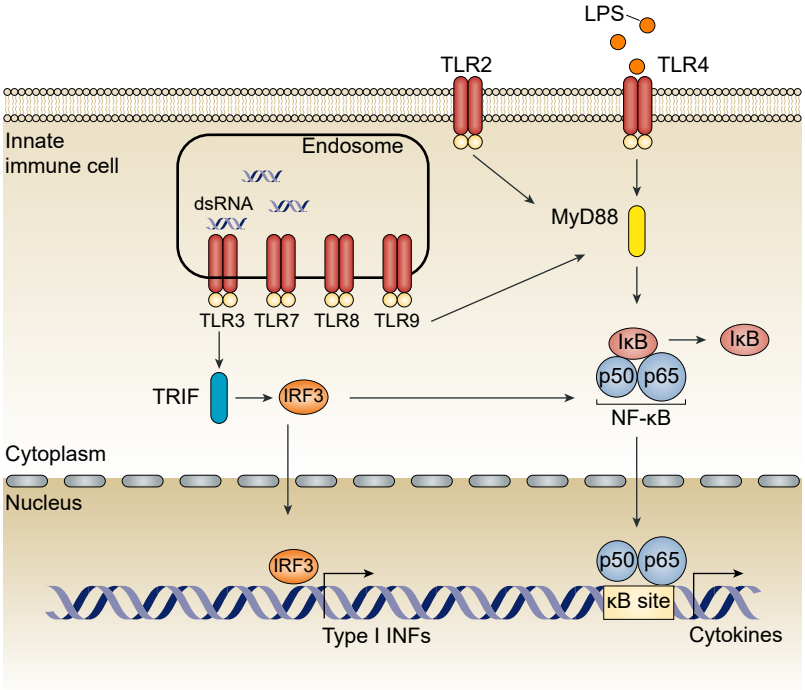

Fig.3. The TLRs signalling pathway. LPS is recognized by TLR-4 receptor which through the adaptor molecule MyD88 transduce the activation signals for IκB phosphorylation and subsequent translocation to the nucleus of the NF-κB heterodimer p50:p65 where it drives the expression of cytokine-related genes. Except TLR3, all TLRs use MyD88 to initiate the NF-κB pathway. Doble-stranded RNA (dsRNA) is recognized by TLR3 in the endosome which through TRIF-dependent signalling pathway activate IRF3 and NF-κB resulting in the induction of cytokines and type I interferon. Adapted from Takeuchi O and Akira S, Cell 2010. Graphics adapted from Rivest S, Nat Rev Immunol 2009.

(Takeuchi & Akira, 2010). Except for TLR3, all TLRs use the adaptor protein MyD88 to transduce activation signals leading to NF-κB translocation to the nucleus for subsequent activation of cytokine transcription and AP-1 transcription factor complex that targets cytokine genes (Akira et al., 2006). On the contrary, except for TLR2, stimulation of TLR3, TLR4, TLR7 and TLR9 induces type I interferon production in addition to proinflammatory signals. This pathway is initiated in a MyD88 independent manner through the adaptor molecule TRIF that interacts with kinases (iKK) that directly phosphorylates IRF-3 and IRF-7 (Fitzgerald & Kagan, 2020). TRIF interaction with other proteins leads to NF-κB activation as well (Meylan et al., 2004) (Fig.3).

Besides the signalling recognition to infectious agents (PAMPs), microglial cells can recognise damage-associated molecular patterns (DAMPs) like protein aggregates. In some CNS diseases like stroke or traumatic brain injury, the triggering agent is known; on the contrary, in neurodegenerative diseases the initial causing agent remains elusive what increases the difficulty of the therapeutic approach. Similar to PAMPs, DAMPs are recognized by PRRs, mainly TLRs and inflammasome, triggering signalling pathways previously described to initiate the inflammatory response.

One of the most studied PRR in response to damage is the NLRP3 (NOD-, LRR- and pyrin domain-containing 3) inflammasome. Inflammasomes are multiprotein complexes, formed of an inflammasome sensor molecule with the adaptor ASC and the effector caspase 1, that induces mostly posttranscriptional processing of IL-1β family cytokines and pyroptotic cell death (Heneka et al., 2018).

Simplifying the great complexity of the immune response, various triggers engaging different TLRs can induce a common outcome that broadly consist of the induction of different type of cytokines via NF-κB and IRF3 and 7 transcription factors.

3.1 Microglia cytokines production. Interleukins and interferon.

Cytokines are mediators produced during the inflammatory response. There are many different classifications but most of them can be distributed into four major families: tumor necrosis factor (TNF) family, interleukins, chemokines, and interferons (Serhan, 2010).

TNF family comprise 17 ligands that exist as membrane proteins with both a membrane-associated proform and a soluble mature form. TNF-α was the first cytokine discovered together with Il1b in the mouse serum during endotoxemia (Carswell et al., 1975). 13 years later, microglia were found to be the main cells producing TNF-α (Welser-Alves & Milner, 2013).

Among interleukins, IL1 has been of great interest in the immunology research. From the 2 isoforms, Il1b is one of the main molecules that modulate inflammation during systemic infection. The transcription of Il1b to pro-Il1b (a precursor inactive form) is triggered by a wide variety of immune insults through NF-κB transcription factor. Pro-Il1b remains in the cytosol until its pro-domain is cleaved by the cysteine protease caspase-1 to its active form. Following this, Il1b is secreted carrying out many different functions.

Interferons can be classified in three different types according to their receptors: INF I, INF II and INF III. Among the 14 subtypes of interferon I, the most studied ones are INFα and INFβ. On the contrary, INFγ is the only type II INF (de Weerd & Nguyen, 2012). Whereas type I and II INF receptors are expressed in microglial cells, astrocytes and to a lesser extent in neurons, type III INF are only expressed by neurons in the brain. Besides, the levels of type III INF are very low in the brain (Owens et al., 2014). Interferons are mostly related with antiproliferative, proapoptotic and antiviral functions although they are secreted also in response to other PAMPs and DAMPs.

Within the interferon family, the 2'-5'-oligoadenylate synthetases (OASs) are proteins playing important roles in the antiviral effect of interferons. There have been identified 12 Oas genes and 2 Oas-like proteins (Oasl1 and Oasl2) in the mouse genome compared to 4 genes found in humans OAS1, 2, 3 and OASL (whose mouse orthologue is Oasl2) (Eskildsen et al., 2002). The OASs protein is activated to produce OASs that activates a latent form of RNAse L resulting in the degradation of cellular and viral RNA and inhibition of viral replication. Furthermore, hOASL/mOasl2 activates recognition receptor RIG-I mediated IFN type 1 production and inhibits RNA virus replication (Zhu et al., 2014).

There are general limitations that need to be considered when interpreting the above-mentioned microglia function related with cytokine production:

A) Most of the data regarding pathways and mediators have been extrapolated from studies performed in bone marrow derived macrophages to microglia that are yolk-sac derived macrophages fully differentiated, surrounded by signals that come exclusively from the brain, without external contribution. This population specificity has gained importance over the years. As part of the ImmGen Project (Shay & Kang, 2013), the first whole mouse genome microarray was performed in 2012 in 4 different resident-macrophages sorted populations (microglia between them) identifying a unique gene-expression profile of macrophages from different organs (Gautier et al., 2012).

B) Most of the studies until the year 2000 had been performed in cultured microglia (Sierra et al., 2019). Microglia are very plastic cells highly influenced by their environment; therefore, many *in vitro* data cannot be extrapolated to *in vivo* function.

3.2 Microglia phagocytosis in the diseased brain

Unlike cytokines, the molecular pathways and receptors involved in the phagocytic activity of microglial cells are not that well explored. In addition, the functional beneficial or deleterious outcomes of microglia phagocytosis in different conditions are not well understood (Sierra et al., 2013). Microglia phagocytosis of cell debris and dying cells in the healthy brain has been addressed as beneficial and necessary to maintain brain homeostasis, while in the diseased brain, phagocytosis has been proposed to be ineffective. Phagocytosis mechanisms both in health and disease are thought to be common and the evidence we have so far, pointed out that it can be divided into three phases known as: “find-me”, “eat-me” and “digest-me”.

The “find-me” step is initiated when microglia encounter signals from apoptotic cells like extracellular nucleotides (ATP or UTP) or the fractalkine Cx3cl1. The “eat-me” step consists of the formation of the phagocytic cup in microglia pseudopodia to engulf the target (Lee et al., 2007). It is initiated with the activation of membrane receptors like TLRs in complex with scavenger receptors like CD14, or other receptors like the TAM receptor tyrosine kinases Mer and Axl, having an important role in the phagocytosis of apoptotic cells (Lemke, 2013). In particular, *Axl* has been shown to be upregulated by microglia in a mouse model of Parkinson disease (Fourgeaud et al., 2016). Other important receptor that signals the internalization of dead cells and protein aggregates is the triggering receptor expressed on myeloid cells (Trem2) that not only has been associated to phagocytosis but also plays an important role in neurodegenerative diseases binding lipoproteins like apolipoprotein-E (ApoE), which form complexes with Aβ aggregates facilitating their uptake by microglia (Han et al., 2017; Krasemann et al., 2017; Yeh et al., 2016). Finally, the “digest-me” phase comprise the phagosome formation around the target, and subsequent fusion with the lysosome to form the phagolysosome in which the target will be degraded (Desjardins et al., 1994). The functional outcomes of microglia phagocytic activity are antigen presentation, the activation of respiratory burst and the modulation of inflammatory response, however, their implications regarding pro- or anti-inflammation are not well understood yet (Sierra et al., 2013).

3.3 Microglia proliferation in the diseased brain

Microglia proliferation in health is a stochastic process, it is not random in disease but follows a selected clonal expansion (Tay et al., 2017). In the healthy brain, microglia proliferation is very important during embryonic development for proper brain colonization, and in adulthood for microglia population self-renewal. In the diseased brain, microglia proliferation seems to be finely tuned and there is controversy regarding its beneficial or detrimental effect. It

has been shown that a unique dose of 1mg/kg of LPS induces microglia proliferation in the hippocampus 48h from the administration (BrdU 200mg/kg) (Fukushima et al., 2015). In a mouse model of AD, microglia have been shown to proliferate in regions close to plaques (Kamphuis et al., 2012). Recent studies inhibiting microglia proliferation by blocking CSF-1 have shown an improvement in the progression of the AD-like pathology (Olmos-Alonso et al., 2016) and ALS pathology (Martinez-Muriana et al., 2016). Conversely, the induction of proliferative activity by blocking Trem2 has been shown to reduce AD pathology (Wang et al., 2020). Recent genome-wide association studies (GWAS) have identified the MS4 family variants (*MS4A4A* and *MA4A6A*) with the development of LOAD (Kamboh et al., 2012; Nguyen et al., 2015). There is little known about the specific function of the Ms4 family. They are transmembrane chemosensors (Greer et al., 2016) that regulate the immune cell function (Eon Kuek et al., 2016) and the cell cycle (Cruse et al., 2015; Cruse et al., 2010; Kutok et al., 2011; Xu et al., 2010). Further studies of the role of Ms4 family could shed light over a possible new therapeutic path.

3.4 Microglia morphology in the diseased brain

Microglia morphology was one of the first features described by Pío del Río Hortega (Río-Hortega, 1932). Microglia morphological plasticity is the result of a rapid actin cytoskeleton remodelling coupled with a complete set of membrane receptors (recently referred to as the sensome) that allow these cells to rapidly sense changes in their microenvironment and react fast modulating their responses (Franco-Bocanegra et al., 2019). Despite the complexity of this process, the study of microglia morphology *in vivo* in healthy mouse brains with time lapse imaging experiments showed that microglia processes are highly motile and present a highly structural dynamics that occur within one hour (Nimmerjahn et al., 2005).

Several articles have tried to make a consensus about the morphological states in which microglia can be found, to name a few: ramified, amoeboid, hypertrophic, dystrophic (senescent) (Savage et al., 2019). Although this is yet to be determined, microglia can be regarded as a spectrum from highly ramified to amoeboid.

Despite microglia state cannot be extracted from their morphology phenotype itself, it is especially useful coupled with transcriptomic of functional analysis. Microglia morphological phenotype is closely related to health or disease conditions; whereas in the healthy brain they are mostly ramified cells with active processes, in disease these cells retract their prolongations and swell their soma. In a mouse model of Alzheimer's disease, it has been shown that microglia present these features in the close proximity of the plaques whereas the distant microglia are more ramified with smaller soma confirming the importance of the microenvironment.

Altogether, the previously described functions occur in microglial cells during the inflammatory response. Understanding microglia transcriptional regulation of these functions is essential to gain insight into microglia diversity of functional states in different contexts or diseases as well as to unravel new therapeutic targets to modulate the detrimental effects of inflammation.

4. Microglia functional diversity in the healthy brain

Microglia heterogeneity has been observed for a long time. Yet in 1990, Lawson, Perry and Gordon described microglia heterogeneous brain distribution and morphology in the healthy mouse brain (Lawson et al., 1990). However, with the development of NGS technologies, this question has been further explored. In 2012, as part of the Immunological Genome (ImmGen) Project (Gautier et al., 2012), the definition of a microglia molecular signature in the healthy homeostatic brain was performed. One year later, Hickman et al., defined the microglia sensome as a group of 99 genes that encodes proteins for sensing endogenous and exogenous ligands (Hickman et al., 2013). Other authors have reported the identification of microglia sensome (Gosselin et al., 2014; Lavin et al., 2014). This characterization of microglia population markers in the healthy brain has been essential for the study of microglia functional diversity and have pointed out the importance of the microenvironment in the establishment of microglia identity both in mice and humans (Galatro et al., 2017; Gosselin et al., 2017). For example, Grabert et al., have shown microglia transcriptional differences between brain regions (cerebellum and hippocampal microglia compared to cortex and

Study	Heterogeneity measurements	Species	Brain area
Lawson JL et al., 1990	Density, morphology	Mm; F; 6-12w	Ctx, Hipp, BG, ot, mesen and rhombencephalon
Grabert K et al., 2016	Microglia bulk RNA-seq	Mm; M; 16w, 12&22mo	Ctx, Hipp, Cbm, Str
De Biase LM et al., 2017	Density, morphology, lysosomal content, microglia bulk RNAseq, electrophisiological properties	Mm; M&F; 8w	BG (Nac, VTA, SNc, SNr)
Ayata P et al., 2018	Microglia bulk and scRNA-seq, ChiP-seq, phagocytosis	Mm; M&F; 12-16w	Ctx, Hipp, Cbm, Str
Guneykaya D et al., 2018	Density, electrophysiology, phagocytosis, microglia bulk RNAseq	Mm; MvsF; 3&13w	Ctx, Hipp, Cbm, Str, amygdala
Masuda T et al., 2019	Microglia scRNA-seq, in-situ hybridization	HS & Mm; E16.5; 3&16w	Ctx, Hipp, Cbm, Cc, Fc, Sc, E16.5 (Fore and midbrain, Cbm, Sc)

Table 1. Studies showing microglia heterogeneity in the healthy brain. Indicating used technology: single-cell (sc), RNAsequencing (RNA-seq), Chromatin immunoprecipitation (ChiP). Individuals age: weeks-old (w) months-old (mo). Analysed brain area: Cortex (ctx), hippocampus (hipp), basal ganglia (BG), nucleus accumbens (Nac), ventral tegmental area (VTA), substantia nigra pars compacta (SNc) and pars reticulata (SNr), striatum (str) cerebellum (cbm) corpus callosum (cc), facial nucleus (fc) spinal cord (sc), olfatory telencephalon (ot).

striatum) and different susceptibility during aging (Grabert et al., 2016); and De Biase et al., identify microglia differences not only at the transcriptional level but also in morphology, lysosomal content, and electrophysiological properties across basal ganglia demonstrating that the characteristics of microglia on each region depend on the local cues (De Biase et al., 2017). Other authors have pointed out transcriptional differences of cerebellum microglia towards a more cell clearance phenotype (Ayata et al., 2018) (Table 1).

Altogether, the previously summarized studies are of great importance because it is the first evidence showing that the environment plays an essential role in the establishment of microglia functional diversity in the healthy brain and sets up the scenario for the study of microglia functional phenotypes in different contexts and diseases.

5. Microglia functional diversity in the diseased brain

With the appearance of RNA-sequencing technology, the search for new therapeutic targets has considerably increased trying to identify altered immune pathways and key factors that could regulate them and restore microglia function.

In 2015, Holtman et al., compare microglia transcriptome of LPS treated mice, a mouse model of AD (APP/PS1), a mouse model of MS (SOD1), and aging, and identify specific microglia expression patterns associated to each condition suggesting that microglia could be primed with aging or disease and giving a glimpse for the first time of microglia heterogeneity in disease (Holtman et al., 2015). By that time, single cell technologies were developing, and it was in 2017 when the first single cell microglia population article came out, showing disease associated microglia (DAM) in a mouse model of AD (5XFAD) and an amyotrophic lateral sclerosis (ALS) model (SOD1-G39A) (Keren-Shaul et al., 2017). Other authors also identify this microglia phenotype associated to neurodegenerative diseases in several models of AD like CK-p25 and APP/PS1 (Mathys et al., 2017; Sala Frigerio et al., 2019). DAM are characterized molecularly by expressing canonical microglia markers (Iba1, *Cst3*, *Hexb*...) together with a downregulation of microglia sensome genes (*P2ry12*, *Cx3cr1*, *CD33*…) and upregulation of genes involved in lysosomal, phagocytic and lipid metabolism like *ApoE*, *Axl*, *Lpl*, and *Trem2* among others.

Recently, a novel mechanism of microglia activation that could be common to all neurodegenerative diseases through neurodegeneration-associated molecular patterns (NAMPs) has been proposed (Deczkowska et al., 2018). Just like the previously described PAMPs and DAMPs, NAMPs could activate microglia by specific PRRs like Trem2 or purinergic receptors. Nevertheless, a common mechanism for sensing CNS damage in neurodegenerative diseases is still not known.

DAM is a common microglia phenotype present in most neurodegenerative diseases, we wonder whether this phenotype is present exclusively associated to neurodegeneration or can be found in other non-neurodegenerative pathologies that may allow us to further study DAM phenotype and establish possible new therapeutic approaches. As previously mentioned, different PAMPs/DAMPs stimulation of different PRRs can induce similar responses, we propose that despite the nature of the stimuli, microglial cells are able to carry out a specific number of transcriptional programs with specific differentially context-dependent regulated functions.

Besides, it has been shown that the establishment of DAM is a 2 stages process in which the transition from homeostatic to stage 1 is Trem2-independent and the factors that mediate this transition are currently unexplored whereas it is known that the transition from stage 1 to stage 2 is mediated by Trem2 signal. A reductionist approach that allows us to study the transition from homeostasis to reactive microglia could shed light in the mechanisms by which stage 1 DAM are established. One of the simplest models that have been widely used is the administration of one single dose of LPS. Most of the articles that include microglia transcriptomic data from LPS-treated mice do not explore the acute neuroinflammatory response but use this data as a proxy of microglia activation at a specific time point, mostly early time points (Bennett et al., 2016; Erny et al., 2015; Hanamsagar et al., 2017; Srinivasan et al., 2016), or several time points to study the restoration of the homeostatic state (Shemer et al., 2020). The two studies whose objective is to study microglia transcriptome during acute neuroinflammation (Hirbec and Sousa) explore microglia response at a specific time point, 24h from 4mg/kg LPS administration (Hirbec et al., 2018; Sousa et al., 2018). Hirbec et al., identify a subset of genes that are shared in acute a chronic neurodegenerative condition (Ms4a family among them). Sousa et al., performed single-cell RNA-seq of microglia isolated cells and showed a downregulation of homeostatic genes and upregulation of proinflammatory cytokines identifying a subset of cells defined as an intermediate activated state suggesting the possibility of existence of microglia heterogeneity under acute inflammatory conditions. In summary, the studies of microglia transcriptome after an acute LPS challenge have poorly addressed the complexity of the acute inflammatory response. Most of them are focused only in one time point after the challenge, which makes it impossible to really understand microglia dynamics.

Despite the extensive knowledge about the activation pathways and mediators that comprise microglia inflammatory response, there is a lack of information about the dynamic regulation of microglia activation and resolution of the inflammatory process that is key to understand how to promote the beneficial outcomes of the inflammatory response.

Besides, as innate immune pathways are amenable to pharmacologic interference, there is a great prospect that a better understanding of the contribution of different pathways to neurodegenerative diseases could lead to future development of targeted therapies.

6. NF-κB as a regulator of inflammation

The nuclear factor binding near the κ-light-chain gene in B cells (NF-κB) is a transcription factor that mediates the inflammatory response. It is formed by five protein monomers that work as hetero- or homodimers, yielding up to 15 NF-κB complexes. The five proteins that comprise the Rel transcription factor family are: p50, p52, RelA (p65) and c-Rel that share N-terminal homology with the v-Rel oncogene. RelA, RelB and c-Rel are synthesized as mature proteins with transcription transactivation domains. The most studied heterodimers are p50:p65 and p52:RelB, although other combinations exist with different functions (Zhang et al., 2017).

In unstimulated cells, NF-κB are mainly cytoplasmic due to the binding of a ser of inhibitory proteins, inhibitor of the kB (iKB) family. The canonical p50:p65 is regulated by the subunit iKBa. The NF-κB induced genes include nearly the entire molecules related to the immune response: chemokines, cytokines, adhesion molecules, inflammatory mediators, giving NF-κB a main role in the regulation of the inflammatory response (Zhang et al., 2017). A big effort has been made to target NF-κB pathway to modulate inflammation pharmacologically, unfortunately, unexpected side effects have been found due to the broad role that hast NF-κB in cellular regulation. Apart from NF-κB key role in immune cells, other functions have been attributed to this transcription factor in the regulation of synaptic plasticity and behaviour in the brain. For example, Meffer et al., show that constitutive depletion of the *RelA*/p65 subunit in mice produces defects in spatial learning (Meffert et al., 2003). Unfortunately, despite *RelA*/p65 is mainly expressed by microglia (Zhang et al., 2014) in the CNS, the constitutive depletion of this subunit did not allow us to attribute the previously mentioned alterations to microglia modulation of neuronal circuits or other cell types of effect.

Altogether, a better understanding of the specific role of *RelA*/p65 subunit in microglia could allow us to gain insight into its function and the beneficial or detrimental effects of its modulation.

OBJECTIVES

During the last decades, evidence has accumulated continuously on the increasing relevance of inflammation and the role of the immune system in CNS diseases onset and progression. Collectively these studies dramatically changed the way of understanding a wide variety of neurological and neuropsychiatric pathologies for which there is no cure nowadays.

As the resident innate immune cells in the central nervous system, microglia are the main mediators of the inflammatory response in the brain. However, very little is known about the transcriptional regulation and the temporal dynamics that underlie microglial cells acute neuroinflammatory response. Understanding this process is critical to improve our knowledge of CNS diseases and to discover new therapeutic approaches.

The specific objectives defined for this thesis are the following:

1. To stablish a protocol to isolate microglial cells by FACS without external modifiers of their transcriptome.
2. To elucidate microglia transcriptome and DNA regulatory elements underlying the acute neuroinflammatory response.
3. To characterize microglia functional diversity during the acute neuroinflammatory response.
4. To correlate microglia functional diversity from acute to chronic inflammatory conditions.
5. To identify marker genes and possible therapeutic targets for the treatment of acute and chronic neuroinflammatory pathologies.
6. To translate the previous findings in mouse models of disease to human diseases with a chronic inflammatory component.
7. To address the role of NFkB-p65 subunit in microglia regulation of the neuroinflammatory process.

MATERIALS AND METHODS

Animals

Mice of both sexes and ages postnatal day 60 (P60) to P160 were used in all experiments except for RNA- and ATAC-sequencing experiments where only male mice were used. Mice were maintained and bred under standard conditions in normal light dark cycle (lights on 8a.m., lights off 8p.m.) and ad libitum water access in the pathogen-free animal facilities at the *Instituto de Neurociencias* consistent with Spanish and European regulations and approved by the Institutional Animal Care and Use Committee. All strains were maintained in a pure C57BL/6J background.

B6.129P2(Cg)-Cx3cr1$^{tm2.1(cre/ERT2)Litt}$/WganJ mice (Cx3cr1$^{cre/ERT2-EYFP}$)

Cx3cr1$^{cre/ERT2-EYFP}$ were originally obtained from Jackson (Stock Nº: 021160). These mice express a Cre-ERT2 fusion protein and an enhanced yellow fluorescent protein (EYFP) from endogenous Cx3cr1 promoter/enhancer elements (Jung et al., 2000). All mice were heterozygous for the transgene.

Cx3cr1$^{cre/ERT2-EYFP}$ x RelA$^{f/f}$ (RelA-cKO)

These mice were generated by crossing Cx3cr1$^{cre/ERT2-EYFP}$ mice (previously described) with RelA$^{f/f}$ mice that present *loxP* sequences flanking exons 5-8 of *RelA* gene that code for the majority of Rel homology domain (essential for interaction with other transcription factors) (Steinbrecher et al., 2008). Control mice were Cx3cr1$^{cre/ERT2-EYFP}$ mice or C57BL6J x RelA$^{f/f}$.

B6.Cg-Zbtb20$^{Tg(PDGFB-APPSwInd)20Lms}$/2Mmjax (J20)

J20 mice express a mutant form of the human amyloid precursor protein (APP) bearing the Swedish (K670/M671L) and the Indiana (V717F) mutations (APPSwInd). Male J20 mice were used for singe-cell RNA-sequencing experiments at 12 months of age.

B6C3-Tg(APPswe,PSEN1dE9)85Dbo/Mmjax (APPswe/PS1dE9)

APPswe/PS1dE9 (APP/PS1) mice present two transgenes inserted at a single locus in Chromosome 9, each transgene is controlled by the mouse prion promoter. One transgene cDNA encodes a chimeric amyloid β (A4) precursor protein (APPswe). In the second transgene the cDNA encodes the “DeltaE9” mutation of human presenilin 1. The DeltaE9 mutation of the human presenilin 1 gene is a deletion of exon 9 and corresponds to a form of early-onset Alzheimer’s disease. Male APP/PS1 mice were used for RNAscope experiments at 20 months of age.

Human tissue

Post-mortem human frontal cortex frozen tissue was provided by Queen Square Brain Bank for Neurological Disorders at the Institute of Neurology, University College of London (UCL), London, UK. 10µm thick Alzheimer's disease donors and age-matched controls were stored at -80ºC under a license from the Human Tissue Authority at the Drug Discovery Institute, UCL.

Compounds

Lipopolysaccharides (LPS)

LPS (*Escherichia Coli* #L2880, SigmaAldrich) was dissolved in sterile PBS1X and administered intraperitoneally (5mg/kg i.p.).

5-Bromodesoxiuridine (BrdU)

BrdU (#B5002, SigmaAldrich) was diluted in sterile NaCl 0,9% and administered at a dose of 50mg/kg intraperitoneally (i.p.). To study proliferation during de first 24h from LPS administration, BrdU was incorporated after 5h, 12h and 22h from LPS administration. To study proliferation from 24h to 72h, BrdU was incorporated at 24h, 36h, 48h, 60h and 70h after LPS administration.

Tamoxifen (TMX)

TMX (#T5648, SigmaAldrich) was resuspended in corn oil (#C8267, SigmaAldrich) (50ºC 1h shaking protected from light) at a concentration of 25mg/mL. Mice were gavaged at 2-3 months of age with five doses of 4mg of TMX each day on alternate days. All the experiments were conducted at least one month after TMX administration.

Immunofluorescence

Mice from P60 to P160 were deeply anesthetized with ketamine (Xilagesic, CALIER) and xylazine (Imalgene, MERIAL LABORATORIOS) cocktail and transcardially perfused with PBS1X followed by 4% paraformaldehyde (PFA) in PBS1X. Brains were post-fixed overnight at 4ºC in 4% PFA and embedded in saccharose 30%. 50µm coronal sections were cut by cryotome and preserved at -20ºC in cryoprotection solution (30% ethylene glycol, 30% glycerol, 30%dH2O, 10% PBS10X).

For immunostaining, coronal sections were washed with PBS1X and PBS1X-0,3% TritonX-100(PBS-T0,3%) and incubated 2h at room temperature (RT) with 5% Newborn Calf Serum (NCS) in PBS-T0,3%. After that, slices were incubated overnight with primary antibodies

dissolved in PBS-T0,3%. Before and after the incubation with the secondary antibodies (2h, RT), washes with PBS-T0,3% were performed. Finally, cell nuclei were counterstained by incubation 10min at RT with 10mM DAPI (1:10000) before mounting. Primary antibodies used in this study included the following: rabbit anti-Iba1 (1:500; Wako), rabbit anti-Ki67 (1:500; abcam #ab15580), rat anti-BrdU (1:500; abcam #ab6326), rat anti-CD68 (1:500; abcam #ab53444), chicken anti-GFP (1:500; Aves lab). Secondary antibodies used in this study included the following: AlexaFluor anti-rabbit 488 (1:500), AlexaFluor anti-rabbit 594 (1:500), AlexaFluor anti-chicken 488 (1:500), AlexaFluor anti-rat 594 (1:500).

For BrdU staining, two additional steps were carried out. For antigen retrieval, slices were incubated with sodium citrate buffer (10mM sodium citrate, 0,05% tween20 pH6) for 30min 80ºC 600rpm. After washing with PBS1X, slices were incubated with HCl 2N for 30min 37ºC 400rpm.

RNAscope *In situ* hybridization

Mouse Tissue

To detect single mRNA molecules, RNAscope was performed on 4% PFA-DEPC treated fixed mice brains from LPS-treated and control mice. 24h post-fixation, brains were embedded in 20% sucrose-DEPC treated and frozen at -80ºC in Tissue-Tek O.C.T. Compound (#4583 Sakura). 20µm sections were cut onto Superfrost slides and dried at -20ºC for 2h and kept at -80ºC. RNAscope was carried out according to manufacturer's instructions with the following catalogue probes: Mm-P2ry12 317601; Mm-Il1b 316891; Mm-Cxcl10; Mm-Oasl2 534501; Mm-Irf7 534541; Mm-Ms4a4a; Mm-Apoe 313271; Mm-Axl 450931. For some experiments RNAscope was followed by IF with anti-Iba1.

Human Tissue

RNAscope was performed on 10um human tissue sections. After thawing, slides were fixed with 4% PFA for 25min RT. RNAscope was carried out using the Multiplex Fluorescent V2 Kit (323110, ACD Bio-Techne) following manufacturer instructions. The probes used for the hybridization step were Hs-IL1B 310361; Hs-AXL 602131; Hs-OASL 540481; Hs-TREM2 420491.

Image acquisition and analysis

Confocal images for all experiments were acquired with Leica SPEII microscope. All images have been acquired in somatosensory cortex.

Proliferation assay

For BrdU and Ki67 assays, 6-9 z-stack confocal images from at least two adjacent brain regions were acquired using a 20X objective and 1µm of z step size. Analysis was performed by Imaris v9.2.1 software (Bitplane) using the semiautomatic spots tool to quantify microglial cells. Algorithm parameters were setup as follows: Source channel corresponds to microglial cells Iba1 marker or GFP. The spot detection estimated XY diameter was 9um, with background subtraction. Filter type was the setup by quality and semiautomatic spots detection was performed. Threshold parameter was modified in order to increase detection accuracy. Spots on the edges of the 3D images were manually removed. Once one spot corresponds to one cell soma, colocalization with BrdU or Ki67 was determined. To do this, a mask of each channel (BrdU or Ki67) was performed. Masked channel was quantified then with spots tool. Algorithm parameters were the same as in the step before, but in this case the source channel corresponds to the masked channel.

Phagocytosis assay

For CD68 assay and morphological analysis, 6-9 z-stack confocal images from at least two adjacent brain regions were acquired using a 40X objective and 0.5µm of z step size. For analysis of CD68 intracellular distribution, individual microglial cells and CD68 signal were reconstructed with Imaris surfaces module.

Morphological analysis

To analyse microglia morphology, Imaris filament module was used, and individual microglial cells were reconstructed. The source channel corresponds to microglial cells Iba1 marker or GFP. Algorithm parameters are setup as follows: Reconstruction starting point is 8.96um. Starting point threshold correspond to cell soma and seed point threshold was set up in order to follow cell signal the more accurate as possible. We remove disconnected segments with a maximum gap length of 5µm (with a separation distance > 5 µm).

Cell density analysis

For cell density quantification, somatosensory cortex images were acquired with an epifluorescence Leica microscope using a 20X or 40X objective depending on the experiment. Quantifications were performed with ImageJ software.

RNAscope analysis

RNAscope analysis were carried out with Imaris software 9.5. For LPS mouse tissue, individual iba1 positive cells were reconstructed with surfaces module. All the probes were

quantified in the same way: a mask of the reconstructed cell was performed and each of the RNAscope positive dots were quantified with Imaris spots module. For APP/PS1 mouse tissue and for human tissue, individual cells where reconstructed with the Imaris cells module considering DAPI staining for nuclei identification and *P2ry12* or *Trem2* positive signal for cell reconstruction.

Mouse behaviour

Behavioural tests were performed in male RelA-cKO mice and their control group (Cx3Cr1::CreERT2-P2A-YFP mice or C57BL6J x RelA$^{f/f}$) during light cycle (08:00 to 20:00). All mice received intragastrical (I.G.) 20 mg of tamoxifen distributed during five alternate days at least 1 month from the last administration before the behavioural tests. All the experiments were blinded.

Open Field

Mice were placed in 48x48x30cm white acrylic boxes and monitored during 30 minutes using the video-tracker software SMART (Panlab S.L., Barcelona, Spain). Total distance and % of time in zones were extracted as a measure of mice locomotor activity.

Elevated Plus Maze

Mice were placed in a central platform (10x10 cm) of a plus maze that consisted of two open arms (50x10 cm) and two enclosed arms (50x10x30cm) elevated to a height of 50cm above the floor. The maze was made of black acrylic glass. The open arms lacked any walls and were indirectly illuminated. The behaviour was recorded for 5 minutes using the software SMART (Panlab S.L., Barcelona, Spain). The % of time in each zone was extracted as a measure of anxiety-like behaviour.

Forced Swimming Test

A transparent cylindrical Plexiglass tube (30x20 cm) was filled with water at 25ºC. Mice were placed in the water and recorded during 7 minutes with the software SMART (Panlab S.L., Barcelona, Spain). The percentage of time immobile was taken as a measure of anhedonia a main characteristic of depressive related behaviour.

Operant conditioning

Skinner box modules (n = 5) measuring 12.5 × 13.5 × 18.5 cm (MED Associates, St. Albans, VT, USA) were used to carry out the operant conditioning tests. The conditioning boxes were housed within sound-attenuating chambers (90 × 55 × 60 cm), which were constantly illuminated (19 W lamp) and exposed to a 45-dB white noise (Cibertec, S.A.,

Madrid, Spain). Each Skinner box was equipped with a food dispenser, a lever and a small light bulb locate over the lever. Before training, mice were handled daily for 7 days and food-deprived to 90% of their free-feeding weight (Jurado-Parras et al., 2012; Madronal et al., 2010). In all cases, training sessions lasted for 20 min. The start and end of each session was indicated by a tone (2 kHz, 200 ms, 70 dB) provided by a loudspeaker located in the recording chamber.

In a first experimental step, mice (19 WT and 17 RelA-cKO) were trained to press the lever to receive pellets (MLabRodent Tablet, 20 mg; Test Diet, Richmond, IN, USA) using a fixed-ratio (1:1) schedule. Animals were maintained on the 1:1 schedule for 10 training sessions. Mice typically reach criterion (pressing the lever ≥ 20 for two successive sessions) after 5–7 days of training (Jurado-Parras et al., 2012; Madronal et al., 2010). All mice were trained for 10 days.

After this first training, mice were further conditioned using a small bulb light on/light off protocol for 10 additional days. In this test, only lever presses performed during the light period (20 s) were reinforced with a pellet. The cued light was provided by the small bulb located over the lever. Lever presses performed during the dark period (20 ± 10 s) were not reinforced and restarted the dark protocol for an additional random (1–10 s) time. The light on/light off coefficient was calculated as follows: (number of lever presses during the light period − number of lever presses during the dark period)/total number of lever presses). In this case, the criterion was to reach a positive performance (i.e. a larger number of lever presses during the light on than during the light off periods) for two successive sessions. Conditioning programs, lever presses, and delivered reinforcements were controlled and recorded by a computer, using a MED-PC program (MED Associates, St. Albans, VT, USA).

Acute brain slices preparation and electrophysiology recordings

Hippocampal slices preparation

Coronal hippocampal slices (300μm thick) were obtained from 3-4-month-old male mice. Deeply anesthetized mice by intraperitoneal injection, were transcardially perfused with cold cutting solution containing (mM) 200 sucrose, 26 $NaHCO_3$, 10 glucose, 3 KCl, 1.25 NaH_2PO_4, 4 $MgSO_4$, and 0.5 $CaCl_2$. Same solution was used during slicing in a Leica VT1000S vibratome. After sectioning, slices were placed in a holding chamber containing standard artificial cerebrospinal fluid solution (ACFS) (mM): 124 NaCl, 26 $NaHCO_3$, 10 glucose, 3 KCl, 1.25 NaH_2PO_4, 1 $MgSO_4$, and 2 $CaCl_2$, and then stored at room temperature (RT) (22–24°C). After an incubation period of at least 1 hr, slices were transferred to a

submersion recording chamber at RT. Incubation solutions were continuously bubbled with a gas mixture of 95% O_2 / 5% CO_2.

Electrophysiology

The recording chamber was perfused with ACSF gassed with 5% CO_2 / 95% O_2. Synaptic responses were evoked with bipolar electrodes using single-voltage pulses (up to 10mA). The stimulating electrodes were placed over the Schaffer collateral fibers in the *stratum radiatum* area. Field excitatory postsynaptic potentials (fEPSPs) were recorded with low-resistance glass electrodes filled with ACSF placed in the apical dendritic layer of CA1 area.

An input–output curve was recorded for each slice to compare basal synaptic transmission under different stimulation intensities (mA): 0.1, 0.5, 1, 5, 10. This curve was also used to set the baseline fEPSP of the maximal slope for the long-term potentiation (LTP) experiments. Baseline stimulation was delivered every 15 s (0.01 ms pulses) for at least 20 min before LTP induction to ensure the stability of the response. LTP was induced by high-frequency stimulation (3 bursts of 100 pulses at 100 Hz in 1 sec given every 10sec, repeated 3 times every 20 sec) and the responses were recorded for 1 h after induction. To monitor the paired-pulse ratio (PPR) 2 pulses were delivered by increasing interstimuli intervals (25, 50, 100, 200, and 400 ms).

Microglia cell sorting

Tissue dissociation and myelin removal

The whole process was carried out at 4ºC. Cx3cr1$^{cre/ERT2-EYFP}$ were sacrificed by cervical dislocation and brain was removed from the skull and put into ice-cold sterile PBS1X. Meninges were removed with dissecting forceps and the two cortex hemispheres were dissected and put into 2mL of dounce buffer (15mM HEPES, 0.5% glucose, HBSS1X). Each cortex hemisphere was cut in small fragments before being transferred to a tissue homogeneizer (FisherScientific #10198611) containing 5mL of dounce buffer. Tissue fragments were then homogeneized after 9-10 strokes. The resulting cell suspension was transferred through a 40µm cell strainer into a 50mL tube in ice containing 0.5mL of dounce buffer. Myelin removal was performed with a) miltenyi myelin removal beads to capture the very early microglia transcriptional response to LPS (1h) in RNA-seq, and b) with percoll gradient for the rest of the times in RNA-seq and ATAC-seq. **A)** Centrifuge the cell suspension 800G 10min 4ºC ac/dc 9/9. The cell pellet was then resuspended in 720µL MACS buffer (0.5% BSA, 2mM EDTA, PBS 1x) and 60uL of myelin removal beads (#130-096-733 MACS Miltenyi Biotec) mixing all by pipetting. The sample was then divided into two 2mL before incubating it 10min

at 4ºC. After this, tubes were re-filled to its maximum capacity (2mL) with MACS buffer and centrifuged 30s at 10K rpm at 4ºC. The washing step was performed one time more and the final cell suspension was transferred through one LS column (previously rinsed with 2mL of MACS buffer) per tube. The flow through was recovered in a 15mL Eppendorf tube in ice and centrifuged 800G 10min 4ºC ac/dc 9/9. The pellet was resuspended in 350uL of FACS buffer (1% BSA, 2mM EDTA, 25mM HEPES, PBS1x) and microglial cells were sorted by fluorescent activated cell sorting (FACS). **B)** To form a percoll gradient, 2.5mL of isotonic percoll solution (SIP) (percoll: PBS10X, 9:1) was added to the cell suspension in order to obtain a final 25% SIP concentration. To form the second phase, 15mL of PBS1x were added. The gradient was centrifuged 800G 15min 4ºC ac/dc 0/0. After this, the myelin (interphase) together with the rest of the supernatant were removed and the cell pellet was resuspended in 2mL of PBS1X, transferred into two 2mL Eppendorf tubes and centrifuged 10K rpm 30s 4ºC. For cell sorting, the pellet was resuspended in 350µL of FACS buffer and microglial cells were sorted by FACS.

For immunostaining, the cell pellet was resuspended in 100µL of FACS buffer. 1µL of blocking solution was added and incubated for 10min at 4ºC. 400µL of FACS buffer were added before centrifugation 10.000rpm 30s 4ºC. The cell pellet was resuspended in 100µL of FACS buffer, 1µL of primary antibody was added and incubated for 30min at 4ºC. 400µL of FACS buffer were added before centrifugation 10.000rpm 30s 4ºC. Finally, the cell pellet was resuspended in 200µL of FACS buffer.

FACS protocol

Microglial cells were sorted in an BD FACS Aria III sorter. After discriminating cell doublets microglial cells were identified by FITC fluorescence intensity for sorting. Nozzle size was 85µm and cell recovery was performed in RLT lysis buffer (#79216 Qiagen) at 4ºC for RNA-sequencing or MACS buffer for ATAC-sequencing.

RNA isolation

RNA from microglia FACS sorted cells was isolated with RNeasy Mini Kit (#74104 Qiagen). Microglial cells were directly recovered in 400µL of RLT lysis buffer, homogenised by vortexing and stored at -80ºC until processing. The process was completed following manufacturer protocol and DNases were column digested with RNase-free DNase set (#79254 Qiagen). RNA yields quality and quantity were measured with 2100Bioanalyzer using RNA Pico chip.

cDNA synthesis and RT-qPCR

First strand cDNA synthesis was performed with Thermo Scientific RevertAid Kit (#K1621).

RNA was incubated with 1µL of random hexamer primers 65ºC for 5 min. After this, 5X reaction buffer, ribolock RNase inhibitor (20U/µL), 10mM dNTP mix and RevertAid M-MuL V RT (200U/ µL) were added in the quantities indicated and incubated 5min 25ºC, 60min 42ºC and 70ºC 5min. Finally, cDNA was stored at -20ºC.

For RT-qPCR, 1µL of primers against the interest target genes were pipetted together with 1µL of cDNA, 4µL of 5x PyroTaq EvaGreen qPCR Mix Plus ROX (#87H24-001 Cmb) and 14µL of miliQ filtered water. Reaction was carried out in Applied Biosystems QuantStudio 3 real-time PCR. Each independent sample was analysed in duplicate and normalized with GAPDH.

Library preparation and RNA-sequencing

RNA isolation for sequencing has been prepared as described above. For RNA-seq, RNA integrity was assessed using RNA Pico Chip on a 2100Bioanalyzer (Agilent, Santa Clara CA). Independent samples were sequenced following manufacturer instructions in a HiSeq2500 sequencer (Illumina, Inc). Each sample correspond to whole cortex microglia sorted cells from individual mice. For microglia kinetic study in response to LPS, single-stranded cDNA prepared from total RNA (≈1 ng/µl) using poly(A) enrichment was generated with NEBNext Ultra II Directional RNA Library Prep Kit for Illumina (NEB #E7760) following manufacturer instructions. For RelA-cKO samples (>0,5ng/µl) double-stranded cDNA by ribosomal RNA depletion was generated with SMARTer Ultra Low RNA Kit for Illumina Sequencing (Cat. No. 634936) following manufacturer instructions. Final libraries were sequenced single end using a HiSeq 2500 sequencer (Illumina Inc).

ATAC assay and library construction

Whole cortex microglia cells (50000 cells) were sorted in 400µL of MACS buffer and pelleted by centrifugation for 15min at 500g 4ºC. Cell pellets were washed with PBS 1X and centrifuged for 15min at 500g 4ºC. Cell pellets were resuspended in 100 µL of lysis buffer (10mM Tris-HCl pH 7.4, 10mM NaCl, 3mM $MgCl_2$, 0,1% Igepal CA-630), incubated 5min on ice and centrifuged for 30min 500G 4ºC. Supernatant was discarded and nuclei were resuspended in 25µL of reaction buffer containing 2.5 µL of Tn5 transposase, 25µL of TD buffer (Illumina Tagment DNA enzyme and buffer kit #20034210) and 22.5µL of Nuclease-Free water. The reaction was incubated for 30 min at 37ºC 400rpm. Tagmented DNA was isolated using Qiagen MinElutePCR purification kit #28004. For library preparation, PCR was performed by mixing 25µL NEBNext Ultra II Q5 Master Mix #M0544S and 1.25 µL of 25µM custom PCR primers with transposed DNA. Conditions were: 72ºC 5min, 98ºC 30s, 98ºC 10s, 63ºC 30s, 72ºC 1min, repeating steps 3 to 5, 5 cycles. To reduce GC and size

bias, qPCR was performed to stop the amplification before saturation. 5µL of previously amplified DNA were added to 10 µL of PCR master mix containing 5µL NEBNext Ultra II Q5 Master Mix, 0.09µL 100X Sybr Green I, 2.5µM custom PCR primers, and 4.41µL Nuclease-Free water and run 20 cycles in a QuantStudio 3 real-time PCR. Based on the RT-qPCR amplification results, 4 extra PCR cycles were added to the remaining 45µL of reaction. Libraries were purified using SPRI size selection kit with a ratio (0.9X-0.5X). Libraries final quality control was assessed with high sensitivity DNA Chip and measured in 2100bioanalyzer. Libraries were quantified with Qubit 2.0 Fluorometer using Qubit dsDNA BR Assay kit #Q32850. Purified libraries were sequenced paired end using HiSeq 6000 sequencer (Illumina Inc).

Microglia single-cell suspension and library preparation for single-cell RNA-sequencing

Centrifuges and sterile tools were prechilled to 4ºC. 12 months old J20 male mice were euthanized by cervical dislocation and brains were quickly removed and placed in ice-cold PBS 1X. After meninges removal, a pool of 6 hippocampi from 3 mice was dounce homogenized in ice-cold dounce buffer (15 mM HEPES, 0.5% glucose and HBSS 1X) 15-20 times. The resulting cell suspension was transferred into a 2mL eppendorf tube and centrifugated 800g for 10 minutes at 4ºC. The supernatant was removed, and the pellet was resuspended in 300µL of FACS buffer (1% BSA, 2mM EDTA, 25 mM HEPES, PBS 1X) and incubated with anti-mouse CD16/CD32 Fc Block™ (1:100 dilution, BD Bioscience) for 10 min at 4ºC. After incubation, the cells were resuspended in 400µL of FACS buffer and centrifuged at 10.000 rpm for 30 sec. The resulting cell pellet was resuspended in 500µL of FACS buffer and stained with anti-mouse CD11b (1:100 dilution, Biolegend) and cells were incubated for 30 min at 4ºC, washed and resuspended in 900µL of FACS buffer. 17.500 CD11b+ cells were sorted on a BD FACS Aria III using an 85µm nozzle. After sorting, a CD11b+ cell suspension volume equivalent to 7000 target cells was used. Emulsion gel beads preparations and libraries were performed with Chromium Controller and Single Cell Gene Expression 3´according to the Chromium Next GEM Single Cell 3´ Reagent Kits v3.1 (Dual Index) user guide. The quality and quantity of libraries were verified by a High-Sensitivity DNA Kit (Agilent Technologies) on a 2100 BioAnalyzer (Agilent Technologies).

Single-nucleus suspension and library preparation for single-nucleus RNA-sequencing

To set up the previous microglia single-cell protocol I took advantage of my experience acquired during early stages of my PhD where I developed a protocol for tissue processing following single-nucleus libraries preparation with 10X Genomics technology. I have carried out this protocol as part of the research article included in this PhD thesis in Annex section

as quality indicator (Lipinski et al., 2020). Single-nucleus RNA-seq experiment was carried out as follows: dKAT3-ifKO mice (CaMKIIα-creERT2, *Ep300*$^{f/f}$, and *Crebbp*$^{f/f}$) lacking both transcriptional coactivators lysine acetyltransferases type 3 (KAT3) family members P300 (*Ep300)* and CBP (*Crebbp)* were used in this experiment. 3 months-old dKAT3-ifKO mice were sacrificed either 2 weeks (2w) or 1 month (1m) after TMX administration. Mouse hippocampi were dissected in ice-cold PBS1X. First, hippocampal tissue was homogenized in a Dounce homogenizer containing 1ml of ice-cold MACS buffer (0.5% bovine serum albumin (BSA), 2mM ethylenediaminetetraacetic acid, PBS 1X)12–15 times with the pestle. The cell suspension was transferred to a 2ml tube and centrifuged 15min at 500g and 4 °C. Second, the cells were lysed by resuspending the cell pellet in 2 ml of lysis buffer (10mM Tris–HCl, 10mM NaCl, 3mM MgCl2, 0,1% IGEPAL). The tissue was incubated in the lysis buffer 5min on ice. Samples were then spun down at 500g for 30min in a pre-chilled centrifuge. Third, the pellet was resuspended in PBS 1X, 1% BSA, and sorted in a BD FACS Aria III (Fig.4). Finally, for the generation of the barcoded single-nuclei suspension and libraries preparation, 15,000 nuclei per sample (pool of 2 animals) were loaded into the single cell A Chip and then the generation of barcode-containing partitions was carried out with the Chromium Controller (10X Genomics). Chromium Single Cell 3' Library & Gel Bead Kit v2 was employed for post-GEM-RT clean-up, cDNA amplification and the generation of barcoded (ChromiumTM i7 Multiplex Kit) libraries. Libraries were sequenced on an Illumina HiSeq 2500 sequencer to an average depth of 290–310 million reads per sample.

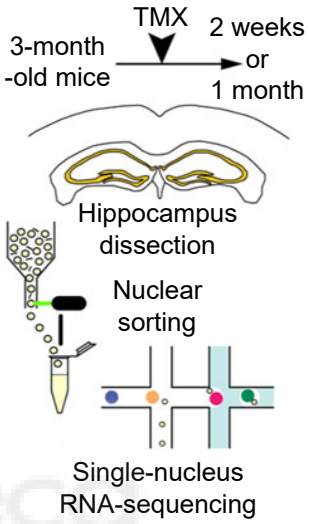

Fig.4. Scheme of the single-nucleus RNA-seq experiment.

Bioinformatic analysis

RNA-sequencing

Next generation sequencing reads were mapped to the mouse genome (mm9) using HISAT2 package (v 2.1.0) (Kim et al., 2015). Reads were counted using HTSeq count package (v.0.11.1) (Anders et al., 2015) against Ensembl v67 annotation. The raw counts were processed using DESeq2 package from R Bioconductor toolset (Love et al., 2014). Principal component analysis (PCA) was performed on the top 500 most-variable genes across all samples. Comparisons were performed on the count data of entire gene transcripts using the DESeq2 package (v1.6.3). Graphical representation was generated with R Bioconductor toolset.

ATAC-sequencing

All sequenced dataset adapters were trimmed using cutadapt (v.1.18) and aligned to mm10 with bowtie2 (version 2.3.4.3) (Langmead & Salzberg, 2012). Duplicate reads were removed using Picardtools (v.2.20.6). Only reads with mapq >30 that map to nuclear chromosomes were used for further analysis. Analysis, annotation, and gene ontology of DARs (differentially accessible regions) was done with R Scripts and the packages diffbind (v.3.0.15), ChIPpeakAnno (v.3.24.2) and biomaRt (v.2.46.3). Regions with FDR < 0.05 were considered significantly changed. For heatmaps, DESeq2 (v1.30.1) and gplots (v.3.1.1) were used. Motif analysis was done with homer (v4.9.1).

Single-cell RNA-sequencing

Quality control of sequenced reads was performed using FastQC (Babraham Institute). Sequenced samples were processed using the Cell Ranger (v6.0.1) pipeline (10x Genomics) and aligned to the pre-built Cell Ranger mouse reference package refdata-gex-mm10-2020-A (July 7, 2020) by 10X: GRCm38 (mm10) mouse reference genome over the gene annotation GENCODE vM23 / Ensembl v98. Barcodes with total unique molecular identifier (UMI) count > 10% of the 99th percentile of the expected recovered cells were selected for further analysis. Using this criterion, we retrieved 7,033 (control), 7,865 (J20) high quality cells per sample. Mean reads per cell were 62,590 (control) and 69,129 (J20). Median genes per cell were 1,129 (control) and 1,812 (J20). Minimum UMI count per cell were 500 (control), 500 (J20), well above the typical quality standards in single-cell sequencing. Single-cell RNA-seq data were subsequently pre-processed and further analysed in R (v.4.0.5) using Seurat (v.4.0.1) (Butler et al., 2018; Stuart & Satija, 2019). An initial exploratory analysis was performed on each dataset separately. After it, filtering parameters were as follows: genes, min.cells = 3; cells, nFeature_RNA > 1,300 & nFeature_RNA < 4,000 & percent.mt < 5. Data were then normalized using global-scaling normalization (method: LogNormalize, scale. factor = 10,000). This analysis retrieved a similar number of populations in each dataset that were approximately equal in size plus a population only detected in J20 sample. We next combined both datasets using merge function. Top 2,000 highly variable genes (HVGs) were detected using FindVariableFeatures function with default parameters. Then, normalized counts on HVGs were scaled and centred using ScaleData function with default parameters. Principal component analysis (PCA) was performed over HVGs with default parameters. Plots of the two principal components of the PCA where cells were coloured by dataset of origin excluded the presence of batch effects. A shared nearest neighbour graph was built with FindNeighbors function over the 8 first PCA dimensions (PC) and cluster detection was carried out with Louvain algorithm in FindClusters function, using 8 first PC and resolution

of 0.5. The IRM population was subset and reanalysed by repeating the previous steps: detection of highly variable genes, PCA, shared nearest neighbour graph building over first 10 PC and cluster detection using 10 first PC and resolution of 0.3; this segmented this population in two subpopulations: Interferon related microglia type 1 (IRM1) and interferon related microglia type 2 (IRM2), that were studied apart from the populations of the whole dataset. Visualization and embedding were performed using uniform manifold approximation and projection (UMAP) (Becht et al., 2018) methods over PCA using the 8 first PC for the whole dataset and 10 first PC for the IRM subset. UMAP plots of gene expression show normalized counts (UMIs) per cell. In all UMAP expression plots, the maximum expression value was adjusted to percentile 95 of the gene expression across all cells. Differential expression analysis (DEA) was used to identify population gene markers. For DEA, the cells of each population were contrasted against all the other cells in the merged dataset using Wilcoxon Rank Sum test on normalized counts. For J20-AD effect analysis, in the merged dataset, the cells of each population from the J20 dataset were contrasted against all the other cells of the same population in control using Wilcoxon Rank Sum test on normalized counts. GO functional enrichment analyses were performed using DAVID (v.6.8) bioinformatics platform (Huang da et al., 2009). Over-represented transcription factor binding site motifs from co-regulated or co-expressed genes were identified using Pscan (Zambelli et al., 2009). All DEA and functional enrichment analyses applies False Discovery Rate (FDR) method by Benjamini-Hochberg post hoc p adjustment, except otherwise specified.

Statistical analysis

Statistical analysis was performed using GraphPad prism v.7 and significance was stablished at $p<0.05$. Normality was tested using Shapiro-Wilk normality test. Outliers were identified with ROUT method Q=1%. All statistical analyses were two-tailed. For pairwise analyses of data with a Gaussian distribution, Student's t-test for unpaired data was performed. Non-normally distributed data was analysed by Mann-Whitney test. To compare the mean of more than two samples with a single variable one-way analysis of variance was performed. In case of two conditions with two independent variables analysis were performed by two-way ANOVA. Bonferroni-corrected pairwise tests were used where appropriate post-hoc to correct for multiple comparisons. The bar plots height represents the mean, and the error bars represent the +/- standard error from the mean. ns: non-significant; *: p-value < 0.05; **: p-value < 0.01; ***: p-value < 0.001; ****p-value < 0.0001.

RESULTS

1. Microglia acute neuroinflammatory response of brain-resident microglia is stepwise regulated

Neuroinflammation is a complex response mediated by microglia, the highly plastic innate immune cells of the CNS. Despite is key role in disease, the gene-regulatory changes driving the acute neuroinflammatory response remains largely unknown.

To investigate the dynamics of the acute neuroinflammatory response in microglia we took advantage of the mouse line Cx3cr1$^{cre/ERT2-EYFP}$ (Jung et al., 2000). In these mice, the exon 2 of the chemokine (C-X3-C) receptor 1 (Cx3cr1) has been replaced with a cre/ERT2 coding sequence, followed by an internal ribosome entry site (IRES) and an enhanced yellow fluorescent protein (EYFP). Cx3cr1 is expressed by cells of the myeloid lineage such as microglia and border-associated macrophages (BAM) in the brain (Fig.5A). To confirm the selective expression of EYFP in microglial cells, we performed co-immunostaining against GFP and the well-established microglial marker ionized calcium-binding adaptor molecule 1 (Iba1) (Ito et al., 1998) (Fig.5B). Quantification analyses in the somatosensory cortex and dentate gyrus (DG) of the hippocampus, show that 100% of Iba1+ cells were also GFP+ (Fig.5C), and 100% of GFP+ were Iba1+ (Fig.5D).

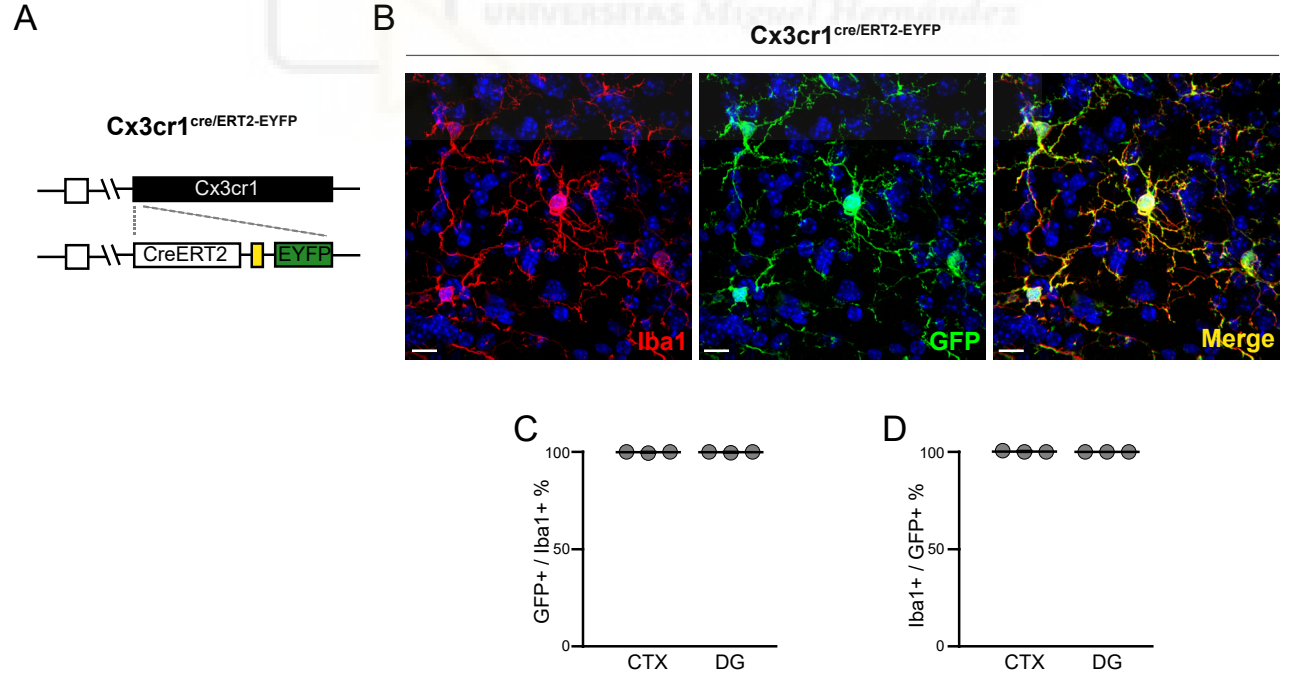

Fig.5. EYFP expression colocalize with the microglia marker Iba1.
A. Schematic representation of the genetic construction of Cx3cr1$^{cre/ERT2-EYFP}$ mice that constitutively express EYFP under Cx3Cr1 promoter. Whyte squares represent previous loci. Yellow square represent the internal ribosomal entry site (IRES).
B. Representative images of coronal somatosensory cortex brain sections from P60 Cx3cr1$^{cre/ERT2-EYFP}$ mice immunostained for Iba1 and GFP. Scale bars indicate 10μm.
C. Percentage of GFP+ cells within Iba1+ microglia in the somatosensory cortex and dentate gyrus. N = 3 mice. Mean ± sem. Legends: somatosensory cortex (CTX), dentate gyrus of hippocampus (DG).
D. Percentage of Iba1+ cells within GFP+ microglia in the somatosensory cortex and dentate gyrus. N = 3 mice. Mean ± sem. Legends: somatosensory cortex (CTX), dentate gyrus of hippocampus (DG).

Microglia account for a small percentage of the total cell population in the mouse brain (5-12%) (Lawson et al., 1990). In order to study microglia population without confounding factors derived from other cells in the brain (like neurons, astrocytes, oligodendrocytes…), we established a protocol for microglia isolation from adult mouse brain. Notably, our protocol that was adapted from Bennet M. et al., 2016, does not rely on enzymatic digestion, but brain tissue (whole mouse cortex) is mechanically dissociated at low temperature (4ºC) using a dounce homogenizer, and myelin debris is removed by MACS technology or percoll gradient at 4ºC (see Methods section). Under these conditions, baseline microglia reactivity is minimized (Bennett et al., 2016) (Fig.6A). After tissue processing, we sorted YFP+ cells in a BD FACS Aria III. The gating strategy was carried out as follows: we first selected the population by forward scatter area (FSC-A) and side scatter area (SSC-A) that define the population based on the size and internal complexity or granularity of the cells respectively; secondly, we gated the single cells by FSC-height (FSC-H) and FSC-A, eliminating possible doublets for the sorting; finally, we sorted the YFP+ population (Fig.6B). YFP+ population identity was confirmed by CD45 and CD11b immunostaining of the tissue homogenate (Fig.7A). In addition, the enrichment of microglia population after sorting was assessed by RT-qPCR of *GFP* (Fig.7B), the microglial markers *Aif1* and *Trem2* (Fig.7C,D), the

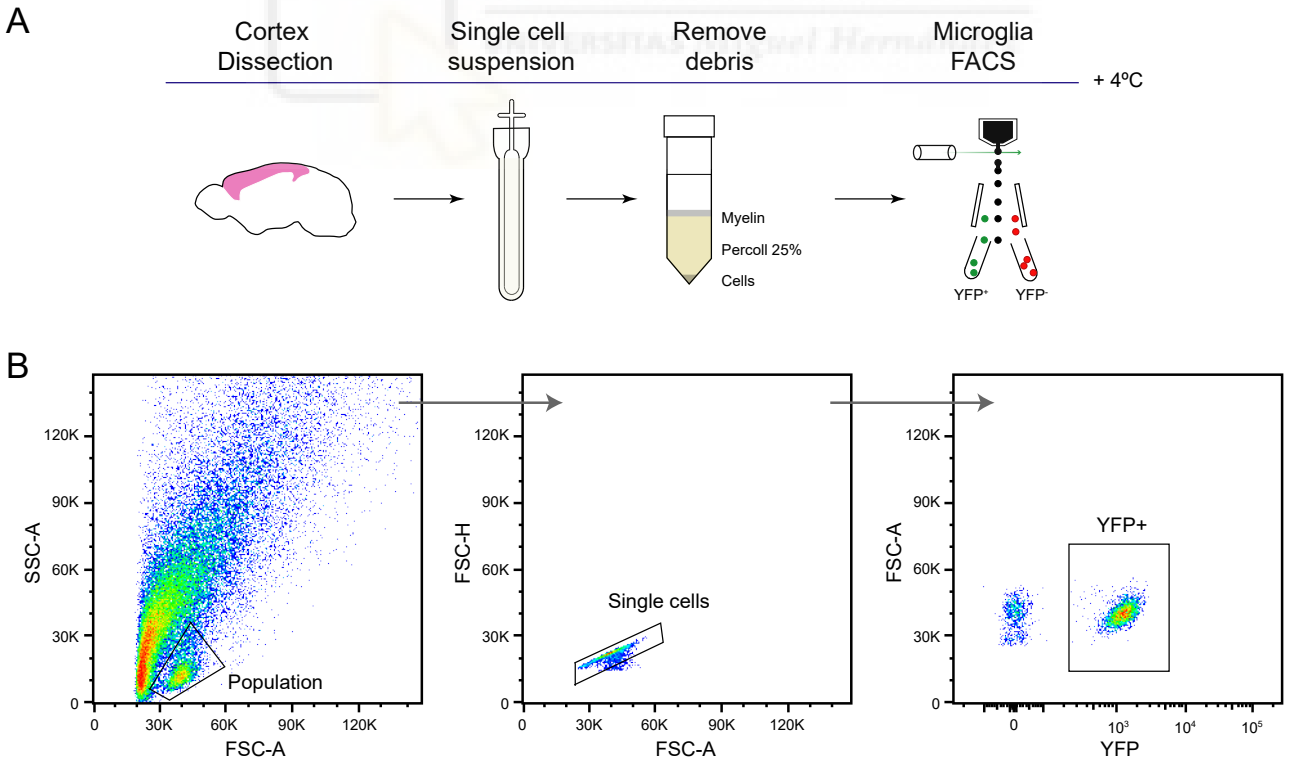

Fig.6. Microglia purification protocol.
A. Schematic representation of microglia purification protocol. Microglial cells were isolated from whole cortex by mechanical dissociation and FACS sorting of YFP positive cells. The whole process was carried out at +4ºC to limit the *ex vivo* activation.
B. Representative FACS scatter plot showing the gating steps for microglia purification. First, the population was identified by FSC and SSC; second, single cells were selected by FSC-H and FSC-A; finally, YFP+ cells were selected for sorting.

astrocyte markers *GFAP* and *Slc1a3* (Fig.7E,F), and the neuronal markers *NeuN* and *Vglut1* (Fig.7G,H). We used the YFP- population as a negative control, and bulk tissue homogenate prior to FACS sorting as the reference population for normalization. As expected, the YFP+ population show increased expression levels of *GFP*, *Aif1*, and *Trem2*, whereas *GFAP*, *Slc1a3*, *Vglut* and *NeuN* transcripts were not detected or greatly reduced confirming that the YPF+ sorted cells were highly enriched in microglial cells.

To elucidate microglia dynamics of the transcriptional landscape changes underlying the acute neuroinflammatory response, we performed a longitudinal study that consist of RNA-sequencing of fluorescence-activated cell sorting (FACS)-purified microglia after 1, 5, 24,

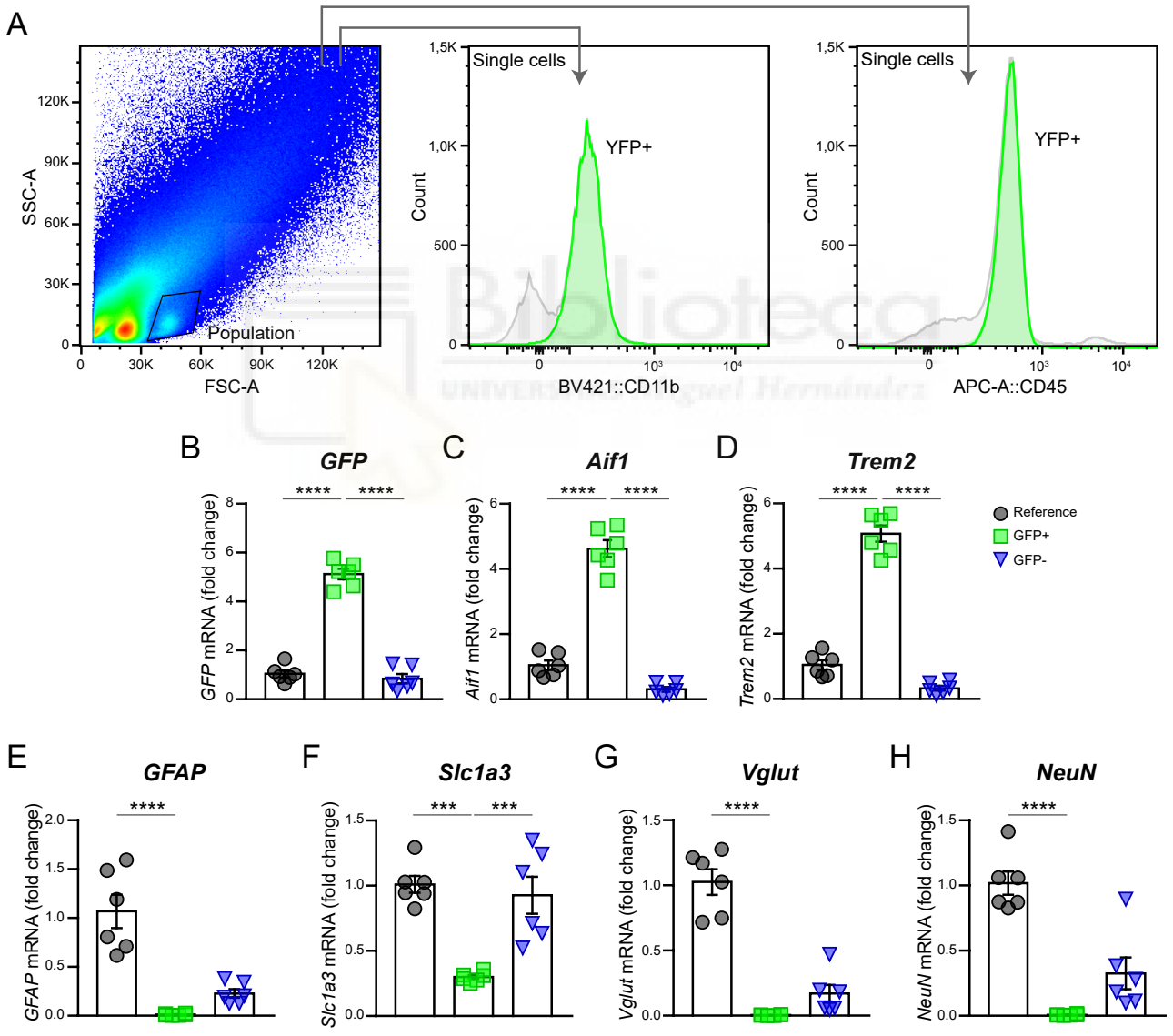

Fig.7. Validation of microglia isolated cells.
A. FACS plot showing characterization of YFP+ microglia cell population by immunostaining of CD11b and CD45.
B. Expression of *GFP*, **C. D.** microglia markers *Aif1* and *Trem2*, **E. F.** astrocytes markers *GFAP* and *Slc1a3*, and **G. H.** neuronal markers *Vglut* and *NeuN* in cell homogenate before sorting (reference), YFP+ and YFP- isolated cells by rt-qPCR. GAPDH expression is used for normalization. N = 6 per condition ****p<0.0001, ***p<0.001, one-way ANOVA Bonferroni multiple comparisons; mean ± sem.

48, and 72h from LPS administration (5mg/kg i.p.) (from now on L1h, L5h, L24h, L48h and L72h) (Fig.8A).

Principal component analysis (PCA) shows that variance across samples is mostly due to the time component after LPS administration. Notably, our time-course study design captures virtually the whole neuroinflammatory response at the transcriptional level, with samples following a circular pattern in the first two principal components of the PCA. We found that samples for most of the distinct time points are located near each other with the exception of L5h, that likely represents the peak of the response, and L72h, with one L72h sample clustered with samples from L48h, another L72h sample clustered with the vehicles, and the remaining L72h samples located halfway between L48h and the vehicles, suggesting a returning to the basal state (Fig.8B).

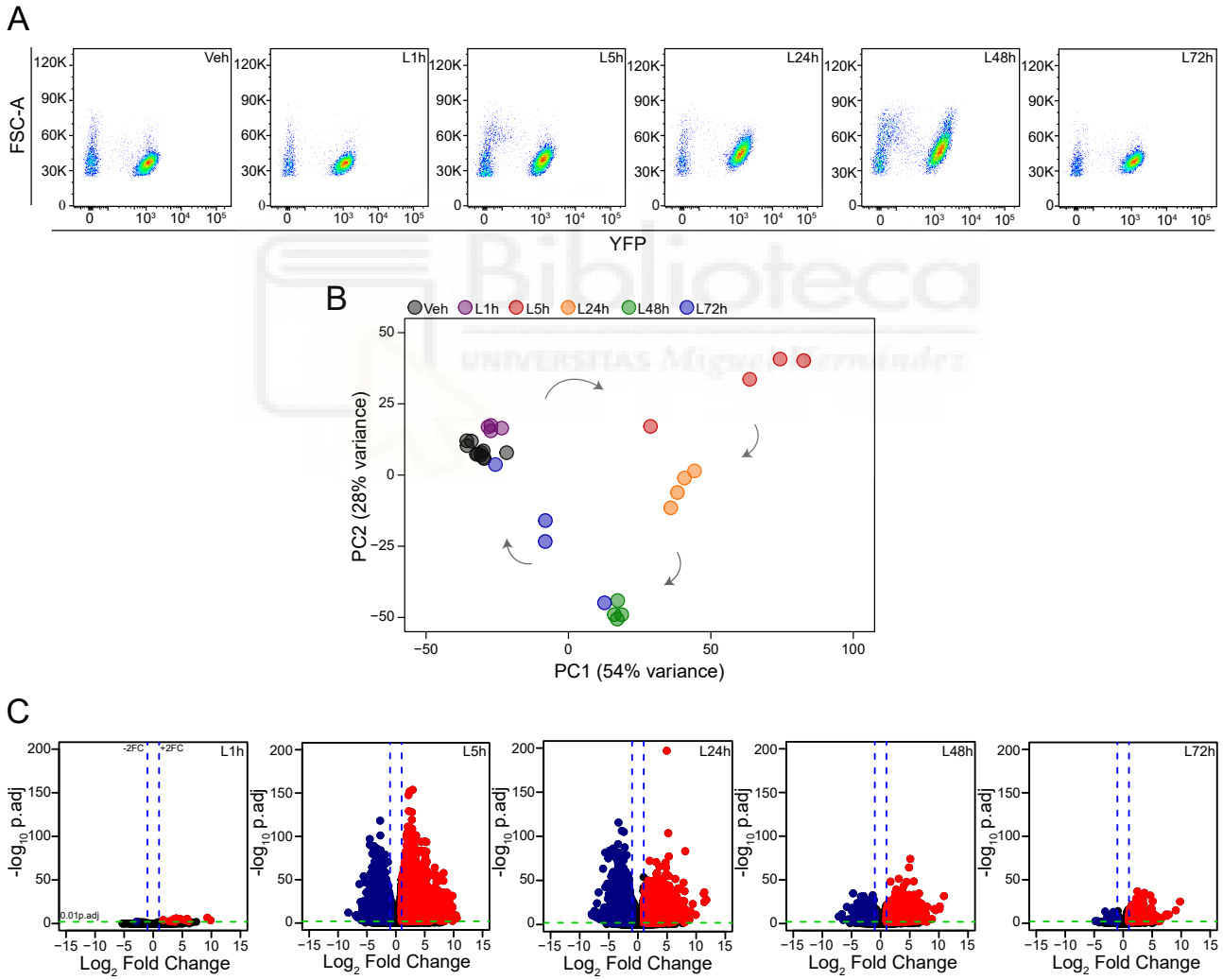

Fig.8. Longitudinal transcriptional landscape of neuroinflammatory response in acutely isolated microglia.

A. Flow-cytometry dot plots show YFP+ cells of Cx3cr1$^{cre/ERT2-EYFP}$ mice administered with vehicle, or 1h, 5h, 24h, 48h, and 72h of LPS (5mg/kg i.p.).

B. Principal component analysis (PCA) of transcriptome of microglial cells from cortex of male mice (P60) at different time points (1h, 5h, 24h, 48h, 72h) from LPS (5mg/kg i.p.) administration. Top 500 genes are shown. VEH: N=11, LPS: N=4 per condition.

C. Volcano plots for differentially expressed genes (DEG) at 1h, 5h, 24h, 48h and 72h from LPS (5mg/kg i.p.) insult. Genes above 2-fold change (blue dotted line) and 0.01 adjusted p value (green dotted line) are shown in red. Genes under 2-fold change and 0.01 adjusted p value are shown in blue.

Differential expression analysis (DEA) shows that microglia respond to systemic LPS as soon as 1h from the insult. We observe an upregulation of 16 genes whereas only 1 gene is significantly downregulated. The highest proportion of the changes were detected at L5h with 2635 upregulated genes and 3086 downregulated gene transcripts. From L5h on, we observe a progressively decrease of the number of significantly differential expressed genes (DEG). At L24h, we identified 1489 upregulated genes, 1253 transcripts at L48h and finally, 505 at L72h. For the downregulated genes we find 1617 at L24h, 617 at L48h, and 57 at L72h (Fig.8C).

Next, we performed unsupervised hierarchical clustering to unveil the dynamics of putative co-regulated genes during the neuroinflammatory response. For upregulated genes (pvalue<0,01; logFC>1), the elbow method led to the identification of 7 clusters. Heatmap of the z-score matrix of upregulated genes reveals that microglial cells show specific gene expression signatures that are associated with each time point. Moreover, this analysis reveals distinct patterns of gene expression dynamics, suggesting that microglia neuroinflammatory response upon an acute LPS challenge is stepwise regulated. (Fig.9A).

Clusters 1 to 4 comprise the early transcriptional response. Whereas cluster 1 is composed of genes that are activated transiently and rapidly (immediate-early response), clusters 2, 3 and 4 consist of genes showing an early-persistent transcriptional response (long-term response). Among the representative genes for each cluster, we found *Spp1*, *Il1b* or *Cxcl10* for cluster 1; *Nhp2*, *Cct* family or *Riok1* for cluster 2; *Tigar*, *Gnmt* or *Prdx6* for cluster 3; and *Oasl2*, *Irf7* or *Ifitm3* for cluster 4 (Fig.9C). On the other hand, clusters 5, 6 and 7 comprise a group of genes with delayed transcriptional regulation. Cluster 6 is composed of genes that are activated transiently, whereas cluster 5 and 7 show prolonged expression. Looking closer into the gene markers associated with each cluster, we have identified *Ms4a4a*, *Gmnn* or *Mcm2* for cluster 5; *Top2a*, *Cdk1* or *E2f7* for cluster 6; and *Axl*, *Apoe* or *H2-M3* for cluster 7 (Fig.9C).

We also performed unsupervised hierarchical clustering of downregulated genes (pvalue<0,01; logFC<1). Contrary to the upregulated genes, the majority of the downregulations occur at L5h, and the recovery of the basal expression occur progressively from L24h to L72h (Fig.9B). Following the methodology mentioned above, we clustered the response in 5 groups. The most salient is the cluster 1, that compared with the other clusters, its gene expression is maintained at L1h but strongly downregulated at L5h, and then, recovers progressively at later time points. Among the genes associated to cluster 1 we identified *Cx3cr1*, *P2ry12*, *Tmem119*, *Trem2* or *Sall1* (Fig.9C).

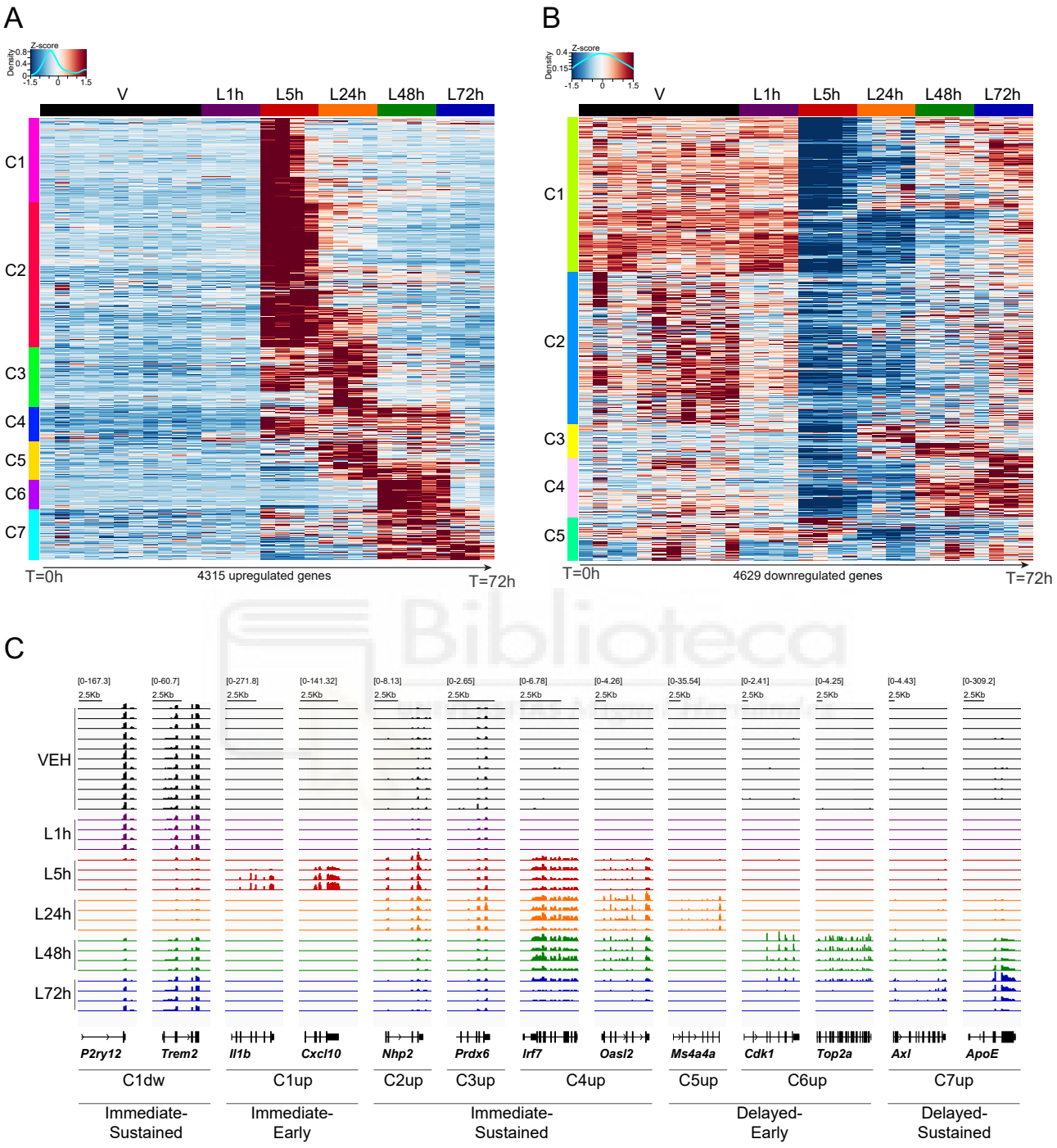

Fig.9. Longitudinal transcriptional landscape of neuroinflammatory response in acutely isolated microglia.

A. Hierarchical clustering and heatmap of upregulated genes (p.adj < 0.01, FC>2; 4315 genes) across the different times (1h, 5h, 24h, 48h, 72h) from LPS (5mg/kg i.p.) in microglia from somatosensory cortex. Each column represents a biological replicate. Legend: C1 = cluster 1, C2 = cluster 2, C3 = cluster 3, C4 = cluster 4, C5 = cluster 5, C6 = cluster 6, C7 = cluster 7. VEH: N=11, LPS: N=4 per condition.

B. Hierarchical clustering and heatmap of downregulated genes (p.adj < 0.01, FC<2; 4629 genes) across the different times (1h, 5h, 24h, 48h, 72h) from LPS (5mg/kg i.p.) in microglia from somatosensory cortex. Each column represents a biological replicate. Legend: C1 = cluster 1, C2 = cluster 2, C3 = cluster 3, C4 = cluster 4, C5 = cluster 5. VEH: N=11, LPS: N=4 per condition.

C. IGV tracks showing representative genes from RNA-seq data of each condition (rows) and cluster (columns). VEH: N=11, LPS: N=4 per condition.

Our bulk population RNA-seq of the microglia during the acute response to systemic immune challenge reveals the dynamics of the transcriptional landscape changes during the neuroinflammatory response. This analysis has further revealed the presence of coordinated stepwise transcriptional programs underlying acute neuroinflammatory response by microglia.

2. Cytokines and interferon programs shape microglia early transcriptional response to LPS

We have previously shown that microglia early transcriptional response comprises 4 clusters of upregulated genes (Fig.9A). We next wondered whether these clusters are associated with specific biological functions. To address this question, we performed GO analysis on clusters 1 to 4. Interestingly, cluster 1, whose upregulation is short-term, almost exclusive from L5h (Fig.10A), is enriched in GO terms classically associated with the inflammatory response. Among the top highly enriched terms, we found toll-like receptor 2 signalling, cell chemotaxis or cytokine-mediated signalling pathway (Fig.10B).

Cluster 2 genes upregulation is an immediate-sustained response, extended form L5h to L24h (Fig.11A). The main function associated with this cluster is the regulation of rRNA processing with ribosome biogenesis, NcRNA processing, and ribonucleoprotein complex biogenesis, among others (Fig.11B). These functions are essential for protein synthesis and cell growth (Chaillou et al., 2014).

In addition, cluster 3 is also an immediate-sustained response, extended form L5h to L24h (Fig.11C), and it is mainly related to the energetic support that microglial cells need. The most enriched functions associated with this cluster are cell redox homeostasis, glycolytic process, response to hypoxia, and coenzyme and cofactor metabolic process (Fig.11D).

Finally, for cluster 4, which present an immediate-sustained response extended from L5h to L48h (Fig.12A), we observe that the functions associated are related to interferon response. The most enriched terms for cluster 4 are response to interferon-alpha and beta, type-I interferon signalling pathway, response to interleukin 4 and defence response to virus (Fig.12B).

In summary, in our microglia-isolated bulk RNA-seq, we identify 4 transcriptional programs that co-exist as part of microglia immediate-response to LPS. As microglia heterogeneity has been identified in chronic neurodegenerative conditions, we next performed single molecule *in situ* hybridization (RNAscope) of previously defined immediate-response markers to determine microglia phenotypical heterogeneity in acute neuroinflammation. For the cytokine

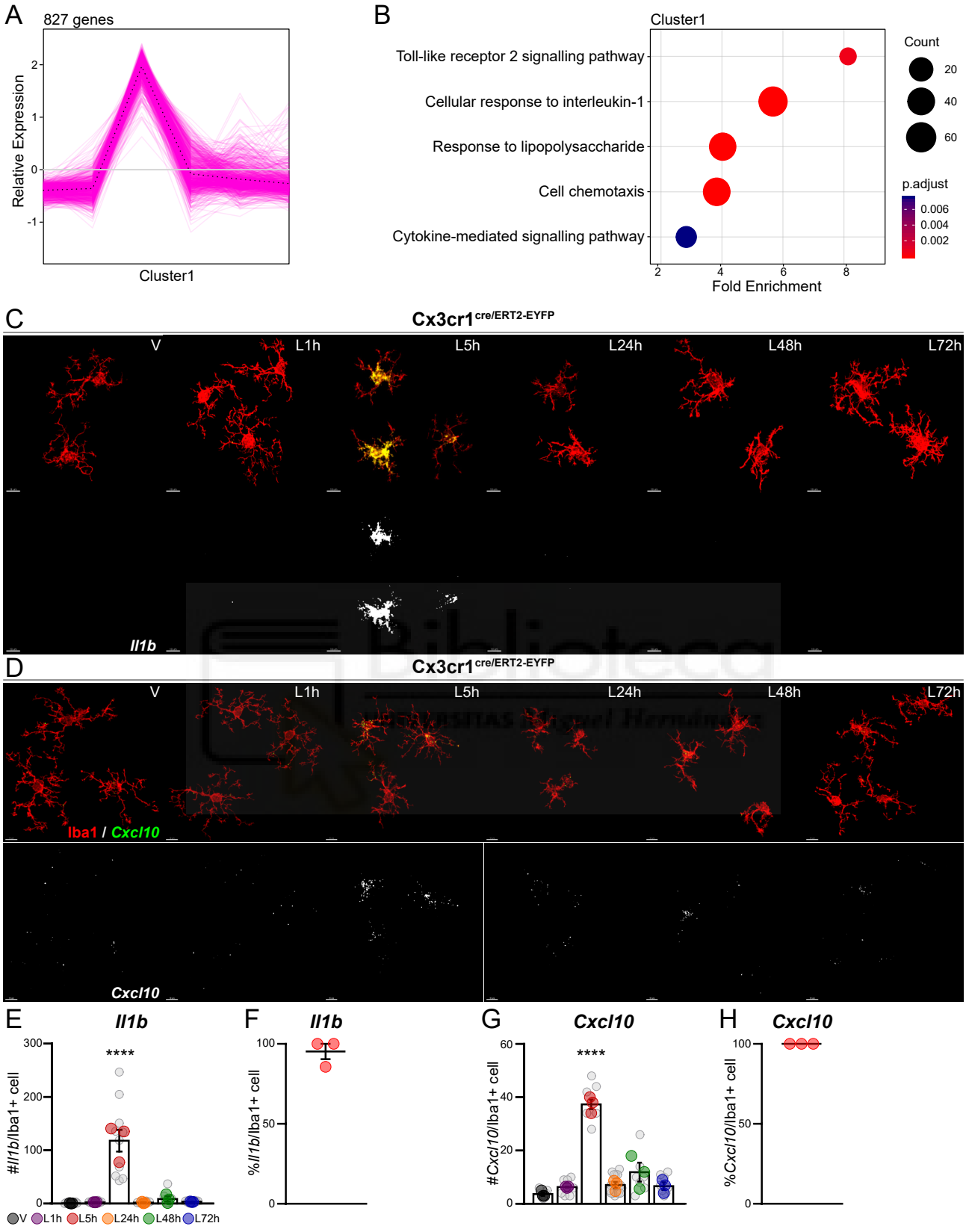

Fig.10. Microglia cytokine program expression define the initiation of the inflammatory response

A. Cluster 1 genes relative expression profile.

B. GO terms biological process associated with cluster 1.

C. Representative image of masked microglia from single molecule in situ hybridization (RNAscope) for Il1b followed by immunofluorescence of Iba1 in P60 Cx3cr1$^{cre/ERT2-EYFP}$. Scale bars indicate 10µm.

D. Representative image of masked microglia from single molecule in situ hybridization (RNAscope) for Cxcl10 followed by immunofluorescence of Iba1 in P60 Cx3cr1$^{cre/ERT2-EYFP}$. Scale bars indicate 10µm.

E. Quantification of Il1b RNA-scope expression per individual Iba1+ microglia in the somatosensory cortex of P60 Cx3cr1$^{cre/ERT2-EYFP}$. N = 3 mice per condition, n= 8 to 12 cells per condition. One-way ANOVA Bonferroni

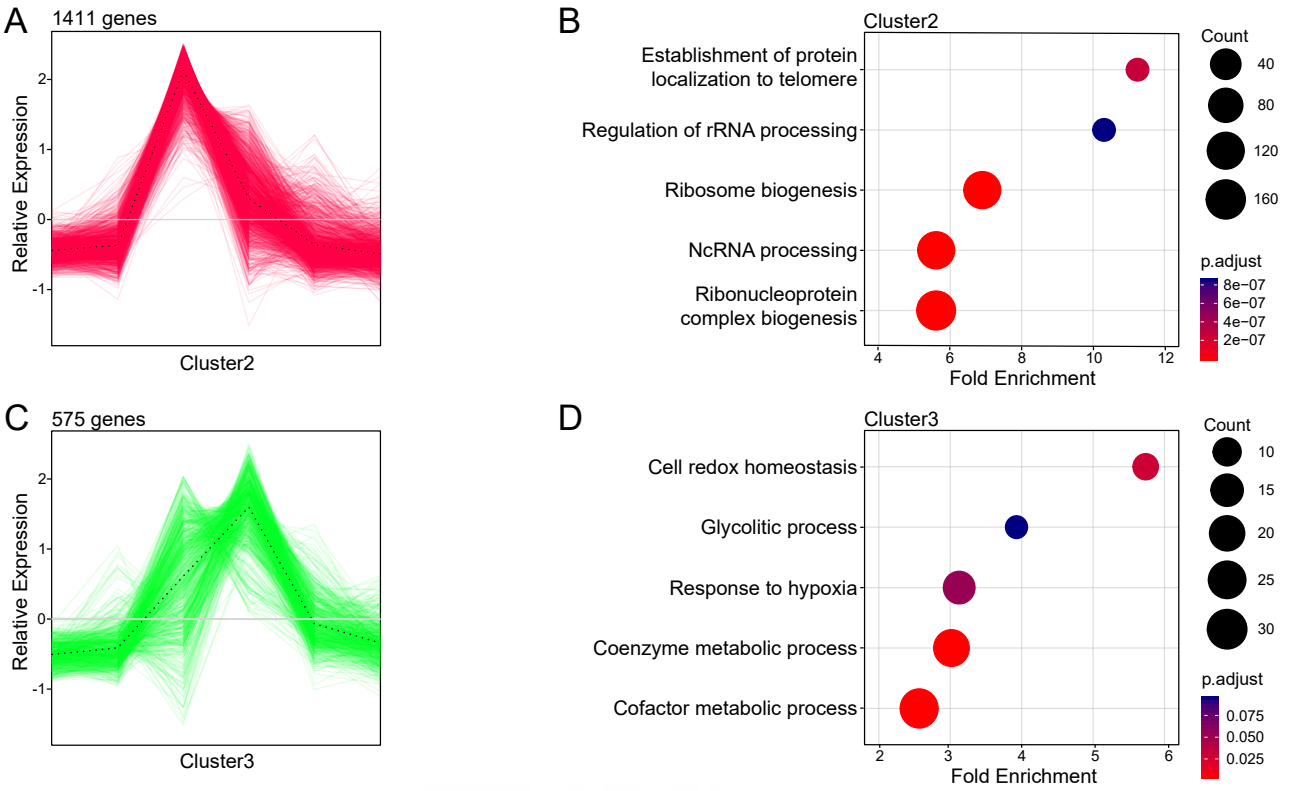

Fig.11. Microglia metabolism and ribosomal machinery are very active at the initiation of the inflammatory response
A. Cluster 2 genes relative expression profile.
B. GO terms biological process associated with cluster 2.
C. Cluster 3 genes relative expression profile.
D. GO terms biological process associated with cluster 3.

response (cluster 1), we observe a significant increase of around 230 molecules of *Il1b* (Fig.10E), and 38 molecules of *Cxcl10* per cell (Fig.10G) at L5h, which is homogeneously expressed in all microglial cells from the cortex at L5h (Fig.10F,H). Related to the interferon response (cluster 4), there is an increase of *Oasl2* from L24h to L72h (Fig.12C) that is significant at L48h. We found an increase of around 10 molecules of *Oasl2* per cell at 48h from the insult (Fig.12D).

Altogether, microglia immediate response to LPS is comprised by 4 transcriptional programs that co-exist and are implemented with different dynamics (early and sustained). Microglia immediate-early cytokine response and immediate-sustained interferon response are population-specific according to the nature of the LPS that diffuses through the brain parenchyma (Rivest, 2009).

multiple comparisons, ****p<0.0001; mean ± sem.
F. % of Il1b positive microglial cells at L5h. Quantifications were performed in 1 to 3 regions of interest (ROI) from somatosensory cortex. N = 3 mice per condition. Mean ± sem.
G. Quantification of Cxcl10 RNA-scope expression per individual Iba1+ microglia in the somatosensory cortex of P60 Cx3cr1$^{cre/ERT2-EYFP}$. N = 3 mice per condition, n= 6 to 17 cells per condition. One-way ANOVA Bonferroni multiple comparisons, ****p<0.0001; mean ± sem.
H. % of Cxcl10 positive microglial cells at L5h. For basal expression levels, at least two dots were considered as positive. Quantifications were performed in 1 to 3 regions of interest (ROI) from somatosensory cortex. N = 3 mice per condition. Mean ± sem.

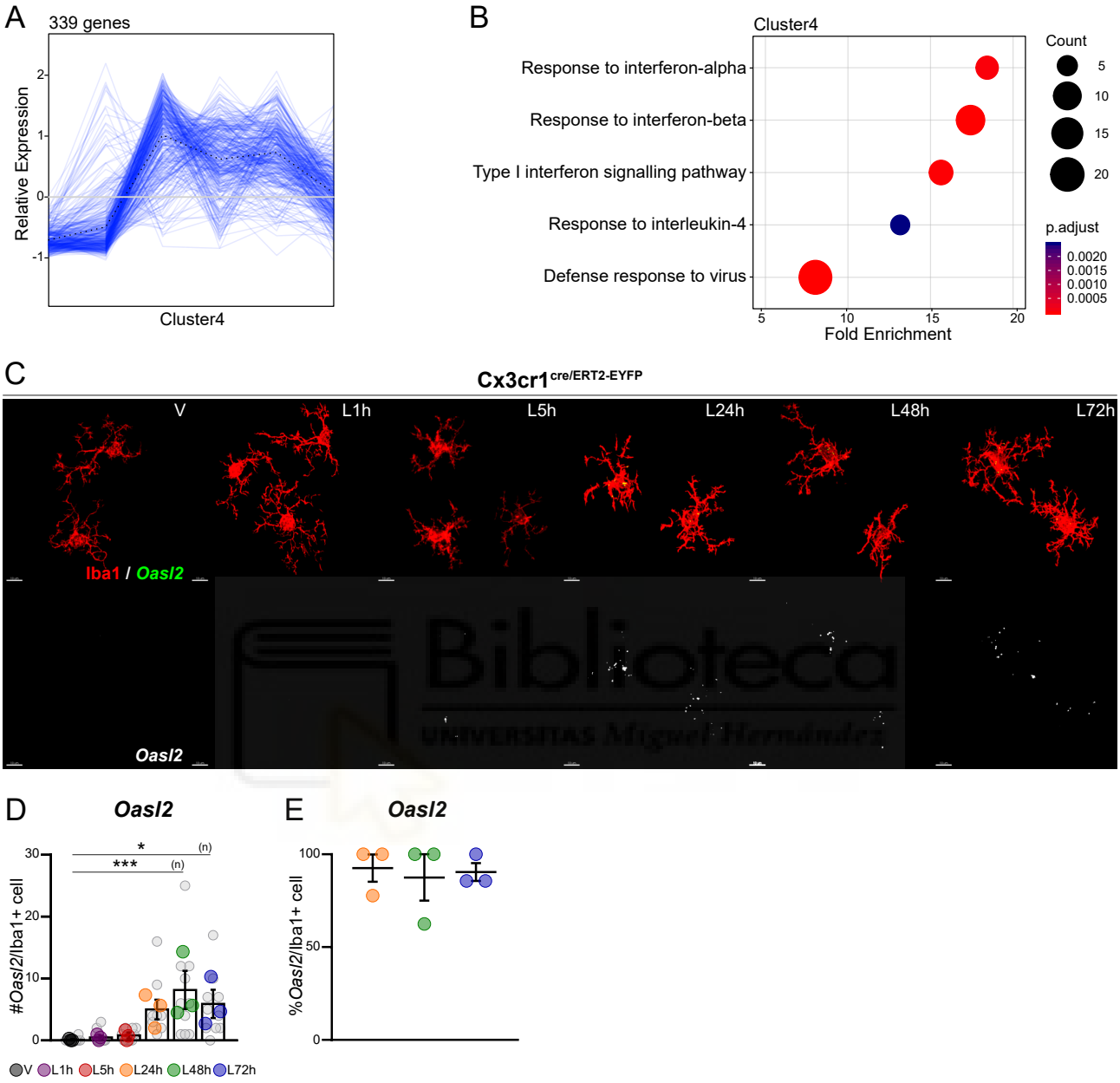

Fig.12. Microglia interferon program expression define the initiation of the inflammatory response

A. Cluster 4 genes relative expression profile.

B. GO terms biological process associated with cluster 4.

C. Representative image of masked microglia from single molecule in situ hybridization (RNAscope) for Oasl2 followed by immunofluorescence of Iba1 in P60 Cx3cr1$^{cre/ERT2-EYFP}$. Scale bars indicate 10µm.

D. Quantification of Oasl2 RNA-scope expression per individual Iba1+ microglia in the somatosensory cortex of P60 Cx3cr1$^{cre/ERT2-EYFP}$. N = 3 mice per condition, n= 8 to 12 cells per condition. One-way ANOVA Bonferroni multiple comparisons, ***p<0.001, **p<0.01; mean ± sem.

E. % of Oasl2 positive microglial cells at L24h, L48h and L72h. Quantifications were performed in 1 to 3 regions of interest (ROI) from somatosensory cortex. N = 3 mice per condition. Mean ± sem.

3. Delayed transcriptional response to LPS sustains heterogeneous microglia proliferation state

Continuing with the clusters characterization we focus on clusters 5 and 6. Cluster 5 is a delayed response that comprise genes upregulated from L24h to L48h (Fig.13A), while cluster 6 is a delayed-early response that comprise genes expressed exclusively at L48h (Fig.13B). GO analysis reveals that cluster 5 and 6 biological functions are closely related to each other. Cluster 5 main functions are associated with DNA replication (Fig.13B) while the biological functions associated to cluster 6 are mostly related with the regulation of mitotic cell cycle and G2/M cell cycle stages transition (Fig.13D).

To further study the tissue distribution of previously identified markers for these two clusters, we performed RNAscope for one of the chosen markers: *Ms4a4a* (Fig.13E). Quantification of *Ms4a4a* RNA molecules per Iba1+ cell shows a bimodal distribution at L24h (Fig.13F). We show that around 15% of microglial cells population express *Ms4a4a* at L24h suggesting that there may be a subpopulation of microglial cells that carry out proliferative activity (Fig.13G). Contrary to the immediate microglia response to LPS that is population-specific, this result suggests that microglia proliferative response to LPS is cell-specific.

To functionally study the proliferative activity of microglia, we then tested the percentage of microglia population that is proliferating during the acute proinflammatory response. To do this, we use 5-bromo-2'-desoxyuridine (BrdU) incorporation assay, a well-established method for studying proliferation in living tissues after LPS challenge (Fig.14A). BrdU is a synthetic nucleoside analogue of thymidine that incorporates into the DNA during the S phase of the cell cycle when DNA is replicated. First, to confirm that proliferation is not occurring during the first 24h of the acute response, we administered intraperitoneally 50mg/kg of BrdU at 5h, 12h and 22h from LPS administration (Fig.14B). Mice were sacrificed 2h after the last BrdU injection to allow the compound to incorporate. After immunostaining and confocal imaging, we analyse the percentage of BrdU+ cells among microglia population in the mouse cortex concluding that microglial cells are not dividing during the first 24h from the LPS insult (Fig.14B',B"). To test the proliferative activity from L24h to L48h, we performed BrdU incorporation at 24h, 36h, and 46h from LPS administration (Fig.14C). Mice were sacrificed 2h after the last BrdU administration. We observe a small increase in the proliferation of few cells suggesting that the proliferation has already started (Fig.14C',C"). Finally, we performed BrdU incorporation at 24h, 36h, 48h, 60h and 70h from LPS administration (Fig.14D). This administration schedule allows us to address microglia proliferation during the middle and last part of the inflammatory response. We found that 10% of the microglia population proliferates in the cortex from L24h to L72h (Fig.14D', D"). Notably, we do not observe

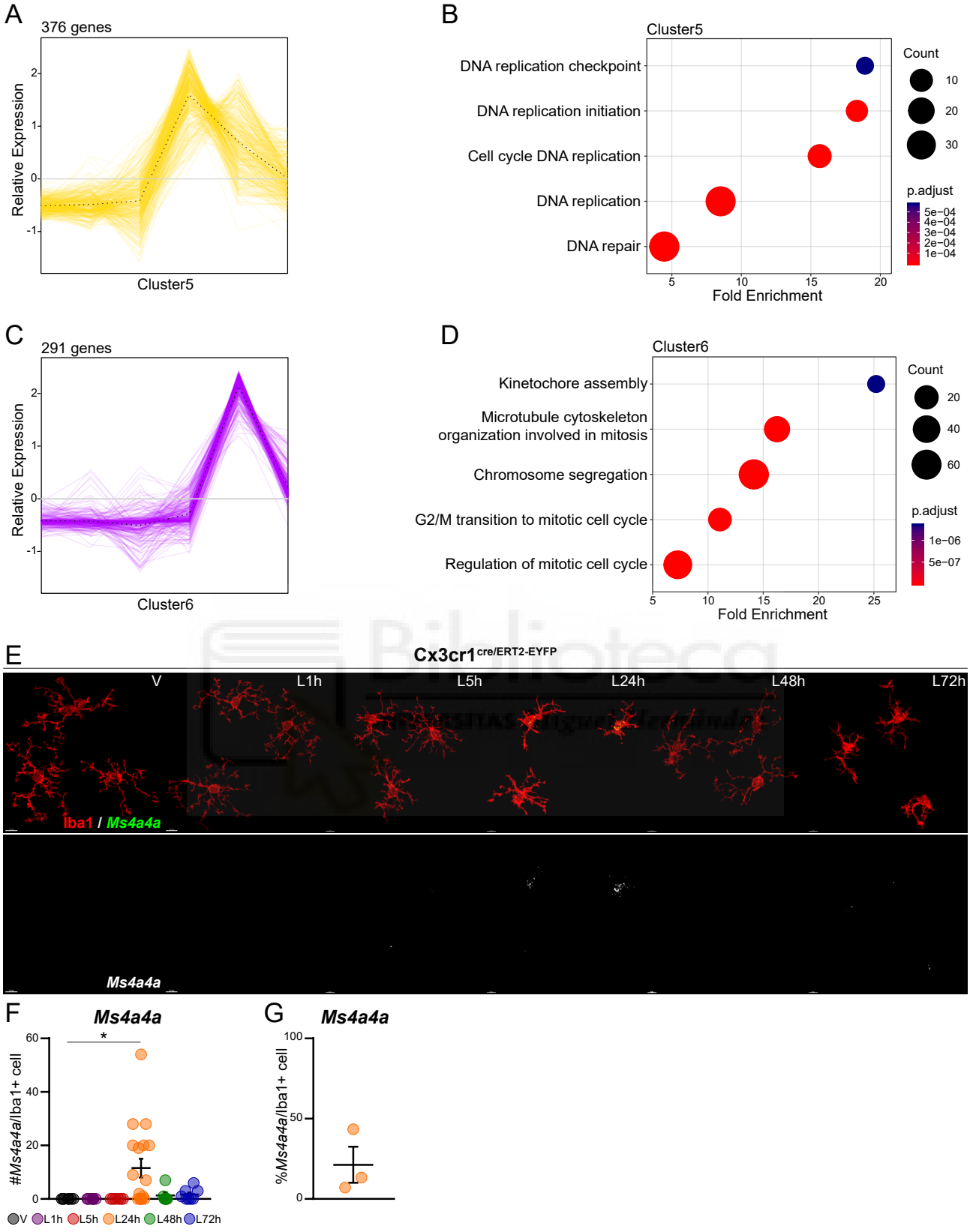

Fig.13. Microglia proliferative transcriptional program is increased from 24h to 48h of an acute inflammatory insult.

A. Cluster 5 genes relative expression profile.
B. GO terms biological process associated with cluster 5.
C. Cluster 6 genes relative expression profile.
D. GO terms biological process associated with cluster 6.
E. Representative image of masked microglia from single molecule in situ hybridization (RNAscope) for Ms4a4a followed by immunofluorescence of Iba1 in P60 Cx3cr1$^{cre/ERT2-EYFP}$. Scale bars indicate 20µm.
F. Quantification of Ms4a4a RNA-scope expression per individual Iba1+ microglia in the somatosensory cortex

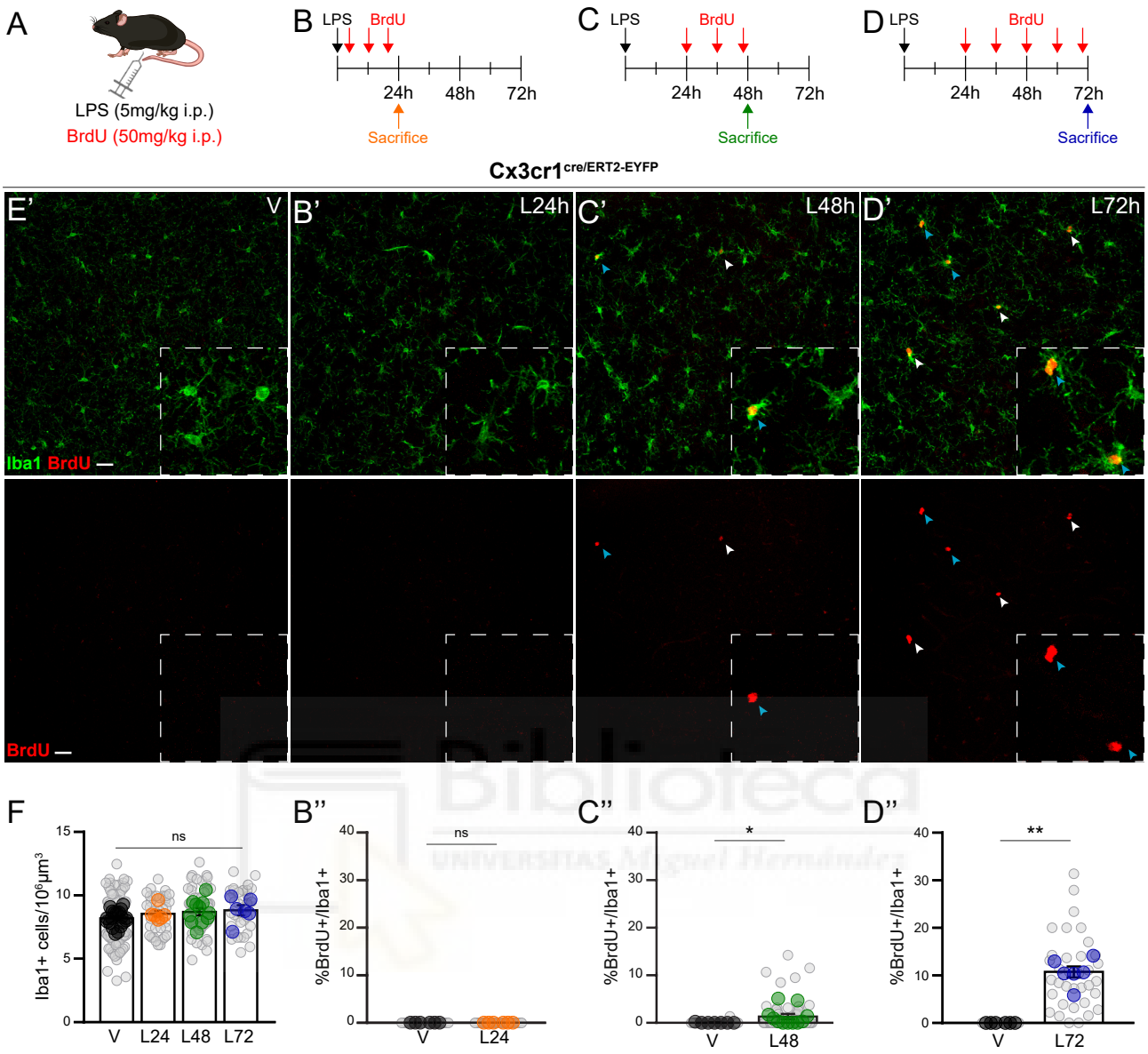

Fig.14. Microglia proliferation addressed by BrdU incorporation is functionally carried out from 24h to 72h of an acute inflammatory insult.

A. Administration scheme. Mice received one single dose of LPS (5mg/kg i.p.) followed by BrdU (50mg/kg i.p.) administration.

B. For the first experiment, mice received one single dose of LPS (5mg/kg i.p.) followed by 3 consecutive doses of BrdU (50mg/kg i.p.) at 5h 12h and 22h from LPS administration. Mice were sacrificed 2h after the last BrdU administration

C. For the second experiment, 24 hours later from one single dose of LPS (5mg/kg i.p.), mice received 3 consecutive doses of BrdU (50mg/kg i.p.) every 12 hours. Mice were sacrificed 2h after the last BrdU administration.

D. For the third experiment, 24 hours later from one single dose of LPS (5mg/kg i.p.), mice received 5 consecutive doses of BrdU (50mg/kg i.p.) every 12 hours. Mice were sacrificed 2h after the last BrdU administration.

B'C'D'E'. Coronal brain sections from male and female P60 Cx3cr1$^{cre/ERT2-EYFP}$ mice were immunostained against the specific microglia marker Iba1 and the thymidine analogue BrdU. Scale bars indicate 20 µm.

B", C", D". Quantification of BrdU+ nuclei per Iba1+ cell in the somatosensory cortex of male and female P60 Cx3cr1$^{cre/ERT2-EYFP}$ mice for BrdU incorporation from **0-24h** (V ROI= 36, N=6; L24h ROI= 36, N=6), Mann-Whitney test P>0.99; **24h-48h** (V ROI= 42, N=7; L48h ROI= 66, N=11), Mann-Whitney test *P = 0.0238; and **24h-72h** (V ROI= 35, N=6; L72h ROI= 35, N=6). Mann-Whitney test **P = 0.0022.

F. Quantification of microglial (Iba1+) cells density in the somatosensory cortex of male and female P60 Cx3cr1$^{cre/ERT2-EYFP}$ mice. (V ROI= 113, N=19; L24h ROI= 36, N=6; L48h ROI= 66, N=11; L72h ROI= 35, N=6). One-way ANOVA Kruskal-Wallis test P = 0,1803.

of P60 Cx3cr1$^{cre/ERT2-EYFP}$. N = 3 mice per condition, n= 8 to 12 cells per condition. One-way ANOVA Kruskal-Wallis, *p<0.05. Individual cells are represented. Mean ± sem.

G. % of Ms4a4a positive microglial cells at L24h. Quantifications were performed in 1 to 3 regions of interest (ROI) from somatosensory cortex. N = 3 mice per condition. Mean ± sem.

differences in cell density across the different time points (Fig.14E). To further explore not only the total amount of cells that are in mitosis but also when are the other phases of the cell cycle occurring, we performed immunostaining against Ki67 (Fig.15B). Ki67 is a well-known nuclear protein that is expressed in the cells during all active phases of the cell cycle (G1, S, G2 and M) but is absent in resting cells (G0). We found that only 10% of microglial cells are positive for Ki67 at L48h and L72h (Fig.15E,F) coincident with BrdU immunostaining, which may suggest that only a percentage of dividing cells will sum up to the stable population of brain microglia. We also measured microglial cells density along the different time points, and we found no significant differences among all times (Fig.15C) which is in agreement with our previous interpretation.

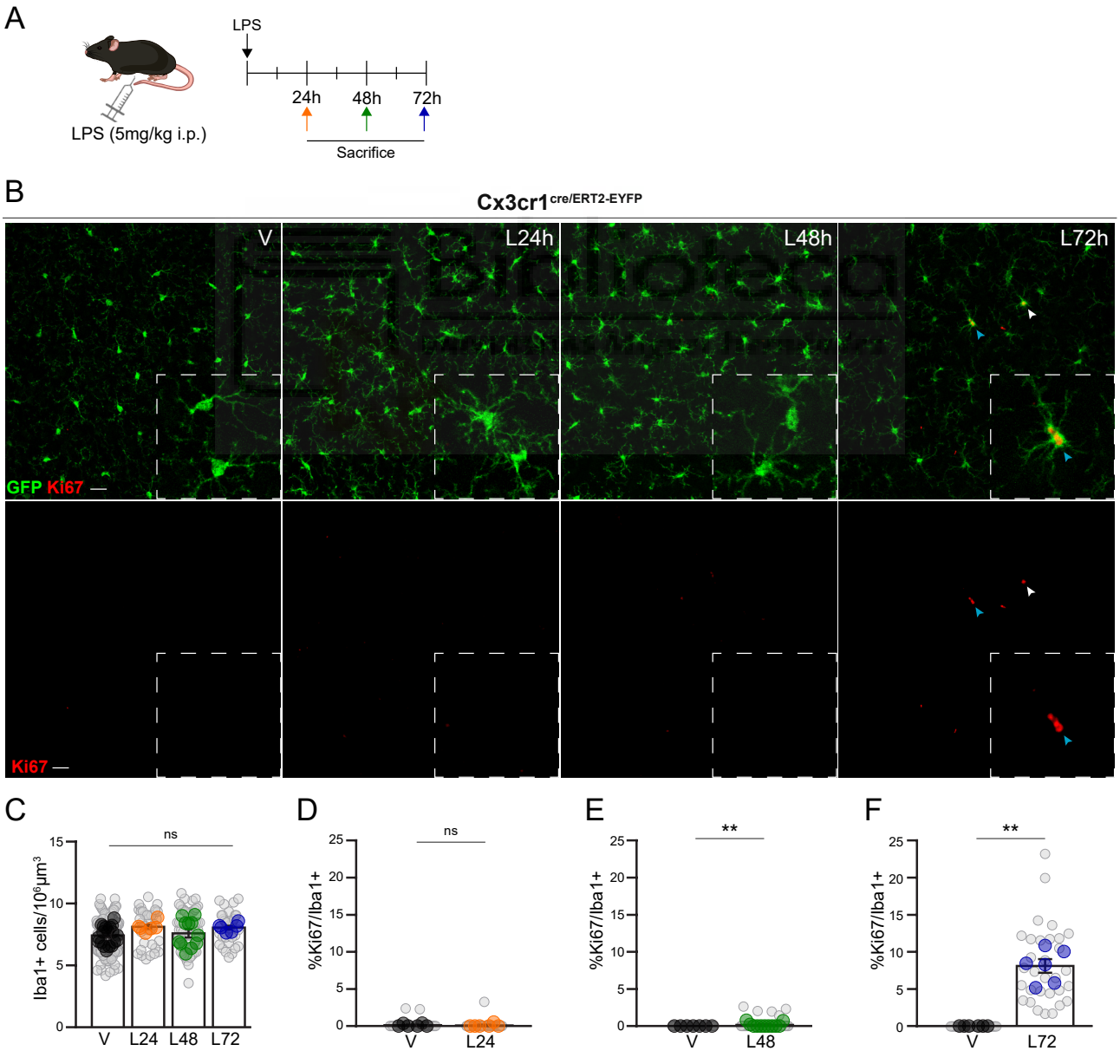

Fig.15. Microglia proliferation addressed by Ki67 staining is functionally carried out at 48h and 72h of an acute inflammatory insult.

(Legend on next page)

4. Late stage of acute inflammation-associated microglia comprise antigens processing and presentation

Next, we performed GO analysis on cluster 7. This cluster is part of the delayed-sustained response as the genes that comprise this cluster are mostly upregulated at 48h and 72h from the LPS insult (Fig.16A). Among the most enriched GO terms in cluster 7, we found antigen processing and presentation and complement activation suggesting the presence of a prominent phagocytic-related activity of microglia during the late stages of the acute inflammatory response (Fig.16B).

For this cluster, we also wonder if the phagocytic-related transcriptional program is carried out by the whole microglia population in response to LPS. To address this question, we performed RNAscope of the previously mentioned marker Axl (Fig.16C). Axl is a TAM receptor tyrosine kinase essential for effective phagocytosis of apoptotic cells (Lemke, 2013). We observe a significant increase in the number of *Axl* RNA molecules at 48h from endotoxin insult in 100% of microglia population (Fig.16D,E).

To study the impact of transcriptional regulation in microglia phagocytic function, we performed immunostaining against CD68. This method is widely used as a measure of microglia digestion of the previously phagocyted debris as CD68 is a glycoprotein that is present on the membrane of the lysosomes. We analysed the colocalization between CD68+ structures and Iba1+ cells with Imaris reconstructions of individual cells (Fig.17A). We identified CD68+ vesicles in all the cells with their average size significantly increasing at L48h (Fig.17D). We found that there is an increase in CD68+ structures total volume and in the number of CD68+ structures per cell at 48 and 72h from LPS administration (Fig.17B,C,D).

Fig.15. Microglia proliferation addressed by Ki67 staining is functionally carried out at 48h and 72h of an acute inflammatory insult.

A. Administration scheme. Mice received one single dose of LPS (5mg/kg i.p.). Mice were sacrificed 24h, 48h, or 72h after LPS administration.

B. Coronal brain sections from male and female P60 Cx3cr1$^{cre/ERT2\text{-}EYFP}$ mice were immunostained against the specific microglia marker Iba1 and Ki67. Scale bars indicate 20 μm.

C. Quantification of microglial (Iba1+) cells density in the somatosensory cortex of male and female P60 Cx3cr1$^{cre/ERT2\text{-}EYFP}$ mice. (V ROI= 113, N=19; L24h ROI = 36, N=6; L48h ROI = 66, N=11; L72h ROI = 34, N=6). One-way ANOVA Kruskal-Wallis test P = 0,2801.

D.E.F. Quantification of Ki67+ nuclei per Iba1+ cell in the somatosensory cortex of male and female P60 Cx3cr1$^{cre/ERT2\text{-}EYFP}$ mice at different time points from LPS (5mg/kg i.p.). administration: **L24h** (V ROI = 36, N=6; L24h ROI = 36, N=6), Unpaired t-test (Mann-Whitney test) P>0.99; **L48h** (V ROI = 41, N=7; L48h ROI = 66, N=11), Unpaired t-test (Mann-Whitney test) **P = 0.0094; and **L72h** (V ROI = 36, N=6; L72h ROI = 31, N=6). Unpaired t-test (Mann-Whitney test) **P = 0.0022.

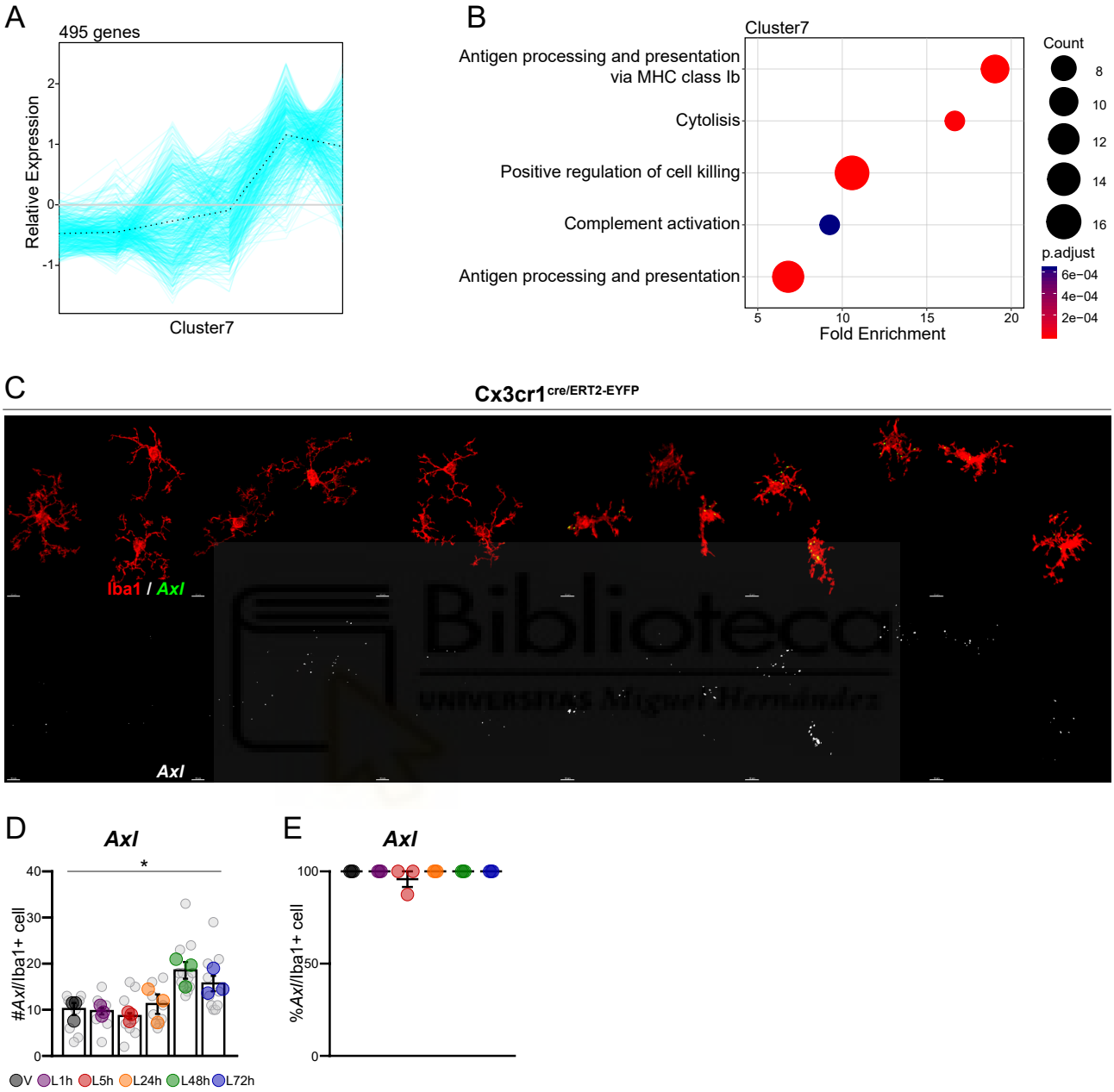

Fig.16. Microglia phagocytic-related transcriptional state is increased after 48h of an acute inflammatory insult.

A. Cluster 7 genes relative expression profile.

B. GO terms biological process associated with cluster 7.

C. Representative image of masked microglia from single molecule in situ hybridization (RNAscope) for Axl followed by immunofluorescence of Iba1 in P60 Cx3cr1$^{cre/ERT2-EYFP}$. Scale bars indicate 10µm.

D. Quantification of Axl RNA-scope expression per individual Iba1+ microglia in the somatosensory cortex of P60 Cx3cr1$^{cre/ERT2-EYFP}$. N = 3 mice per condition, n= 7 to 12 cells per condition. One-way ANOVA Kruskal-Wallis, *p=0.0373. Mean of individual cells ± sem.

E. % of Axl positive microglial cells. Quantifications were performed in 1 to 3 regions of interest (ROI) from somatosensory cortex. N = 3 mice per condition. Mean ± sem.

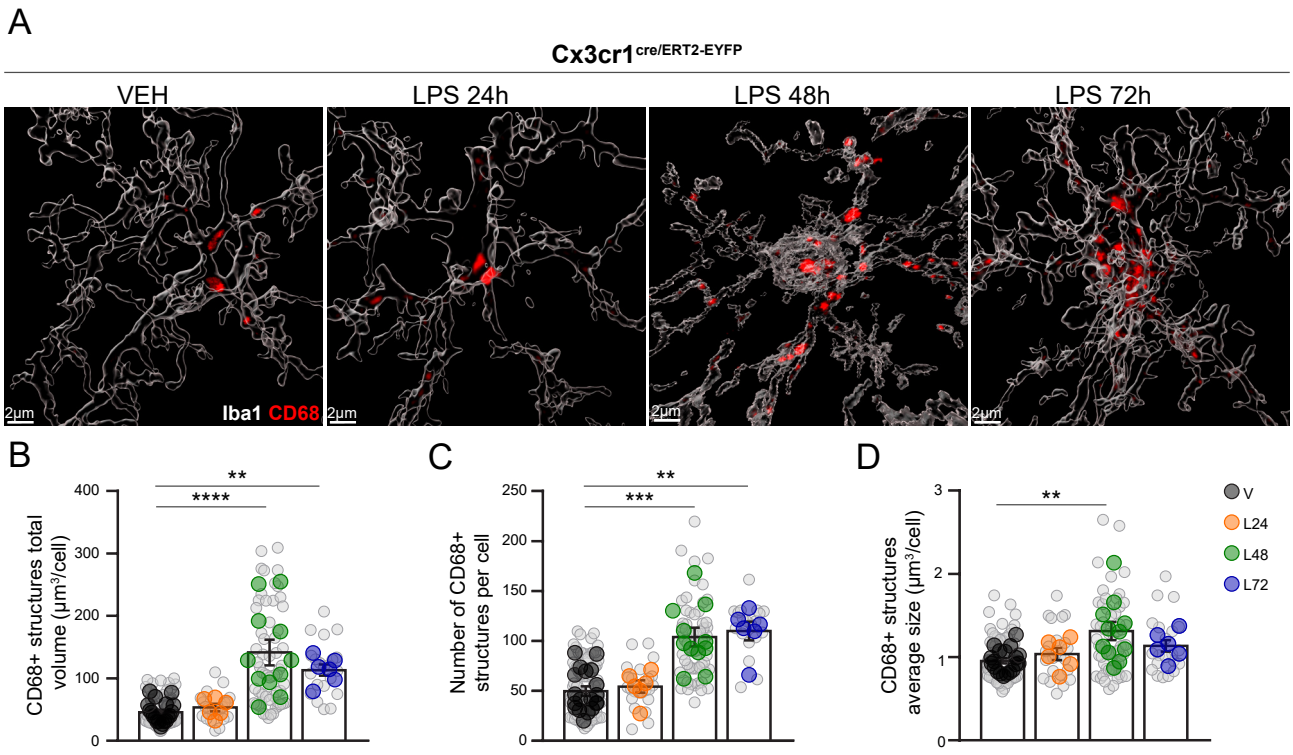

Fig.17. Microglia phagocytic-related activity is increased after 48h of an acute inflammatory insult.
A. Representative images of masked microglia from P60 Cx3cr1$^{cre/ERT2-EYFP}$ mouse coronal brain sections immunostained for the specific microglia marker Iba1 and lysosome membrane specific marker CD68 at 24h, 48h and 72h after one single dose of LPS (5mg/kg i.p). Scale bars indicate 2µm.
B.C.D. Quantification of CD68+ structures total volume from male and female P60 Cx3cr1$^{cre/ERT2-EYFP}$ mice (V n= 87, N=19; L24h n= 23, N=6; L48h n= 62, N=11; L72h n= 21, N=6), One-way ANOVA Kruskal-Wallis test ****P < 0,0001, **P=0.0025; number of CD68+ structures (V n= 87, N=19; L24h n= 23, N=6; L48h n= 62, N=11; L72h n= 21, N=6), ***P = 0,0005, **P=0.0016; and CD68+ structures average size (V n= 87, N=19; L24h n= 23, N=6; L48h n= 62, N=11; L72h n= 21, N=6). One-way ANOVA Kruskal-Wallis test **P=0.0059.

5. Acute neuroinflammatory response is associated with a transient loss of microglia homeostatic state

We have previously shown that in response to an acute trigger (LPS), microglial cells implement a wide variety of functions both cell and population specific that may move away microglia from their physiological balance promoting a loss of their homeostatic function. In the healthy brain, Hickman et al., describe the microglia sensome as a set of 99 genes that encode proteins for sensing both endogenous ligands and infectious agents (Hickman et al., 2013). Microglial cells downregulate 80% of these genes during ageing and in neuroinflammatory conditions.

To further study the changes associated with the loss of homeostatic state of microglial cells during acute neuroinflammation, we performed unsupervised hierarchical clustering of downregulated genes (Fig.6B). From 1612 genes that comprise cluster1 (of downregulated genes) (Fig.18A), 27 are sensome genes. We identify among them *Cx3cr1*, *Gpr34, P2ry12, Siglech, Slc2a5, Tmem119* and *Trem2* (Fig.18B,C). Besides, when we compare IGV profiles of *P2ry12* or *Gpr34* with the representative genes for the upregulated response, we

observe how this downregulation of sensome genes coexist along the time with most of the upregulated genes representative of the microglia functions during acute neuroinflammation (Fig.9C). Moreover, we observe that most of the sensome-regulated genes upon acute systemic LPS show a sharp downregulation at early time points and their response is gradually increased over time. Notably, a proportion of these genes, such as *P2ry12* and *Trem2*, are still significantly downregulated at L72h, when the deferred programs comprising increased expression of phagocytosis-related genes, such as *ApoE* and *Axl* is present.

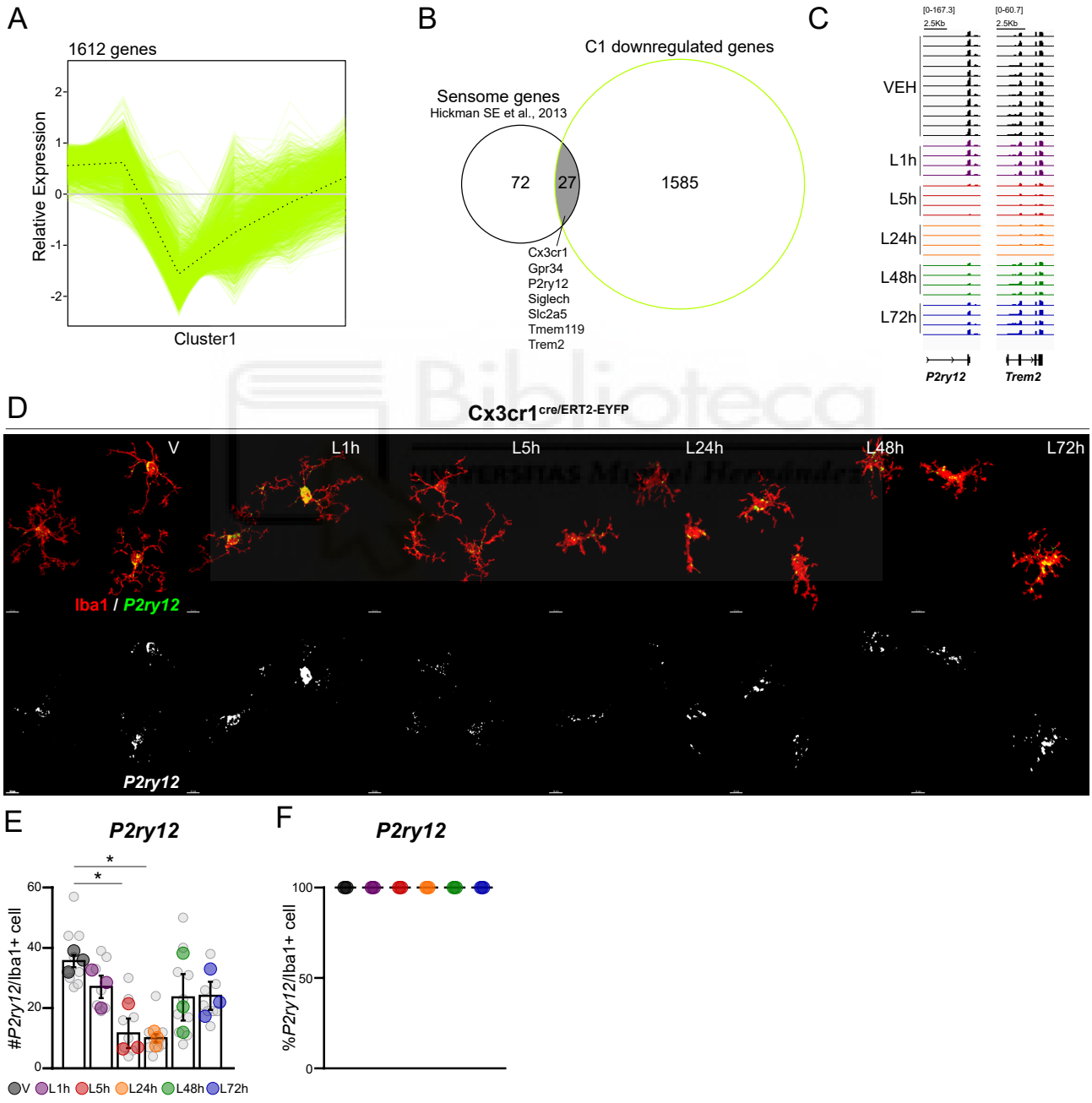

Fig.18. Microglia downregulate homeostatic genes during acute neuroinflammation.
A. Cluster 1 (of downregulated genes) relative expression profile.
B. Venn diagram showing the common genes between the microglia sensome genes (Hickman SE et al., 2013) and the downregulated genes in cluster 1.
C. IGV tracks showing representative genes from cluster 1. VEH: N=11, LPS: N=4 per condition.
D. Representative image of masked microglia from single molecule in situ hybridization (RNAscope) for P2ry12

We next asked whether this downregulation of sensome genes occur in all microglial cells, and therefore, the homeostatic state of microglia may be temporarily lost during acute neuroinflammation. To do this, we performed RNAscope of *P2ry12* (Fig.18D). We observed a strong downregulation in the expression of *P2ry12* from L5h to L24h in the whole microglial population, that is progressively recovered at later time points (Fig.18E,F).

We performed GO analysis of each of the downregulated cluster. We did not identify significantly enriched functions for any of the clusters except for cluster 1. The main functions associated with this cluster were related to actin filament bundle assembly and the regulation of cell morphogenesis (Fig.19A). Some of the genes that we identify associated to these functions are *Rhob, Pak1, Rock2* (Fig.19B). Microglia morphological changes after damage are one of the most salient features that can be observed, even more, they were one of the first features that del Río-Hortega observed back at the beginning of the XX century (Río-Hortega, 1932). To further address the GO biological functions identified, we performed analysis of microglia morphology along the defined acute neuroinflammation course. To do this, we performed immunostaining for Iba1 at 1h,5h,24h, 48h and 72h from LPS (5mg/kg i.p.) administration (Fig.19C) and we, subsequently, performed 3D microglia Sholl analysis with Imaris software. Coincident with transcriptomic data, microglia cell complexity decreases after 5h of LPS and it is progressively recovered from 24h to 72h from LPS administration (Fig.19D). When we look to the dendritic complexity index (DCI=(Σ branch tip orders + # branch tips)×(total dendritic length/total number of primary dendrites) (Pillai et al., 2012), another measurement of the complexity of the cell, we observe the same pattern as Sholl analysis (Fig.19E). We also measured the sum of filaments length and the dendrite branch points. There is a significant decrease of both parameters after 5h and 24h from the LPS administration (Fig.19F,G).

Altogether, this data show that microglia ramified morphology characteristic of the homeostatic state is transiently lost, together with the downregulation of homeostatic genes. As the inflammatory stimuli disappear, the expression of homeostatic genes is recovered along with dendritic arbour ramification suggesting a restoration/re-establishment of the homeostatic state of the cell and therefore the resolution of the neuroinflammation.

followed by immunofluorescence of Iba1 in P60 Cx3cr1$^{cre/ERT2\text{-}EYFP}$. Scale bars indicate 10µm.

E. Quantification of P2ry12 RNA-scope expression per individual Iba1+ microglia in the somatosensory cortex of P60 Cx3cr1$^{cre/ERT2\text{-}EYFP}$. N = 3 mice per condition, n= 7 to 10 cells per condition. One-way ANOVA, *P(V-L5h) =0.0447, *P(V-L24h) =0.0282. Mean of individual cells ± sem.

F. % of P2ry12 positive microglial cells. Quantifications were performed in 1 to 3 regions of interest (ROI) from somatosensory cortex. N = 3 mice per condition. Mean ± sem.

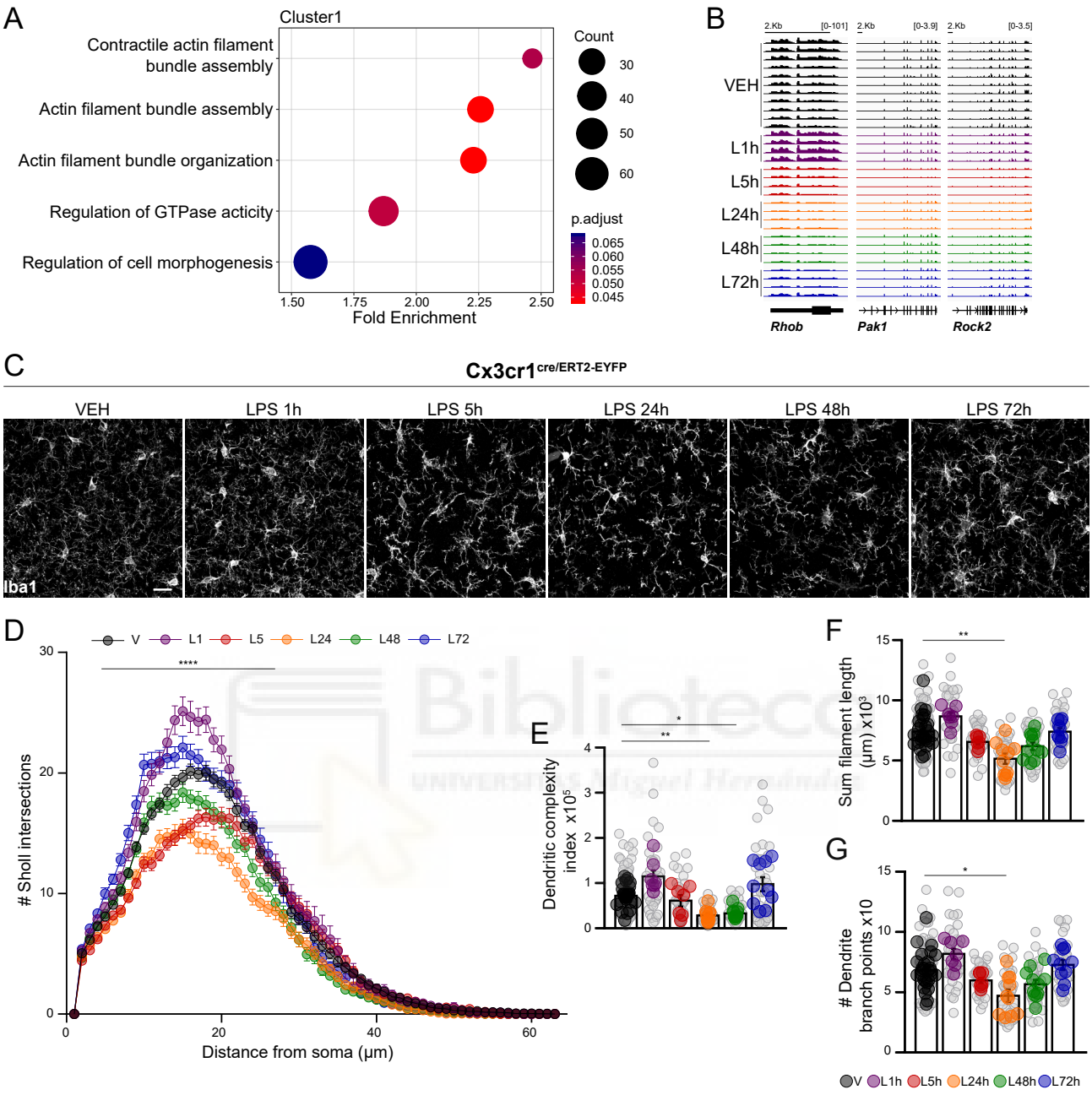

Fig.19. Microglia morphology follows a dynamic temporal transition after an acute inflammatory insult.
A. GO terms biological process associated with cluster 1 (of downregulated genes).
B. IGV tracks showing representative genes from cluster 1. VEH: N=11, LPS: N=4 per condition.
C. Coronal brain sections from P60 Cx3Cr1_CreERT2_YFP mice were immunostained against the specific microglia marker Iba1 at 1h, 5h, 24h, 48h and 72h after one single dose of LPS (5mg/kg i.p.). Scale bars indicate 10µm.
D. 3D Sholl analysis showing means +/- SD for IMARIS reconstructed microglia of somatosensory cortex from P60 male and female Cx3Cr1_CreERT2_YFP mice. V: n=80 N=28; L1h: n=35 N= 7; L5h: n= 32 N= 7; L24h: n= 37 N=10; L48h: n=44 N=11; L72h: n=36 N=10. One way ANOVA repeated measures. ****P<0.0001
E. Dendritic Complexity Index=(Σ branch tip orders + # branch tips)×(total dendritic length/total number of primary dendrites) of individual microglia of somatosensory cortex from P60 male and female Cx3Cr1_CreERT2_YFP mice reconstructed cells with Imaris. V: n=80 N=28; L1h: n=35 N= 7; L5h: n= 32 N= 7; L24h: n= 37 N=10; L48h: n=44 N=11; L72h: n=36 N=10. One way ANOVA Kruskal-Wallis ****P > 0.0001; Dunn's multiple comparisons test (V vs L24h **P=0.0027, V vs L48h *P=0.0132).
F.G. Filament length (sum) and Dendrite Branch Point of individual microglia of somatosensory cortex from P60 male and female Cx3Cr1_CreERT2_YFP mice reconstructed cells with Imaris. V: n=80 N=28; L1h: n=35 N= 7; L5h: n= 32 N= 7; L24h: n= 37 N=10; L48h: n=44 N=11; L72h: n=36 N=10. Fill Length: One-way ANOVA Kruskal-Wallis ****P > 0,0001; Dunn's multiple comparisons test (V vs L24h **P=0.0037); B. Points: One-way ANOVA Kruskal-Wallis ***P > 0,0001; Dunn's multiple comparisons test (V vs L24h *P=0.0301).

6. *In silico* motif analysis predict specific regulatory elements of microglia acute neuroinflammatory response

To further explore the regulatory elements that are associated to each of the transcriptional programs underlying microglia acute neuroinflammation we performed an enrichment motif analysis with Homer. We examined 200 base pair upstream and 50 downstream of the promoter regions of each gene. We identified specific transcription factor motif enrichment associated with each of the clusters. Among the most representative, we identified NF-κB/ p65 enriched in cytokine related cluster (cluster 1), interferon regulatory factor (IRF) enriched in interferon related cluster (cluster 4) or E2F and CHR transcription factors enriched in clusters related with proliferative function (clusters 5 and 6) (Fig.20A). These results indicate that microglia transcriptional control of the inflammatory response is highly regulated. Further studies to better understand the specific role of the previously identified transcription factors in the regulation of microglia acute neuroinflammatory response will be needed.

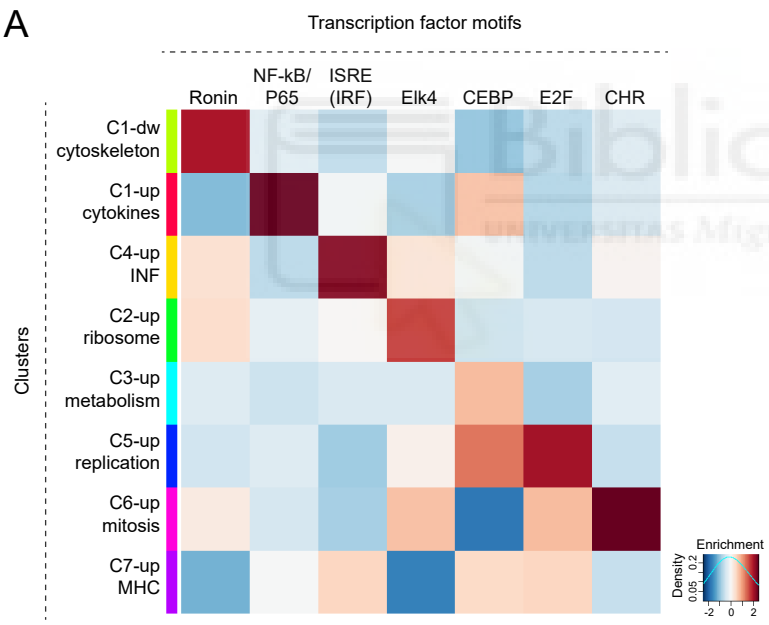

Fig.20. Microglia *in silico* homer analysis of DEG predicts specific transcription factor motif enrichment associated to each of the previously described microglia clusters.
A. Heatmap shows enrichment of transcription factor motifs associated to LPS longitudinal study clusters. INF: interferon; MHC: major histocompatibility complex.

7. Dynamic chromatin accessibility landscape changes associated with acute neuroinflammatory response.

Microglia are plastic cells that constantly adapt to environmental signals. The tissue environment influences microglia and other tissue-resident macrophages phenotypes by activating a common enhancer repertoire where the transcription factor PU.1 plays a main role (Gosselin et al., 2014). Peritoneal resident macrophages transplanted to the alveolar cavity are reprogrammed by the new environment and acquire lung-resident macrophages identity, emphasizing even more the role of the microenvironment in shaping the functional identity of tissue-resident macrophages (Lavin et al., 2014). In the CNS, microglia chromatin

accessibility varies from embryonic development to adulthood and is influenced by changes in the microbiome indicating the important influence of the microenvironment in microglia in the CNS (Thion et al., 2018). To further address microglia chromatin accessibility landscape modifications during the acute neuroinflammatory response, we performed an assay for transposase accessible chromatin with high-throughput sequencing (ATAC-seq) (Buenrostro et al., 2013; Thion et al., 2018) of FACS purified microglia at 1, 5, 24, 48, and 72h from an acute insult with 5mg/kg LPS.

PCA shows that the time component defines the main variance across samples. Our time-course study captures virtually almost the whole chromatin accessibility changes associated with the neuroinflammatory response, with samples following a circular pattern in the first two principal components of the PCA. We found that most of the samples are located near each other. The higher variance is attributed to L24h samples that represent the great majority of the changes. We found that samples for most of the distinct time points are located near each other with the exception of L5h, that likely represents the peak of the response. (Fig.21A). Contrary to RNA-seq data, L72h has not return to basal state. Differentially accessible regions (DARs) analysis across the different time points shows that the majority of chromatin changes occur at L24h (Fig.21B) opposite to the majority of transcriptional changes that are observed at L5h in our RNA-sequencing study (Fig.21C). Clustering analysis shows that the accessibility of chromatin across the acute neuroinflammatory response is stepwise regulated (Fig.21C). Altogether, these data suggest that chromatin accessibility changes are especially important not in the initiation but in the transition to the resolution phase of the acute neuroinflammatory response.

8. Microglia states associated with neurodegenerative diseases are also found in acute neuroinflammation.

Neuroinflammation is a common feature in neurodegenerative diseases and strategies to modulate neuroinflammatory processes are increasingly considered as therapeutic options. Alzheimer's disease clinical landscape is moving from therapies focused on amyloid and tau-related drugs to metabolism, synaptic plasticity, vasculature and inflammation among others (Cummings et al., 2020). How neuroinflammation contributes to the progression of neurodegenerative diseases is still unclear. Recent epidemiological and GWAS data supports the new hypothesis of innate immunity as a cause and/or driver of AD (Guerreiro et al., 2013; Holmes et al., 2009; Karch & Goate, 2015; Lambert et al., 2013). All these studies, together with the functional diversity of microglia associated with neurodegenerative diseases support the importance of innate immunity dysregulation in pathologies with a chronic inflammatory component. In particular, from 2016, with the incorporation of single-cell RNA-sequencing

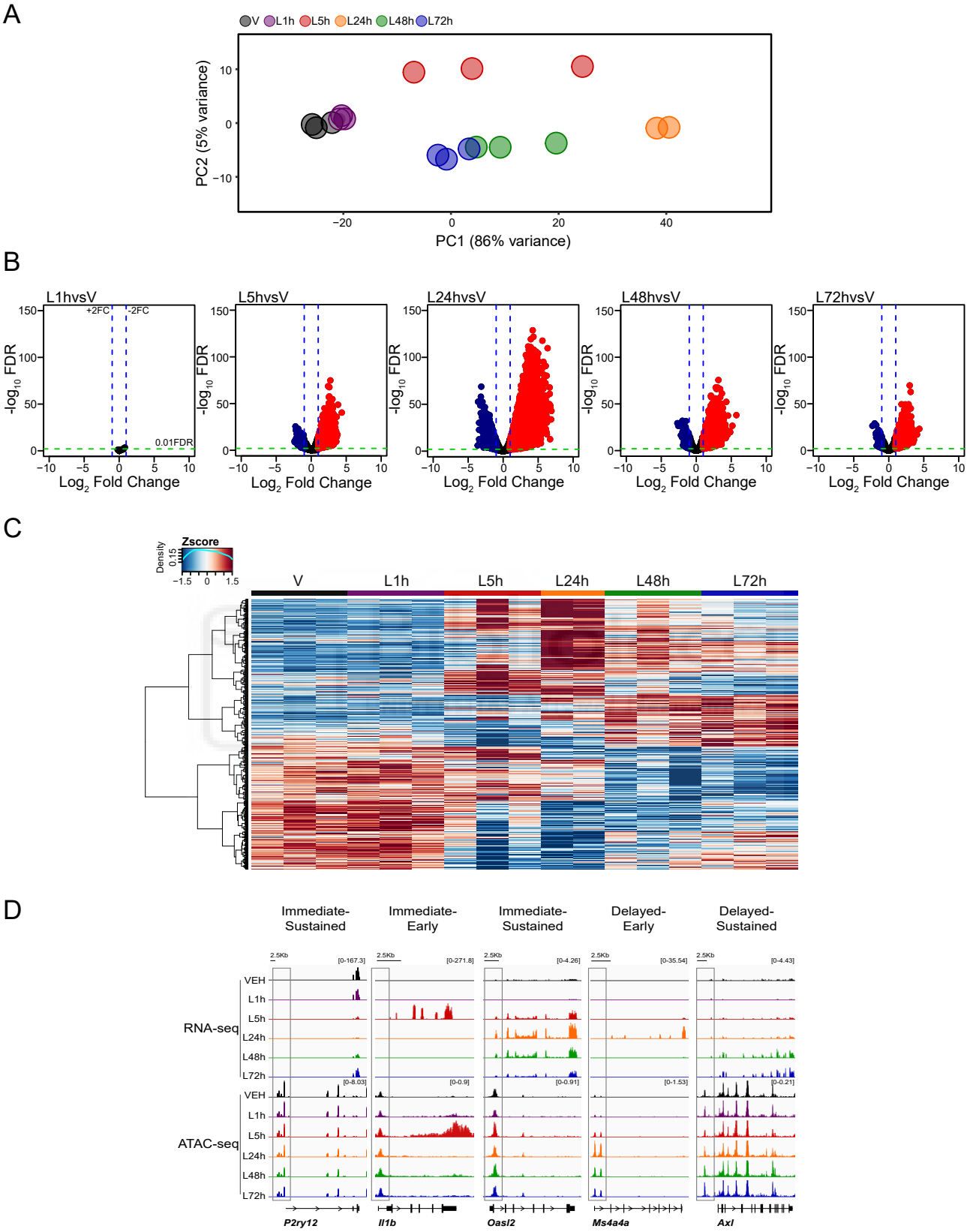

Fig.21. ATAC-Seq reveals changes in chromatin accessibility during the acute neuroinflammatory response

A. PCA of normalized counts.

B. Volcano plots showing the differentially accessible regions (DAR) (FDR < 0.01, FC>2) at L1h, L5h, L24h, L48h, L72h.

C. Heatmap showing the hierarchical clustering of all DARs (FDR < 0.01, FC>2). Each column is a biological replicate of purified microglia from mouse cortex.

D. IGV tracks from RNA-seq and ATAC-seq normalized read counts of representative genes per cluster.

techniques, several publications unveil a disease-associated microglia phenotype in different models of neurodegenerative disease (Keren-Shaul et al., 2017; Mathys et al., 2017; Sala Frigerio et al., 2019). Besides DAM, it has been shown that microglia can be found in other states during neurodegenerative diseases expressing interferon, proliferative o phagocytic markers. Shemer et al., also found *in silico* some genes associated with DAM phenotype, present in microglia during acute neuroinflammatory conditions (Shemer et al., 2020). We hypothesize that there is a limited number of microglia functional states that are differentially implemented depending on the context. To test this hypothesis, we meta-analysed published DAM markers with our longitudinal LPS study on microglia isolated cells. We show that DAM genes are modulated in the delayed microglia response to LPS as well (Fig.22). In view of this, we performed single-cell RNA-sequencing of hippocampal microglia isolated cells from 12 months old J20 mouse model of AD and age-matched controls. The whole tissue process and microglia purification by FACS were performed in ice-cold conditions to minimize artefactual activation. We FACS-purified microglia stained for CD11b and RNA transcripts from single cells were barcoded, reverse transcribed and sequenced using 10X genomics platform (Fig.23A). We sequenced a total of 7.865 single cells in J20 and 7.033 in control mice.

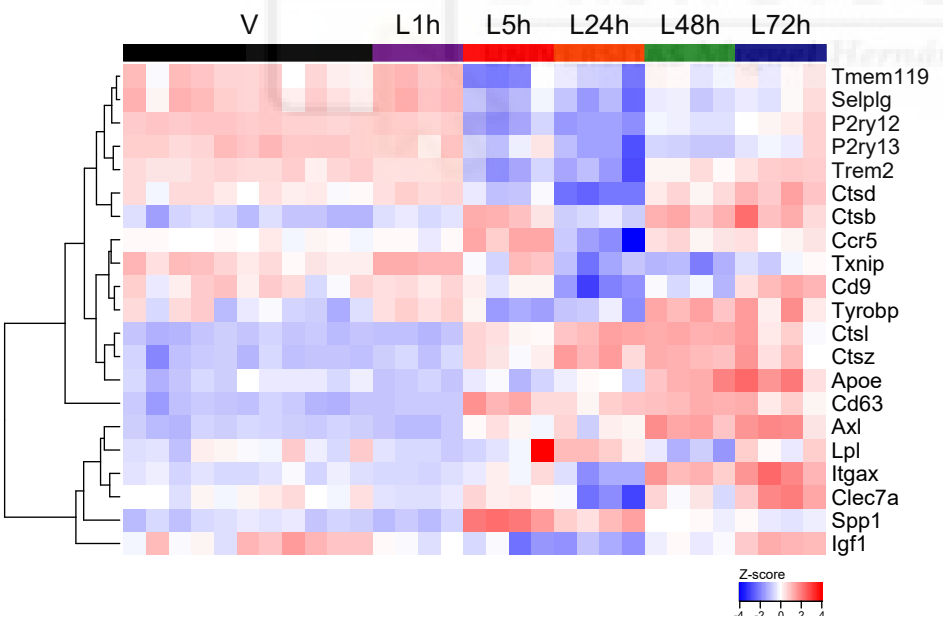

Fig.22. DAM signature is present in the late stages of microglia response to LPS
Heatmap showing the expression levels of published DAM markers in our microglia RNA-seq data in response to LPS.

We next performed unsupervised clustering analysis for the identification of major subpopulations. We identified 11 clusters that downstream were aggregated into 7 populations. These clusters were annotated based on differential expression of known cell type-specific marker genes (Keren-Shaul et al., 2017; Mathys et al., 2017; Sala Frigerio et al., 2019). The majority of cells captured in our single-cell RNA-sequencing were microglia: Homeostatic microglia (HM), interferon related microglia (IRM), proliferative microglia (PM), disease associated microglia type 1 (DAM1) and disease associated microglia type 2 (DAM2); with

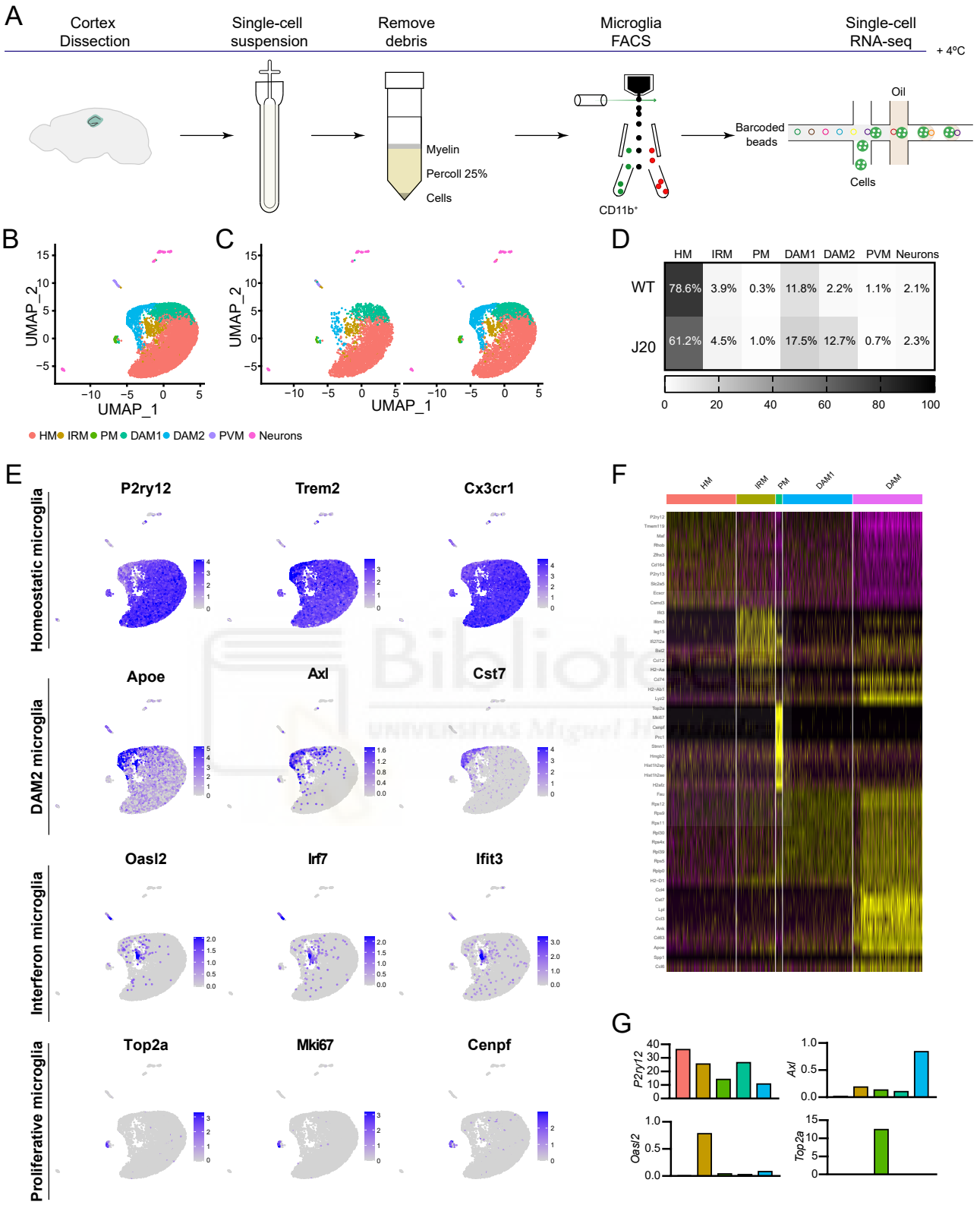

Fig.23. Single-cell RNAseq of J20 mice reveals 5 microglia populations

A. Schema showing microglia isolation process and libraries preparation with 10X genomics. Microglia were isolated from the hippocampi of 12 months old J20 mouse and age-matched controls.

B. UMAP of microglia subclustered from CD11b+ cells. HM-homeostatic microglia; IRM-interferon response microglia; PM-proliferative microglia; DAM1/2-disease-associated microglia 1/2; PVM-perivascular macrophages; Neurons.

C. UMAP plot of WT and J20 conditions. Each condition is a pool of 6 hippocampi from 3 mice.

D. Heatmap of the percentage of cells per cluster.

E. UMAP plot showing the expression of canonical microglia markers associated with homeostatic microglia population, DAM2, interferon responsive and proliferative microglia.

significant lower numbers of 2 other cell populations: perivascular macrophages (PVM) and neurons (Fig.23B). These populations displayed different distribution between genotypes (Fig.23C). In J20 mice, we identify a sharply decrease of HM (61.2% J20 vs 78.6% WT), an increase of IRM (4.5% J20 vs 3.4% WT) and DAM1 (17.5% J20 vs 11.8% WT), and a robust increase of DAM2 being mostly expressed in J20 mice (12.7% J20 vs 2.2% WT). PM, PVM and neurons are between the 0.3 and 2.3% of the total sequenced cells (Fig.23D). Homeostatic microglia are expressing high levels of known microglia markers (*P2ry12, Trem2, Cx3cr1*) (Fig.23E) in both WT and J20, with expression levels varying in the rest of subpopulations identified. We identified 2 clusters of disease associated microglia (DAM1 and DAM2). DAM1 is identified in both WT and J20 but DAM2 subpopulation is specifically present in J20. DAM2 is characterized by expression of markers like Apoe, Axl or Cst7 and a decrease in the expression of homeostatic markers (*P2ry12*, *Trem2*, *Cx3cr1*) (Fig.23E). The IRM cluster is also highly present in J20 compared to controls and it is characterized by the upregulation of markers related with interferon response like *Oasl2*, *Irf7* or *Ifit3* (Fig.23E). The last microglia cluster identified accounts for a 0.3%-1.0% of total microglia pool (PM) (Fig.23D). This cluster was enriched in genes involved in microglia proliferation like Top2a, Mki67 or Cenpf (Fig.23E) and did not display selective enrichment for any of both genotypes, maybe representing a small pool of cycling microglia (Askew et al., 2017). Microglia populations identified in our study in the J20 mouse model of AD are in close agreement with previously published data in other mouse models of AD like APP^{NL-G-F}, 5XFAD or Ck-p25 (Keren-Shaul et al., 2017; Mathys et al., 2017; Sala Frigerio et al., 2019; Wang et al., 2020).

9. Interferon and phagocytic-related markers are selectively upregulated in microglial cells located in the proximity of the amyloid-β plaques in a mouse model of Alzheimer's disease

Given the above mentioned single-cell data, where we identify common microglia subpopulations in a chronic inflammatory condition (AD) and acute inflammatory insult (LPS), we next examine the spatial distribution at the single-cell level of common identified markers with RNAscope in 20 months old APP/PS1 and age-matched controls mice. The ageing chosen in both animal models (J20 and APP/PS1) resembles the chronic stage of the AD pathology. We use P2ry12 as a marker for microglia, UMAP and normalized expression plot show that P2ry12 is still present in J20 mice although its expression is lower compared with WT (Fig.24A,B). We first tested the expression of *P2ry12 in situ* (Fig.24C). We observed that there is a downregulation of P2ry12 associated with the proximity (less than 25μm from the

F. Gene expression heatmap for clusters previously identified. Genes shown are the top gene markers for each cluster defined by Wilcoxon rank-sum test
G. Bar plots showing average expression for key signature genes on UMAP: P2ry12, Axl, Oasl2, and Top2a.

core of the plaque) of both compact and diffuse plaques. The expression is progressively recovered, being at the same level as controls in cells that are further than 50µm from the centre of the plaque (Fig.24D). We then performed RNAscope of previously selected markers for microglia states, *Il1b*, *Oasl2*, *Ms4a4a* and *Axl*, in 20 months old APP/PS1 mice and age-matched controls. We do not detect expression of *Il1b* and *Ms4a4a* in microglial cells of APP/PS1 mice (Fig.25; Fig.26), suggesting that cytokines and proliferation are not occurring in areas close nor far from the β-amyloid plaques. Interestingly, we observe an increase of *Oasl2* in the proximity of diffuse plaques whereas we cannot observe this in areas surrounding compact plaques suggesting specificity in the interferon response that could be related to the toxicity of the diffuse Aβ plaques (Fig.27C,D). Besides, when we look

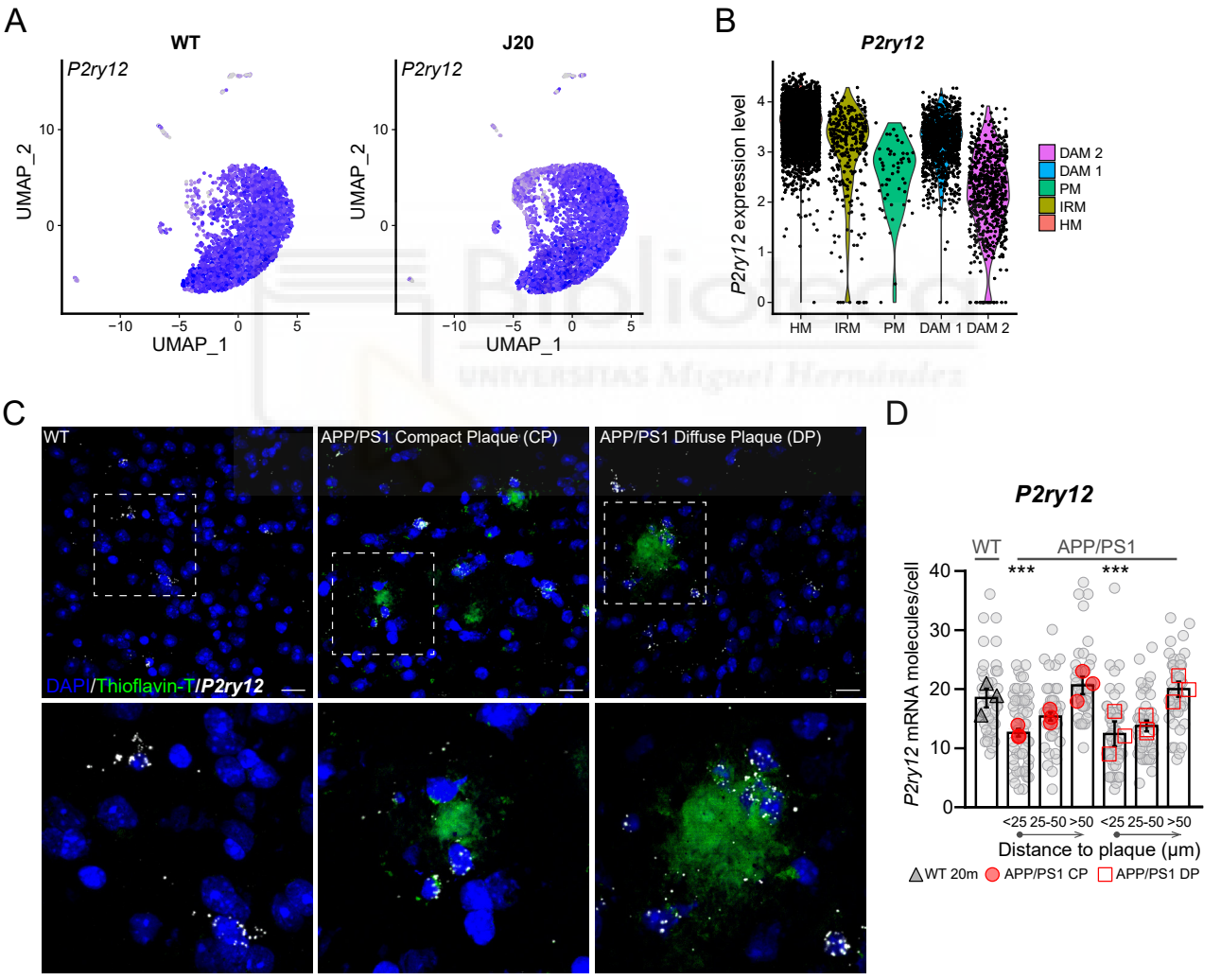

Fig.24. Microglia P2ry12 is selectively downregulated in the vicinity of β-amyloid plaques.
A. UMAP plot of P2ry12 expression in WT and APP/PS1 mice.
B. P2ry12 average expression in all microglia subpopulations identified by single-cell RNA-sequencing.
C. Representative images and magnifications of 20 months old male APP/PS1 mice. Coronal brain sections from somatosensory cortex stained by RNAscope for P2ry12 probe and Thioflavin-T for β-amyloid plaques. Scale bars indicate 20µm.
D. Quantification of P2ry12 mRNA dots per individual microglial cell reconstructed by Imaris. WT: n=13 N=3; J20: n=10-14 cell per condition N= 3; **N**: One-way ANOVA F(6, 14) **P=0.0015 Bonferroni multiple comparisons test (0-25µm vs 25-50 µm *P < 0,01). **n**: One-way ANOVA F(6, 304) ****P<0.0001 Bonferroni multiple comparisons test (***P<0.001 CT vs 0-25µm CP and DP).

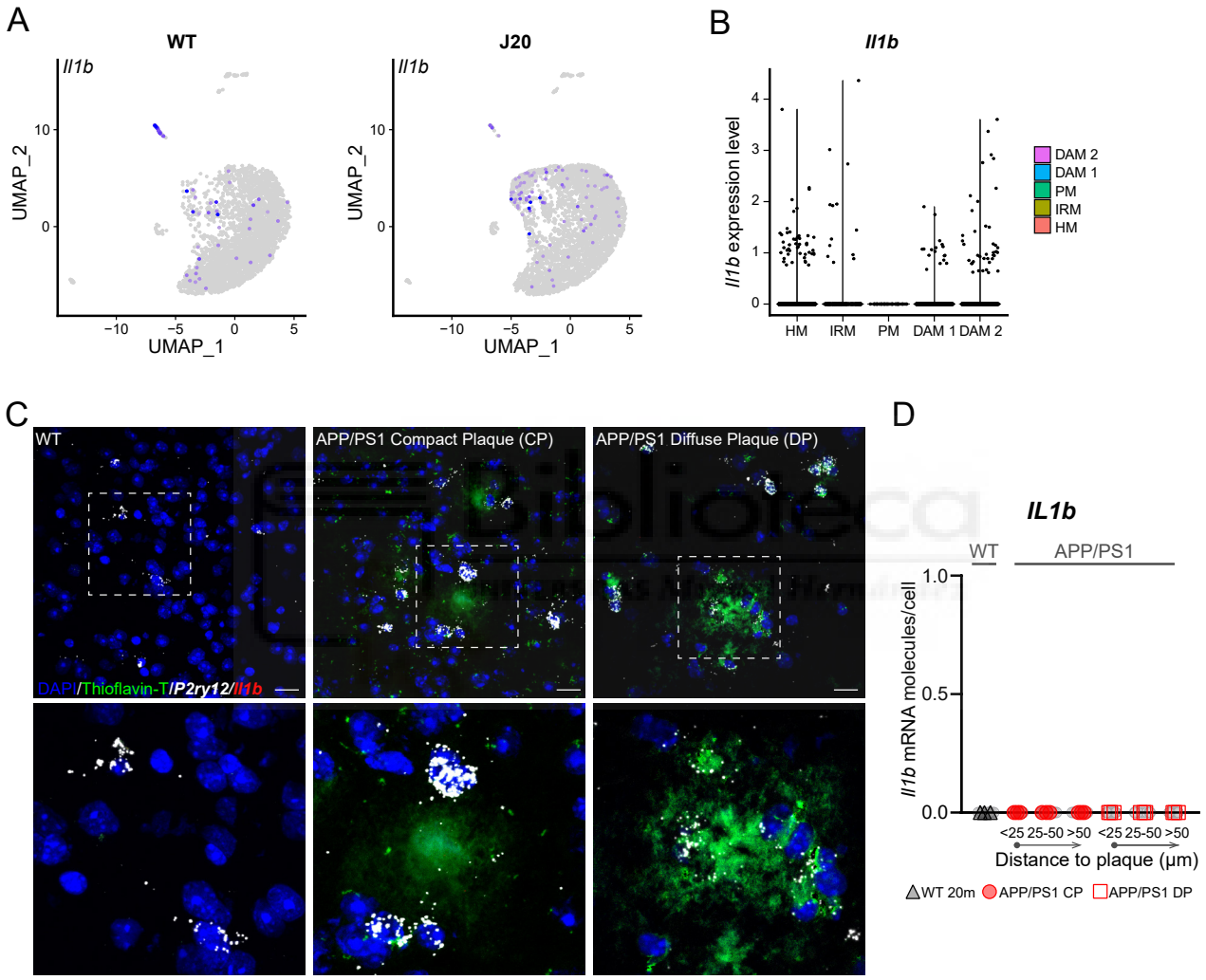

Fig.25. Microglia cytokines expression (Il1b) is not identified in situ in 20 months old APP/PS1 mouse brain.

A. UMAP plot of Il1b expression in WT and APP/PS1 mice.

B. Il1b average expression in all microglia subpopulations identified by single-cell RNA-sequencing.

C. Representative images and magnifications of 20 months old male APP/PS1 mice. Coronal brain sections from somatosensory cortex stained by RNAscope for Il1b probe and Thioflavin-T for β-amyloid plaques. Scale bars indicate 20µm.

D. Quantification of Il1b mRNA dots per individual microglial cell reconstructed by Imaris. WT: n=10 N=3; J20: n=10-11 cell per condition N= 3; **N**: all values are 0 **n**: all values are 0. SD=0.

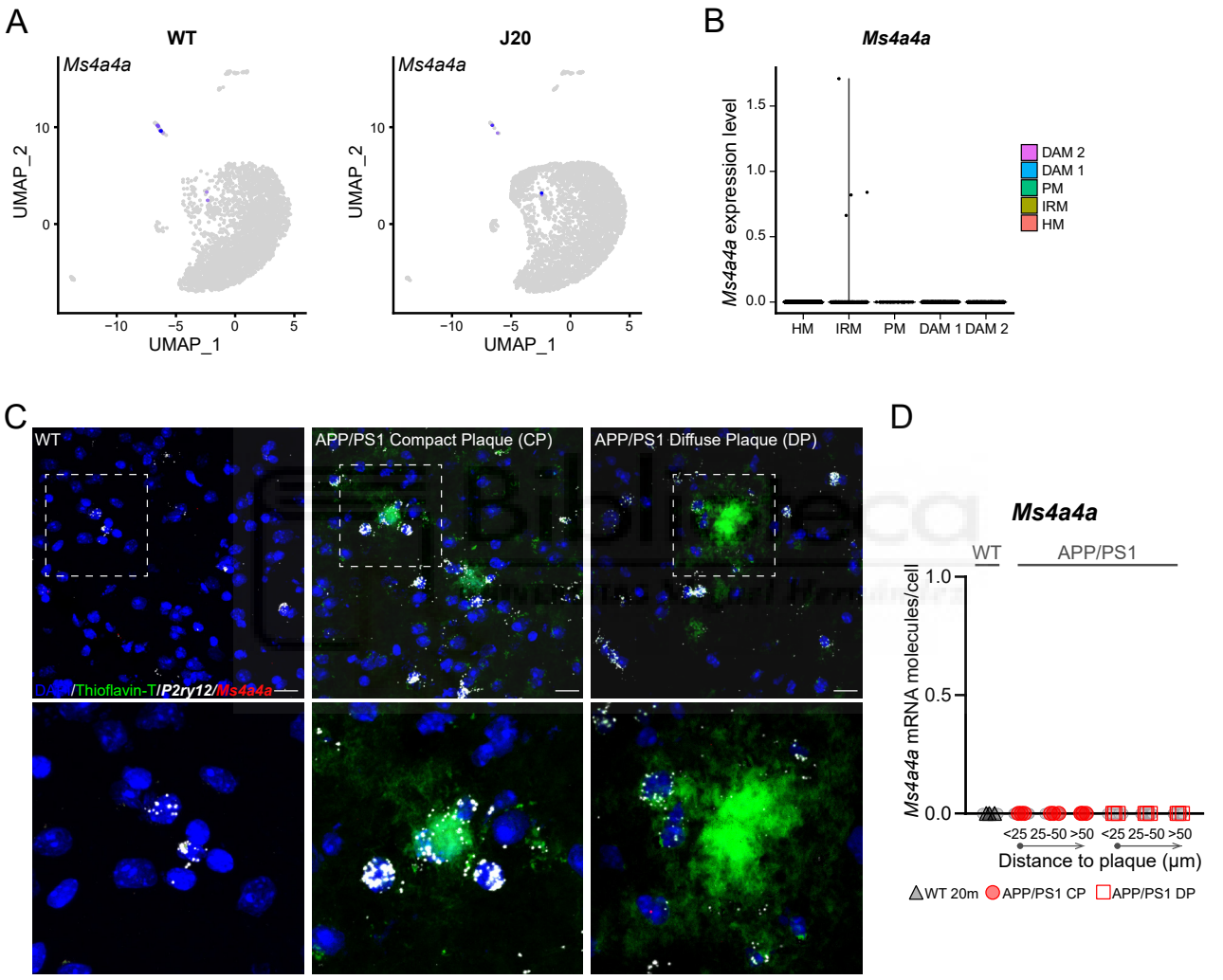

Fig.26. Proliferative microglia (Ms4a4a) is not identified in situ in 20 months old APP/PS1 mouse brain.
A. UMAP plot of Ms4a4a expression in WT and APP/PS1 mice.
B. Ms4a4a average expression in all microglia subpopulations identified by single-cell RNA-sequencing.
C. Representative images and magnifications of 20 months old male APP/PS1 mice. Coronal brain sections from somatosensory cortex stained by RNAscope for Ms4a4a probe and Thioflavin-T for β-amyloid plaques. Scale bars indicate 20µm.
D. Quantification of Ms4a4a mRNA dots per individual microglial cell reconstructed by Imaris. WT: n=8 N=3; J20: n=6-16 cell per condition N= 3; **N**: all values are 0 **n**: all values are 0. SD=0.

at the phagocytic-related marker *Axl*, we observe a specific increase in the expression of this marker in areas close to both diffuse and compact plaques (Fig.28C,D). In summary, these results suggest that all microglial cells surrounding plaques are phagocyting but only the ones that surround toxic plaques are also expressing interferon. We hypothesize that interferon-related pathway could potentially be targeted to modulate the plaque toxicity associated to Alzheimer's disease. We show both *in silico* and *in situ* for the first time to our knowledge, that interferon and phagocytic phenotypes that have previously been associated to neurodegenerative disease can be also found during the acute neuroinflammatory response. We have shown for the first time, that these diverse microglia states can be

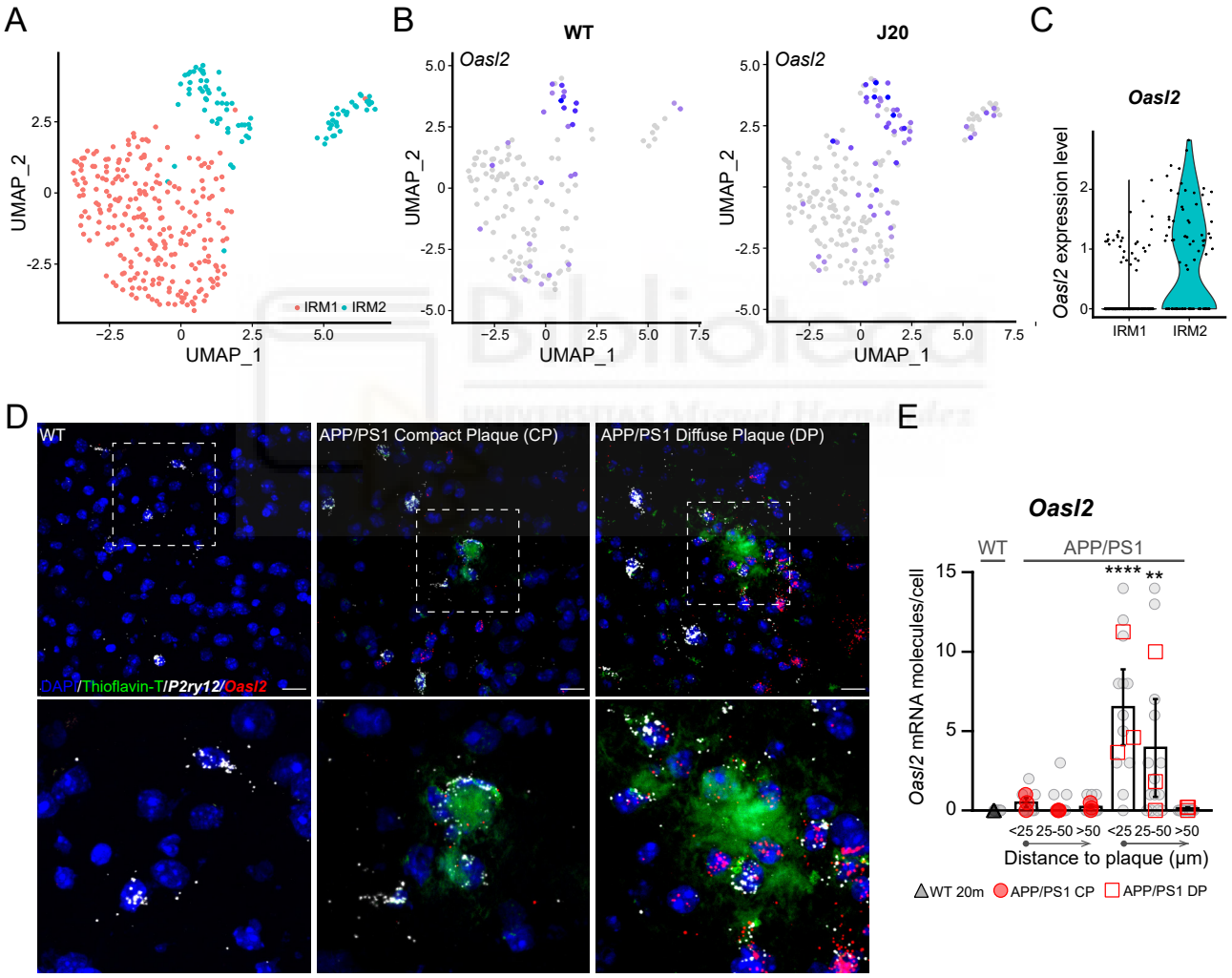

Fig.27. Interferon marker Oasl2 is upregulated by microglia in the proximity of diffuse β-amyloid plaques.
A. UMAP plot of Oasl2 expression in WT and APP/PS1 mice.
B. Oasl2 average expression in all microglia subpopulations identified by single-cell RNA-sequencing.
C. Representative images and magnifications of 20 months old male APP/PS1 mice. Coronal brain sections from somatosensory cortex stained by RNAscope for Oasl2 probe and Thioflavin-T for β-amyloid plaques. Scale bars indicate 20µm.
D. Quantification of Oasl2 mRNA dots per individual microglial cell reconstructed by Imaris. WT: n=13 N=3; J20: n=10-14 cell per condition N= 3; **N**: One-way ANOVA (F6,14) *P=0.0399. **n**: One-way ANOVA F(6, 78) ****P<0.0001 Bonferroni multiple comparisons test (****P<0.0001 CT vs 0-25µm DP and **P=0.092 CT vs 25-50µm DP).

found during an acute neuroinflammatory response, not as individual entities but as part of a coordinated response that comprises different transcriptional programs.

10. OASL and AXL are upregulated in the brain of AD patients

DAM phenotype is well established in mouse models of AD but, until the moment, its presence in the brain of AD patients remains elusive. Single-nucleus RNA-seq data shows divergent enrichment for genes related to neurodegenerative disease being the signature of the murine DAM phenotype (like *CD74* or genes related with MHCII) present but distributed into several independent microglia subsets (Mathys et al., 2019; Olah et al., 2018). Given

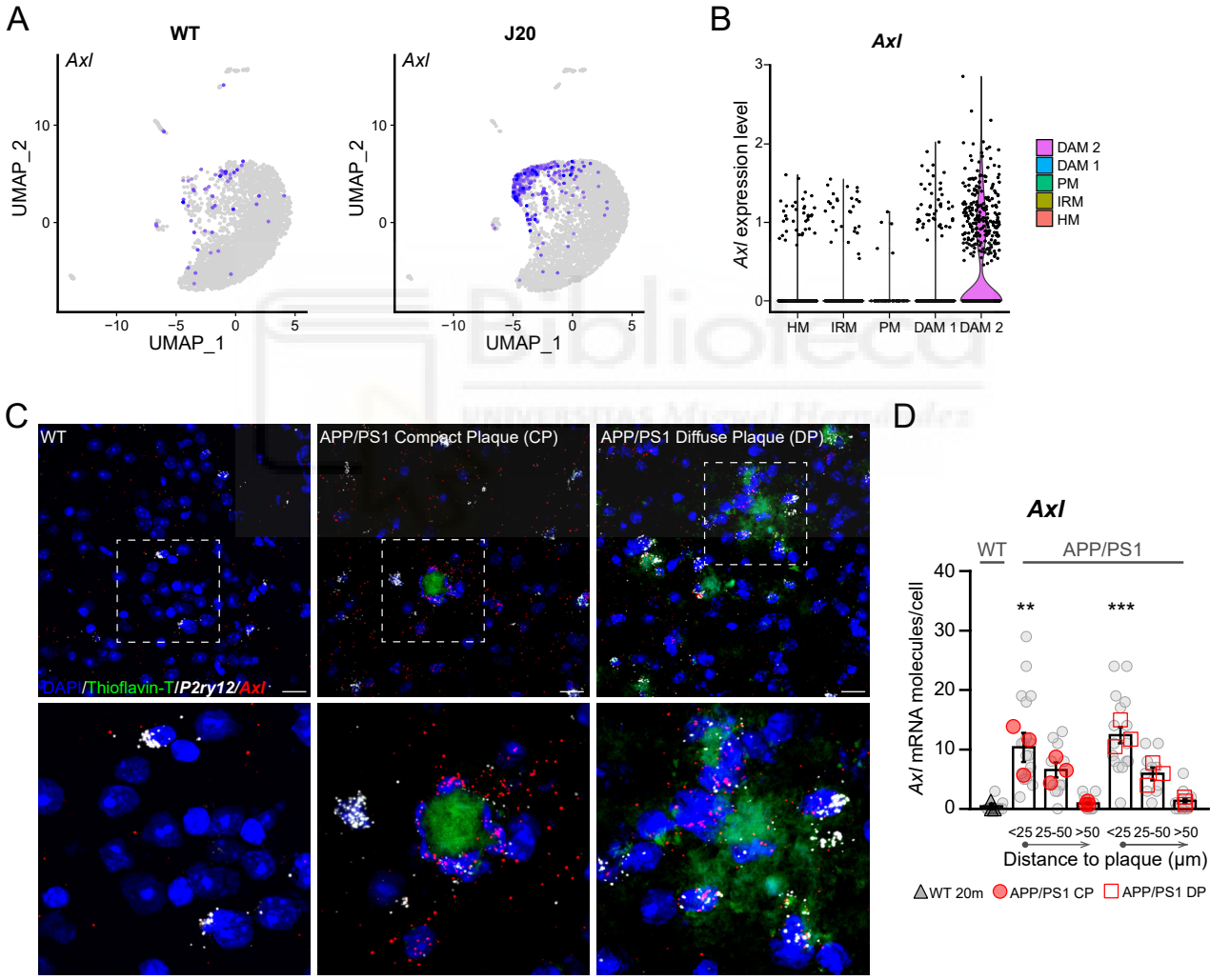

Fig.28. Phagocytic-related marker Axl is upregulated by microglia in the proximity of both compact and diffuse β-amyloid plaques.
A. UMAP plot of Axl expression in WT and APP/PS1 mice.
B. Axl average expression in all microglia subpopulations identified by single-cell RNA-sequencing.
C. Representative images and magnifications of 20 months old male APP/PS1 mice. Coronal brain sections from somatosensory cortex stained by RNAscope for Axl probe and Thioflavin-T for β-amyloid plaques. Scale bars indicate 20µm.
D. Quantification of Axl mRNA dots per individual microglial cell reconstructed by Imaris. WT: n=9 N=3; J20: n=11-18 cell per condition N= 3; **N**: One-way ANOVA (F6,14) **** P<0.0001. Bonferroni multiple comparisons test (**P=0.013 CT vs 0-25µm CP and ***P=0.0002 CT vs 0-25µm DP). **n**: One-way ANOVA F(6, 78) ****P<0.0001 Bonferroni multiple comparisons test (****P<0.0001 CT vs 0-25µm CP and (****P<0.0001 CT vs 0-25µm DP).

this, we wonder if we can observe the upregulation of the IRM microglia state marker *Oasl2* and the DAM2 microglia state marker *Axl* in human brain tissue of patients with Alzheimer's disease. Of note, these markers are not expressed in basal conditions in the healthy brain but are induced in response to damage. For this, we obtained frontal cortex tissue from 3 male with non-familiar late-onset AD and 3 male age-matched control patients, and we performed RNAscope of *hIL1b*, *hOASL* and *hAXL*.

We revealed for the first time, an increase in the expression of *hAXL* and *hOASL* in human *post-mortem* brain tissue of Alzheimer's disease patients in comparison with age-matched controls (Fig.29A,B,C).

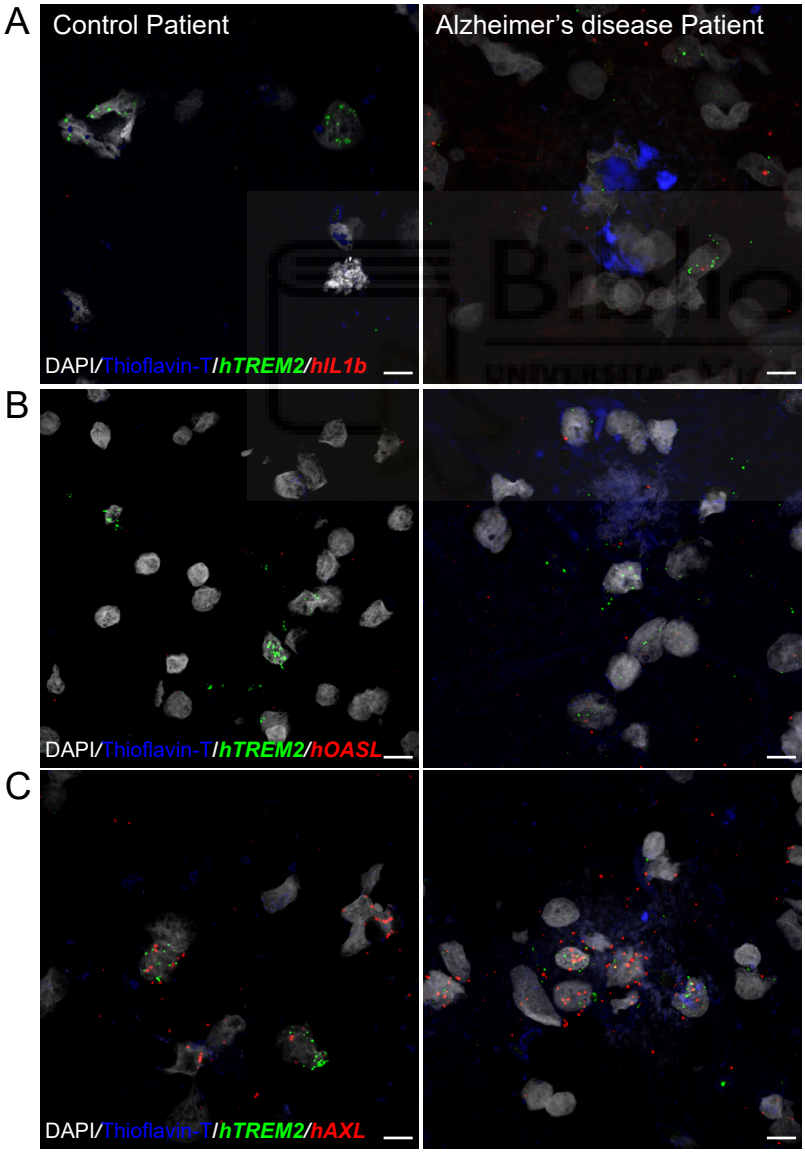

Fig.29. Microglia interferon-responding (*OASL*) and phagocytic (*AXL*) subpopulations are upregulated in human AD.

A. Representative images of age-matched controls and human sporadic AD *post-mortem* brain frontal cortex stained by RNAscope for *hIL1b* and *hTREM2* probes. Thioflavin-T was used to stain β-amyloid plaques and DAPI for nuclei staining. Scale bars indicate 10μm.

B. Representative images of age-matched controls and human sporadic AD *post-mortem* brain frontal cortex stained by RNAscope for *hOASL* and *hTREM2* probes. Thioflavin-T was used to stain β-amyloid plaques and DAPI for nuclei staining. Scale bars indicate 10μm.

C. Representative images of age-matched controls and human sporadic AD *post-mortem* brain frontal cortex stained by RNAscope for *hAXL* and *hTREM2* probes. Thioflavin-T was used to stain β-amyloid plaques and DAPI for nuclei staining. Scale bars indicate 10μm.

11. *RelA*/p65-mediated microglia reprogramming towards interferon-related and phagocytic phenotype modulates neuronal circuits and behaviour in mice

NF-κB is a transcription factor that play a key role in the regulation of the inflammatory response. We previously identified the *RelA*/p65 subunit of NF-κB as a key regulatory element of microglia cytokine-related transcriptional program in response to LPS (Fig.20A). To address the role of *RelA*/p65 in microglia regulation of the inflammatory response we selectively eliminated p65 from exon 5 to exon 8 in adult mice microglia and brain associated macrophages using the inducible Cre recombinase under the control of Cx3Cr1 promoter (Fig.30A). Mice developed normal and from 10 to 12 weeks of age, we administered tamoxifen (TMX) by oral gavage on alternate days. All the experiments were performed 1 month after the last TMX administration (Fig.30A). Gene ablation was reported in microglia isolated cells by RT-qPCR of p65 exons 6 to 7 targeting the depleted region and exons 1 to 3 previous to the floxed region. We observe a reduction of 100% of p65 mRNA expression levels of p65

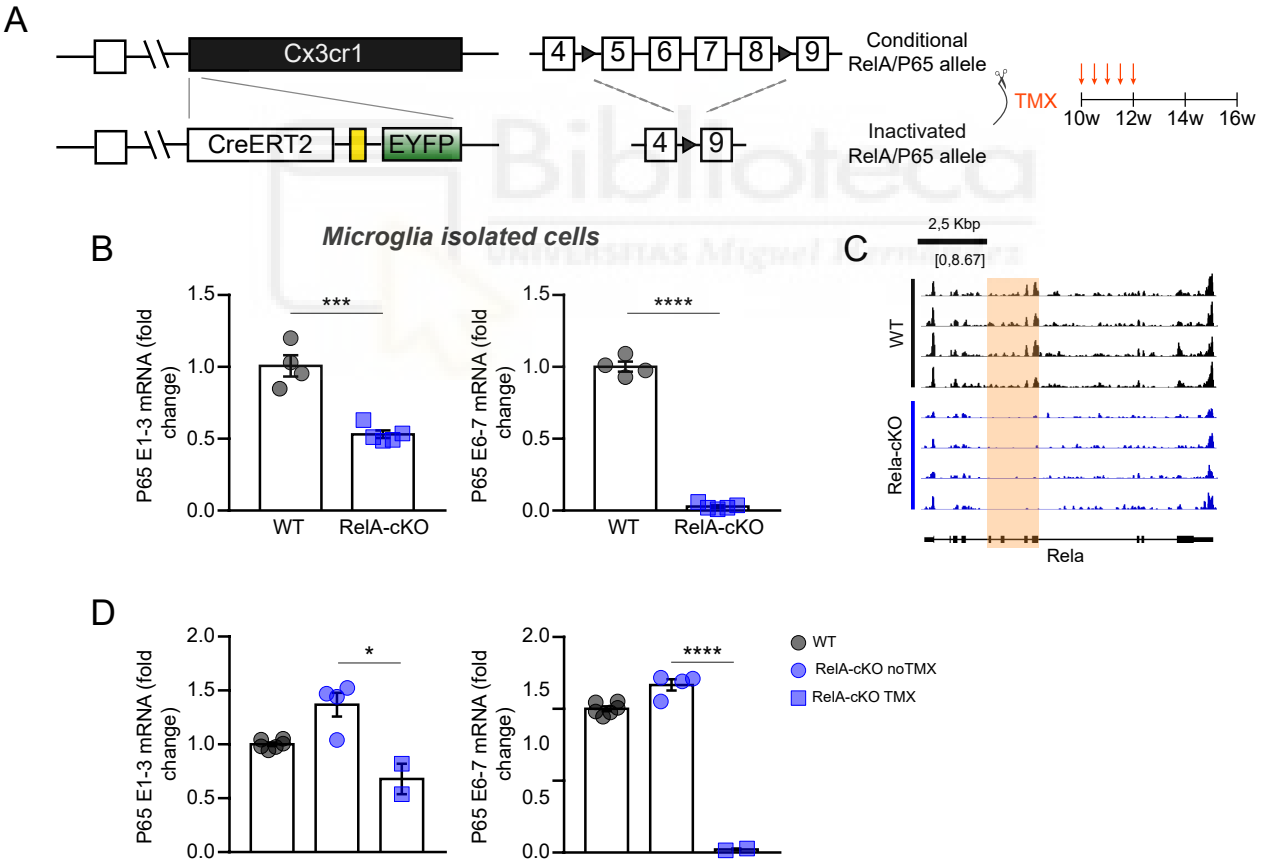

Fig.30. *RelA* conditional deletion in myeloid cells of adult mouse brain.

A. Schematic representation of targeting strategy for Cre/loxP-mediated removal of *RelA* exons 5 to 8 in adult mouse brain after 5 doses of TMX administered on alternate days from week 10 to week 12. Experiments were carried out 1 month after the last TMX administration.

B. mRNA expression of RelA exons 1-3 and 6-7. WT (N=4) and RelA-cKO mice (N=5). **E1-3**: Mann-Whitney test ***P= 0.0003. **E6-7**: Mann-Whitney test ****P 0.0001.

C. RNA-seq tracks of control and microglia-inducible RelA-cKO in the RelA locus. Orange box highlights exons 5-8.

D. mRNA expression of RelA exons 1-3 and 6-7. WT (N=4), RelA-cKO mice without TMX (N=4), and RelA-cKO mice 1 month after TMX (N=2). **E1-3**: One-way ANOVA Kruskall-Wallis test **P = 0.052; Dunn's multiple comparisons: RelA-cKO no TMX vs TMX *P=0.0195. **E6-7**: One-way ANOVA Kruskall-Wallis test **P = 0.019; Dunn's multiple comparisons: RelA-cKO no TMX vs TMX *P=0.0152.

E6-7 and 50% of p65 E1-3(Fig.30B). Besides, p65 E5-8 depletion was observed also in IGV profiles of microglia isolated cells RNA-sequencing data of RelA-cKO mice compared with controls (Fig.30C). To confirm that mice developed normal and p65 depletion is occurring after TMX administration in adulthood, we performed RT-qPCR of microglia isolated cells from RelA-cKO mice before and after TMX administration. We observe a reduction of 100% in *RelA* E6-7 and 50% in *RelA* E1-3 expression after TMX administration compared with controls and RelA-cKO mice before TMX (Fig.30D).

To characterize microglia basal transcriptome in absence of p65, we first performed RNA-seq of microglia isolated cells from RelA-cKO and control mice. Taking advantage of principal component analysis (PCA), we observe a variance of 58% between the two genotypes (Fig.31A). We then examined the differential expressed genes (DEG) and we identified 97 upregulated genes. Among the most significantly expressed are *Axl, Ifi213, Oasl2, Oas2* or *Irf7* (Fig.31B). To further explore the biological function, we performed GO analysis on significantly upregulated genes. We identified response to interferon-β or antigen processing and presentation between the most significantly enriched functions (Fig.31C). These results

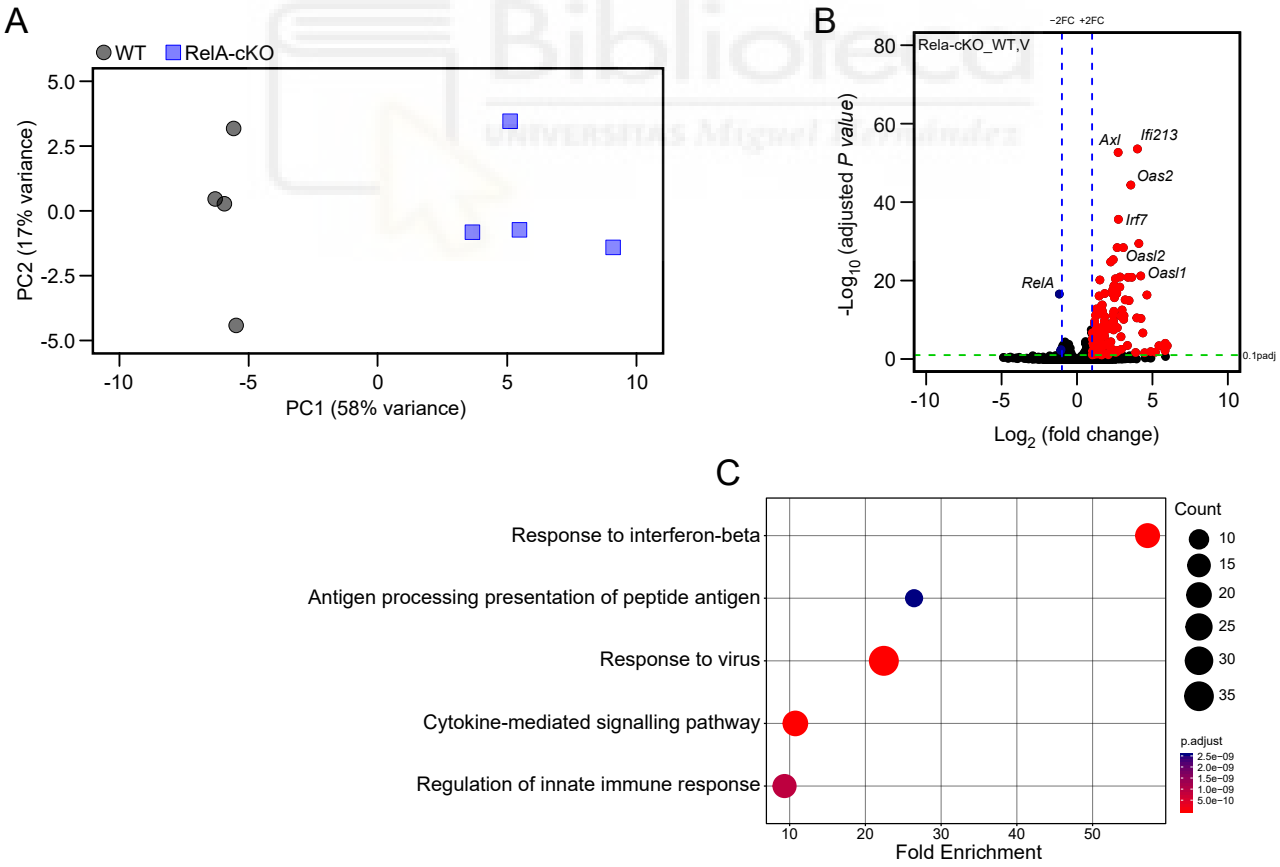

Fig.31. *RelA* conditional deletion in microglia promotes an upregulation of interferon and phagocytic genes under steady-state conditions in the CNS.
A. Principal component analysis (PCA) of cortex microglia transcriptome of P60 WT and RelA-cKO mice. N=4 per group.
B. Volcano plot of fold changes and significance for the comparison of transcriptional profiles from RelA-cKO and WT adult microglia. Upregulated and downregulated genes are coloured in red and blue, respectively.
C. GO analysis for biological processes of DEG from RelA-cKO vs WT mice.

indicated that the p65 subunit of NF-κB could be a repressor in basal conditions necessary for the maintenance of microglia in the homeostatic state.

To correlate the previous findings with microglia function *in vivo*, we performed CD68 staining as a proxy of microglia phagocytic activity (Fig.32A). We observe an increase of CD68 total volume and number of structures suggesting an increase in microglia phagocytic activity according to RNA-seq data (Fig.32B,C). We analyse microglia morphology of RelA-cKO mice by 3D sholl analysis of individual reconstructed Iba1+ cells from somatosensory cortex (Fig.33A). We observe that the number of Sholl intersections is preserved in RelA-cKO compared to WT mice (Fig.33B). We also examined microglia proliferative activity by BrdU incorporation. We administered 5 doses of BrdU every 12h during 48h (Fig.33D). Mice were perfused 2h after the last BrdU administration and we performed immunofluorescence of BrdU and Iba1 (Fig.33C). We do not observe significant differences in the % of BrdU positive microglia of RelA-cKO compared with control mice (Fig.33E).

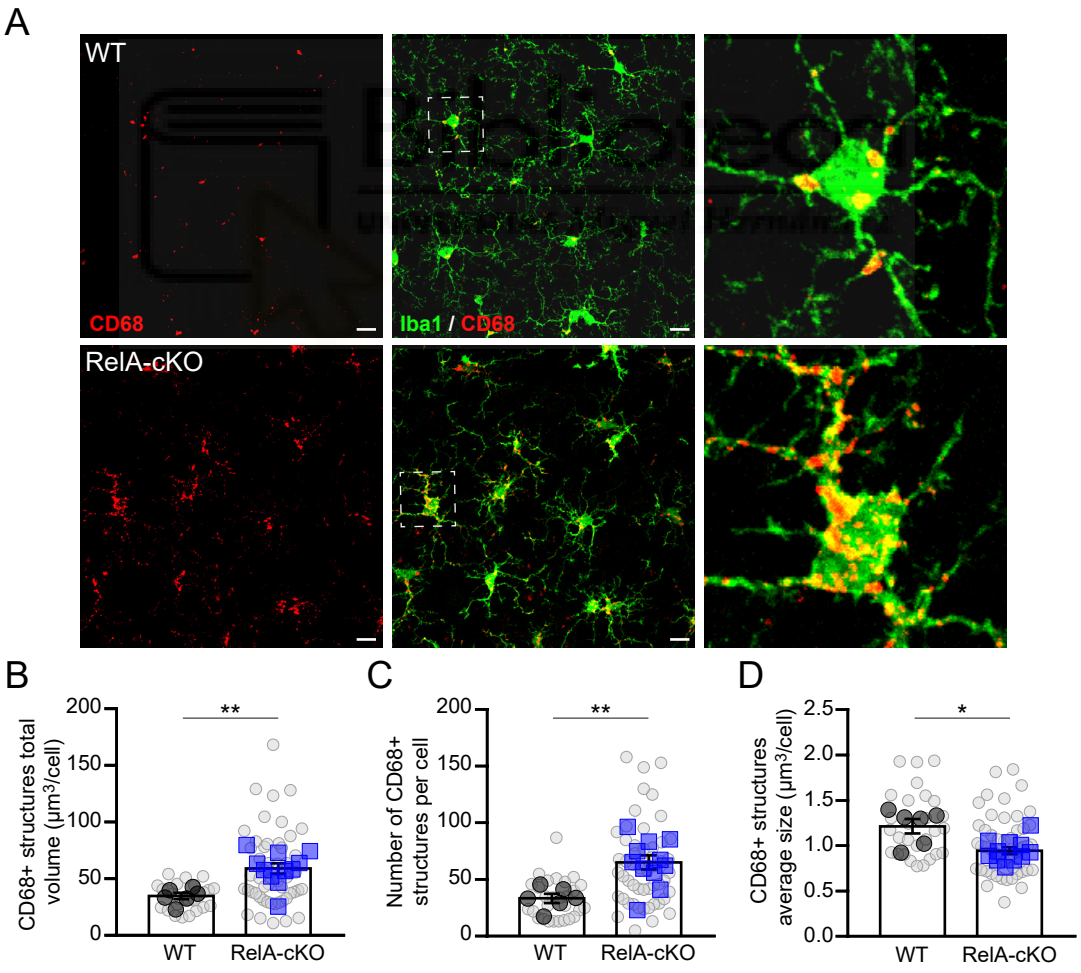

Fig.32. CD68 expression is increased in RelA-cKO mice.
A. Coronal brain sections from control and RelA-cKO mice were immunostained against the specific microglia marker Iba1 and lysosome membrane specific marker CD68. Scale bars indicate 10µm.
B. Quantification of CD68+ structures total volume (WT: n=27, N= 6; Rela-cKO: n=51, N= 11), number of CD68+ structures (WT: n=28, N= 6 ; Rela-cKO: n=52, N=11) and CD68+ structures average size (WT: n=28, N=6; Rela-cKO: n=52, N=11). **N:** Mann-Whitney test **P= 0,0048; **P = 0,0071; P = 0.0529 respectively.

Microglia has been shown to prune synapsis in healthy and disease conditions. Besides, a recent role for Axl in microglia phagocytosis of β-amyloid plaques (Huang et al., 2021). To evaluate if the previously addressed increase in phagocytic-related markers and activity observed in absence of *RelA* in microglia could have an impact on the modulation of neuronal circuits, we performed a battery of behavioural tests to evaluate RelA-cKO mice cognitive function. Whereas RelA-cKO mice do not present alterations in locomotor activity and anxiety or depressive-related behaviour (Fig.34A,B,C), we observe a defect in instrumental learning and memory in the skinner box test (Fig.34D) and light/dark paradigm (Fig.34E) suggesting that NF-κB in microglia is contributing to synaptic plasticity in the healthy brain.

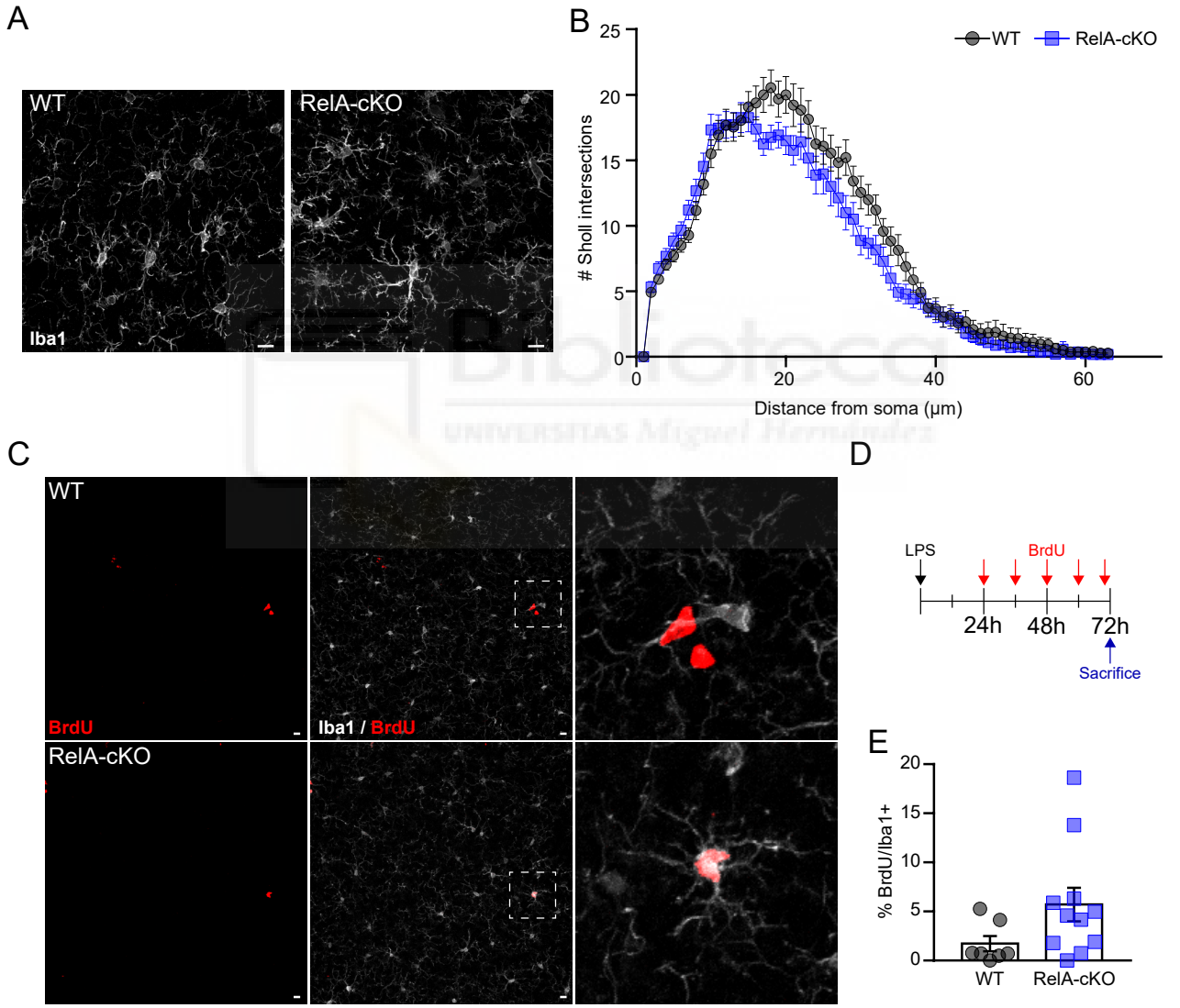

Fig.33. Morphology and proliferative activity are preserved in RelA-cKO mice.

A. Coronal brain sections from control and RelA-cKO adult mice were immunostained against the specific microglia marker Iba1 and the green fluorescent protein GFP. Scale bars indicate 10μm.

B. 3D Sholl Analysis show means +/- SD for IMARIS reconstructed cells. (WT: n=24, N=7; RelA-cKO: n=24, N=11). Unpaired t-test *P = 0.04525.

C. Coronal brain sections from control and RelA-cKO adult mice were immunostained against the specific microglia marker Iba1 and the thymidine analoge BrdU. Scale bars indicate 10μm.

D. Administration scheme. Mice received one single dose of LPS (5mg/kg i.p.). 24 hours later, mice were administered with 5 consecutive doses of BrdU (50mg/kg i.p.) every 12 hours. Mice were sacrificed 2h after the last BrdU administration.

F. Quantification of BrdU+ nuclei per Iba1+ cell (WT: N=7; RelA-cKO: N=11). Mann-Whitney test *P = 0.0456.

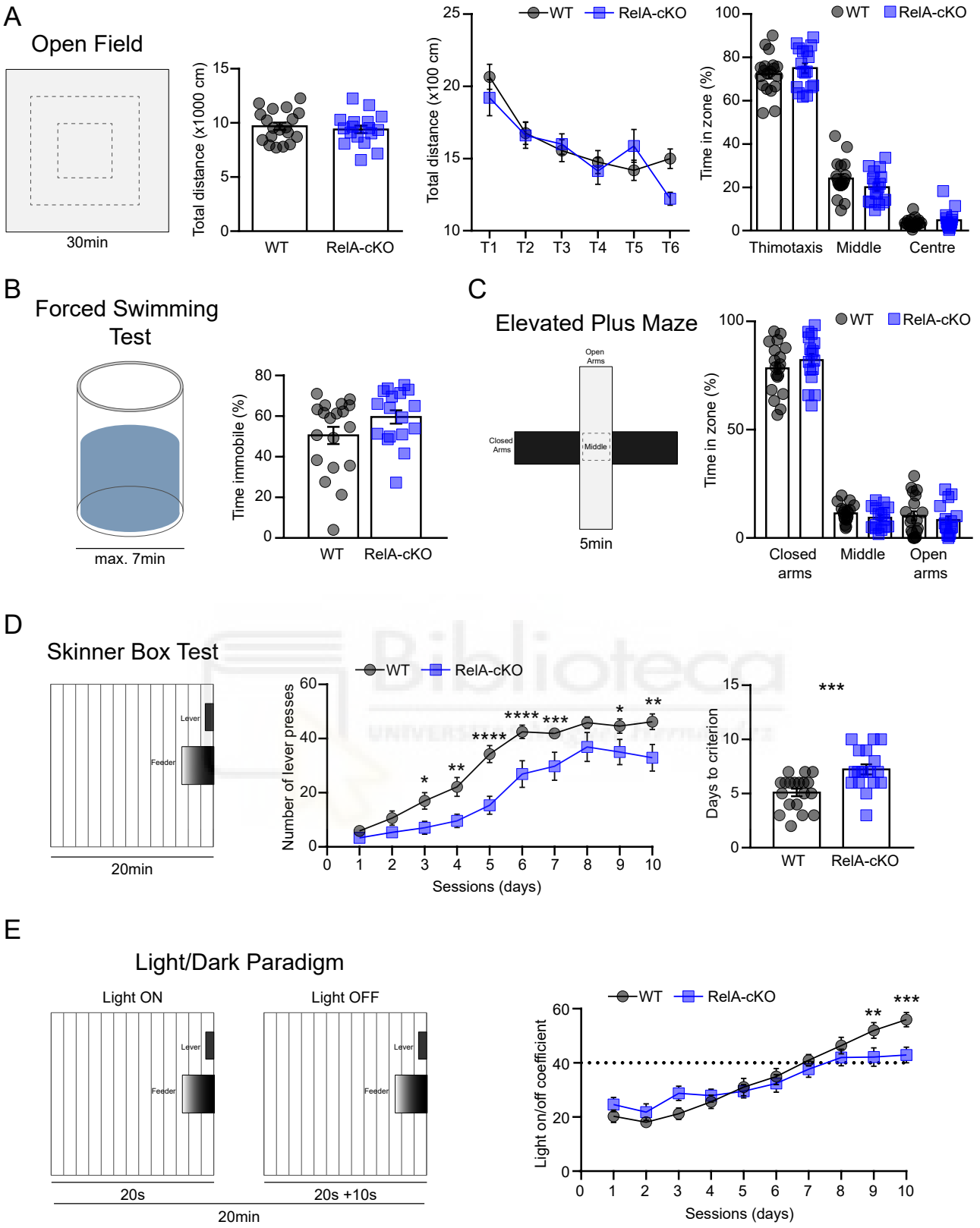

Fig.34. RelA-cKO mice present deficits in instrumental memory and learning

A. Schema showing the centre, middle and periphery area for the open field test. Mice were tested for 30 minutes. No differences were found in total distance during the total 30 minutes nor in the measurement by 5 minutes stretches. No differences were found neither in the time spent in the periphery, middle or centre of the arena. (WT: N=19; RelA-cKO: N=17). Total distance: Unpaired t-test P = 0.5581; total distance T5 min: multiple t-tests P=0.18; 0.49; 0.94; 0.83; 0.77; 0.42; 0.19; %Time in zone: Unpaired t-test (Thigmotaxis: P = 0.3804; Middle: P=0.1367; Centre: P=0.2716).

B. Schema showing the representative cylinder where the test is performed. The total duration of the test was 7 minutes. No significant differences were found in the percentage of immobility time (in seconds) between WT and RelA-cKO mice. (WT: N=19; RelA-cKO: N=17). Unpaired t-test P = 0.1043.

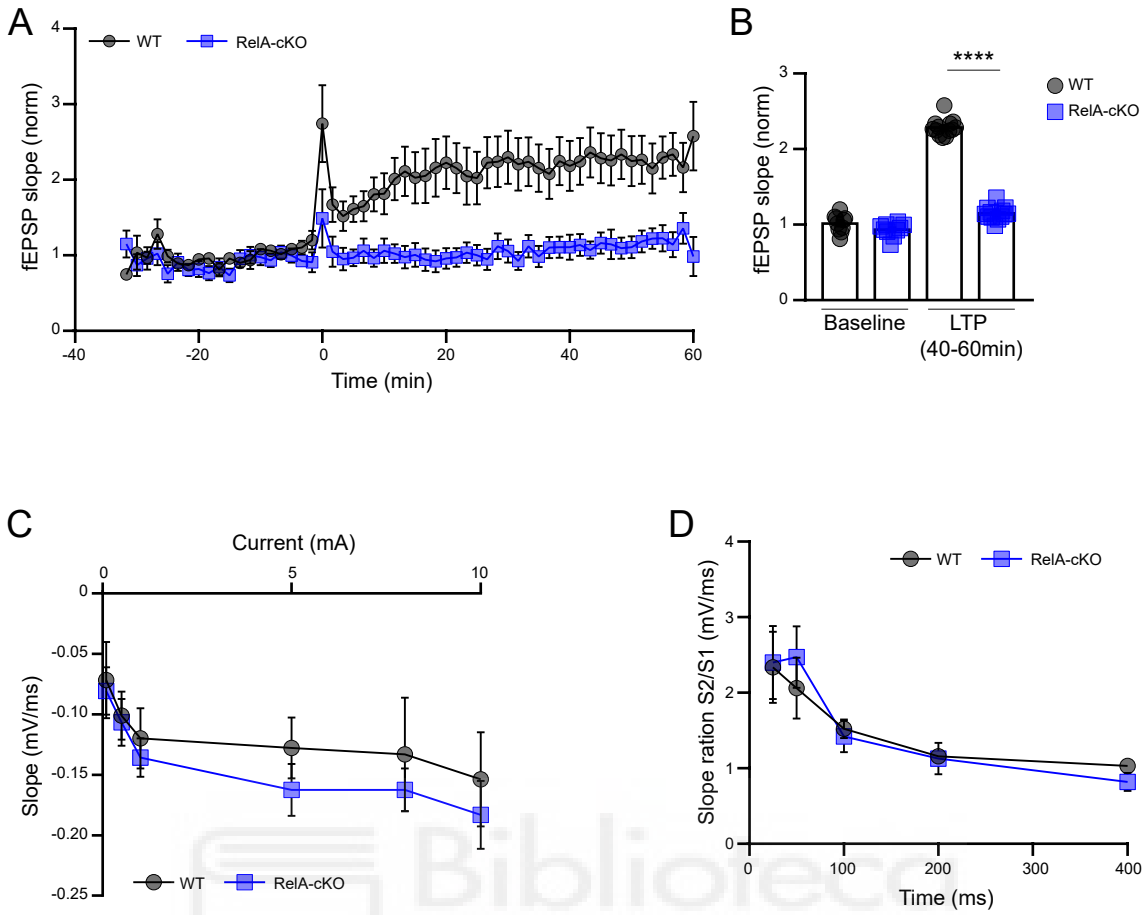

Fig.35. LTP is altered in RelA-cKO mice

A. Time course of normalized fEPSP during HFS-LTP from hippocampal acute slices from WT (N=8) and RelA-cKO mice (N=9). Multiple t-tests. P < 0.05 from t>5sec.

B. Average of responses collected from the last 20 minutes of the recording and normalized to the baseline. Potentiation of RelA-cKO slices after HFS-LTP was significantly diminished in comparison to WT slices. WT (N=8) and RelA-cKO mice (N=9). Mann-Whitney P=0.00001.

C. fEPSP input-output ratio at different stimulation intensities from WT (N=9) and RelA-cKO mice (N=8). Data indicates RelA-cKO exhibit normal efficacy of basal synaptic transmission.

D. Graph depicts paired-pulse facilitation (PRP ratio) evoked by stimulation at increasing interstimulus intervals (25, 50, 100, 200 and 400ms) from WT (N=8) and RelA-cKO mice (N=8). Data indicates presynaptic function of RelA-cKO is similar to WT animals.

C. Schema showing the different parts of the maze that are measured (open arms, middle area, closed arms). The total duration of the test was 5 minutes. No significant differences were found in the percentage of time spent in the open, middle, or closed arms between WT and RelA-cKO mice. (WT: N=20; RelA-cKO: N=17). Unpaired t-test (closed arms: P = 0.3206; centre: P = 0.1910; open arms: P = 0.5102.

D. Schema showing Skinner Box test where animals were trained for 20 minutes to press a lever to obtain a food pellet with a fixed-ratio schedule 1:1. The number of lever presses during each individual session were significantly lower in RelA-cKO compared with WT mice. WT mice significantly reached the established criterion (to press the lever at least 20 times per session) before RelA-cKO mice. (WT: N=20; RelA-cKO: N=17). Number of lever presses: multiple t-tests ****p<0.0001, ***p<0.001, **p<0.01, *p<0.05; reach to criterion: Unpaired t-test ***P = 0.0007.

E. Schema showing the light on/ light off protocol test where animals were only rewarded when the lever presses occur meanwhile a small light bulb located over the lever was switched on. Lever presses while the bulb was off were punished with a time penalty of ≤ 10 s during which the bulb would not turn on. Graph shows the performance of mice light on/on test measured as a coefficient of (number of lever presses during light on – number of lever presses during light off) / total of number of lever presses. RelA-cKO mice significantly did not reach the light on/off coefficient compared with WT mice. (WT: N=20; RelA-cKO: N=17). Multiple t-tests ****p<0.0001, ***p<0.001, **p<0.01, *p<0.05.

To test this hypothesis, we performed electrophysiological recordings in acute hippocampal slices from RelA-cKO mice and controls, where we measured the slope of the field excitatory postsynaptic potential (fEPSP) recorded from the stratum radiatum of CA1, and stimulated Schaffer collateral fibers. We observed a significantly diminished potentiation of the (fEPSP) after LTP induction in RelA-cKO mice compared with controls (Fig.35A,B). We also evaluated postsynaptic basal properties (input-out curve; Fig.35C) and presynaptic paired pulse facilitation (PRP ratio; Fig.35D). Both parameters are not altered in RelA-cKO mice compared with control animals, meaning that synapsis exhibited normal basal transmission. Therefore, we conclude that only the LTP is altered in RelA-cKO mice confirming specific defects in synaptic plasticity and not in basal transmission.

Altogether we propose a new role for the p65 subunit of the transcription factor NF-κB. P65 is necessary to maintain microglia homeostatic phenotype and subsequent neuromodulation in learning and memory processes. Microglia in absence of p65 is reprogrammed towards interferon and phagocytic phenotype that is representative of the functional states associated with AD and acute neuroinflammation.

DISCUSSION

1. Methodological considerations for the study of microglia

In this PhD thesis, we provide the most complete *in vivo* study of microglia chromatin accessibility and transcriptional landscape dynamics during the acute inflammatory response both *in silico* and *in situ* and we provide functional validation for the main transcriptional programs identified.

This is the first study to our knowledge, that takes into account important considerations for microglial cells research:

1) As first shown by Bennet et al., in 2016, mechanical dissociation of brain tissue and subsequent microglia isolation by FACS at low temperature is critical to limit microglia activation that is associated with other methods for acute isolation of microglia from adult mouse brain. Most of the studies previous to this date use incubation at 37ºC with an enzymatic cocktail to dissociate the tissue which has been consistently shown to induce changes in the microglia transcriptome associated with reactive cell states (Ayata et al., 2018; Bennett et al., 2016; Hirbec et al., 2018). In our study, the tissue has been dissociated by dounce homogenization at 4ºC avoiding the use of enzymes and incubation of the tissue homogenate at high temperatures. Myelin has been removed with either MACS technology or percoll gradient. All the procedure has been made in ice-cold conditions. The only longitudinal survey of the transcriptome landscape upon peripheral endotoxin challenge has been very recently contributed by the group of Steffen Jung (Shemer et al., 2020). In their study, Shemer et al., performed acute isolation of microglia from adult female mouse brain using enzymatic digestion of the tissue with collagenase D and DNaseI, at high temperature (37ºC for 20 min). In addition, most studies, including Shemer et al., subject the cell dissociate to antibody labelling with antibodies against canonical microglial markers before flow-cytometry analysis and cell sorting. Here, we use microglia-reporter mouse strain to acutely isolate microglia from adult male mouse brain (Parkhurst et al., 2013). Differences in methods for tissue dissociation and cell purification approaches have been shown to introduce important confounds to the samples that need to be taken into consideration when interpreting this data (Bennett et al., 2016; Marsh et al., 2020).

2) The use of bulk population RNA-seq as a predictor of the biological function of microglia whole population. Single-cell transcriptome profiling (scRNA-seq) has proved to reveal cell heterogeneity at unprecedented resolution. This technique that is particularly suited to tackle cell diversity of cell states in complex scenarios, such as neurodegenerative diseases, is primarily limited by its poor sensitivity due to the high dropout noise level and the lack of

uniform read coverage of each transcript. Current scRNA-seq methods can detect only a small fraction of the mRNA molecules present per cell (~10%) making low-expression genes difficult to detect and limiting the functional interpretation of the data. To avoid these limitations, we decided to use a systemic challenge with LPS at a high dose (5mg/kg) (von Drygalski et al., 2013) to elicit a robust neuroinflammatory response by microglia that maximizes the likelihood that microglial cells respond homogeneously to the insult and performed whole-transcriptome analysis with total RNA-seq of FACS-sorted microglia from a reporter mouse model that genetically labels myeloid cells (Parkhurst et al., 2013).

3) The combination of RNA-seq or scRNA-seq with fluorescent single-molecule *in situ* hybridization (RNAscope) to map cell-type and state-specific gene markers back to the tissue context. We performed RNAscope of selected targets to validate the identified functional states of microglia in acute (systemic LPS) and chronic (AD mouse model) and further characterize their cellular distribution at the tissue level. Furthermore, we also validate our findings in human brain *post-mortem* tissue from AD patients.

4) The biological relevance of the observed changes in the transcriptome and chromatin landscapes of microglia. We provide functional validation for morphological, proliferative, and phagocytic functions associated with each of the transcriptional states identified *in silico*.

We anticipate that microglia transcriptional signatures identified in this PhD thesis will provide ground information required to interrogate microglia function and the subsequent development of new tools. We provide a new perspective for the understanding and classification of microglia in different contexts of disease where the heterogeneity of this population and the importance of the microenvironment has been previously observed but whose implications in disease progression remains elusive.

2. State-specific microglia signatures during acute neuroinflammation

Microglia duality of phenotypes M1 and M2 has been largely discarded (Ransohoff, 2016). Microglia is no longer conceived adopting a pro-inflammatory or an anti-inflammatory phenotype. Single-cell profiling studies are revealing heterogeneity of microglia states under chronic conditions (Masuda et al., 2020). However, the relevance of these phenotypes for disease onset and progression remains elusive. Although initial attempts have been recently reported, the heterogeneity and dynamics of the neuroinflammatory response by microglia in acute endotoxin challenge remain largely unknown (Hirbec et al., 2018; Shemer et al., 2020; Sousa et al., 2018). We show that microglia acute inflammatory response is stepwise regulated and comprise a variety of distinct functional states that are dynamically modulated during the course of the response.

We show that the most widely known part of the response, the cytokine response, is only part of an intricate process that involves the activation of complex gene expression programs. The cytokine storm consists of an immediate-early response that coexists with other gene programs related to protein synthesis, cell metabolism, and interferon response. All these functions reach their maximum at L5h but show different temporal dynamics.

Cytokines are the principal and the most studied mediators of the inflammatory response. As part of this program, we identified classical cytokines like *Tnf*, *Il1b*, *Il6*, *Cd74*, *Cxcl10* or NF-κB transcription factor subunits (NF-κB1, NF-κB2, Rel, RelA, Relb). As expected, we found significant enrichment for the NF-κB transcription factor motif associated with this cluster. One of the most potent cytokines, Il1b, has tried to be used as a potential neuroinflammation biomarker and the targeting of inflammasomes, the protein complexes responsible for the cleavage of pro-Il1b to its active form, has been shown to be key players in neurodegenerative diseases (Heneka et al., 2018). We show that a strong acute neuroinflammatory challenge triggers the expression of Il1b by virtually all microglial cells. Notably, this homogeneously distributed early response is transient and return to undetectable levels at L24h from the initial insult. This data suggests that cytokines response is tightly regulated. However, the mechanisms regulating the extent and duration of this response remains largely unknown.

Interferons have been also widely studied mostly as part of the immune response to viruses. In response to LPS, the upregulation of this transcriptional program occurs as part of the immediate-sustained response at L5h, but contrary to cytokines, it is wider and extended in time coexisting with later functions in microglial cells. We identify key interferon family members as *Irf7*, *Ifitm3*, *Oasl2*, *Oas1b*, or *Oas1a* as part of this cluster. We further show *in situ* that *Oasl2*, is expressed by the majority of microglia population suggesting that interferons are produced almost homogeneously by the whole microglia population.

Of note is that gene programs related to protein synthesis and metabolism are also part of the immediate-sustained response. These functions are closely related to each other, and they are essential for the proper response of microglial cells to a constantly changing environment (Lauro & Limatola, 2020), for example, alterations in microglia lipid metabolism have been associated with AD pathology (Keren-Shaul et al., 2017; Wang et al., 2020).

We also identify a delayed transcriptional response, from L24h, that is associated with cell cycle progression. We identify genes related to this function like *Mcm2*, *Pole*, *Cdk1*, *Top2a*, *E2f7*, or *Ms4a4a*. Notably, we show that *Ms4a4a* is expressed by 15% of microglia population suggesting that only a small proportion of microglial cells proliferate in response to an acute systemic neuroinflammatory challenge. We confirmed these results by BrdU incorporation

assay and immunostaining with Ki67. However, microglia population cell density remains stable which suggests that mechanisms coupling proliferation and apoptosis may be taking place (Askew et al., 2017).

Finally, a cluster of co-regulated genes shows delayed and sustained expression. This cluster comprises genes associated with the complement system and antigen digestion suggesting a modulation of the phagocytic activity at later time points of the acute response to endotoxin. We identify genes like *ApoE* or *Axl* within this cluster. We show that this response is homogeneous both transcriptional and functionally by *in situ* expression of *Axl*, and by immunofluorescence of CD68 respectively. Given the association of these two genes with DAM microglia phenotype in AD (Keren-Shaul et al., 2017), we hypothesize that this phenotype is not exclusive from neurodegenerative diseases, but it is also differentially modulated in response to LPS.

The downregulation of homeostatic genes is one of the features associated with microglia during ageing or neurodegenerative diseases (Hickman et al., 2013; Keren-Shaul et al., 2017; Sala Frigerio et al., 2019). We show that microglial cells during the acute inflammatory response also transiently downregulate key homeostatic genes (*P2ry12*, *Trem2* among others). Other genes identified within this cluster are associated with the actin cytoskeleton like *Rhob*, *Pak1* or *Rock2*. Notably, we also show a transient retraction of microglia prolongations that is temporarily coupled with the downregulation of homeostatic genes. Although morphological analysis perse cannot be associated directly with a specific function, we combine different approaches that allow us to associate microglia dendrites retraction with a release of cytokines, interferon, metabolic activity, and initiation of proliferation. Uniform classification of microglia morphology will facilitate their identification and shed light on a specific functional association.

We provide here, solid evidence of the temporal microglia transcriptional regulation of the inflammatory response and functional validation *in vivo*. Other authors have previously studied microglia transcriptome in acute neuroinflammation. Hirbec et al., and Sousa et al., define a set of genes that differentiates reactive from homeostatic microglia at L24h by RNA-seq and scRNA-seq respectively (Hirbec et al., 2018; Sousa et al., 2018). Some of these genes are common to the genes we identify in our dataset at L24h, like the upregulation of the Ms4 family or downregulation of homeostatic genes like *Gpr34* or *P2ry12*. In addition to this, we show that microglia transcriptional response comprises not only the L24h reaction signature but specific transcriptional programs are implemented at different time points during the whole duration of the inflammatory response.

In summary, we identify the dynamics of microglia transcriptional response during acute neuroinflammation. We hope our contribution improves our understanding of the inflammatory response. How these functions are related to each other will need to be tested using genetic manipulation of master regulators for each of the associated transcriptional programs. This will help to gain insight into microglia reprogramming to a beneficial state that could alleviate the deleterious effects of inflammation associated with CNS diseases.

3. State-specific microglia signatures during chronic neuroinflammation

Microglia heterogeneity has been described as associated with neurodegenerative diseases. In AD, different authors have performed a longitudinal study using different mouse models (5XFAD, Ck-p25 and App^{NL-G-F}) and have identified 5 main populations of microglia: homeostatic, interferon, proliferative, and the so-called disease-associated microglia (Keren-Shaul et al., 2017; Mathys et al., 2017; Sala Frigerio et al., 2019). We extend these findings to the J20 and APPswe/PS1dE9 mouse models of AD. Moreover, we reveal the presence of such subpopulations in situ both during the acute neuroinflammatory response and AD. Our data provide a new vista on the interpretation of microglia heterogeneity. We propose that microglia respond to internal and external environmental factors with a limited number of functional outputs that are dynamically regulated depending on the context of disease. Future work should be done to test the role of the distinct putative functional states of microglia in ageing and disease.

There are some studies comparing microglia transcriptomic profile after different triggers suggesting that microglia from LPS differ from chronic neurodegenerative conditions. Chiu et al., compared spinal cord microglia from SOD1 mice with LPS 48h treated mice. They found significant differences between the two conditions concluding that ALS and LPS 48h microglia display distinct modes of activation (Chiu et al., 2013). Another study comparing microglia transcriptomes in ageing, AD, ALS and LPS 4h shows that microglia from LPS treated mice differ from neurodegenerative microglia (Holtman et al., 2015). A major limitation of these studies is that only one specific time point from LPS administration is included which did not allow us to capture all microglia phenotypes present throughout the acute neuroinflammatory response as we show in our dataset. In fact, Hirbec et al., identify in silico a subset of 86 genes that are deregulated in microglia both after LPS 24h and in a mouse model of chronic neurodegeneration (ALS-SOD1) (Hirbec et al., 2018). Besides, Sousa et al., meta-analyse their microglia L24h scRNA-seq data with published DAM genes, identifying a 12% of overlap between two conditions (Sousa et al., 2018). This goes in line with our results where we observe that genes upregulated in the delayed microglia response to LPS (L24h to L72h) are shared with DAM phenotype in AD. We also observed the upregulation of some

of these markers (*Oasl2* and *Axl*) *in situ* associated with Aβ plaques in our mouse model of LPS, APP/PS1 AD mouse model and human AD suggesting that microglia in different pathological contexts share common molecular signatures.

Most of the genomic studies to date have revealed microglia heterogeneity in health and disease, whether putative-associated functions play a protective or deleterious role in chronic inflammatory conditions remains controversial.

Il1b is a classical cytokine that has been a candidate marker for the modulation of inflammation associated with AD. It has been shown *in vitro* that high levels of Il1b contribute to the progression of AD pathology (Yates et al., 2000). Besides, Il1b release, through inflammasome activation, has been associated with Aβ plaque core facilitating Aβ deposition (Venegas et al., 2017). On the contrary, Il1b overexpression in the hippocampus of APPswe/PS1dE9 led to a reduction in amyloid pathology improving the disease (Shaftel et al., 2007). Of note, *Il1b* is not expressed in microglia scRNA-seq from different mouse models of AD (Keren-Shaul et al., 2017; Mathys et al., 2017; Sala Frigerio et al., 2019), nor *in situ* by spatial transcriptomics (Chen et al., 2020; Navarro et al., 2020), or in a murine model of prion disease (Walsh et al., 2001). We observe *Il1b* expression as part of the immediate-early inflammatory response to LPS. Conversely, we do not observe *Il1b* expression in J20 microglia scRNA-seq nor at the single-cell *in situ* level in 20 months old APP/PS1 mice. Studies at earlier stages of AD pathology would be necessary to evaluate the expression of Il1b in AD. Whether the absence of Il1b, at least at later stages of the disease, is beneficial or detrimental needs to be tested.

A similar scenario can be observed with microglia proliferative activity. We do observe microglia proliferation at later time points of the acute neuroinflammatory challenge (L48-L72h). In the case of AD, we detect very few cells undergoing proliferation in our J20 scRNA-seq. *In situ*, we observed, by the expression marker *Ms4a4a*, that microglia proliferative response is heterogeneous during acute neuroinflammation. Conversely, we do not observe *Ms4a4a* expression *in situ* in APP/PS1 mouse model. The role of proliferation-associated with diseases has been widely studied and has been the focus of controversy. CSF-1 is essential for microglia viability (Erblich et al., 2011) and has been associated with microglia proliferation. Two variants of this gene have been associated with early-onset AD (Giau et al., 2019). Proliferation has been reported by BrdU in mouse models of AD (Kamphuis et al., 2012). On the contrary, we observe a marginal proliferative response both *in situ* and *in silico* coincident with most microglia scRNA-seq studies where it is present mainly associated to early stages of AD (Keren-Shaul et al., 2017; Mathys et al., 2017; Sala Frigerio et al., 2019). Besides, Trem2 blockade has been shown to promote microglia proliferation

producing beneficial effects in the progression of the disease (Wang et al., 2020) inhibition of the proliferative activity with a CSF-1 antibody shows beneficial effects (Olmos-Alonso et al., 2016). Beyond this controversy, the modulation of the proliferative response might be a promising therapeutic approach in the prodromal stages of AD.

Regarding interferon-related function, the contribution of microglia INF production to AD pathology has been under-investigated. Recently, it has been shown that intracranial type I interferon administration resulted in synapse loss in AD *in vivo* in a complement C3-dependent manner, suggesting that microglia INF response is critical for the promotion of neuroinflammation in AD (Roy et al., 2020) identified *Oasl2* to be specifically upregulated in microglia surrounding diffuse but not compact Aβ plaques. Diffuse β amyloid plaques consist of Aβ aggregates with branched amyloid fibrils that protrude into de brain parenchyma causing severe axonal damage being more neurotoxic and potentially presenting a great abundance of nucleic acids (Bussiere et al., 2004; Wang et al., 2020). This goes in line with evidence showing the presence of amyloid fibrils containing nucleic acids that could induce INF production (Di Domizio et al., 2012). The specificity of the expression of *Oasl2* associated with diffuse plaques points out Oasl2 as a potential target for the modulation of INF pathway in AD.

Finally, microglia phagocytic activity has been shown to mediate synapse loss in AD. Recently, Axl has been shown to be essential for Aβ plaques recognition and engulfment (Huang et al., 2021). Huang et al., propose that dense core Aβ plaques are constructed from loosely organized Aβ material by phagocytic microglia mediated by TAM receptors. Here, we observe *in situ* an increase in *Axl* expression in the areas surrounding both compact and diffuse Aβ plaques in a mouse model of AD.

Altogether, these findings point out the importance of the environment in microglia reprogramming into specific functional states. Our finding of common interferon and phagocytic phenotypes found in later stages of the acute inflammation and later stages of AD pathology indicate that similar signalling mechanisms are activating microglial cells but with different dynamics due to the acute or chronic nature of the trigger. However, it cannot be ruled out the presence of other microglia functional phenotypes (cytokines or proliferative microglia) at earlier stages of AD.

4. State-specific microglia signatures in human AD

The translation of findings in mouse models of AD to human disease presents several difficulties. First, despite animal models provide a valuable tool for research in a controlled systematic way, they do not recapitulate the complexity of human disease but only mimic

some specific features; second, the evolutionary differences between species; or third, the differences in cellular composition of tissues, among others.

Despite microglia transcriptome between mouse and human has been shown to be broadly similar, human microglia show, for example, higher expression of complement system-related genes (Gosselin et al., 2017). Besides, although multiple microglia phenotypes have been shown to exist in human CNS (Sankowski et al., 2019), human AD microglia exhibit distinct markers compared with mouse DAM (Olah et al., 2018; Zhou et al., 2020). Only one study has shown common markers between human AD microglia and DAM like *ApoE* and *Tyrobp* but human microglia also present ribosomal genes that are absent in mouse DAM (Mathys et al., 2019; Yang et al., 2021). Of note is that both, Zhou et al., and Mathys et al., performed single nuclei RNA-seq instead of single-cell RNA-seq which has been shown to not be suitable for the detection of microglia activation genes in humans (Thrupp et al., 2020). Given the limitation of performing single-cell RNA-seq in fresh frozen tissue, we performed single-molecule *insitu* hybridization of our mouse cytokine marker (*IL1b*), IRM marker *Oasl2* (human *OASL*) and DAM marker (*Axl*) in human *post-mortem* brain tissue. We observe an increase in the expression of both *OASL* and *AXL* in human AD. Conversely, we do not observe *IL1b* expression in human AD.

In summary, Interferon-response microglia (*Oasl2*) and DAM/ARM (*Axl*) have been identified by scRNA-seq by other authors and by us in mouse models of AD. We disclose here the presence of both markers *in situ* in the proximity of Aβ plaques in a mouse model of AD and in the *post-mortem* brain tissue from AD patients. Evaluating the role of the distinct microglia states in the onset and progression of AD could be useful for the establishment of new therapeutic approaches.

5. Therapeutic targeting of microglia

Evidence accumulates suggesting an important role of microglial cells in most CNS diseases, which makes microglial cells especially attractive for therapeutic targeting. The complexity of the regulation of the inflammatory response together with the controversy of the findings regarding the modulation of microglia functions have made it difficult to identify good targets. The complete study of the dynamics of microglial inflammatory response that we provide in this PhD thesis will set up a complete context that allows us to better understand the transcriptional programs and functions that comprise the inflammatory response to acute and chronic triggers in a time-dependent manner. We provide 4 main microglia functional states that could be targeted although the interdependency between them needs to be further investigated. This will shed light on the double-edged sword that currently is the modulation

of microglia functions. For example, the role of microglia cytokines release (Heneka et al., 2018; Keren-Shaul et al., 2017) or proliferative activity (Olmos-Alonso et al., 2016; Wang et al., 2020) in AD pathology and the beneficial or detrimental effects of microglial phagocytic activity in neurodegeneration are controversial. On one hand, microglia phagocytosis may facilitate the clearance of misfolded proteins at disease onset; on the other hand, it can facilitate amyloid spreading and contribute to aberrant synapse loss in AD (Doty et al., 2015). For this, microglia phagocytic activity needs to be carefully targeted. We show *Axl* (TAM receptor essential for microglia phagocytosis (Lemke, 2013) to be upregulated in the proximity of both diffuse and compact Aβ plaques in the APP/PS1 mouse model of AD. *Axl* depletion in microglial cells promotes dense-core instead of diffuse Aβ plaques accumulation, suggesting that microglia play a key role in the formation of diffuse plaques (Huang et al., 2021). Whether the therapeutic targeting of Axl is beneficial or detrimental still remains poorly understood. The fourth microglia phenotype that we address is related to interferon response. We show that *Oasl2*, a component of the interferon pathway is selectively upregulated in the proximity of diffuse toxic Aβ plaques. Oasl2 has been shown to play an important role in the antiviral modulation of the interferon pathway (Zhu et al., 2014). In neurodegenerative disease, type I interferon receptor blockade in microglia diminished neuroinflammation and synapse loss in a mouse model of AD (Roy et al., 2020), suggesting that interferon contributes to the pathogenesis of AD. The modulation of the interferon pathway may open new therapeutic approaches for the treatment of neurodegenerative diseases.

6. Role of p65 in microglia

One of the most interesting approaches of our study is to genetically manipulate the master regulators of each transcriptional program identified not only to try to understand the role of each of them in the regulation of the inflammatory response, but also the interdependency between them. For this, we specifically deplete the *RelA*/p65 subunit of the transcription factorNF-κB in adult microglia (RelA-cKO mice). NF-κB, and in particular the p65 subunit has been shown to play a key role in the regulation of the inflammatory response. We identify an *in silico* NF-κB-p65 transcription factor motif associated with cytokine response (cluster 1). Unexpectedly, the depletion of *RelA*/p65 subunit in adult microglia induces in basal state the upregulation of genes related to the interferon and phagocytic activity. Moreover, we observe alterations in instrumental learning and LTP in RelA-cKO mice in physiological conditions suggesting that microglia is playing a key role in the modulation of neuronal circuits in basal state. We also observe an increase of CD68 vesicles which may indicate that an increase of microglial phagocytic activity could underlie the instrumental learning deficits observed in RelA-cKO mice. This goes in line with previous evidence by Parkhurst et al., showing a

key role for microglia in learning and memory by promoting learning-dependent synapse formation through BDNF signalling (Parkhurst et al., 2013). Previously, other authors like Meffer et al., showed that mice constitutively lacking p65 presented learning deficits in the radial arm maze (Meffert et al., 2003). These alterations could not be attributed to a specific cell type or developmental alterations by that time due to the constitutive depletion of p65 in all cell types from developmental stages. We here provide evidence that p65 depletion in microglial cells in adult mouse brain reprogram microglia towards interferon and phagocytic phenotype together with alterations in synaptic plasticity and behaviour that are representative of microglia functional states and memory deficits associated with AD and the delayed response to LPS.

CONCLUSIONS

1. The early acute neuroinflammatory response is governed by a fast cytokine storm (immediate-early response) together with an extended interferon production (immediate-sustained response) coordinated by the whole microglia population. Protein synthesis and cell metabolism transcriptional programs are also part of the immediate-sustained response.
2. The delayed acute neuroinflammatory response comprises a heterogeneous proliferative response and a homogeneous phagocytic activity.
3. Microglia morphology is transitorily retracted together with a downregulation of homeostatic genes at the early stages of the acute neuroinflammatory response and recovered at the later stages (immediate-sustained response).
4. The chromatin accessibility of microglial cells is coordinated with the transcriptional changes.
5. Loss of microglia homeostatic gene *P2ry12* occurs in microglia surrounding Aβ plaques.
6. Cytokine-related transcriptional program (*Il1b*) is not upregulated by microglial cells in APP/PS1.
7. Microglia in the proximity of diffuse but not compact plaques upregulate interferon-related transcriptional program (*Oasl2*).
8. Microglial cells proliferation marker Ms4a4a is not upregulated in 20 months old APP/PS1 mice.
9. Phagocytosis-related transcriptional program (*Axl*) upregulation by microglial cells occurs specifically in the proximity of both diffuse and compact plaques.
10. Cytokine-related transcriptional program (*IL1b)* is not upregulated by microglial cells in AD human *post-mortem* brain tissue.
11. Microglia from AD human *post-mortem* brain tissue upregulate interferon-related transcriptional program (*OASL*).
12. Microglia from AD human *post-mortem* brain tissue upregulate phagocytosis-related transcriptional program (*AXL*).
13. An upregulation of the interferon (*Oasl2)* and MHC (*Axl*) transcriptional programs occurs in microglial cells in the absence of NF-κB together with alterations in phagocytosis-related activity.
14. Instrumental learning and LTP are impaired in RelA-cKO mice.

CONCLUSIONES

1. La respuesta inflamatoria aguda temprana está gobernada por una rápida tormenta de citoquinas (respuesta temprana-corta) junto con una producción de interferón más extendida a lo largo del tiempo (respuesta temprana-sostenida). Ambas repuestas las lleva a cabo la totalidad de la población homogéneamente. La síntesis de proteínas y el metabolismo celular también son programas que forman parte de la respuesta temprana sostenida.
2. La respuesta tardía comprende la proliferación heterogénea de una parte de la población de microglía junto con actividad fagocítica homogénea.
3. La morfología de la microglía varía durante la respuesta inflamatoria agua con una retracción transitoria de los procesos junto con la disminución en la expresión de genes homeostáticos que vuelven a su estado basal tras L72h (respuesta temprana-sostenida).
4. La accesibilidad de la cromatina en las células de microglía durante la respuesta inflamatoria aguda es coordinada junto con los cambios transcripcionales.
5. La pérdida del gen homeostático *P2ry12* ocurre en microglía alrededor de las placas de Aβ
6. El programa relacionado con la expresión de citoquinas (*Il1b)* no aumenta su expresión en microglía en los ratones APP/PS1.
7. La microglía en la proximidad de las placas β amiloides difusas, pero no compactas aumenta la expresión de los programas transcripcionales relacionados con el interferón (*Oasl2*).
8. El marcador de microglía proliferativa *Ms4a4a* no aumenta su expresión en los ratones APP/PS1 de 20 meses de edad.
9. Los programas transcripcionales relacionados con la fagocitosis (*Axl*) aumentan su expresión en células de microglía en la proximidad de las placas β amiloides tanto difusas como compactas.

10. El programa transcripcional relacionado con las citoquinas (*IL1b)* no aumenta su expresión en células de microglía en el tejido de cerebro *post-mortem* de pacientes con enfermedad de Alzheimer.

11. La microglía del tejido de cerebro *post-mortem* de pacientes con enfermedad de Alzheimer aumenta la expresión de programas relacionados con la respuesta al interferón (*OASL*).

12. La microglía del tejido de cerebro *post-mortem* de pacientes con enfermedad de Alzheimer aumenta la expresión de programas relacionados con la fagocitosis (*AXL*).

13. En ausencia de la subunidad *RelA*/p65 del factor de transcripción NF-κB específicamente en la microglía, se produce un aumento en la expresión de genes relacionados con el interferón (*Oasl2*) y la fagocitosis (*Axl*).

14. El aprendizaje instrumental y la LTP están alteradas en los ratones RelA-cKO.

BIBLIOGRAPHY

Akira, S., Uematsu, S., & Takeuchi, O. (2006). Pathogen recognition and innate immunity. *Cell*, *124*(4), 783-801. https://doi.org/10.1016/j.cell.2006.02.015

Alliot, F., Godin, I., & Pessac, B. (1999). Microglia derive from progenitors, originating from the yolk sac, and which proliferate in the brain. *Brain Res Dev Brain Res*, *117*(2), 145-152. https://doi.org/10.1016/s0165-3806(99)00113-3

Anders, S., Pyl, P. T., & Huber, W. (2015). HTSeq--a Python framework to work with high-throughput sequencing data. *Bioinformatics*, *31*(2), 166-169. https://doi.org/10.1093/bioinformatics/btu638

Askew, K., Li, K., Olmos-Alonso, A., Garcia-Moreno, F., Liang, Y., Richardson, P., Tipton, T., Chapman, M. A., Riecken, K., Beccari, S., Sierra, A., Molnar, Z., Cragg, M. S., Garaschuk, O., Perry, V. H., & Gomez-Nicola, D. (2017). Coupled Proliferation and Apoptosis Maintain the Rapid Turnover of Microglia in the Adult Brain. *Cell Rep*, *18*(2), 391-405. https://doi.org/10.1016/j.celrep.2016.12.041

Ayata, P., Badimon, A., Strasburger, H. J., Duff, M. K., Montgomery, S. E., Loh, Y. E., Ebert, A., Pimenova, A. A., Ramirez, B. R., Chan, A. T., Sullivan, J. M., Purushothaman, I., Scarpa, J. R., Goate, A. M., Busslinger, M., Shen, L., Losic, B., & Schaefer, A. (2018). Epigenetic regulation of brain region-specific microglia clearance activity. *Nat Neurosci*, *21*(8), 1049-1060. https://doi.org/10.1038/s41593-018-0192-3

Becht, E., McInnes, L., Healy, J., Dutertre, C. A., Kwok, I. W. H., Ng, L. G., Ginhoux, F., & Newell, E. W. (2018). Dimensionality reduction for visualizing single-cell data using UMAP. *Nat Biotechnol*. https://doi.org/10.1038/nbt.4314

Bennett, M. L., Bennett, F. C., Liddelow, S. A., Ajami, B., Zamanian, J. L., Fernhoff, N. B., Mulinyawe, S. B., Bohlen, C. J., Adil, A., Tucker, A., Weissman, I. L., Chang, E. F., Li, G., Grant, G. A., Hayden Gephart, M. G., & Barres, B. A. (2016). New tools for studying microglia in the mouse and human CNS. *Proc Natl Acad Sci U S A*, *113*(12), E1738-1746. https://doi.org/10.1073/pnas.1525528113

Bocchini, V., Mazzolla, R., Barluzzi, R., Blasi, E., Sick, P., & Kettenmann, H. (1992). An immortalized cell line expresses properties of activated microglial cells. *J Neurosci Res*, *31*(4), 616-621. https://doi.org/10.1002/jnr.490310405

Bohlen, C. J., Bennett, F. C., Tucker, A. F., Collins, H. Y., Mulinyawe, S. B., & Barres, B. A. (2017). Diverse Requirements for Microglial Survival, Specification, and Function Revealed by Defined-Medium Cultures. *Neuron*, *94*(4), 759-773 e758. https://doi.org/10.1016/j.neuron.2017.04.043

Brown, G. C., & Neher, J. J. (2014). Microglial phagocytosis of live neurons. *Nat Rev Neurosci*, *15*(4), 209-216. https://doi.org/10.1038/nrn3710

Buenrostro, J. D., Giresi, P. G., Zaba, L. C., Chang, H. Y., & Greenleaf, W. J. (2013). Transposition of native chromatin for fast and sensitive epigenomic profiling of open chromatin, DNA-binding proteins and nucleosome position. *Nat Methods*, *10*(12), 1213-1218. https://doi.org/10.1038/nmeth.2688

Bussiere, T., Bard, F., Barbour, R., Grajeda, H., Guido, T., Khan, K., Schenk, D., Games, D., Seubert, P., & Buttini, M. (2004). Morphological characterization of Thioflavin-S-positive amyloid plaques in transgenic Alzheimer mice and effect of passive Abeta immunotherapy on their clearance. *Am J Pathol*, *165*(3), 987-995. https://doi.org/10.1016/s0002-9440(10)63360-3

Butler, A., Hoffman, P., Smibert, P., Papalexi, E., & Satija, R. (2018). Integrating single-cell transcriptomic data across different conditions, technologies, and species. *Nat Biotechnol*, *36*(5), 411-420. https://doi.org/10.1038/nbt.4096

Butovsky, O., Jedrychowski, M. P., Moore, C. S., Cialic, R., Lanser, A. J., Gabriely, G., Koeglsperger, T., Dake, B., Wu, P. M., Doykan, C. E., Fanek, Z., Liu, L., Chen, Z., Rothstein, J. D., Ransohoff, R. M., Gygi, S. P., Antel, J. P., & Weiner, H. L. (2014). Identification of a unique TGF-beta-dependent molecular and functional signature in microglia. *Nat Neurosci*, *17*(1), 131-143. https://doi.org/10.1038/nn.3599

Butovsky, O., & Weiner, H. L. (2018). Microglial signatures and their role in health and disease. *Nat Rev Neurosci*, *19*(10), 622-635. https://doi.org/10.1038/s41583-018-0057-5

Campion, D., Dumanchin, C., Hannequin, D., Dubois, B., Belliard, S., Puel, M., Thomas-Anterion, C., Michon, A., Martin, C., Charbonnier, F., Raux, G., Camuzat, A., Penet, C., Mesnage, V., Martinez, M., Clerget-Darpoux, F., Brice, A., & Frebourg, T. (1999). Early-onset autosomal dominant Alzheimer disease: prevalence, genetic heterogeneity, and mutation spectrum. *Am J Hum Genet*, *65*(3), 664-670. https://doi.org/10.1086/302553

Carswell, E. A., Old, L. J., Kassel, R. L., Green, S., Fiore, N., & Williamson, B. (1975). An endotoxin-induced serum factor that causes necrosis of tumors. *Proc Natl Acad Sci U S A*, *72*(9), 3666-3670. https://doi.org/10.1073/pnas.72.9.3666

Chaillou, T., Kirby, T. J., & McCarthy, J. J. (2014). Ribosome biogenesis: emerging evidence for a central role in the regulation of skeletal muscle mass. *J Cell Physiol*, *229*(11), 1584-1594. https://doi.org/10.1002/jcp.24604

Chakravarty, S., & Herkenham, M. (2005). Toll-like receptor 4 on nonhematopoietic cells sustains CNS inflammation during endotoxemia, independent of systemic cytokines. *J Neurosci*, *25*(7), 1788-1796. https://doi.org/10.1523/JNEUROSCI.4268-04.2005

Cheadle, L., Rivera, S. A., Phelps, J. S., Ennis, K. A., Stevens, B., Burkly, L. C., Lee, W. A., & Greenberg, M. E. (2020). Sensory Experience Engages Microglia to Shape Neural Connectivity through a Non-Phagocytic Mechanism. *Neuron*, *108*(3), 451-468 e459. https://doi.org/10.1016/j.neuron.2020.08.002

Chen, W. T., Lu, A., Craessaerts, K., Pavie, B., Sala Frigerio, C., Corthout, N., Qian, X., Lalakova, J., Kuhnemund, M., Voytyuk, I., Wolfs, L., Mancuso, R., Salta, E., Balusu, S., Snellinx, A., Munck, S., Jurek, A., Fernandez Navarro, J., Saido, T. C., Huitinga, I., Lundeberg, J., Fiers, M., & De Strooper, B. (2020). Spatial Transcriptomics and In Situ Sequencing to Study Alzheimer's Disease. *Cell*, *182*(4), 976-991 e919. https://doi.org/10.1016/j.cell.2020.06.038

Chiu, I. M., Morimoto, E. T., Goodarzi, H., Liao, J. T., O'Keeffe, S., Phatnani, H. P., Muratet, M., Carroll, M. C., Levy, S., Tavazoie, S., Myers, R. M., & Maniatis, T. (2013). A neurodegeneration-specific gene-expression signature of acutely isolated microglia from an amyotrophic lateral sclerosis mouse model. *Cell Rep*, *4*(2), 385-401. https://doi.org/10.1016/j.celrep.2013.06.018

Cruse, G., Beaven, M. A., Music, S. C., Bradding, P., Gilfillan, A. M., & Metcalfe, D. D. (2015). The CD20 homologue MS4A4 directs trafficking of KIT toward clathrin-independent endocytosis pathways and thus regulates receptor signaling and recycling. *Mol Biol Cell*, *26*(9), 1711-1727. https://doi.org/10.1091/mbc.E14-07-1221

Cruse, G., Kaur, D., Leyland, M., & Bradding, P. (2010). A novel FcepsilonRIbeta-chain truncation regulates human mast cell proliferation and survival. *FASEB J*, *24*(10), 4047-4057. https://doi.org/10.1096/fj.10-158378

Cummings, J., Lee, G., Ritter, A., Sabbagh, M., & Zhong, K. (2020). Alzheimer's disease drug development pipeline: 2020. *Alzheimers Dement (N Y)*, *6*(1), e12050. https://doi.org/10.1002/trc2.12050

Cunningham, C. L., Martinez-Cerdeno, V., & Noctor, S. C. (2013). Microglia regulate the number of neural precursor cells in the developing cerebral cortex. *J Neurosci*, *33*(10), 4216-4233. https://doi.org/10.1523/JNEUROSCI.3441-12.2013

Daneman, R., & Prat, A. (2015). The blood-brain barrier. *Cold Spring Harb Perspect Biol*, *7*(1), a020412. https://doi.org/10.1101/cshperspect.a020412

De Biase, L. M., Schuebel, K. E., Fusfeld, Z. H., Jair, K., Hawes, I. A., Cimbro, R., Zhang, H. Y., Liu, Q. R., Shen, H., Xi, Z. X., Goldman, D., & Bonci, A. (2017). Local Cues Establish and Maintain Region-Specific Phenotypes of Basal Ganglia Microglia. *Neuron*, *95*(2), 341-356 e346. https://doi.org/10.1016/j.neuron.2017.06.020

de Weerd, N. A., & Nguyen, T. (2012). The interferons and their receptors--distribution and regulation. *Immunol Cell Biol*, *90*(5), 483-491. https://doi.org/10.1038/icb.2012.9

Deczkowska, A., Keren-Shaul, H., Weiner, A., Colonna, M., Schwartz, M., & Amit, I. (2018). Disease-Associated Microglia: A Universal Immune Sensor of Neurodegeneration. *Cell*, *173*(5), 1073-1081. https://doi.org/10.1016/j.cell.2018.05.003

Desjardins, M., Huber, L. A., Parton, R. G., & Griffiths, G. (1994). Biogenesis of phagolysosomes proceeds through a sequential series of interactions with the endocytic apparatus. *J Cell Biol*, *124*(5), 677-688. https://doi.org/10.1083/jcb.124.5.677

Di Domizio, J., Dorta-Estremera, S., Gagea, M., Ganguly, D., Meller, S., Li, P., Zhao, B., Tan, F. K., Bi, L., Gilliet, M., & Cao, W. (2012). Nucleic acid-containing amyloid fibrils potently induce type I interferon and stimulate systemic autoimmunity. *Proc Natl Acad Sci U S A*, *109*(36), 14550-14555. https://doi.org/10.1073/pnas.1206923109

Doty, K. R., Guillot-Sestier, M. V., & Town, T. (2015). The role of the immune system in neurodegenerative disorders: Adaptive or maladaptive? *Brain Res*, *1617*, 155-173. https://doi.org/10.1016/j.brainres.2014.09.008

Eon Kuek, L., Leffler, M., Mackay, G. A., & Hulett, M. D. (2016). The MS4A family: counting past 1, 2 and 3. *Immunol Cell Biol*, *94*(1), 11-23. https://doi.org/10.1038/icb.2015.48

Erblich, B., Zhu, L., Etgen, A. M., Dobrenis, K., & Pollard, J. W. (2011). Absence of colony stimulation factor-1 receptor results in loss of microglia, disrupted brain development and olfactory deficits. *PLoS One*, *6*(10), e26317. https://doi.org/10.1371/journal.pone.0026317

Erny, D., Hrabe de Angelis, A. L., Jaitin, D., Wieghofer, P., Staszewski, O., David, E., Keren-Shaul, H., Mahlakoiv, T., Jakobshagen, K., Buch, T., Schwierzeck, V., Utermohlen, O., Chun, E., Garrett, W. S., McCoy, K. D., Diefenbach, A., Staeheli, P., Stecher, B., Amit, I., & Prinz, M. (2015). Host microbiota constantly control maturation and function of microglia in the CNS. *Nat Neurosci*, *18*(7), 965-977. https://doi.org/10.1038/nn.4030

Eskildsen, S., Hartmann, R., Kjeldgaard, N. O., & Justesen, J. (2002). Gene structure of the murine 2'-5'-oligoadenylate synthetase family. *Cell Mol Life Sci*, *59*(7), 1212-1222. https://doi.org/10.1007/s00018-002-8499-2

Fitzgerald, K. A., & Kagan, J. C. (2020). Toll-like Receptors and the Control of Immunity. *Cell*, *180*(6), 1044-1066. https://doi.org/10.1016/j.cell.2020.02.041

Fourgeaud, L., Traves, P. G., Tufail, Y., Leal-Bailey, H., Lew, E. D., Burrola, P. G., Callaway, P., Zagorska, A., Rothlin, C. V., Nimmerjahn, A., & Lemke, G. (2016). TAM receptors regulate multiple features of microglial physiology. *Nature*, *532*(7598), 240-244. https://doi.org/10.1038/nature17630

Franco-Bocanegra, D. K., McAuley, C., Nicoll, J. A. R., & Boche, D. (2019). Molecular Mechanisms of Microglial Motility: Changes in Ageing and Alzheimer's Disease. *Cells*, *8*(6). https://doi.org/10.3390/cells8060639

Fukushima, S., Furube, E., Itoh, M., Nakashima, T., & Miyata, S. (2015). Robust increase of microglia proliferation in the fornix of hippocampal axonal pathway after a single LPS stimulation. *J Neuroimmunol*, *285*, 31-40. https://doi.org/10.1016/j.jneuroim.2015.05.014

Galatro, T. F., Holtman, I. R., Lerario, A. M., Vainchtein, I. D., Brouwer, N., Sola, P. R., Veras, M. M., Pereira, T. F., Leite, R. E. P., Moller, T., Wes, P. D., Sogayar, M. C., Laman, J. D., den Dunnen, W., Pasqualucci, C. A., Oba-Shinjo, S. M., Boddeke, E., Marie, S. K. N., & Eggen, B. J. L. (2017). Transcriptomic analysis of purified human cortical microglia reveals age-associated changes. *Nat Neurosci*, *20*(8), 1162-1171. https://doi.org/10.1038/nn.4597

Gautier, E. L., Shay, T., Miller, J., Greter, M., Jakubzick, C., Ivanov, S., Helft, J., Chow, A., Elpek, K. G., Gordonov, S., Mazloom, A. R., Ma'ayan, A., Chua, W. J., Hansen, T. H., Turley, S. J., Merad, M., Randolph, G. J., & Immunological Genome, C. (2012). Gene-expression profiles and transcriptional regulatory pathways that underlie the identity and diversity of mouse tissue macrophages. *Nat Immunol*, *13*(11), 1118-1128. https://doi.org/10.1038/ni.2419

Giau, V. V., Senanarong, V., Bagyinszky, E., An, S. S. A., & Kim, S. (2019). Analysis of 50 Neurodegenerative Genes in Clinically Diagnosed Early-Onset Alzheimer's Disease. *Int J Mol Sci*, *20*(6). https://doi.org/10.3390/ijms20061514

Ginhoux, F., Greter, M., Leboeuf, M., Nandi, S., See, P., Gokhan, S., Mehler, M. F., Conway, S. J., Ng, L. G., Stanley, E. R., Samokhvalov, I. M., & Merad, M. (2010). Fate mapping analysis reveals that adult microglia derive from primitive macrophages. *Science*, *330*(6005), 841-845. https://doi.org/10.1126/science.1194637

Giulian, D., & Baker, T. J. (1986). Characterization of ameboid microglia isolated from developing mammalian brain. *J Neurosci*, *6*(8), 2163-2178. https://www.ncbi.nlm.nih.gov/pubmed/3018187

Goldmann, T., Wieghofer, P., Jordao, M. J., Prutek, F., Hagemeyer, N., Frenzel, K., Amann, L., Staszewski, O., Kierdorf, K., Krueger, M., Locatelli, G., Hochgerner, H., Zeiser, R., Epelman, S., Geissmann, F., Priller, J., Rossi, F. M., Bechmann, I., Kerschensteiner, M., Linnarsson, S., Jung, S., & Prinz, M. (2016). Origin, fate and dynamics of macrophages at central nervous system interfaces. *Nat Immunol*, *17*(7), 797-805. https://doi.org/10.1038/ni.3423

Gosselin, D., Link, V. M., Romanoski, C. E., Fonseca, G. J., Eichenfield, D. Z., Spann, N. J., Stender, J. D., Chun, H. B., Garner, H., Geissmann, F., & Glass, C. K. (2014). Environment drives selection and function of enhancers controlling tissue-specific macrophage identities. *Cell*, *159*(6), 1327-1340. https://doi.org/10.1016/j.cell.2014.11.023

Gosselin, D., Skola, D., Coufal, N. G., Holtman, I. R., Schlachetzki, J. C. M., Sajti, E., Jaeger, B. N., O'Connor, C., Fitzpatrick, C., Pasillas, M. P., Pena, M., Adair, A., Gonda, D. D., Levy, M. L., Ransohoff, R. M., Gage, F. H., & Glass, C. K. (2017). An environment-dependent transcriptional network specifies human microglia identity. *Science*, *356*(6344). https://doi.org/10.1126/science.aal3222

Grabert, K., Michoel, T., Karavolos, M. H., Clohisey, S., Baillie, J. K., Stevens, M. P., Freeman, T. C., Summers, K. M., & McColl, B. W. (2016). Microglial brain region-dependent diversity and selective regional sensitivities to aging. *Nat Neurosci*, *19*(3), 504-516. https://doi.org/10.1038/nn.4222

Greer, P. L., Bear, D. M., Lassance, J. M., Bloom, M. L., Tsukahara, T., Pashkovski, S. L., Masuda, F. K., Nowlan, A. C., Kirchner, R., Hoekstra, H. E., & Datta, S. R. (2016). A Family of non-GPCR Chemosensors Defines an Alternative Logic for Mammalian Olfaction. *Cell*, *165*(7), 1734-1748. https://doi.org/10.1016/j.cell.2016.05.001

Guerreiro, R., Wojtas, A., Bras, J., Carrasquillo, M., Rogaeva, E., Majounie, E., Cruchaga, C., Sassi, C., Kauwe, J. S., Younkin, S., Hazrati, L., Collinge, J., Pocock, J., Lashley, T., Williams, J., Lambert, J. C., Amouyel, P., Goate, A., Rademakers, R., Morgan, K., Powell, J., St George-Hyslop, P., Singleton, A., Hardy, J., & Alzheimer Genetic Analysis, G. (2013). TREM2 variants in Alzheimer's disease. *N Engl J Med*, *368*(2), 117-127. https://doi.org/10.1056/NEJMoa1211851

Han, J., Wang, M., Ren, M., & Lou, H. (2017). Contributions of triggering-receptor-expressed-on-myeloid-cells-2 to neurological diseases. *Int J Neurosci*, *127*(4), 368-375. https://doi.org/10.1080/00207454.2016.1264072

Hanamsagar, R., Alter, M. D., Block, C. S., Sullivan, H., Bolton, J. L., & Bilbo, S. D. (2017). Generation of a microglial developmental index in mice and in humans reveals a sex difference in maturation and immune reactivity. *Glia*, *65*(9), 1504-1520. https://doi.org/10.1002/glia.23176

Heneka, M. T., Carson, M. J., El Khoury, J., Landreth, G. E., Brosseron, F., Feinstein, D. L., Jacobs, A. H., Wyss-Coray, T., Vitorica, J., Ransohoff, R. M., Herrup, K., Frautschy, S. A., Finsen, B., Brown, G. C., Verkhratsky, A., Yamanaka, K., Koistinaho, J., Latz, E., Halle, A., Petzold, G. C., Town, T., Morgan, D., Shinohara, M. L., Perry, V. H., Holmes, C., Bazan, N. G., Brooks, D. J., Hunot, S., Joseph, B., Deigendesch, N., Garaschuk, O., Boddeke, E., Dinarello, C. A., Breitner, J. C., Cole, G. M., Golenbock, D. T., & Kummer, M. P. (2015). Neuroinflammation in Alzheimer's disease. *Lancet Neurol*, *14*(4), 388-405. https://doi.org/10.1016/S1474-4422(15)70016-5

Heneka, M. T., McManus, R. M., & Latz, E. (2018). Inflammasome signalling in brain function and neurodegenerative disease. *Nat Rev Neurosci*, *19*(10), 610-621. https://doi.org/10.1038/s41583-018-0055-7

Hickman, S. E., Kingery, N. D., Ohsumi, T. K., Borowsky, M. L., Wang, L. C., Means, T. K., & El Khoury, J. (2013). The microglial sensome revealed by direct RNA sequencing. *Nat Neurosci*, *16*(12), 1896-1905. https://doi.org/10.1038/nn.3554

Hirbec, H., Marmai, C., Duroux-Richard, I., Roubert, C., Esclangon, A., Croze, S., Lachuer, J., Peyroutou, R., & Rassendren, F. (2018). The microglial reaction signature revealed by RNAseq from individual mice. *Glia*, *66*(5), 971-986. https://doi.org/10.1002/glia.23295

Holm, T. H., Draeby, D., & Owens, T. (2012). Microglia are required for astroglial Toll-like receptor 4 response and for optimal TLR2 and TLR3 response. *Glia*, *60*(4), 630-638. https://doi.org/10.1002/glia.22296

Holmes, C., Cunningham, C., Zotova, E., Woolford, J., Dean, C., Kerr, S., Culliford, D., & Perry, V. H. (2009). Systemic inflammation and disease progression in Alzheimer disease. *Neurology*, *73*(10), 768-774. https://doi.org/10.1212/WNL.0b013e3181b6bb95

Holtman, I. R., Raj, D. D., Miller, J. A., Schaafsma, W., Yin, Z., Brouwer, N., Wes, P. D., Moller, T., Orre, M., Kamphuis, W., Hol, E. M., Boddeke, E. W., & Eggen, B. J. (2015). Induction of a common microglia gene expression signature by aging and neurodegenerative conditions: a co-expression meta-analysis. *Acta Neuropathol Commun*, *3*, 31. https://doi.org/10.1186/s40478-015-0203-5

Huang da, W., Sherman, B. T., & Lempicki, R. A. (2009). Systematic and integrative analysis of large gene lists using DAVID bioinformatics resources. *Nat Protoc*, *4*(1), 44-57. https://doi.org/10.1038/nprot.2008.211

Huang, Y., Happonen, K. E., Burrola, P. G., O'Connor, C., Hah, N., Huang, L., Nimmerjahn, A., & Lemke, G. (2021). Microglia use TAM receptors to detect and engulf amyloid beta plaques. *Nat Immunol*, *22*(5), 586-594. https://doi.org/10.1038/s41590-021-00913-5

Ito, D., Imai, Y., Ohsawa, K., Nakajima, K., Fukuuchi, Y., & Kohsaka, S. (1998). Microglia-specific localisation of a novel calcium binding protein, Iba1. *Brain Res Mol Brain Res*, *57*(1), 1-9. https://doi.org/10.1016/s0169-328x(98)00040-0

Jankowsky, J. L., Fadale, D. J., Anderson, J., Xu, G. M., Gonzales, V., Jenkins, N. A., Copeland, N. G., Lee, M. K., Younkin, L. H., Wagner, S. L., Younkin, S. G., & Borchelt, D. R. (2004). Mutant presenilins specifically elevate the levels of the 42 residue beta-amyloid peptide in vivo: evidence for augmentation of a 42-specific gamma secretase. *Hum Mol Genet*, *13*(2), 159-170. https://doi.org/10.1093/hmg/ddh019

Jung, S., Aliberti, J., Graemmel, P., Sunshine, M. J., Kreutzberg, G. W., Sher, A., & Littman, D. R. (2000). Analysis of fractalkine receptor CX(3)CR1 function by targeted deletion and green fluorescent protein reporter gene insertion. *Mol Cell Biol*, *20*(11), 4106-4114. https://doi.org/10.1128/mcb.20.11.4106-4114.2000

Jurado-Parras, M. T., Gruart, A., & Delgado-Garcia, J. M. (2012). Observational learning in mice can be prevented by medial prefrontal cortex stimulation and enhanced by nucleus accumbens stimulation. *Learn Mem*, *19*(3), 99-106. https://doi.org/10.1101/lm.024760.111

Kamboh, M. I., Demirci, F. Y., Wang, X., Minster, R. L., Carrasquillo, M. M., Pankratz, V. S., Younkin, S. G., Saykin, A. J., Alzheimer's Disease Neuroimaging, I., Jun, G., Baldwin, C., Logue, M. W., Buros, J., Farrer, L., Pericak-Vance, M. A., Haines, J. L., Sweet, R. A., Ganguli, M., Feingold, E., Dekosky, S. T., Lopez, O. L., & Barmada, M. M. (2012). Genome-wide association study of Alzheimer's disease. *Transl Psychiatry*, *2*, e117. https://doi.org/10.1038/tp.2012.45

Kamphuis, W., Orre, M., Kooijman, L., Dahmen, M., & Hol, E. M. (2012). Differential cell proliferation in the cortex of the APPswePS1dE9 Alzheimer's disease mouse model. *Glia*, *60*(4), 615-629. https://doi.org/10.1002/glia.22295

Karch, C. M., & Goate, A. M. (2015). Alzheimer's disease risk genes and mechanisms of disease pathogenesis. *Biol Psychiatry*, *77*(1), 43-51. https://doi.org/10.1016/j.biopsych.2014.05.006

Keren-Shaul, H., Spinrad, A., Weiner, A., Matcovitch-Natan, O., Dvir-Szternfeld, R., Ulland, T. K., David, E., Baruch, K., Lara-Astaiso, D., Toth, B., Itzkovitz, S., Colonna, M., Schwartz, M., & Amit, I. (2017). A Unique Microglia Type Associated with Restricting Development of Alzheimer's Disease. *Cell*, *169*(7), 1276-1290 e1217. https://doi.org/10.1016/j.cell.2017.05.018

Kim, D., Langmead, B., & Salzberg, S. L. (2015). HISAT: a fast spliced aligner with low memory requirements. *Nat Methods*, *12*(4), 357-360. https://doi.org/10.1038/nmeth.3317

Krasemann, S., Madore, C., Cialic, R., Baufeld, C., Calcagno, N., El Fatimy, R., Beckers, L., O'Loughlin, E., Xu, Y., Fanek, Z., Greco, D. J., Smith, S. T., Tweet, G., Humulock, Z., Zrzavy, T., Conde-Sanroman, P., Gacias, M., Weng, Z., Chen, H., Tjon, E., Mazaheri, F., Hartmann, K., Madi, A., Ulrich, J. D., Glatzel, M., Worthmann, A., Heeren, J., Budnik, B., Lemere, C., Ikezu, T., Heppner, F. L., Litvak, V., Holtzman, D. M., Lassmann, H., Weiner, H. L., Ochando, J., Haass, C., & Butovsky, O. (2017). The TREM2-APOE Pathway Drives the Transcriptional Phenotype of Dysfunctional Microglia in Neurodegenerative Diseases. *Immunity*, *47*(3), 566-581 e569. https://doi.org/10.1016/j.immuni.2017.08.008

Kutok, J. L., Yang, X., Folkerth, R., & Adra, C. N. (2011). Characterization of the expression of HTm4 (MS4A3), a cell cycle regulator, in human peripheral blood cells and normal and malignant tissues. *J Cell Mol Med*, *15*(1), 86-93. https://doi.org/10.1111/j.1582-4934.2009.00925.x

Lambert, J. C., Ibrahim-Verbaas, C. A., Harold, D., Naj, A. C., Sims, R., Bellenguez, C., DeStafano, A. L., Bis, J. C., Beecham, G. W., Grenier-Boley, B., Russo, G., Thorton-Wells, T. A., Jones, N., Smith, A. V., Chouraki, V., Thomas, C., Ikram, M. A., Zelenika, D., Vardarajan, B. N., Kamatani, Y., Lin, C. F., Gerrish, A., Schmidt, H., Kunkle, B., Dunstan, M. L., Ruiz, A., Bihoreau, M. T., Choi, S. H., Reitz, C., Pasquier, F., Cruchaga, C., Craig, D., Amin, N., Berr, C., Lopez, O. L., De Jager, P. L., Deramecourt, V., Johnston, J. A., Evans, D., Lovestone, S., Letenneur, L., Moron, F. J., Rubinsztein, D. C., Eiriksdottir, G., Sleegers, K., Goate, A. M., Fievet, N., Huentelman, M. W., Gill, M., Brown, K., Kamboh, M. I., Keller, L., Barberger-Gateau, P., McGuiness, B., Larson, E. B., Green, R., Myers, A. J., Dufouil, C., Todd, S., Wallon, D., Love, S., Rogaeva, E., Gallacher, J., St George-Hyslop, P., Clarimon, J., Lleo, A., Bayer, A., Tsuang, D. W., Yu, L., Tsolaki, M., Bossu, P., Spalletta, G., Proitsi, P., Collinge, J., Sorbi, S., Sanchez-Garcia, F., Fox, N. C., Hardy, J., Deniz Naranjo, M. C., Bosco, P., Clarke, R., Brayne, C., Galimberti, D., Mancuso, M., Matthews, F., European Alzheimer's Disease, I., Genetic, Environmental Risk in Alzheimer's, D., Alzheimer's Disease Genetic, C., Cohorts for, H., Aging Research in Genomic, E., Moebus, S., Mecocci, P., Del Zompo, M., Maier, W., Hampel, H., Pilotto, A., Bullido, M., Panza, F., Caffarra, P., Nacmias, B., Gilbert, J. R., Mayhaus, M., Lannefelt, L., Hakonarson, H., Pichler, S., Carrasquillo, M. M., Ingelsson, M., Beekly, D., Alvarez, V., Zou, F., Valladares, O., Younkin, S. G., Coto, E., Hamilton-Nelson, K. L., Gu, W.,

Razquin, C., Pastor, P., Mateo, I., Owen, M. J., Faber, K. M., Jonsson, P. V., Combarros, O., O'Donovan, M. C., Cantwell, L. B., Soininen, H., Blacker, D., Mead, S., Mosley, T. H., Jr., Bennett, D. A., Harris, T. B., Fratiglioni, L., Holmes, C., de Bruijn, R. F., Passmore, P., Montine, T. J., Bettens, K., Rotter, J. I., Brice, A., Morgan, K., Foroud, T. M., Kukull, W. A., Hannequin, D., Powell, J. F., Nalls, M. A., Ritchie, K., Lunetta, K. L., Kauwe, J. S., Boerwinkle, E., Riemenschneider, M., Boada, M., Hiltuenen, M., Martin, E. R., Schmidt, R., Rujescu, D., Wang, L. S., Dartigues, J. F., Mayeux, R., Tzourio, C., Hofman, A., Nothen, M. M., Graff, C., Psaty, B. M., Jones, L., Haines, J. L., Holmans, P. A., Lathrop, M., Pericak-Vance, M. A., Launer, L. J., Farrer, L. A., van Duijn, C. M., Van Broeckhoven, C., Moskvina, V., Seshadri, S., Williams, J., Schellenberg, G. D., & Amouyel, P. (2013). Meta-analysis of 74,046 individuals identifies 11 new susceptibility loci for Alzheimer's disease. *Nat Genet*, *45*(12), 1452-1458. https://doi.org/10.1038/ng.2802

Langmead, B., & Salzberg, S. L. (2012). Fast gapped-read alignment with Bowtie 2. *Nat Methods*, *9*(4), 357-359. https://doi.org/10.1038/nmeth.1923

Lauro, C., & Limatola, C. (2020). Metabolic Reprograming of Microglia in the Regulation of the Innate Inflammatory Response. *Front Immunol*, *11*, 493. https://doi.org/10.3389/fimmu.2020.00493

Lavin, Y., Winter, D., Blecher-Gonen, R., David, E., Keren-Shaul, H., Merad, M., Jung, S., & Amit, I. (2014). Tissue-resident macrophage enhancer landscapes are shaped by the local microenvironment. *Cell*, *159*(6), 1312-1326. https://doi.org/10.1016/j.cell.2014.11.018

Lawson, L. J., Perry, V. H., Dri, P., & Gordon, S. (1990). Heterogeneity in the distribution and morphology of microglia in the normal adult mouse brain. *Neuroscience*, *39*(1), 151-170. https://doi.org/10.1016/0306-4522(90)90229-w

Lee, W. L., Mason, D., Schreiber, A. D., & Grinstein, S. (2007). Quantitative analysis of membrane remodeling at the phagocytic cup. *Mol Biol Cell*, *18*(8), 2883-2892. https://doi.org/10.1091/mbc.e06-05-0450

Lemaitre, B., Nicolas, E., Michaut, L., Reichhart, J. M., & Hoffmann, J. A. (1996). The dorsoventral regulatory gene cassette spatzle/Toll/cactus controls the potent antifungal response in Drosophila adults. *Cell*, *86*(6), 973-983. https://doi.org/10.1016/s0092-8674(00)80172-5

Lemke, G. (2013). Biology of the TAM receptors. *Cold Spring Harb Perspect Biol*, *5*(11), a009076. https://doi.org/10.1101/cshperspect.a009076

Lipinski, M., Munoz-Viana, R., Del Blanco, B., Marquez-Galera, A., Medrano-Relinque, J., Carames, J. M., Szczepankiewicz, A. A., Fernandez-Albert, J., Navarron, C. M., Olivares, R., Wilczynski, G. M., Canals, S., Lopez-Atalaya, J. P., & Barco, A. (2020). KAT3-dependent acetylation of cell type-specific genes maintains neuronal identity in the adult mouse brain. *Nat Commun*, *11*(1), 2588. https://doi.org/10.1038/s41467-020-16246-0

Liu, Y. U., Ying, Y., Li, Y., Eyo, U. B., Chen, T., Zheng, J., Umpierre, A. D., Zhu, J., Bosco, D. B., Dong, H., & Wu, L. J. (2019). Neuronal network activity controls microglial process surveillance in awake mice via norepinephrine signaling. *Nat Neurosci*, *22*(11), 1771-1781. https://doi.org/10.1038/s41593-019-0511-3

Love, M. I., Huber, W., & Anders, S. (2014). Moderated estimation of fold change and dispersion for RNA-seq data with DESeq2. *Genome Biol*, *15*(12), 550. https://doi.org/10.1186/s13059-014-0550-8

Madronal, N., Lopez-Aracil, C., Rangel, A., del Rio, J. A., Delgado-Garcia, J. M., & Gruart, A. (2010). Effects of enriched physical and social environments on motor performance, associative learning, and hippocampal neurogenesis in mice. *PLoS One*, *5*(6), e11130. https://doi.org/10.1371/journal.pone.0011130

Marsh, S. E., Kamath, T., Walker, A. J., Dissing-Olesen, L., Hammond, T. R., Young, A. M. H., Abdulraouf, A., Nadaf, N., Dufort, C., Murphy, S., Kozareva, V., Vanderburg, C., Hong, S., Bulstrode, H., Hutchinson, P. J., Gaffney, D. J., Franklin, R. J. M., Macosko, E. Z., & Stevens, B. (2020). Single Cell Sequencing Reveals Glial Specific Responses to Tissue Processing & Enzymatic Dissociation in Mice and Humans. *bioRxiv*, 2020.2012.2003.408542. https://doi.org/10.1101/2020.12.03.408542

Martinez-Muriana, A., Mancuso, R., Francos-Quijorna, I., Olmos-Alonso, A., Osta, R., Perry, V. H., Navarro, X., Gomez-Nicola, D., & Lopez-Vales, R. (2016). CSF1R blockade slows the progression of amyotrophic lateral sclerosis by reducing microgliosis and invasion of macrophages into peripheral nerves. *Sci Rep*, *6*, 25663. https://doi.org/10.1038/srep25663

Masuda, T., Sankowski, R., Staszewski, O., & Prinz, M. (2020). Microglia Heterogeneity in the Single-Cell Era. *Cell Rep*, *30*(5), 1271-1281. https://doi.org/10.1016/j.celrep.2020.01.010

Mathys, H., Adaikkan, C., Gao, F., Young, J. Z., Manet, E., Hemberg, M., De Jager, P. L., Ransohoff, R. M., Regev, A., & Tsai, L. H. (2017). Temporal Tracking of Microglia Activation in Neurodegeneration at Single-Cell Resolution. *Cell Rep*, *21*(2), 366-380. https://doi.org/10.1016/j.celrep.2017.09.039

Mathys, H., Davila-Velderrain, J., Peng, Z., Gao, F., Mohammadi, S., Young, J. Z., Menon, M., He, L., Abdurrob, F., Jiang, X., Martorell, A. J., Ransohoff, R. M., Hafler, B. P., Bennett, D. A., Kellis, M., & Tsai, L. H. (2019). Single-cell transcriptomic analysis of Alzheimer's disease. *Nature*, *570*(7761), 332-337. https://doi.org/10.1038/s41586-019-1195-2

Medzhitov, R., Preston-Hurlburt, P., & Janeway, C. A., Jr. (1997). A human homologue of the Drosophila Toll protein signals activation of adaptive immunity. *Nature*, *388*(6640), 394-397. https://doi.org/10.1038/41131

Meffert, M. K., Chang, J. M., Wiltgen, B. J., Fanselow, M. S., & Baltimore, D. (2003). NF-kappa B functions in synaptic signaling and behavior. *Nat Neurosci*, *6*(10), 1072-1078. https://doi.org/10.1038/nn1110

Meylan, E., Burns, K., Hofmann, K., Blancheteau, V., Martinon, F., Kelliher, M., & Tschopp, J. (2004). RIP1 is an essential mediator of Toll-like receptor 3-induced NF-kappa B activation. *Nat Immunol*, *5*(5), 503-507. https://doi.org/10.1038/ni1061

Mucke, L., Masliah, E., Yu, G. Q., Mallory, M., Rockenstein, E. M., Tatsuno, G., Hu, K., Kholodenko, D., Johnson-Wood, K., & McConlogue, L. (2000). High-level neuronal expression of abeta 1-42 in wild-type human amyloid protein precursor transgenic mice: synaptotoxicity without plaque formation. *J Neurosci*, *20*(11), 4050-4058. https://www.ncbi.nlm.nih.gov/pubmed/10818140

Navarro, J. F., Croteau, D. L., Jurek, A., Andrusivova, Z., Yang, B., Wang, Y., Ogedegbe, B., Riaz, T., Stoen, M., Desler, C., Rasmussen, L. J., Tonjum, T., Galas, M. C., Lundeberg, J., & Bohr, V. A. (2020). Spatial Transcriptomics Reveals Genes Associated with Dysregulated Mitochondrial Functions and Stress Signaling in Alzheimer Disease. *iScience*, *23*(10), 101556. https://doi.org/10.1016/j.isci.2020.101556

Nguyen, T. T., Huang, J., Wu, Q., Nguyen, T., & Li, M. (2015). Genome-wide association data classification and SNPs selection using two-stage quality-based Random Forests. *BMC Genomics*, *16 Suppl 2*, S5. https://doi.org/10.1186/1471-2164-16-S2-S5

Nimmerjahn, A., Kirchhoff, F., & Helmchen, F. (2005). Resting microglial cells are highly dynamic surveillants of brain parenchyma in vivo. *Science*, *308*(5726), 1314-1318. https://doi.org/10.1126/science.1110647

Olah, M., Patrick, E., Villani, A. C., Xu, J., White, C. C., Ryan, K. J., Piehowski, P., Kapasi, A., Nejad, P., Cimpean, M., Connor, S., Yung, C. J., Frangieh, M., McHenry, A., Elyaman, W., Petyuk, V., Schneider, J. A., Bennett, D. A., De Jager, P. L., & Bradshaw, E. M. (2018). A transcriptomic atlas of aged human microglia. *Nat Commun*, *9*(1), 539. https://doi.org/10.1038/s41467-018-02926-5

Olmos-Alonso, A., Schetters, S. T., Sri, S., Askew, K., Mancuso, R., Vargas-Caballero, M., Holscher, C., Perry, V. H., & Gomez-Nicola, D. (2016). Pharmacological targeting of CSF1R inhibits microglial proliferation and prevents the progression of Alzheimer's-like pathology. *Brain*, *139*(Pt 3), 891-907. https://doi.org/10.1093/brain/awv379

Owens, T., Khorooshi, R., Wlodarczyk, A., & Asgari, N. (2014). Interferons in the central nervous system: a few instruments play many tunes. *Glia*, *62*(3), 339-355. https://doi.org/10.1002/glia.22608

Paolicelli, R. C., Bolasco, G., Pagani, F., Maggi, L., Scianni, M., Panzanelli, P., Giustetto, M., Ferreira, T. A., Guiducci, E., Dumas, L., Ragozzino, D., & Gross, C. T. (2011). Synaptic pruning by microglia is necessary for normal brain development. *Science*, *333*(6048), 1456-1458. https://doi.org/10.1126/science.1202529

Parkhurst, C. N., Yang, G., Ninan, I., Savas, J. N., Yates, J. R., 3rd, Lafaille, J. J., Hempstead, B. L., Littman, D. R., & Gan, W. B. (2013). Microglia promote learning-dependent synapse formation through brain-derived neurotrophic factor. *Cell*, *155*(7), 1596-1609. https://doi.org/10.1016/j.cell.2013.11.030

Pillai, A. G., de Jong, D., Kanatsou, S., Krugers, H., Knapman, A., Heinzmann, J. M., Holsboer, F., Landgraf, R., Joels, M., & Touma, C. (2012). Dendritic morphology of hippocampal and amygdalar neurons in adolescent mice is resilient to genetic differences in stress reactivity. *PLoS One*, *7*(6), e38971. https://doi.org/10.1371/journal.pone.0038971

Pont-Lezica, L., Beumer, W., Colasse, S., Drexhage, H., Versnel, M., & Bessis, A. (2014). Microglia shape corpus callosum axon tract fasciculation: functional impact of prenatal inflammation. *Eur J Neurosci*, *39*(10), 1551-1557. https://doi.org/10.1111/ejn.12508

Presta, I., Vismara, M., Novellino, F., Donato, A., Zaffino, P., Scali, E., Pirrone, K. C., Spadea, M. F., Malara, N., & Donato, G. (2018). Innate Immunity Cells and the Neurovascular Unit. *Int J Mol Sci*, *19*(12). https://doi.org/10.3390/ijms19123856

Ransohoff, R. M. (2016). A polarizing question: do M1 and M2 microglia exist? *Nat Neurosci*, *19*(8), 987-991. https://doi.org/10.1038/nn.4338

Reu, P., Khosravi, A., Bernard, S., Mold, J. E., Salehpour, M., Alkass, K., Perl, S., Tisdale, J., Possnert, G., Druid, H., & Frisen, J. (2017). The Lifespan and Turnover of Microglia in the Human Brain. *Cell Rep*, *20*(4), 779-784. https://doi.org/10.1016/j.celrep.2017.07.004

Río-Hortega, P. d. (1919). El "Tercer Elemento" de los Centros Nerviosos. I. La Microglía en Estado Normal. *Boletín de la Sociedad Española de Biología VIII*, 67-82.

Río-Hortega, P. d. (1932). *Cytology and cellular pathology of the nervous system* (N. Y. Hoeber, Ed.).

Rivest, S. (2009). Regulation of innate immune responses in the brain. *Nat Rev Immunol*, *9*(6), 429-439. https://doi.org/10.1038/nri2565

Roy, E. R., Wang, B., Wan, Y. W., Chiu, G., Cole, A., Yin, Z., Propson, N. E., Xu, Y., Jankowsky, J. L., Liu, Z., Lee, V. M., Trojanowski, J. Q., Ginsberg, S. D., Butovsky, O., Zheng, H., & Cao, W. (2020). Type I interferon response drives neuroinflammation and synapse loss in Alzheimer disease. *J Clin Invest*, *130*(4), 1912-1930. https://doi.org/10.1172/JCI133737

Sala Frigerio, C., Wolfs, L., Fattorelli, N., Thrupp, N., Voytyuk, I., Schmidt, I., Mancuso, R., Chen, W. T., Woodbury, M. E., Srivastava, G., Moller, T., Hudry, E., Das, S., Saido, T., Karran, E., Hyman, B., Perry, V. H., Fiers, M., & De Strooper, B. (2019). The Major Risk Factors for Alzheimer's Disease: Age, Sex, and Genes Modulate the Microglia Response to Abeta Plaques. *Cell Rep*, *27*(4), 1293-1306 e1296. https://doi.org/10.1016/j.celrep.2019.03.099

Sankowski, R., Bottcher, C., Masuda, T., Geirsdottir, L., Sagar, Sindram, E., Seredenina, T., Muhs, A., Scheiwe, C., Shah, M. J., Heiland, D. H., Schnell, O., Grun, D., Priller, J., & Prinz, M. (2019). Mapping microglia states in the human brain through the integration of high-dimensional techniques. *Nat Neurosci*, *22*(12), 2098-2110. https://doi.org/10.1038/s41593-019-0532-y

Sarlus, H., & Heneka, M. T. (2017). Microglia in Alzheimer's disease. *J Clin Invest*, *127*(9), 3240-3249. https://doi.org/10.1172/JCI90606

Sasaguri, H., Nilsson, P., Hashimoto, S., Nagata, K., Saito, T., De Strooper, B., Hardy, J., Vassar, R., Winblad, B., & Saido, T. C. (2017). APP mouse models for Alzheimer's disease preclinical studies. *EMBO J*, *36*(17), 2473-2487. https://doi.org/10.15252/embj.201797397

Savage, J. C., Carrier, M., & Tremblay, M. E. (2019). Morphology of Microglia Across Contexts of Health and Disease. *Methods Mol Biol*, *2034*, 13-26. https://doi.org/10.1007/978-1-4939-9658-2_2

Schafer, D. P., Lehrman, E. K., Kautzman, A. G., Koyama, R., Mardinly, A. R., Yamasaki, R., Ransohoff, R. M., Greenberg, M. E., Barres, B. A., & Stevens, B. (2012). Microglia sculpt postnatal neural circuits in an activity and complement-dependent manner. *Neuron*, *74*(4), 691-705. https://doi.org/10.1016/j.neuron.2012.03.026

Schafer, D. P., & Stevens, B. (2015). Microglia Function in Central Nervous System Development and Plasticity. *Cold Spring Harb Perspect Biol*, *7*(10), a020545. https://doi.org/10.1101/cshperspect.a020545

Schulz, C., Gomez Perdiguero, E., Chorro, L., Szabo-Rogers, H., Cagnard, N., Kierdorf, K., Prinz, M., Wu, B., Jacobsen, S. E., Pollard, J. W., Frampton, J., Liu, K. J., & Geissmann, F. (2012). A lineage of myeloid cells independent of Myb and hematopoietic stem cells. *Science*, *336*(6077), 86-90. https://doi.org/10.1126/science.1219179

Selkoe, D. J., & Hardy, J. (2016). The amyloid hypothesis of Alzheimer's disease at 25 years. *EMBO Mol Med*, *8*(6), 595-608. https://doi.org/10.15252/emmm.201606210

Serhan, C. N. (2010). *Fundamentals of Inflammation*. Camdrige University Press.

Shaftel, S. S., Kyrkanides, S., Olschowka, J. A., Miller, J. N., Johnson, R. E., & O'Banion, M. K. (2007). Sustained hippocampal IL-1 beta overexpression mediates chronic neuroinflammation and ameliorates Alzheimer plaque pathology. *J Clin Invest*, *117*(6), 1595-1604. https://doi.org/10.1172/JCI31450

Shay, T., & Kang, J. (2013). Immunological Genome Project and systems immunology. *Trends Immunol*, *34*(12), 602-609. https://doi.org/10.1016/j.it.2013.03.004

Shemer, A., Scheyltjens, I., Frumer, G. R., Kim, J. S., Grozovski, J., Ayanaw, S., Dassa, B., Van Hove, H., Chappell-Maor, L., Boura-Halfon, S., Leshkowitz, D., Mueller, W., Maggio, N., Movahedi, K., & Jung, S. (2020). Interleukin-10 Prevents Pathological Microglia Hyperactivation following Peripheral Endotoxin Challenge. *Immunity*, *53*(5), 1033-1049 e1037. https://doi.org/10.1016/j.immuni.2020.09.018

Sierra, A., Abiega, O., Shahraz, A., & Neumann, H. (2013). Janus-faced microglia: beneficial and detrimental consequences of microglial phagocytosis. *Front Cell Neurosci*, *7*, 6. https://doi.org/10.3389/fncel.2013.00006

Sierra, A., Encinas, J. M., Deudero, J. J., Chancey, J. H., Enikolopov, G., Overstreet-Wadiche, L. S., Tsirka, S. E., & Maletic-Savatic, M. (2010). Microglia shape adult hippocampal neurogenesis through apoptosis-coupled phagocytosis. *Cell Stem Cell*, *7*(4), 483-495. https://doi.org/10.1016/j.stem.2010.08.014

Sierra, A., Paolicelli, R. C., & Kettenmann, H. (2019). Cien Anos de Microglia: Milestones in a Century of Microglial Research. *Trends Neurosci*, *42*(11), 778-792. https://doi.org/10.1016/j.tins.2019.09.004

Sousa, C., Golebiewska, A., Poovathingal, S. K., Kaoma, T., Pires-Afonso, Y., Martina, S., Coowar, D., Azuaje, F., Skupin, A., Balling, R., Biber, K., Niclou, S. P., & Michelucci, A. (2018). Single-cell transcriptomics reveals distinct inflammation-induced microglia signatures. *EMBO Rep*, *19*(11). https://doi.org/10.15252/embr.201846171

Squarzoni, P., Oller, G., Hoeffel, G., Pont-Lezica, L., Rostaing, P., Low, D., Bessis, A., Ginhoux, F., & Garel, S. (2014). Microglia modulate wiring of the embryonic forebrain. *Cell Rep*, *8*(5), 1271-1279. https://doi.org/10.1016/j.celrep.2014.07.042

Srinivasan, K., Friedman, B. A., Larson, J. L., Lauffer, B. E., Goldstein, L. D., Appling, L. L., Borneo, J., Poon, C., Ho, T., Cai, F., Steiner, P., van der Brug, M. P., Modrusan, Z., Kaminker, J. S., & Hansen, D. V. (2016). Untangling the brain's neuroinflammatory and neurodegenerative transcriptional responses. *Nat Commun*, *7*, 11295. https://doi.org/10.1038/ncomms11295

Steinbrecher, K. A., Harmel-Laws, E., Sitcheran, R., & Baldwin, A. S. (2008). Loss of epithelial RelA results in deregulated intestinal proliferative/apoptotic homeostasis and susceptibility to inflammation. *J Immunol*, *180*(4), 2588-2599. https://doi.org/10.4049/jimmunol.180.4.2588

Stowell, R. D., Sipe, G. O., Dawes, R. P., Batchelor, H. N., Lordy, K. A., Whitelaw, B. S., Stoessel, M. B., Bidlack, J. M., Brown, E., Sur, M., & Majewska, A. K. (2019). Noradrenergic signaling in the wakeful state inhibits microglial surveillance and synaptic plasticity in the mouse visual cortex. *Nat Neurosci*, *22*(11), 1782-1792. https://doi.org/10.1038/s41593-019-0514-0

Stuart, T., & Satija, R. (2019). Integrative single-cell analysis. *Nat Rev Genet*, *20*(5), 257-272. https://doi.org/10.1038/s41576-019-0093-7

Takeuchi, O., & Akira, S. (2010). Pattern recognition receptors and inflammation. *Cell*, *140*(6), 805-820. https://doi.org/10.1016/j.cell.2010.01.022

Talamonti, G., D'Aliberti, G., & Cenzato, M. (2020). Aulus Cornelius Celsus and the Head Injuries. *World Neurosurg*, *133*, 127-134. https://doi.org/10.1016/j.wneu.2019.09.119

Tay, T. L., Mai, D., Dautzenberg, J., Fernandez-Klett, F., Lin, G., Sagar, Datta, M., Drougard, A., Stempfl, T., Ardura-Fabregat, A., Staszewski, O., Margineanu, A., Sporbert, A., Steinmetz, L. M., Pospisilik, J. A., Jung, S., Priller, J., Grun, D., Ronneberger, O., & Prinz, M. (2017). A new fate mapping system reveals context-dependent random or clonal expansion of microglia. *Nat Neurosci*, *20*(6), 793-803. https://doi.org/10.1038/nn.4547

Thion, M. S., & Garel, S. (2017). On place and time: microglia in embryonic and perinatal brain development. *Curr Opin Neurobiol*, *47*, 121-130. https://doi.org/10.1016/j.conb.2017.10.004

Thion, M. S., Low, D., Silvin, A., Chen, J., Grisel, P., Schulte-Schrepping, J., Blecher, R., Ulas, T., Squarzoni, P., Hoeffel, G., Coulpier, F., Siopi, E., David, F. S., Scholz, C., Shihui, F., Lum, J., Amoyo, A. A., Larbi, A., Poidinger, M., Buttgereit, A., Lledo, P. M., Greter, M., Chan, J. K. Y., Amit, I., Beyer, M., Schultze, J. L., Schlitzer, A., Pettersson, S., Ginhoux, F., & Garel, S. (2018). Microbiome Influences Prenatal and Adult Microglia in a Sex-Specific Manner. *Cell*, *172*(3), 500-516 e516. https://doi.org/10.1016/j.cell.2017.11.042

Thrupp, N., Sala Frigerio, C., Wolfs, L., Skene, N. G., Fattorelli, N., Poovathingal, S., Fourne, Y., Matthews, P. M., Theys, T., Mancuso, R., de Strooper, B., & Fiers, M. (2020). Single-Nucleus RNA-Seq Is Not Suitable for Detection of Microglial Activation Genes in Humans. *Cell Rep*, *32*(13), 108189. https://doi.org/10.1016/j.celrep.2020.108189

Tonnesen, J., Inavalli, V., & Nagerl, U. V. (2018). Super-Resolution Imaging of the Extracellular Space in Living Brain Tissue. *Cell*, *172*(5), 1108-1121 e1115. https://doi.org/10.1016/j.cell.2018.02.007

Venegas, C., Kumar, S., Franklin, B. S., Dierkes, T., Brinkschulte, R., Tejera, D., Vieira-Saecker, A., Schwartz, S., Santarelli, F., Kummer, M. P., Griep, A., Gelpi, E., Beilharz, M., Riedel, D., Golenbock, D. T., Geyer, M., Walter, J., Latz, E., & Heneka, M. T. (2017). Microglia-derived ASC specks cross-seed amyloid-beta in Alzheimer's disease. *Nature*, *552*(7685), 355-361. https://doi.org/10.1038/nature25158

Villegas-Llerena, C., Phillips, A., Garcia-Reitboeck, P., Hardy, J., & Pocock, J. M. (2016). Microglial genes regulating neuroinflammation in the progression of Alzheimer's disease. *Curr Opin Neurobiol*, *36*, 74-81. https://doi.org/10.1016/j.conb.2015.10.004

von Drygalski, A., Furlan-Freguia, C., Ruf, W., Griffin, J. H., & Mosnier, L. O. (2013). Organ-specific protection against lipopolysaccharide-induced vascular leak is dependent on the endothelial protein C receptor. *Arterioscler Thromb Vasc Biol*, *33*(4), 769-776. https://doi.org/10.1161/ATVBAHA.112.301082

Walsh, D. T., Betmouni, S., & Perry, V. H. (2001). Absence of detectable IL-1beta production in murine prion disease: a model of chronic neurodegeneration. *J Neuropathol Exp Neurol*, *60*(2), 173-182. https://doi.org/10.1093/jnen/60.2.173

Wang, S., Mustafa, M., Yuede, C. M., Salazar, S. V., Kong, P., Long, H., Ward, M., Siddiqui, O., Paul, R., Gilfillan, S., Ibrahim, A., Rhinn, H., Tassi, I., Rosenthal, A., Schwabe, T., & Colonna, M. (2020). Anti-human TREM2 induces microglia proliferation and reduces pathology in an Alzheimer's disease model. *J Exp Med*, *217*(9). https://doi.org/10.1084/jem.20200785

Weinhard, L., di Bartolomei, G., Bolasco, G., Machado, P., Schieber, N. L., Neniskyte, U., Exiga, M., Vadisiute, A., Raggioli, A., Schertel, A., Schwab, Y., & Gross, C. T. (2018). Microglia remodel synapses by presynaptic trogocytosis and spine head filopodia induction. *Nat Commun*, *9*(1), 1228. https://doi.org/10.1038/s41467-018-03566-5

Welser-Alves, J. V., & Milner, R. (2013). Microglia are the major source of TNF-alpha and TGF-beta1 in postnatal glial cultures; regulation by cytokines, lipopolysaccharide, and vitronectin. *Neurochem Int*, *63*(1), 47-53. https://doi.org/10.1016/j.neuint.2013.04.007

Xu, H., Yan, Y., Williams, M. S., Carey, G. B., Yang, J., Li, H., Zhang, G. X., & Rostami, A. (2010). MS4a4B, a CD20 homologue in T cells, inhibits T cell propagation by modulation of cell cycle. *PLoS One*, *5*(11), e13780. https://doi.org/10.1371/journal.pone.0013780

Yang, H. S., Onos, K. D., Choi, K., Keezer, K. J., Skelly, D. A., Carter, G. W., & Howell, G. R. (2021). Natural genetic variation determines microglia heterogeneity in wild-derived mouse models of Alzheimer's disease. *Cell Rep*, *34*(6), 108739. https://doi.org/10.1016/j.celrep.2021.108739

Yates, S. L., Burgess, L. H., Kocsis-Angle, J., Antal, J. M., Dority, M. D., Embury, P. B., Piotrkowski, A. M., & Brunden, K. R. (2000). Amyloid beta and amylin fibrils induce increases in proinflammatory cytokine and chemokine production by THP-1 cells and murine microglia. *J Neurochem*, *74*(3), 1017-1025. https://doi.org/10.1046/j.1471-4159.2000.0741017.x

Yeh, F. L., Wang, Y., Tom, I., Gonzalez, L. C., & Sheng, M. (2016). TREM2 Binds to Apolipoproteins, Including APOE and CLU/APOJ, and Thereby Facilitates Uptake of Amyloid-Beta by Microglia. *Neuron*, *91*(2), 328-340. https://doi.org/10.1016/j.neuron.2016.06.015

Zambelli, F., Pesole, G., & Pavesi, G. (2009). Pscan: finding over-represented transcription factor binding site motifs in sequences from co-regulated or co-expressed genes. *Nucleic Acids Res*, *37*(Web Server issue), W247-252. https://doi.org/10.1093/nar/gkp464

Zhang, Q., Lenardo, M. J., & Baltimore, D. (2017). 30 Years of NF-kappaB: A Blossoming of Relevance to Human Pathobiology. *Cell*, *168*(1-2), 37-57. https://doi.org/10.1016/j.cell.2016.12.012

Zhang, Y., Chen, K., Sloan, S. A., Bennett, M. L., Scholze, A. R., O'Keeffe, S., Phatnani, H. P., Guarnieri, P., Caneda, C., Ruderisch, N., Deng, S., Liddelow, S. A., Zhang, C., Daneman, R., Maniatis, T., Barres, B. A., & Wu, J. Q. (2014). An RNA-sequencing transcriptome and splicing database of glia, neurons, and vascular cells of the cerebral cortex. *J Neurosci*, *34*(36), 11929-11947. https://doi.org/10.1523/JNEUROSCI.1860-14.2014

Zhao, J., Bi, W., Xiao, S., Lan, X., Cheng, X., Zhang, J., Lu, D., Wei, W., Wang, Y., Li, H., Fu, Y., & Zhu, L. (2019). Neuroinflammation induced by lipopolysaccharide causes cognitive impairment in mice. *Sci Rep*, *9*(1), 5790. https://doi.org/10.1038/s41598-019-42286-8

Zhou, Y., Song, W. M., Andhey, P. S., Swain, A., Levy, T., Miller, K. R., Poliani, P. L., Cominelli, M., Grover, S., Gilfillan, S., Cella, M., Ulland, T. K., Zaitsev, K., Miyashita, A., Ikeuchi, T., Sainouchi, M., Kakita, A., Bennett, D. A., Schneider, J. A., Nichols, M. R., Beausoleil, S. A., Ulrich, J. D., Holtzman, D. M., Artyomov, M. N., & Colonna, M. (2020). Human and mouse single-nucleus transcriptomics reveal TREM2-dependent and TREM2-independent cellular responses in Alzheimer's disease. *Nat Med*, *26*(1), 131-142. https://doi.org/10.1038/s41591-019-0695-9

Zhu, J., Zhang, Y., Ghosh, A., Cuevas, R. A., Forero, A., Dhar, J., Ibsen, M. S., Schmid-Burgk, J. L., Schmidt, T., Ganapathiraju, M. K., Fujita, T., Hartmann, R., Barik, S., Hornung, V., Coyne, C. B., & Sarkar, S. N. (2014). Antiviral activity of human OASL protein is mediated by enhancing signaling of the RIG-I RNA sensor. *Immunity*, *40*(6), 936-948. https://doi.org/10.1016/j.immuni.2014.05.007

ANNEX

The article “KAT3-dependent acetylation of cell type-specific genes maintains neuronal identity in the adult mouse brain.” that Jose P. Lopez-Atalaya and me, Carmen María Navarrón Izquierdo co-authored as part of a collaboration with the laboratory of Prof. Ángel Barco Guerrero has been published in ***Nature Communications*** 2020 May 22;11(1):2588. DOI 10.1038/s41467-020-16246-0

Title: KAT3-dependent acetylation of cell type-specific genes maintains neuronal identity in the adult mouse brain.

Authors: 1,#Michal Lipinski, 1,#Rafael Muñoz-Viana, 1,#Beatriz del Blanco, 1Angel Marquez-Galera, 1Juan Medrano-Relinque, 1Jose M. Carames, 2Andrzej A. Szczepankiewicz, 1Jordi Fernandez-Albert, 1**Carmen M. Navarrón**, 1Roman Olivares, 2Grzegorz M. Wilczynski, 1Santiago Canals, 1**Jose P. Lopez-Atalaya**, and 1,†Angel Barco. #Equal contribution

Author affiliations:

1 Instituto de Neurociencias (Universidad Miguel Hernández – Consejo Superior de Investigaciones Científicas). Av. Santiago Ramón y Cajal s/n. Sant Joan d'Alacant 03550, Alicante, Spain.
2 Nencki Institute of Experimental Biology, Polish Academy of Science, 3 Pasteur Street, 02-093 Warsaw, Poland.

† **Corresponding author:** Angel Barco, Instituto de Neurociencias (Universidad Miguel Hernández – Consejo Superior de Investigaciones Científicas), Av. Santiago Ramón y Cajal s/n. Sant Joan d'Alacant 03550, Alicante, Spain. Tel: +34 965 919232. Email: abarco@umh.es

Keywords: Cell fate, terminal selector, CBP, p300, KAT3, lysine acetylation, epigenomics, enhancer, super-enhancer, neuronal identity

Abstract

The lysine acetyltransferases type 3 (KAT3) family members CBP and p300 are important transcriptional co-activators, but their specific functions in adult post-mitotic neurons remain unclear. Here, we show that the combined elimination of both proteins in forebrain excitatory neurons of adult mice resulted in a rapidly progressing neurological phenotype associated with severe ataxia, dendritic retraction and reduced electrical activity. At the molecular level, we observed the downregulation of neuronal genes, as well as decreased H3K27 acetylation and pro-neural transcription factor binding at the promoters and enhancers of canonical neuronal genes. The combined deletion of CBP and p300 in hippocampal neurons resulted in the rapid loss of neuronal molecular identity without de- or transdifferentiation. Restoring CBP expression or lysine acetylation rescued neuronal-specific transcription in cultured neurons. Together, these experiments show that KAT3 proteins maintain the excitatory neuron identity through the regulation of histone acetylation at cell type specific promoter and enhancer regions.

Introduction

Neuronal identity is established through the action of a particular class of transcription factors (TFs), referred to as terminal selectors, that bind to cis regulatory elements of terminal identity genes and regulate the establishment of neuron-specific gene programs[1,2]. Many of these terminal selectors are also required at later stages of development[3], which led to the idea that the identity of postmitotic neurons needs to be actively maintained throughout life by the action of the same TFs that controlled the last steps of differentiation[4]. However, the mechanisms responsible for such maintenance remain elusive. Chromatin-modifying enzymes are also involved in identity acquisition[5] and maintenance[6]. The KAT3 family of transcriptional co-activators comprises the CREB binding protein CBP (aka KAT3a) and the E1A binding protein p300 (aka KAT3b)[7]. Both proteins have a lysine acetyltransferase (KAT) catalytic domain and interact with numerous other proteins, including histones, TFs, the RNA polymerase II complex (RNAPII), protein kinases and other chromatin modifying enzymes[8] that also are substrates of the CBP/p300 catalytic activity[9]. Consistent with this central function, KAT3 proteins play a critical and dose-dependent role during neurodevelopment[10]. Deletions and inactivating mutations in KAT3 genes cause early embryonic death and neuronal tube closure defects[11], whereas hemizygous mutations cause a syndromic disorder associated with intellectual disability known as Rubinstein–Taybi syndrome (RSTS)[12]. After birth, CBP loss in postmitotic forebrain neurons impairs memory in specific tasks, but does not interfere with cell viability and animal survival[13–15]. The consequences of p300 loss in adult neurons have been less explored, but the only study conducted so far revealed very mild defects[16]. The relatively modest consequences of the postembryonic loss of either one of these central transcriptional regulators could indicate that their role is limited to development. Alternatively, since both proteins are still expressed in adult neurons, they could be functionally redundant and thus mutually compensate for each other loss. To define KAT3-specific functions in the adult brain, we generate mice with inducible and restricted ablation of CBP and/ or p300 in forebrain principal neurons. The characterization of these strains reveals that while both proteins are individually dispensable for the normal function of mature neurons, their combined ablation has devastating and rapid consequences: dendrites retract, synapses are lost, and electrical activity and neuron-specific gene programs established during development are shutdown. These phenotypes lead to severe neurological defects and premature death. Epigenomic screens and rescue experiments demonstrate that both KAT3 proteins are jointly essential for maintaining the identity of excitatory forebrain neurons (and likely other cell types) throughout life by preserving acetylation levels at cell type-specific genes and enhancers.

Results

Combined loss of CBP and p300 in adult excitatory neurons. To elucidate the neuronal roles of CBP and p300 in the adult brain, we selectively eliminated CBP, p300, or both KAT3 proteins in forebrain excitatory neurons of adult mice using the inducible Cre-recombinase driver CaMKIIα-CreERT2 (Fig. 1a)17. The three inducible forebrain-specific knockout strains (referred to as CBP-ifKO, p300-ifKO, and dKAT3-ifKO, respectively) do not show any neurological symptom before gene(s) ablation (Supplementary Table 1). After tamoxifen (TMX) treatment of 3- month old mice, loss of immunoreactivity was observed in virtually 100% of the pyramidal neurons in the CA1 and cortex, and granule neurons in the dentate gyrus (DG; Fig. 1b and Supplementary Fig. 1a), while brain regions in which the CaMKIIα promoter is not active, such as the cerebellum and the basal ganglia, were spared17. Importantly, the loss of either one of these paralogous proteins did not affect the expression level of the other (Supplementary Fig. 1b). Consistent with the characterization of other forebrain-specific KO strains for CBP or p30013,14,16, CBP- and p300-ifKO mice had a normal lifespan and showed no overt neurological abnormalities (Fig. 1c). However, the situation was markedly different in dKAT3-ifKOs. When CBP and p300 were simultaneously removed in the forebrain of adult mice, the animals displayed a dramatic and rapidly progressing deteriorating phenotype (Supplementary Table 1 and Supplementary Fig. 1c, d). In the 1st week following TMX administration, the mice were hyperactive and frequently froze in bizarre positions during manipulation. One week later, the same mice showed severe ataxia, and loss of the righting reflex, escaping response and tail suspension-evoked stretching (Supplementary Movie 1). Although different animals reached the terminal phenotype at different times, initially all the mice died within the first 2–3 weeks after TMX administration. Upon facilitating access to food and water, survival increased by about 40% within the 1st month after TMX (Fig. 1c), which suggests that the ataxic mice had problems reaching the cage feeder and bottle. Remarkably, mice carrying just a single functional allele encoding either one of the two KAT3s did not die prematurely and showed normal basic reflexes (Supplementary Table 1 and Supplementary Fig. 1d, e).

Synaptic loss and reduced electrical activity in dKAT3-ifKOs. Consistent with the severe neurological phenotype, the very few dKAT3-ifKOs that survived for more than 2 months after TMX (less than 5%) showed a reduction of cerebral cortex volume, whereas other brain regions not targeted by gene deletion, such as the cerebellum, were unaffected (Fig. 1d). Interestingly, histological analyses indicated that this reduction was caused by a loss ofneuropils rather than a loss of neuronal cells. For instance, in the hippocampus of dKAT3-ifKOs, the stratum pyramidale—a layer occupied by the somas of CA1 pyramidal

neurons—had a normal thickness and did not show any obvious sign of neurodegeneration (Fig. 1e and Supplementary Fig. 2a, b) even several weeks after TMX treatment. In contrast, the stratum radiatum—a layer occupied by the basal dendrites of the CA1 neurons—was markedly thinner in dKAT3-ifKOs as soon as 1 month after TMX (Fig. 1e). In agreement with these quantifications, Golgi staining revealed a retraction of dendrites in the DG (Fig. 1f, g) and electron microscopy analyses confirmed the massive loss of synapses in dKAT3-ifKOs (Fig. 1h, i). Furthermore, as early as 2 weeks after gene ablation, dKAT3-ifKOs implanted with multichannel electrodes displayed a dramatic reduction in both spontaneous (Fig. 1j, k and Supplementary Fig. 2c, d) and evoked (Fig. 1l, m and Supplementary Fig. 2e) electrical activity. Overall, these data demonstrate that the simultaneous loss of CBP and p300 alters neuronal morphology and impairs electrical responses leading to dramatic neurological defects. Strikingly, these severe changes occur in the absence of cell death. TUNEL staining (Supplementary Fig. 3a) and immunostaining against active caspase 3 (Fig. 1n), which label cells undergoing apoptosis, were both negative. Immunostaining against the histone H2A.X variant (Supplementary Fig. 3b) that labels cells suffering DNA damage was also negative. EM images revealed a stratum pyramidale with a similar density of somas in dKAT3-ifKOs and control littermates (Supplementary Fig. 3c). Neuronal nuclei did not present apoptotic bodies, although the nucleoplasm appeared clearer and with slightly larger heterochromatic domains in dKAT3 ifKOs than in controls (Supplementary Fig. 3d). To monitor the evolution of double KO neurons in a cell autonomous manner, we infected the DG of the Crebbpf/f::Ep300f/f (dKAT3-floxed) mice with adeno-associated virus (AAV) expressing Cre recombinase under the synapsin promoter (Supplementary Fig. 3e). Immunostaining confirmed the efficient and complete elimination of CBP and p300 in granule neurons in the absence of detectable neurodegeneration even 10 weeks after genes ablation (Supplementary Fig. 3f, g).

Maintenance of neuronal identity requires at least one KAT3. To determine the molecular basis of the abovementioned phenotypes, we conducted a RNA seq screen in the hippocampus of dKAT3-ifKOs and control littermates. Differential gene expression profiling revealed 1952 differentially expressed genes (DEGs; |log2FC| > 1) in dKAT3-ifKOs, with a clear preponderance both in number and magnitude of gene downregulations (Fig. 2a, b, Supplementary Fig. 4a, and Supplementary Data 1). Gene Ontology (GO) enrichment analysis indicated that these downregulations affect a large number of neuronal functions (Fig. 2c, blue bars). Hundreds of genes with neuronal functions such as genes encoding channels and proteins important for synaptic transmission were severely downregulated in the dKAT3-ifKO hippocampus, which explains the reduced neuronal firing and lack of electrical responses. Gene upregulation was much more restricted, including a modest inflammatory

signature (Fig. 2c, red bars) but no activation of cell death pathways (Supplementary Fig. 4b). In fact, several positive regulators of neuronal death were strongly downregulated in dKAT3-ifKOs (e.g., Hrk; Supplementary Fig. 4c). Consistent with the survival of these cells, housekeeping genes remained largely unchanged (Fig. 2b and Supplementary Fig. 4d). Immunodetection experiments for neuronal proteins like CaMKIV, NeuN, and hippocalcin confirmed the dramatic loss of expression of neuronal proteins (Fig. 2d, e and Supplementary Fig. 4e). Notably, the loss of neuronal markers expression was not detected in mice bearing a single functional KAT3 allele (Supplementary Fig. 4f), indicating that this minimal gene dose is sufficient to preserve their expression. To determine if these deficits were cell-autonomous, we examined the hippocampus of dKAT3-floxed mice monolaterally infected with Cre-recombinase-expressing AAVs. We observed a dramatic loss of neuronal marker expression only in the transduced DG (Fig. 2f). Moreover, the cells depleted of KAT3 proteins completely failed to respond to kainic acid, a strong agonist of glutamate receptors, further confirming the loss of excitatory neuron properties (Supplementary Fig. 5). Similarly, experiments in primary neuronal cultures (PNCs) produced from the hippocampi of Crebbpf/f::Ep300f/f embryos and infected with a Cre-recombinase-expressing lentivirus (Fig. 2g) did not show enhanced neuronal death after the simultaneous elimination of CBP and p300 (Supplementary Fig. 6a, b). These cells, however, showed abnormal morphology (Fig. 2h), downregulation of neuron-specific transcripts and proteins (Fig. 2i and Supplementary Fig. 6c), and severe hypoacetylation of KAT3 targets (Supplementary Fig. 6d).

dKAT3-KO neurons acquire a novel, molecularly undefined fate. The altered morphology, electrophysiological properties, and gene expression all suggest that the excitatory neurons rapidly lose their identity after the elimination of both KAT3 genes. To tackle this hypothesis, we compared the set of DEGs in dKAT3- ifKOs with transcriptome information for the different cell types in the adult mouse brain using single-cell RNA-seq (scRNA-seq) data from the mouse cortex18 (Fig. 3a). Our analysis revealed that the genes typically expressed in CA1 and S1 pyramidal neurons were significantly downregulated in the hippocampus of dKAT3- ifKOs, whereas other cell-type specific transcriptional programs were unaffected except for a modest increase of microglia genes related to inflammation. Importantly, although identity loss is often associated with dedifferentiation (i.e., the regression to an earlier stage of differentiation), we did not detect an upregulation of stemness genes19, nor neuronal stem cell (NSC)- or neuroprogenitor (NPC)-specific gene expression20 (Fig. 3a and Supplementary Fig. 7a, b). Trans-differentiation can be also discarded because we did not detect the upregulation of the transcriptional signatures of other brain cell-types. To determine more precisely the fate of excitatory neurons after losing

their identity, we conducted single nucleus RNA-seq analyses 2 and 5 weeks after TMX treatment (Fig. 3b, c and Supplementary Fig. 7c). We observed a progressive confluence of CA1/CA3 pyramidal neurons and DG granule neurons in a common cell cluster depleted of neuronal type-specific markers (Fig. 3d, Supplementary Fig. 7d, e, f, g and Supplementary Data 2) and in which no other distinctive markers appear (Fig. 3e, Supplementary Fig. 7h, i, and Supplementary Data 2). Of note, these cells do not show a reduction in RNA content and still express a large number of transcripts, confirming that the reduction is restricted to a specific gene set (Supplementary Fig. 8). To further investigate the transitional states of dKAT3- KOs neurons, we used manifold learning leveraged in nearest neighbor information to automatically organize excitatory neurons in trajectories along a principal tree21. This analysis produced a topological structure with five main branches and three bifurcation points (Fig. 3f). Pseudotime analysis revealed a trajectory in which cells travel from the roots in branches A (corresponding to DG granule cells), B and C (both populated by pyramidal neurons) towards branches D and E that are almost exclusively populated by the cells depleted of cell-type-specific markers (Fig. 3g). Altogether, these results indicate that the different main types of excitatory hippocampal neurons in dKAT3-KOs lose their neuronal identity, but do not die, dedifferentiate or transdifferentiate to other cell types. Instead, these cells seem to be trapped in an undifferentiated, nonfunctional interstate deadlock.

CBP and p300 bind to the same regulatory regions. The evidence above indicates that KAT3 proteins play a redundant role in preserving neuronal identity. To explore the basis of such redundancy, we next mapped the occupancy of hippocampal chromatin by CBP and p300. Chromatin immunoprecipitation followed by whole-genome sequencing (ChIP-seq) using antibodies that differentiate between the two paralogous proteins (Supplementary Figs. 1b and 9a) retrieved 37,359 peaks in the chromatin of wild type mice (Fig. 4a, Supplementary Fig. 9b, and Supplementary Data 3). Considering the different efficiencies of the two antibodies, we detected an almost complete overlap between the CBP and p300 peaks throughout the whole genome (Fig. 4b and Supplementary Fig. 9c). This result indicates that these two essential epigenetic enzymes largely occupy the same sites in neuronal chromatin and underscores their functional redundancy. As both proteins are ubiquitously expressed yet gene ablation only takes place in excitatory neurons, the signal detected in the hippocampal chromatin of dKAT3-ifKOs must correspond to CBP/p300 binding in other cell types. We combined this information with ATAC-seq (a technique that investigates chromatin occupancy and requires much lower input tan ChIP-seq) in sorted NeuN+ hippocampal nuclei22 to discriminate between neuronal-specific, non-neuronal-cell-specific and “pancellular” KAT3 binding (Fig. 4c, d, Supplementary Fig. 10a, and Supplementary Data

3). Intriguingly, pancellular KAT3 peaks are found in the promoter of genes involved in basic cellular functions, such as RNA processing and metabolism, while celltype- specific peaks (neuronal and non-neuronal) primarily locate at introns and intergenic regions with enhancer features (Supplementary Fig. 10b) and associate with cell-type-specific processes (Fig. 4e, f and Supplementary Data 4). We used binding and expression target analysis (BETA)23 to integrate ChIP-seq and RNA-seq data (Fig. 4g), and found that the loss of neuronal KAT3 binding (~14,000 peaks) is an excellent predictor of transcriptional downregulation ($p = 3.3 \times 10-72$, Fig. 4h). Up to 74% of the downregulated genes in dKAT3-ifKOs are linked to the loss of KAT3s at proximal regulatory regions. Comparison of ATAC-seq profiles of control and dKAT3-ifKO neuronal nuclei retrieved more than 6000 regions with differential accessibility (Supplementary Data 5). Most of these differentially accessible regions (DARs) displayed reduced accessibility in dKAT3-ifKO neurons (Supplementary Fig. 10c), were located at enhancers (Supplementary Fig. 10d) and coincided with the downregulation of the proximal gene (Supplementary Fig. 10e).

KAT3s preserve acetylation of neuron-specific enhancers. In agreement with a recent acetylome analysis9, immunostaining against specific lysine residues in the histone tails revealed their variable dependence on CBP/p300 (Supplementary Fig. 11a) as well as the particular sensitivity of H3K27ac to the loss of CBP and p300 (Fig. 5a). This histone modification is enriched in active enhancers and its levels correlate with tissue specification24. The dramatic reduction in H3K27ac was not accompanied by an increase in the signal or changes in the distribution of H3K27me3 (Supplementary Fig. 11b). H3K9me3, a histone modification associated with heterochromatin, also seemed unaffected (Supplementary Fig. 11c). We next investigated the genomic distribution of H3K27ac in hippocampal chromatin of dKAT3-ifKOs and control littermates. We retrieved 37,732 H3K27ac-enriched regions (Fig. 5b) that largely overlap with KAT3 peaks (Supplementary Fig. 11d). More than one-third of these H3K27ac peaks were strongly reduced in dKAT3-ifKOs (Supplementary Data 6), particularly those that overlap with neuronal KAT3 binding (~80%). In contrast, less than 5% of pancellular and non-neuronal H3K27ac peaks were affected (Fig. 5b). To explore in greater detail these differences, we classified neuronal KAT3 peaks into promoters and enhancers based on their location and H3K4me1/me3 content (Fig. 5c and Supplementary Fig. 11e). KAT3 binding, H3K27ac and ATACseq signals were all strongly reduced in the enhancers (Fig. 5d) and promoters (Supplementary Fig. 11f) of neuronal genes in dKAT3-ifKOs, although the changes were more abundant and significant for enhancers than promoters (Supplementary Fig. 11g). In contrast, the promoters associated with pancellular-KAT3 peaks were spared (Supplementary Fig. 11f), which suggests that other KATs

contribute to maintain H3K27ac at the promoter of pancellular genes. The acetylation of H3K9,14 that primarily decorates promoters only showed a modest reduction in dKAT3-ifKOs (Supplementary Fig. 11h), indicating that other KATs are responsible for maintaining this form of acetylation. We also observed a strong correlation between the loss of H3K27ac and transcript downregulation. Out of 1376 genes downregulated in dKAT3-ifKOs, 78% showed a strong reduction in H3K27ac. Reciprocally, 74% of the genes with reduced acetylation were neuronal genes with reduced expression in dKAT3-ifKOs. Super-enhancers constitute a special type of regulatory region that plays a critical role in controlling cell identity25. Their conspicuous features include the association with highly transcribed genes, broad domains of H3K27 acetylation, and a high

density of TF binding sites. To identify putative neural superenhancers, we fused together enhancers that are closer than 5 kb from each other (Supplementary Data 7). The retrieved regions were associated with highly expressed genes in hippocampal neurons that are downregulated in dKAT3-ifKOs (Fig. 5e). Furthermore, more than 85% of these super-enhancers-associated genes were strongly hypoacetylated in dKAT3-ifKOs (Fig. 5f) and encoded bona fide neuronal regulators related with synaptic transmission and neuronal plasticity (Fig. 5g). Together, these results show that KAT3 proteins control the status of neuronspecific genes by regulating lysine acetylation levels at enhancers and super-enhancers.

bHLH TFs drive KAT3 binding to neuron-specific genes. Since KAT3 proteins do not directly bind to DNA, we next asked which proteins are responsible for recruiting CBP and p300 to these neuron-specific regulatory regions. Motif prediction analysis on KAT3 binding peaks revealed remarkable differences between pancellular and neuronal-specific regions. Pancellular KAT3 binding was associated with general TFs such as Sp, Fox, and Ets, all of which have been reported to bind CBP or p3008 (Fig. 5h). In contrast, neuronal KAT3 peaks presented a very prominent enrichment (E-value = 1.0 × 10−1223) for the DNA binding motif of basic helix–loop–helix (bHLH) TFs (Fig. 5h). Regions losing occupancy in dKAT3-ifKOs were also highly enriched for bHLHbound motifs (Fig. 5i and Supplementary Fig. 12a). Among these bHLH TFs, there are important pro-neural TFs involved in neuronal development26,27 (e.g., Ascl1, Neurod1-6, Neurogenin1-3, and Atoh1). Our differential expression analysis retrieved 20 bHLH TF-encoding genes that were downregulated in the hippocampus of dKAT3-ifKOs (Supplementary Fig. 12b and Supplementary Data 1). In fact, NeuroD2 and NeuroD6, which encode TFs with putative terminal selector activity4,28, were among the most downregulated genes in the hippocampi of dKAT3-ifKOs (Fig. 5j). To directly assess the occupancy of these sites before and after the ablation of KAT3s,

we analyzed their digital footprints in DARs and detected robust differences (Fig. 5k and Supplementary Fig. 12c), confirming that some changes in chromatin occupancy reflect the reduced binding of members of this family. This finding is consistent with the large overlap between bHLH TF footprints detected in the ATAC-seq profiles and Neurod2 ChIP-seq data29 (Supplementary Fig. 12d). Altogether these experiments indicate that CBP and p300 interact with bHLH proneural TFs in neuronal-specific genomic locations to maintain neuron-specific transcription (Fig. 5l and Supplementary Fig. 12e show some representative examples).

Other cell type fates also require KAT3 proteins. Previous studies have shown that KAT3 proteins play a critical role in the differentiation of several cell types and the establishment of celltype- specific transcription30–33. To investigate if cell fate maintenance in other cell types also requires the KAT3 activity, we next examined astrocytes derived from dKAT3-floxed mice (Fig. 6a). We prepared astrocyte cultures from the hippocampi of Crebbpf/f::Ep300f/f embryos and infected them with a Crerecombinase- expressing lentivirus. Similar to our results in neurons, primary cultures of cortical astrocytes missing both KAT3 proteins lose both the expression of glial genes such as Gfap and their characteristic morphology (Fig. 6b–d), indicating that KAT3 proteins are also responsible for identity maintenance in other cell types. To examine this possibility in cells from other lineages, we investigated the profiles of p300 binding in different tissues available at ENCODE (there are no tissue-specific profiles for CBP). We found that, similarly to our observations in brain tissue, p300 peaks were associated with genesets highly enriched in tissue-specific functions (Supplementary Fig. 13a). Furthermore, in each tissue, p300-bound regulatory regions wereenriched for distinct binding motifs (Supplementary Fig. 13b) and tissue-specific p300 binding was observed into and upstream of loci presenting tissue-specific transcription (Supplementary Fig. 13c). Thus, we detected a very high enrichment for GATA TFs in liver. TFs belonging to this family are essential during liver development and are still expressed in mature tissue34, indicating that they may work as terminal selectors for hepatocytes.

Scaffold and KAT activities are both required. To explore the specific contribution of the scaffolding and KAT activities of KAT3 proteins to the loss of cell-type-specific transcription, we turned to PNCs. Transfection of a heterologous full-length CBP in neurons that have lost the endogenous expression of both CBP and p300 (Fig. 7a, b) prevented the downregulation of the neuronal markers NeuroD2 and hippocalcin (Fig. 7c, d). We next examined whether the expression of the N-terminus or the Cterminus (bearing the KAT domain) halves of CBP, as well as the full-length reconstituted protein (Fig. 7e, f) could also rescue the transcriptional impairment. To specifically assess the contribution of KAT activity,

we also transfected a variant of the C-terminus half of CBP (referred to as KATmut) bearing the R1378P mutation linked to RSTS35. We found that only the reconstruction of full-length CBP with an intact KAT domain prevented the downregulation of the neuronal marker NeuroD2 (Fig. 7g, h). These results indicate that both activities of CBP, as molecular scaffold and KAT, are necessary to preserve the active status of target loci. We also investigated whether heterologous NeuroD2 expression exerted the same protection. This bHLH TF is highly expressed in mature excitatory neurons, regulates its own expression, and holds the features of a neuronal terminal selector4. Furthermore, it is strongly downregulated in dKAT3- ifKOs neurons (Fig. 5j and Supplementary Fig. 12b), and its occupancy profile in cortical chromatin29 shows a large overlap with DARs in dKAT3-ifKOs (Supplementary Fig. 14a, b). Conversely to CBP, NeuroD2 alone was not sufficient to re-establish neuronal-specific transcription in dKAT3-KO PNCs (Supplementary Fig. 14c).

Locus-specific epi-editing rescue transcriptional impairment. Next, we examined whether increasing lysine acetylation is sufficient to rescue the transcriptional deficit. To this end, we took advantage of recently developed tools for epi-editing based on the expression of an inactive Cas9 enzyme (dCas9) fused to the KAT domain of p300 (dCas9-KAT)36. This system enables targeting specific genomic regions for p300-dependent acetylation using adequate guide RNAs (gRNA). We selected Neurod2 as the target gene because it is both severely downregulated and H3K27- hypoacetylated in dKAT3-ifKOs (Fig. 8a). The infection of PNCs with lentiviruses that express dCas9-KAT and a gRNA that recruits this chimeric protein to the most proximal KAT3 peak of Neurod2 (Fig. 8a, b) prevented the downregulation of NeuroD2 observed in dKAT3-KO neurons (Fig. 8c, d). Moreover, cotransfection of dCas9-KAT and the Neurod2 gRNA in dKAT3- KO cells that had already lost Neurod2 expression also caused a significant recovery of the expression of this gene (Fig. 8e–g). These experiments indicate that histone/lysine deacetylation is the main cause for the downregulation of neuronal genes after KAT3 loss. We noted that transcriptional rescue was observed in Neurod2, which is a gene that had not lost chromatin accessibility at their promoter, but not in Hpca, which showed a severe loss of accessibility (compare ATAC-seq profiles in Figs. 5l and 8a). This suggests that the efficacy of the rescue also depends on other features of the locus.

Discussion

The differentiation of neuronal lineages during brain development requires the participation of TFs and chromatin-modifying enzymes such as CBP and p3005,10,37–41. These proteins are often referred to as gatekeepers of cell fate. Here, we used an inducible knockout system to demonstrate that KAT3 proteins are jointly required in excitatory neurons to preserve their postmitotic neuronal identity, thereby acting as fate-keepers. This evidence indicates that the epigenetic landscape of neuronal genes is not self-sufficient and requires the active and continuous presence of KAT3 enzymes, which opens up the possibility of using controlled KAT3 inhibition for dedifferentiation and reprogramming in cell therapy strategies. Supporting this view, a recent study showed that treatment with competitive inhibitors targeting the bromodomains of CBP and p300 enhanced the reprogramming of human fibroblasts into iPSCs, while KAT inhibition prevented iPSC formation42 (which is consistent with our observation that dKAT3-KO cells fail to express stem cell markers). Strikingly, the loss of neuronal identity did not lead to apoptosis or other forms of neuronal death even weeks after KAT3 elimination both in culture and *in vivo*. This may be the result of the inability of dKAT3-KO cells to trigger the programmed cell death program. As shown in Supplementary Fig. 4b, numerous genes involved in neuronal apoptosis and death are strongly downregulated in dKAT3-KO, including important initiators of neuronal apoptosis such as Hrk43,44. This gene is highly expressed in neurons and as many other neuronal genes present a dramatic downregulation that is accompanied by the loss of CBP/p300 binding and the H3K27 deacetylation of the locus (Supplementary Fig. 11e). Together these results suggest that KAT3 proteins are essential to safeguard cell identity but also to activate any alternative cell fate, including stemness and programmed cell death. Thanks to their ability to interact with cell-type-specific TFs, KAT3 proteins are recruited to specific genomic locations where they act as an “acetyl-spray” targeting accessible lysine residues on proximal histones and non-histone proteins9 to support active transcription10. Interestingly, a single Crebbp or Ep300 functional allele is sufficient to sustain neuronal identity, which underscores the robustness of the epigenetic mechanisms involved in cell type maintenance. Robustness and redundancy are even greater in ubiquitous and highly expressed genes for which we detected neither downregulation nor severe hypoacetylation in dKAT3- ifKOs, likely because other KATs maintain the acetylation at these loci. Consistent with this hypothesis, our RNA-seq screen shows that KATs such as Gcn5/KAT2A, Tip60/KAT5, and MOF/ KAT8, which are expressed in neurons and localize to promoters45,46, are not downregulated in dKAT3-ifKO neurons (Supplementary Fig. 11e shows the profile of Kat5; a similar pattern is observed in Kat2A and Kat8). The recent discovery that KAT5, contrary to KAT3 proteins, is required for

neuronal viability[47] further supports an essential role for that KAT in cell homeostasis. Our experiments show that the recruitment of KAT3 proteins to cell-type-specific enhancers in excitatory hippocampal neurons is likely mediated by bHLH TFs belonging to the NeuroD family. Various bHLH TFs are differentially expressed throughout neuronal proliferation and specification. For instance, Hes1 and Hes5 promote NSC/NPC renewal and inhibit specification, but are replaced by Ascl1 or Neurog2 to trigger the differentiation to cortical neurons[48]. These two TFs are followed or accompanied by other factors like NeuroD1 and other family members, such as NeuroD2 or NeuroD6, whose expression is maintained throughout the lifetime of the neuron[49]. Although we cannot be certain which specific bHLH TF or set of TFs actually recruit CBP and p300 in adult neurons, the two KATs are known to interact with multiple bHLH TFs including MyoD[50], Ascl1[51], Neurogenins[37,52], Twist[53], and NeuroD2[54]. Since bHLH proteins form dimers[48], and the binding to a dimerized TF has recently been shown as essential for the control of KAT3 activity[55], these TFs represent suitable candidates to regulate KAT3 function and drive chromatin acetylation at different stages of neurodevelopment. The loss of neuronal identity observed in the brain of dKATifKOs is unlikely to be a mere consequence of the downregulation of pro-neural TFs because this phenotype was not observed after elimination of Neurod1, Neurod2, Ascl1, or other bHLH genes in neurons[49,56], nor was this phenotype rescued by NeuroD2 overexpression. It is also unlikely to be the direct consequence of a general loss of the enhancer's building factors because our differential gene expression analysis indicates that, besides the two KAT3 proteins, the components of the enhanceosome[57] are not downregulated in dKAT3-ifKOs. Instead, our experiments show that identity loss is strongly associated with chromatin hypoacetylation and that it can be avoided by targeted KAT activity. These results suggest that the main role of terminal selectors might be to recruit the KAT3 enzymes for maintaining the acetylated status of cell-type-specific enhancers in differentiated cells. These findings have broad clinical implications because impaired CBP/p300 function, histone hypoacetylation, and the loss or attenuation of epigenetic profiles underlying cell fate are features of several neurological disorders, including Alzheimer's and Huntington's diseases and aging-related senescence[58,59]. Importantly, the role of KAT3 proteins as fate-keepers is not restricted to neurons. Our experiments in astrocytes, analysis of KAT3 peaks in different tissues and previous observations in other cell types demonstrating that the combined loss of CBP and p300 causes impaired cell-type-specific transcription[30–33], all support this view. Further supporting this model, a very recent study in mice with skeletal muscle-specific and inducible combined ablation of p300 and CBP revealed that the two proteins are also jointly required for the control and maintenance of contractile function and transcriptional homeostasis in skeletal muscle[60]. What may differ between cell types is the specific set of TFs that recruit

the KAT3 proteins to cell-type-specific loci. Future studies should identify their cell-type-specific partners and targets governing tissue specification. The role of KAT3 proteins in preserving cell-type-specific gene statuses can be particularly relevant for neurons given their tremendous diversity and long lifespan. The critical importance of KAT3s for brain function may explain the duplication of the ancestral KAT3 gene in the first vertebrates coinciding with the emergence of a neural crest and cephalization10,61. Although the two KAT3 proteins have evolved some individual functions in postmitotic cells (e.g., forebrain restricted CBP knockouts show phenotypes related to cognitive dysfunction58 and p300 seems to play a prominent role in muscle biology62), our study demonstrates that they still share a joint and more essential role in preserving epigenetic identity.

Methods

Animals and treatments. Animals were housed according to the Spanish and European regulations and the experiments were approved by the Animal Welfare Committee at the Instituto de Neurociencias and the CSIC Ethical Committee. Mice were caged in ventilated cages in a pathogen-free facility with 12 h light/dark cycle, food and water available ad libitum, and controlled temperature (23 °C) and humidity (40–60%). Both male and female mice were used in the experiments. CaMKIIα-creERT217, Ep300f/f63, and Crebbpf/f64 mice were crossed to obtain p300- ifKO, CBP-ifKO, and dKAT3-ifKO mice. These CaMKIIα-creERT2 carrying mouse lines were maintained in standard housing for 3–4 months. Then, they were treated with tamoxifen (TMX)65 to trigger the elimination of either p300, CBP, or both proteins in forebrain excitatory neurons. CaMKIIα-creERT2− littermates were considered as controls. dKAT3-ifKO animals in poor state or showing signs of pain were sacrificed. To improve their survival, we provided dKAT3-ifKOs and their control littermates with high-protein food pellets (Teklad Global Diets® 2919, Envigo) on the bedding.

Lentiviral production and plasmid constructs. Lentiviral particles (LV) were produced according to the methods established in our laboratory66. The following lentiviral constructs were acquired from Addgene: LV-CRE-GFP (Addgene #20781), LV-CRE-mCherry (Addgene #27546), and LV-RFP (Addgene #17619) were used to label neurons and astrocytes with fluorescent reporter proteins; dCas9-KAT (Addgene #61357), LV-dCas9-KAT (Addgene #83889), and LVU6gRNA- Cherry (Addgene #85708) were used in epi-editing experiments; and LVphND2- N174 (Addgene #31822) was used to overexpress human NeuroD2. All the designed gRNAs were cloned in LV-U6gRNA-Cherry using the oligonucleotides pairs indicated in Supplementary Table 2. The locations of the gRNAs were selected based on the enrichment for CBP, p300, and H3K27ac in the chromatin of dKAT3-iKOs. To produce LV-CREw/oGFP we digested LV-CRE-GFP with XbaI and BsrGI to remove GFP. As a control for Cre recombinase transduction, we infected the neurons with a synapsin promoter-bearing lentiviral vector derived from LenLox 3.7, LV-syn-syn-GFP67. The constructs encoding CBP fragments were subcloned by PCR from full-length CBP: N-terminus-CBP-vhhGFP4 spans amino acids (aa) 1–1098; GFP C-terminus-CBP spans aa 1099–2441; NLSKATGFP includes a sequence encoding a nuclear localization signal (KKKRKVD) fused to aa 1088–1758 of CBP and to full-length GFP. pDsRed-Express2-C1 (Clontech) was used in the analysis of neuronal morphology in hippocampal cultures.

Primary cultures and lentiviral infection. Primary hippocampal and cortical cultures were prepared from Crebbpf/f::Ep300f/f and Crebbpf/f::Ep300f/f::CAG/ loxP/STOP/loxP/ tdTomato embryos. Their hippocampi were dissected, pooled together, and dissociated for

neuronal extraction66. Cells were plated in 24-well plates at 0.11 × 106 neurons/well. After 24 h, the primary cultures were infected with the indicated viruses (day *in vitro* 1, DIV1). In the experiments preventing CBP loss, neuronal cultures were co-infected at DIV1 with the indicated viruses and the cultures were processed after 11 days. In rescue experiments, neurons were first infected with the Cre recombinase-expressing LV at DIV1, the same neurons were transfected with the indicated vectors at DIV12 and the cultures were fixed at DIV13. To produce the astrocyte primary cultures, astrocytes were isolated from cortices of P1-P3 Crebbpf/f::Ep300f/f pups. The cortices were dissected, cut into pieces, and washed twice with HBBS 1× (Lonza BE10547F). The tissue was disrupted with a Pasteur pipette with rounded edges in 2 ml of complete medium (DMED from Gibco, 21969-035 plus 10% fetal bovine serum and 1% penicillin/streptomycin). The homogenate was filtered with a 70 µm cell strainer (Falcon #352350), centrifuged, and resuspended in complete medium. The astrocytes from two pups were pooled together and plated in 24-well plates. Astrocytes cultures were infected at DIV10 with LV-CRE-mCherry or LV-RFP as a control, and fixed with PFA 4% at DIV17 or DIV30. In all immunohistochemistry experiments, cells were cultured on glass coverslips coated with poly-lysine.

RNA isolation, RT-qPCR, and transfection. Total RNA from hippocampal or cortical cultures was extracted with TRI reagent (Sigma-Aldrich) and reverse transcribed to cDNA using the RevertAid First-Strand cDNA Synthesis kit (Fermentas). RT-qPCR was performed in an Applied Biosystems 7300 Real Time PCR unit or a QuantStudio 3 unit using Eva Green RT-PCR reagent mix and the primer pairs indicated in Supplementary Table 2. The transfections were done using Lipofectamine 2000 (Invitrogen) at DIV12 and the cultures were fixed at DIV13 for morphology analysis and rescue experiments.

ChIP-assay. H3K27ac chromatin immunoprecipitation was performed as described68. The CBP and p300 ChIP experiments required the following adjustments: minced hippocampal tissue was fixed in 1% PFA for 30 min at 37 °C (as suggested in ref. 69), which allowed for crosslinking of the KAT3 cofactors to the DNAbinding proteins and to the DNA itself. Because KAT3 proteins are almost completely degraded after a few rounds of sonication in 1% sodium dodecyl sulfate (SDS), the sonication buffer was changed to one containing 0.1% SDS, 1% IGEPAL (Sigma-Aldrich), and 0.5% sodium deoxycholate. Ten additional sonication cycles of 30″ on/30″ off were added to fragment the highly fixed DNA. ChIP-qPCR assays were performed in a QuantStudio 3 unit using the primer pairs indicated in Supplementary Table 2. **Antibodies.** The following primary antibodies have been used in this study: anti- CBP, Santa Cruz sc-583 (IHC: 1:500; ChIP: 10 µg); anti-CBP, Santa Cruz sc 369 (ICC: 1:100); anti-CBP, Santa Cruz sc-7300 (IHC: 1:100; ICC: 1:100); anti-p300,

Santa Cruz sc-585 (IHC: 1:100; ICC: 1:100; ChIP: 10 µg); anti-NeuroD2, Abcam ab109406 (ICC: 1:100); anti-H2Aac70, (IHC: 1:100); anti-H2Bac70, (IHC: 1:1000; ICC: 1:1000); anti-H3K9,14ac70, (IHC: 1:400); anti-H3K27ac, Abcam ab4729 (IHC: 1:1000; ICC: 1:1000; ChIP: 5 µg); anti-H3K27me3 07-449 Millipore (IHC: 1:100); anti-H3K9me3 ab8898 Abcam (IHC: 1:100); anti-H4ac70, (IHC: 1:100); anti-NeuN, MAB377 Millipore (IHC: 1:500; FANS: 1:500); anti-Hpca, Abcam ab24560 (IHC: 1:500; ICC: 1:500); anti-CaMKIV, BD Transduction Laboratories C28420 (IHC: 1:500); anti-Cleaved-Cas3, Cell Signalling #9661 (IHC: 1:200); anti-Fos, Synaptic Systems #226004 (IHC: 1:500); anti-mCherry/dsRed, Clontech 632496 (ICC: 1:1000); anti-GFP, Aves Labs GFP-1020 (IHC: 1:1000; ICC: 1:1000); anti-GFAP, Sigma G9269 (IHC: 1:200; ICC: 1:100); anti-H2A.Xγ, Abcam ab2893 (IHC: 1:200). Biotinylated anti-mouse (Sigma B0529, 1:500) and anti-rabbit (Sigma B8895, 1:3000) antibodies were used in the DAB staining (Sigma Cat. 11718096001). Fluorophore-coupled secondary antibodies were acquired from Invitrogen and used in a dilution 1:400.

Behavioral testing. Behavioral testing was conducted with both male and female mice. Animal's survival and well-being were monitored daily starting with the 1st day after TMX administration (Day 1) for at least 1 month (Day 30). CamKIIa- CreERT2::Crebbpf/f::Ep300f/f, CamKIIa-CreERT2::Crebbpf/f::Ep300f/+, and Cam- KIIa-CreERT2::Crebbpf/+::Ep300f/f mice were first examined in the SHIRPA test71 2 days before TMX treatment and again 3 days after the last TMX injection (Day 12). SHIRPA phenotyping categories and scoring can be found in Supplementary Table 1.

Stereotaxic surgeries and virus administration. Three-month-old Crebbpf/f::Ep300f/f mice were deeply anesthetized with a mixture of midazolam (5 mg/kg), medetomidine (1 mg/kg), and fentanyl (0.05 mg/kg) mixed in NaCl (0.9%). As soon as a total loss of reflexes was observed, the animals were positioned in a digital stereotaxic frame (Stoelting). At this point the body temperature was constantly monitored and maintained during the surgery at 37 °C using an electric blanket. Local anesthetic (EMLA 25%, lidocaine/prilocaine, AstraZeneca) was applied on the ear bars and the ophthalmologic gel (Viscotears, Bausch+Lomb) was administered on the eyes to avoid the formation of ulcers. Once the cranium was exposed, a hole was drilled in the calvaria in the location corresponding to the hippocampus. A glass capillary (Word Precision Instruments) containing the adeno-associated virus (AAV) was placed to reach the coordinates of the hippocampal hilus (−2.0, ±1.35, −1.95; in mm relative to bregma) and left in place for 5 min. 500 nl of either AAVs rAAV5-hSyn-GFP-Cre or rAAV5-hSyn-mCherry-Cre (Vector Core at the University of North Carolina at Chapel Hill) were delivered. The capillary was then left in place for another 5 min and withdrawn. After the surgery, anesthesia was reversed with subcutaneous atipamezole (0.02 mg/kg).

Buprenorphine in food pellets (1 mg/ml) was placed in the home cages to reduce post-surgery pain and mice were monitored daily until full recovery.

In vivo **electrophysiology.** Mice were deeply anesthetized with 4% isoflurane (Isoflo®, Esteve Veterinaria S.A.) in 0.8 L/min oxygen and fixed in a stereotaxic setup (Narishige Group) over a heating pad at 37 °C. Isoflurane was kept at 1–2%, 0.8 L/min oxygen to maintain the anesthesia. After checking the lack of reflexes, mice were placed and fixed in a stereotaxic frame (Narishige Group). The skin of the head was cut, and the scalp and periosteum were separated. Two 1.8mm Ø holes were made in the skull using a milling cutter (FST 18004-18, Fine ScienceTools) attached to a cordless micro drill (58610V, Stoelting Co.) in the appropriated coordinates to introduce the electrodes. Then one bipolar stimulating electrode (10–15 kΩ, 325 µm Ø, TM53CCNON, World Precision Instruments) was introduced in the perforant pathway (from bregma, in mm: −4.3 AP, +2.5 ML, +1.4 DV, 12° angle), and one recording probe (single shank, 50 µm contact spacing, 32 channels; NeuroNexus Technologies) was targeted to the hippocampus CA1 and dentate gyrus regions (from bregma, in mm: −2 AP, +1.5 ML, −2 DV). Recording and stimulating electrodes were implanted following stereotaxic standard procedures and optimized based on the online recording to have the best quality of the signal in the dentate gyrus and CA1, especially taking into account the typical evoked potential in dentate gyrus. A custom-made Ag/AgCl wire was placed in contact with the skin and used as a ground. After optimizing the final position, the tissue was allowed to rest for 30 min before acquiring electrophysiological data. The position of the electrodes was confirmed post mortem. The stimulating electrode was connected to a pulse generator and current source (STG2004, Multichannel Systems) controlled by MC_Stimulus v3.4 (Multichannel Systems). Electrophysiological data from the recording probes were filtered (0.1–3 kHz), amplified and digitalized (20 kHz sampling rate for evoked potentials and 32 kHz for spontaneous activity recordings) and analyzed off-line using the Spike2 v6(Cambridge Electronic Design Limited) or MATLAB R2016b (MathWorks) using the ICAofLFPs v1.02 package. Stimulating and recording protocols entailed spontaneous recordings (5 min) and evoked potentials, that consisted of a classical input–output (IO) stimulation protocol (stimulation intensities of 0.05, 0.1, 0.2, 0.4, 0.6, 0.8, 1, and 1.2 mA). For evaluating the excitatory post-synaptic potential the deepest slope of the evoked potential in molecular layer (dentate gyrus) was measured. To reflect the population spike (PS) the amplitude of the spike recorded in hilus was measured. Data were averaged by animal, per stimulation intensity, and then by group. Spontaneous activity signals coming from representative channels in dentate gyrus were selected to analyze the power of the frequency bands and the wavelet spectrum. Briefly, after down-sampling of spontaneous

recordings to 2.5 kHz, the signals were filtered (high pass at 0.5 Hz and notch at 50 and 100) and then analyzed to extract: (a) its power density by frequency bands; (b) the wavelet spectrum, using the Fourier transformation or the wavelet spectrum analysis, respectively, implemented in the MATLAB package ICAofLFPs. Single unit activity (SUA), as local activity reflex, was analyzed using a supervised tool integrated in Spike2 software. Briefly, after applying a band pass (0.3–3 kHz, Butterworth digital filter), the different waveforms were extracted with intensity threshold set at ±3−4 mV (to avoid noise) for all the putative SUA-spikes recorded nearby the recording electrode in the dentate gyrus or in CA1. After the complete scan of the electrophysiological signal, per area, we manually chose only those waveforms that clearly fit with the typical one reflecting neuronal activity (supervised procedure). The number of spikes was averaged by area, animal, and then by group to avoid an overestimation of the total n for the statistical comparisons.

Histology and image processing. Mice were anesthetized using a mix of xylazine (Xilagesic, CALIER) and ketamine (Imalgene, MERIAL LABORATORIOS) and perfused transcardially, first with phosphate-buffered saline (PBS, pH 7.4) to removed whole blood, then with a solution containing 4% paraformaldehyde in PBS. Brains were postfixed overnight (4% paraformaldehyde) and subsequently cut on vibratome into 50 µm sections. Sections were used for immunohistochemistry (fluorescent and diaminobenzidine) or Nissl staining65. Some antibodies used for the fluorescent immunohistochemistry required a 30min antigen retrieval in 80 °C sodium citrate buffer (10mM sodium citrate, 0.05% Tween 20, pH 6.0). Golgi–Cox impregnation was performed using the FD Rapid GolgiStain™ Kit (FD NeuroTechnologies, Inc.). To this end, animals were anesthetized using a mix of xylazine and ketamine and sacrificed through cervical dislocation. The brains were instantly removed from the skull, rinsed very briefly with double distilled water, and placed in the impregnation solution at room temperature. The solution was changed to a fresh one after the first 24 h. After 10 days the brains were immersed in solution C for 72 h, after which it was changed to a fresh solution C for further 24 h. Subsequently, the brains were cut into 100 µm sections in a 1:1 mix of PBS and solution C using a vibratome. These sections were mounted on gelatin-coated slides, revealed using solutions D and E, dehydrated using ethanol and xylene and covered using Neo-Mount® (Merck). This protocol resulted in sparsely marked neurons. Brain slices labeled using Golgi staining were visualized under a bright field microscope with a motorized stage. Dentate gyrus granule neurons with intact dendritic trees were traced and reconstructed using the Neurolucida software (MBF Bioscience). These reconstructions were used to perform a Sholl analysis where the number of intersections was calculated every 2 µm starting from 5 µm from the soma. The thickness of CA1 sub-regions was quantified

based on bright field images of Nissl stained sagittal brain slices, using the ×2.5 objective. Four lines were drawn perpendicularly to the CA1 and the thickness of stratum pyramidale and stratum radiatum were measured along these lines using Fiji-ImageJ software. For electron microscopy (EM) experiments, mice were anesthetized and perfused as indicated above with the addition of 2.5% glutaraldehyde in the fixation solution. Brains were cut in 100 µm-thick slices using a vibratome. Slices with dorsal hippocampus were postfixed with 1% osmium tetroxide for 1 h at room temperature. Dehydration was performed by incubating the slices in increasing ethanol concentrations and in pure propylene oxide. During dehydration, tissue was stained with 1% uranyl acetate in 70% ethanol. Slices were then embedded in the Epon resin between two Aclar sheets. After polymerization, Cornu Ammonis (CA1), stratum radiatum, and dentate gyrus regions fragments were cut out and stuck to an empty block of resin. Next, 75 nm sections were prepared and post stained with uranyl acetate and Reynold's lead citrate. Electron micrographs were taken with JEM 1400 transmission electron microscope at 80 kV (JEOL Ltd. 2008). Quantification of synapses and heterochromatin clumps number were performed using Fiji-ImageJ software with the Cell Counter plugin or macro based on the Analyze Particles function, respectively.

Fluorescence-activated nuclear sorting (FANS). Experimental mice were sacrificed by cervical dislocation and the hippocampal tissue was extracted from the brains. This tissue was subsequently homogenized using a Douncer tissue grinder (Kontes® 2 ml) in a buffer containing 0.5% IGEPAL and filtered on a 35 µm nylonmesh (Falcon #352235). The resulting suspension of hippocampal nuclei was stained against NeuN and DAPI. At this point three independent samples were pooled to form a single replicate that was centrifuged in Optiprep (MERCK) gradient. Nuclei purified this way were sorted using a BD FACS Aria III Flow Cytometer based on their size (FSC), complexity (SSC), and DAPI and NeuN signals. Specific gate was set up in the flow cytometer to isolate nuclei weakly immunofluorescent for NeuN in dKAT3-ifKO (but still expressing higher NeuN levels than non-neuronal cell-types) for the ATAC-seq experiments (NeuN+, Fig. 4c). Approximately 50,000 nuclei were obtained in each sample (41.5% of events in control and 46.45% in dKAT3-ifKO).

Genomic data processing and access. Adapters were trimmed using cutadapt v1.18 and aligned to mm10. Only reads longer than 25 bp, with mapq > 30 and mapping to nuclear chromosomes were used in ulterior analyses. Data was processed with custom R scripts (R version 3.5.1, 2018), Samtools v1.9, Bedtools v2.27.1, and DeepTools v3.2.0. Whole genome alignments were normalized to 10× RPM (read per 10 million sequenced reads) and visualized using IGV v2.5.0. mRNA-seq: Extraction of RNA from the hippocampal tissue was performed using TRI-reagent (MERCK)72. Total RNA was treated with DNase I

(Qiagen) and its quality was confirmed using nanodrop, Bioanalyzer and RT-qPCR assays. Three independent samples were prepared for control and dKAT3-ifKO mice. Each sample, corresponding to a single mouse, was used to prepare a polyA library and sequenced on a HiSeq 2500 sequencer (Illumina, Inc.). Reads were aligned with HISAT2 v2.1.0 to the mouse genome (mm10). Mapped reads were annotated to genes from Ensemble (GRCm38.89) and quantified using HTseq v0.11.1. Differential expression analysis was performed using DESeq2 v1.10.073. Genes with FDR < 0.05 and |log2FC| > 1 were considered significantly deregulated; the number of DEGs would be much higher if we used a lower log2FC threshold. GO terms were analyzed using GOstats v2.44.0. Tissue-specific gene expression was taken from GTEx74, selecting Brain Hippocampus, Heart-Left Ventricle, Liver, and Lung. Assay for the transposase accessible chromatin followed by high-throughput sequencing (ATAC-seq): Sorted neuronal nuclei were centrifuged and resuspended in the transposase reaction mix (TD buffer and Tn5 transposase, Illumina). The mix was placed in 37 °C for 30 min and immediately after the DNA was extracted using Qiagen MinElute PCR Purification Kit. A DNA library was then prepared using Custom Nextera PCR primers 1 and 222,75. We monitored the saturation of the library using an RT-PCR and afterwards extracted the DNA using the kit. DNA libraries were sequenced using HiSeq 2500 sequencer (Illumina, Inc.). Paired-end reads were aligned with Bowtie2 v2.3.4.2 to mm10 mouse genome. Duplicated reads were removed with Picardtools v2.18.21 (https://broadinstitute.github.io/ picard/). Only paired reads were used for posterior analysis. Peak calling was performed with MACS2 v2.1.1. Following ENCODE recommendations, to filter the most reproducible and better quality peaks, called peaks from ChIP replicates were subjected to irreproducible discovery rate (IDR) selection and only peaks with IDR < 0.15 were taken for downstream analysis. DARs analysis was performed using DiffBind v2.6.6. Regions with FDR < 0.05 and |log2FC| > 1 were considered significantly regulated. DARs were annotated to closest genes from Ensembl (GRCm38.89) using the Bioconductor package ChIPpeakAnno v3.20.1. Predictive relationship of DARs to gene expression changes was performed using BETA v1.0.723 using as reference genes from Ensembl (GRCm38.89). Motif analysis of ATAC regions was performed using MEME-suite v4.12.0. For digital footprint we used the ATAC-seq dedicated software HINT v0.12.3. ChIP-seq: Reads were aligned with Bowtie2 v2.3.4.2 to the mm10 mouse genome. Peak calling was performed with MACS2 v2.1.1. Following ENCODE recommendations, we used IDR < 0.05 to avoid false positives and retrieve the most reliable peaks. Heatmaps were performed with DeepTools v3.2.0. Circos plot was drawn with the R package Circlice v0.4.8. Differential protein binding analysis was performed using DiffBind v2.6.6. Regions with FDR < 0.05 and |log2FC| > 1 were considered significantly regulated. Annotation and analysis of ChIP peaks was performed with ChIPseeker v1.22.1 and ChIPpeakAnno v3.20.1. ChIP

peaks were annotated to the closest gene from Ensembl (GRCm38.89). Motif analysis of regions occupied by ChIP peaks was performed using MEME-suite v4.12.0. For the classification of regulatory regions categorized by genomic features, neuronal and pancellular KAT3 peaks were split according to H3K27ac enrichment and H3K4me1/H3K4me3 content (information of H3K4me1 ChIP-seq from ENCODE (ENCFF545CTN) and H3K4me3 ChIP-seq from ref. 72). Most H3K4me3-rich regions lie up to 1 kb from the TSSs corresponding to what could consider promoters of active genes, while H3K4me1-rich peaks preferentially locate into introns and intergenic regions and were labeled as enhancers. We defined as neuronal enhancers those regions that contain neuronal peaks for KAT3 binding, ATAC-seq, H3K27ac, enriched in H3K4me1 and located in introns or intergenic regions. Peaks that contain KAT3, ATAC-seq, H3K27ac, and H3K4me3 enrichment located at promoters were labeled as active promoters. To retrieve putative neuronal super-enhancers we used similar criteria than Whyte et al.25, H3K27ac regions closer than 5 kb were stitched together and tested according to the afore referred criteria. Regions containing neuronal enhancers were carried over for further analyses. Those regions longer than 5 kb (the length at which gene expression deviates from linear correlation in Fig. 5e) and associated with highly expressed genes (i.e., expression 1 order of magnitude higher than average, 100 RPKM) were labeled as neuronal super-enhancers (SEnh). The information of Neurod2 ChIP-seq was extracted from ref. 29. The Phenotype analysis wasperformed using the WEB-based application GEne SeT AnaLysis Toolkit (http:// www.webgestalt.org/). The p300 ChIP-seq data for heart (ENCSR777VNA), liver (ENCSR765RPR) and lung (ENCSR527DME) of C57BL/6 P0 mice were obtained from ENCODE (https://genome.ucsc.edu/ENCODE/downloadsMouse.html).

Single-nucleus RNA sequencing and analysis. For the single-nucleus RNA-seq experiment, dKAT3-ifKO mice were sacrificed either 2 weeks (2w) or 1 month (1m) after TMX administration. The hippocampi of each mouse were dissected in cold PBS and transferred to a Dounce homogenizer containing 1ml of ice-cold MACS buffer (0.5% bovine serum albumin (BSA), 2mM ethylenediaminetetraacetic acid, PBS 1×) and homogenized 12–15 times with the pestle. The cell suspension was transferred to a 2ml tube and centrifuged 15min at 500g and 4 °C. Cell pellet was resuspended in 2 ml of lysis buffer (10mM Tris–HCl, 10mM NaCl, 3mM MgCl2, 0,1% IGEPAL) and kept 5min on ice. Samples were then spun down at 500g for 30min in a pre-chilled centrifuge. The pellet was resuspended in PBS 1×, 1% BSA, and sorted in a BD FACS Aria III. 15,000 nuclei per sample (pool of 2 animals) were loaded into the single cell A Chip and then the generation of barcode-containing partitions was carried out with the Chromium Controller (10X Genomics). Chromium Single Cell 3′ Library & Gel Bead Kit v2 was employed for post-GEM-RT clean-up, cDNA amplification

and the generation of barcoded (ChromiumTM i7 Multiplex Kit) libraries. Libraries were sequenced to an average depth of 290–310 million reads per sample on an Illumina HiSeq 2500 sequencer. Quality control of sequenced reads was performed using FastQC v0.11.9. Sequenced samples were processed using the Cell Ranger v2.2.0 pipeline (10X Genomics) and aligned to the CRGm38 (mm10) mouse reference genome customized to count reads in exons and introns (pre-mRNA) (gene annotation version 94). We retrieved 1791 (control), 1133 (dKAT3-ifKO 2w), and 1465 (dKAT3-ifKO 1m) high quality nuclei per sample. Mean reads per nucleus were 172,879 (control), 271,535 (dKAT3-ifKO 2w), and 197,840 (dKAT3-ifKO 1m). Singlen ucleus RNA-seq data were subsequently pre-processed and further analyzed in R using Seurat v2.3.4. Filtering parameters were as follows: genes, nCell <5; cells, nGene <200. Data were then normalized using global-scaling normalization (method: LogNormalize, scale.factor=10.000). To identify major cell populations in the dorsal hippocampus of adult mice, control and dKAT3-ifKO datasets were analyzed separately. Highly variable genes (HVGs) were detected using FindVariableGenes function with default parameters. Then, normalized counts on HVGs were scaled and centered using ScaleData function with default parameters. Principal component analysis (PCA) was performed over the first ranked 1000 HVGs, and cluster detection was carried out with Louvain algorithm using 20 first PCA dimensions at resolution=0.6 (the default and the optimal according to cell number, data dispersion, and coexpression of previously reported cell markers). Visualization and embedding were performed using tSNE and UMAP over PCA using the 20 first PCA dimensions. UMAP plots of gene expression show normalized count (UMIs) per nucleus. The equalized expression between fixed percentiles was plotted according to the following criteria: the minimum expression was adjusted to 25% and the maximum expression was adjusted to 95% in all expression plots. For longitudinal analysis, datasets from the 3 conditions were merged and HVGs were identified for each dataset as indicated above. Only HVGs that were detected in all datasets were used to perform the visualization and embedding. Clustering was performed on merged dataset from 3 conditions and populations were identified combining these results with clustering information obtained in control and dKAT3-ifKO-1m datasets separately, together with co-expression of population markers. Differential expression analysis (DEA) was used to identify population gene markers. For DEA, the nuclei of each population were contrasted against all the other nuclei in the merged dataset using Wilcoxon Rank Sum test on normalized counts. Trajectory analysis was performed in unbiased manner using Monocle 2 (v.2.8.0)21. First, we selected from Seurat merged dataset those clusters containing principal excitatory neurons and transformed this subset to a Monocle object. The following population clusters were present in the Monocle

object: Granule cell, CA3 pyr. neuron, CA1 pyr. neuron A, CA1 pyr. neuron B, Former CApyr. neuron, and Former granule cell. We then filtered those genes whose expression was detected in less than 10 cells per cluster. 13,935 genes were retained after this filtering step. Next, the size factor and dispersion of the subset was estimated, and data was normalized and preprocessed. Genes under the minimum level detection threshold of 0.1 (average expression level) were further removed leaving 2406 genes to perform discriminative dimensionality reduction with trees (DDRTree). DDRTree was applied inside the function reduce Dimension, with default parameters: norm_method ="log", pseudo_expr=1, relative_ expr=TRUE, auto_param_selection=TRUE (automatically calculate the proper value for the n center (number of centroids)) and scaling=TRUE (scale each gene before running trajectory reconstruction). Prior the dimensional reduction, the function reduce Dimension also performed a variance stabilization of the data (because the expression Family of the data was neg binomial. size). Finally, the cells were ordered according to pseudo-time with the function order Cells, which added a pseudo-time value and state for each cell.

Statistical analysis. All the statistics in the following work have been done using RStudio v3.5.1, GraphPad Prism v8.0.1, and MATLAB R2016b, depending on the experiment. Statistical tests used in the study are indicated in the figure legend. All statistical tests used in this study were two-sided, except for the Hypergeometric test. For a comparison of two groups, each group was first tested for the normality using Shapiro–Wilks test. If normality assumption was not violated, a t-test was performed. If the normality null hypothesis was rejected, Mann–Whitney U test was performed. In the analysis of the SHIRPA paradigm, Fisher exact test was used for the categories carrying just two possible outcomes (indicated in Supplementary Table 1). For multiple testing of the same sample, p-values were corrected using Bonferroni method. For two factor comparisons, two-way ANOVA was used. In all bar plots, the height represents the mean and the error bars the standard error of mean (SEM).

Reporting summary. Further information on research design is available in

the Nature Research Reporting Summary linked to this article.

Data availability

The genomic data sets generated in this study can be accessed at the GEO public repository using the accession number GSE133018. We used the following publicly available webtools: GEne SeT AnaLysis Toolkit (http://www.webgestalt.org/) and MEME-suite (MEME-suite.org/). The p300 ChIP-seq data for heart (ENCSR777VNA),liver (ENCSR765RPR), and lung (ENCSR527DME) of C57BL/6 P0 mice were obtained from ENCODE (https://genome.ucsc.edu/ENCODE/downloadsMouse.html).

References

1. Hobert, O. Regulation of terminal differentiation programs in the nervous system. Annu. Rev. Cell Dev. Biol. 27, 681–696 (2011).
2. Vierbuchen, T. et al. Direct conversion of fibroblasts to functional neurons by defined factors. Nature 463, 1035–1041 (2010).
3. O'Meara, M. M., Zhang, F. & Hobert, O. Maintenance of neuronal laterality in Caenorhabditis elegans through MYST histone acetyltransferase complex components LSY-12, LSY-13 and LIN-49. Genetics 186, 1497–1502 (2010).
4. Deneris, E. S. & Hobert, O. Maintenance of postmitotic neuronal cell identity. Nat. Neurosci. 17, 899–907 (2014).
5. Gallegos, D. A., Chan, U., Chen, L. F. & West, A. E. Chromatin regulation of neuronal maturation and plasticity. Trends Neurosci. 41, 311–324 (2018).
6. Becker, J. S. et al. Genomic and proteomic resolution of heterochromatin and its restriction of alternate fate genes. Mol. Cell 68, 1023–1037 (2017).
7. Allis, C. D. et al. New nomenclature for chromatin-modifying enzymes. Cell 131, 633–636 (2007).
8. Dancy, B. M. & Cole, P. A. Protein lysine acetylation by p300/CBP. Chem. Rev. 115, 2419–2452 (2015).
9. Weinert, B. T. et al. Time-resolved analysis reveals rapid dynamics and broad scope of the CBP/p300 acetylome. Cell 174, 231–244 (2018).
10. Lipinski, M., Del Blanco, B. & Barco, A. CBP/p300 in brain development and plasticity: disentangling the KAT's cradle. Curr. Opin. Neurobiol. 59, 1–8 (2019).
11. Yao, T. P. et al. Gene dosage-dependent embryonic development and proliferation defects in mice lacking the transcriptional integrator p300. Cell 93, 361–372 (1998).
12. Lopez-Atalaya, J. P., Valor, L. M. & Barco, A. Epigenetic factors in intellectual disability: the Rubinstein–Taybi syndrome as a paradigm of neurodevelopmental disorder with epigenetic origin. Prog. Mol. Biol. Transl. Sci. 128, 139–176 (2014).
13. Chen, G., Zou, X., Watanabe, H., van Deursen, J. M. & Shen, J. CREB binding protein is required for both short-term and long-term memory formation. J. Neurosci. 30, 13066–13077 (2010).
14. Valor, L. M. et al. Ablation of CBP in forebrain principal neurons causes modest memory and transcriptional defects and a dramatic reduction of histone acetylation, but does not affect cell viability. J. Neurosci. 31, 1652–1663 (2011).
15. Barrett, R. M. et al. Hippocampal focal knockout of CBP affects specific histone modifications, long-term potentiation, and long-term memory. Neuropsychopharmacology 36, 1545–1556 (2011).
16. Oliveira, A. M. et al. Subregion-specific p300 conditional knock-out mice exhibit long-term memory impairments. Learn. Mem. 18, 161–169 (2011).
17. Erdmann, G., Schutz, G. & Berger, S. Inducible gene inactivation in neurons of the adult mouse forebrain. BMC Neurosci. 8, 63 (2007).
18. Zeisel, A. et al. Brain structure. Cell types in the mouse cortex and hippocampus revealed by single-cell RNA-seq. Science 347, 1138–1142 (2015).
19. Ramalho-Santos, M., Yoon, S., Matsuzaki, Y., Mulligan, R. C. & Melton, D. A. "Stemness": transcriptional profiling of embryonic and adult stem cells. Science 298, 597–600 (2002).
20. Habib, N. et al. Div-Seq: single-nucleus RNA-Seq reveals dynamics of rare adult newborn neurons. Science 353, 925–928 (2016).
21. Qiu, X. et al. Reversed graph embedding resolves complex single-cell trajectories. Nat. Methods 14, 979–982 (2017).
22. Fernandez-Albert, J. et al. Immediate and deferred epigenomic signatures of in vivo neuronal activation in mouse hippocampus. Nat. Neurosci. 22, 1718–1730 (2019).
23. Wang, S. et al. Target analysis by integration of transcriptome and ChIP-seq data with BETA. Nat. Protoc. 8, 2502–2515 (2013).
24. Nord, A. S., Pattabiraman, K., Visel, A. & Rubenstein, J. L. R. Genomic perspectives of transcriptional regulation in forebrain development. Neuron85, 27–47 (2015).
25. Whyte, W. A. et al. Master transcription factors and mediator establish superenhancers at key cell identity genes. Cell 153, 307–319 (2013).
26. Ohtsuka, T. et al. Gene expression profiling of neural stem cells and identification of regulators of neural differentiation during cortical development. Stem Cells 29, 1817–1828 (2011).
27. Bertrand, N., Castro, D. S. & Guillemot, F. Proneural genes and the specification of neural cell types. Nat. Rev. Neurosci. 3, 517–530 (2002).
28. Toda, T. & Gage, F. H. Review: adult neurogenesis contributes to hippocampal plasticity. Cell Tissue Res. 373, 693–709 (2018).
29. Bayam, E. et al. Genome-wide target analysis of NEUROD2 provides new insights into regulation of cortical projection neuron migration and differentiation. BMC Genomics 16, 681 (2015).
30. Gomez, R. A., Pentz, E. S., Jin, X., Cordaillat, M. & Sequeira Lopez, M. L. CBP and p300 are essential for renin cell identity and morphological integrity of the kidney. Am. J. Physiol. Heart Circ. Physiol. 296, H1255–H1262 (2009).
31. Hennig, A. K., Peng, G. H. & Chen, S. Transcription coactivators p300 and CBP are necessary for

photoreceptor-specific chromatin organization and gene expression. PLoS ONE 8, e69721 (2013).
32. Pentz, E. S. et al. Histone acetyl transferases CBP and p300 are necessary for maintenance of renin cell identity and transformation of smooth muscle cells to the renin phenotype. Am. J. Physiol. Heart Circ. Physiol. 302, H2545–H2552 (2012).
33. Fang, F. et al. Coactivators p300 and CBP maintain the identity of mouse embryonic stem cells by mediating long-range chromatin structure. Stem Cells 32, 1805–1816 (2014).
34. Tremblay, M., Sanchez-Ferras, O. & Bouchard, M. GATA transcription factors in development and disease. Development 145, dev164384 (2018).
35. Murata, T. et al. Defect of histone acetyltransferase activity of the nuclear transcriptional coactivator CBP in Rubinstein-Taybi syndrome. Hum. Mol. Genet. 10, 1071–1076 (2001).
36. Hilton, I. B. et al. Epigenome editing by a CRISPR-Cas9-based acetyltransferase activates genes from promoters and enhancers. Nat. Biotechnol. 33, 510–517 (2015).
37. Lee, S., Lee, B., Lee, J. W. & Lee, S. K. Retinoid signaling and neurogenin2 function are coupled for the specification of spinal motor neurons through a chromatin modifier CBP. Neuron 62, 641–654 (2009).
38. Merk, D. J. et al. Opposing effects of CREBBP mutations govern the phenotype of Rubinstein–Taybi syndrome and adult SHH medulloblastoma. Dev. Cell 44, 709–724 (2018).
39. Medrano-Fernandez, A. et al. The epigenetic factor CBP is required for the differentiation and function of medial ganglionic eminence-derived interneurons. Mol. Neurobiol. 56, 4440–4454 (2019).
40. Del Blanco, B. et al. CBP and SRF co-regulate dendritic growth and synaptic maturation. Cell Death Differ. 26, 2208–2222 (2019).
41. Wang, J. et al. CBP histone acetyltransferase activity regulates embryonic neural differentiation in the normal and Rubinstein–Taybi syndrome brain. Dev. Cell 18, 114–125 (2010).
42. Ebrahimi, A. et al. Bromodomain inhibition of the coactivators CBP/EP300 facilitate cellular reprogramming. Nat. Chem. Biol. 15, 519–528 (2019).
43. Towers, E. et al. The proapoptotic dp5 gene is a direct target of the MLK-JNKc- Jun pathway in sympathetic neurons. Nucleic Acids Res. 37, 3044–3060 (2009).
44. Ma, C. et al. dp5/HRK is a c-Jun target gene and required for apoptosis induced by potassium deprivation in cerebellar granule neurons. J. Biol. Chem. 282, 30901–30909 (2007).
45. Ravens, S., Yu, C., Ye, T., Stierle, M. & Tora, L. Tip60 complex binds to active Pol II promoters and a subset of enhancers and co-regulates the c-Myc network in mouse embryonic stem cells. Epigenet. Chromatin 8, 45 (2015).
46. Sheikh, B. N. & Akhtar, A. The many lives of KATs—detectors, integrators and modulators of the cellular environment. Nat. Rev. Genet. 20, 7–23 (2019).
47. Urban, I. et al. TIP60/KAT5 is required for neuronal viability in hippocampal CA1. Sci. Rep. 9, 16173 (2019).
48. Dennis, D. J., Han, S. & Schuurmans, C. bHLH transcription factors in neural development, disease, and reprogramming. Brain Res. 1705, 48–65 (2019).
49. Bormuth, I. et al. Neuronal basic helix-loop-helix proteins Neurod2/6 regulate cortical commissure formation before midline interactions. J. Neurosci. 33, 641–651 (2013).
50. Puri, P. L. et al. Differential roles of p300 and PCAF acetyltransferases in muscle differentiation. Mol. Cell 1, 35–45 (1997).
51. Vojtek, A. B. et al. Akt regulates basic helix–loop–helix transcription factor–coactivator complex formation and activity during neuronal differentiation. Mol. Cell. Biol. 23, 4417–4427 (2003).
52. Sun, Y. et al. Neurogenin promotes neurogenesis and inhibits glial differentiation by independent mechanisms. Cell 104, 365–376 (2001).
53. Hamamori, Y. et al. Regulation of histone acetyltransferases p300 and PCAF by the bHLH protein twist and adenoviral oncoprotein E1A. Cell 96, 405–413 (1999).
54. Mutoh, H., Naya, F. J., Tsai, M. J. & Leiter, A. B. The basic helix–loop–helix protein BETA2 interacts with p300 to coordinate differentiation of secretin expressing enteroendocrine cells. Genes Dev. 12, 820–830 (1998).
55. Ortega, E. et al. Transcription factor dimerization activates the p300 acetyltransferase. Nature 562, 538–544 (2018).
56. Olson, J. M. et al. NeuroD2 is necessary for development and survival of central nervous system neurons. Dev. Biol. 234, 174–187 (2001).
57. van Tienen, L. M., Mieszczanek, J., Fiedler, M., Rutherford, T. J. & Bienz, M. Constitutive scaffolding of multiple Wnt enhanceosome components by Legless/BCL9. eLife 6, e20882 (2017).
58. Valor, L. M., Viosca, J., Lopez-Atalaya, J. P. & Barco, A. Lysine acetyltransferases CBP and p300 as therapeutic targets in cognitive and neurodegenerative disorders. Curr. Pharm. Des. 19, 5051–5064 (2013).
59. Francelle, L., Lotz, C., Outeiro, T., Brouillet, E. & Merienne, K. Contribution of neuroepigenetics to Huntington's disease. Front. Hum. Neurosci. 11, 17 (2017).
60. Svensson, K. et al. p300 and cAMP response element-binding protein-binding protein in skeletal muscle homeostasis, contractile function, and survival. J. Cachexia Sarcopenia Muscle 11, 464–477 (2020).
61. Giles, R. H., Dauwerse, H. G., van Ommen, G. J. & Breuning, M. H. Do human chromosomal bands 16p13 and 22q11-13 share ancestral origins? Am. J. Hum. Genet. 63, 1240–1242 (1998).
62. Roth, J. F. et al. Differential role of p300 and CBP acetyltransferase during myogenesis: p300 acts upstream of MyoD and Myf5. EMBO J. 22, 5186–5196 (2003).

63. Kasper, L. H. et al. Conditional knockout mice reveal distinct functions for the global transcriptional coactivators CBP and p300 in T-cell development. Mol. Cell. Biol. 26, 789–809 (2006).
64. Zhang, Z., Hofmann, C., Casanova, E., Schutz, G. & Lutz, B. Generation of a conditional allele of the CBP gene in mouse. Genesis 40, 82–89 (2004).
65. Fiorenza, A. et al. Blocking miRNA biogenesis in adult forebrain neurons enhances seizure susceptibility, fear memory, and food intake by increasing neuronal responsiveness. Cereb. Cortex 26, 1619–1633 (2016).
66. Scandaglia, M. et al. Fine-tuned SRF activity controls asymmetrical neuronal outgrowth: implications for cortical migration, neural tissue lamination and circuit assembly. Sci. Rep. 5, 17470 (2015).
67. Gascon, S., Paez-Gomez, J. A., Diaz-Guerra, M., Scheiffele, P. & Scholl, F. G. Dual-promoter lentiviral vectors for constitutive and regulated gene expression in neurons. J. Neurosci. Methods 168, 104–112 (2008).
68. Galvao-Ferreira, P., Lipinski, M., Santos, F., Barco, A. & Costa, R. M. Skill learning modulates RNA Pol II poising at immediate early genes in the adult striatum. eNeuro 4, https://doi.org/10.1523/ENEURO.0074-17.2017 (2017).
69. Gasper, W. C. et al. Fully automated high-throughput chromatin immunoprecipitation for ChIP-seq: identifying ChIP-quality p300 monoclonal antibodies. Sci. Rep. 4, 5152 (2014).
70. Lopez-Atalaya, J. P., Ito, S., Valor, L. M., Benito, E. & Barco, A. Genomic targets, and histone acetylation and gene expression profiling of neural HDAC inhibition. Nucleic Acids Res. 41, 8072–8084 (2013).
71. Viosca, J., Schuhmacher, A. J., Guerra, C. & Barco, A. Germline expression of H-Ras(G12V) causes neurological deficits associated to Costello syndrome. Genes Brain Behav. 8, 60–71 (2009).
72. Scandaglia, M. et al. Loss of Kdm5c causes spurious transcription and prevents the fine-tuning of activity-regulated enhancers in neurons. Cell Rep. 21, 47–59 (2017).
73. Love, M. I., Huber, W. & Anders, S. Moderated estimation of fold change and dispersion for RNA-seq data with DESeq2. Genome Biol. 15, 550 (2014).
74. Gamazon, E. R. et al. Using an atlas of gene regulation across 44 human tissues to inform complex disease- and trait-associated variation. Nat. Genet. 50, 956–967 (2018).
75. Buenrostro, J. D., Giresi, P. G., Zaba, L. C., Chang, H. Y. & Greenleaf, W. J. Transposition of native chromatin for fast and sensitive epigenomic profiling of open chromatin, DNA-binding proteins and nucleosome position. Nat. Methods 10, 1213–1218 (2013).
76. Eisenberg, E. & Levanon, E. Y. Human housekeeping genes, revisited. Trends Genet. 29, 569–574 (2013).

Acknowledgements

The authors thank P. Arlotta, O. Hobert, N. Flames, E. Herrera, M.A. Nieto, A. Rada-Iglesias, and J.V. Sanchez-Mut for critical reading of the manuscript. The authors thank A. Caler, N. Cascales-Picó, M. Llinares, A. Medrano-Fernández, and S. Rivero for their assistance in specific experiments and V. Makarov for the ICAofLFPs MatLab package. M.L. is recipient of a Santiago Grisolia fellowship given by the Generalitat Valenciana, J. M.C. is recipient of a fellowship from the Spanish Ministry of Education, Culture and Sport (MECD), J.F.-A. and C.M.N. are recipients of fellowships from the Spanish Ministry of Science and Innovation (MICINN). The ultrastructure research was supported by the Polish National Science Center Grant UMO-2014/15/N/NZ3/04468 and by the European Regional Development Fund POIG 01.01.02-00-008/08. J.P.L.-A. research is supported by Grants RYC-2015-18056 and RTI2018-102260-B-I00 from MICINN cofinanced by ERDF. A.B. research is supported by Grants SAF2017-87928-R, PCIN-2015- 192-C02-01, and SEV-2017-0723 from MICINN co-financed by ERDF, PROMETEO/ 2016/026 from the Generalitat Valenciana, and RGP0039/2017 from the Human Frontiers Science Program Organization (HFSPO). The Instituto de Neurociencias is a “Centre of Excellence Severo Ochoa”.

Author contributions

Conceptualization: M.L., R.M.-V., B.d.B., and A.B. Methodology: M.L., B.d.B., J.F.-A., C. M.N., R.O., A.A.S., and J.M.C. Software: R.M.-V. and A.M.-G. Investigation: M.L., B.d.B., and J.M.-R. Data Curation and Visualization: R.M. V., A.M.-G., and M.L. Writing— Original Draft: A.B. and M.L. Supervision: A.B., J.P.L.-A., S.C., and G.M.W. Funding Acquisition: A.B.

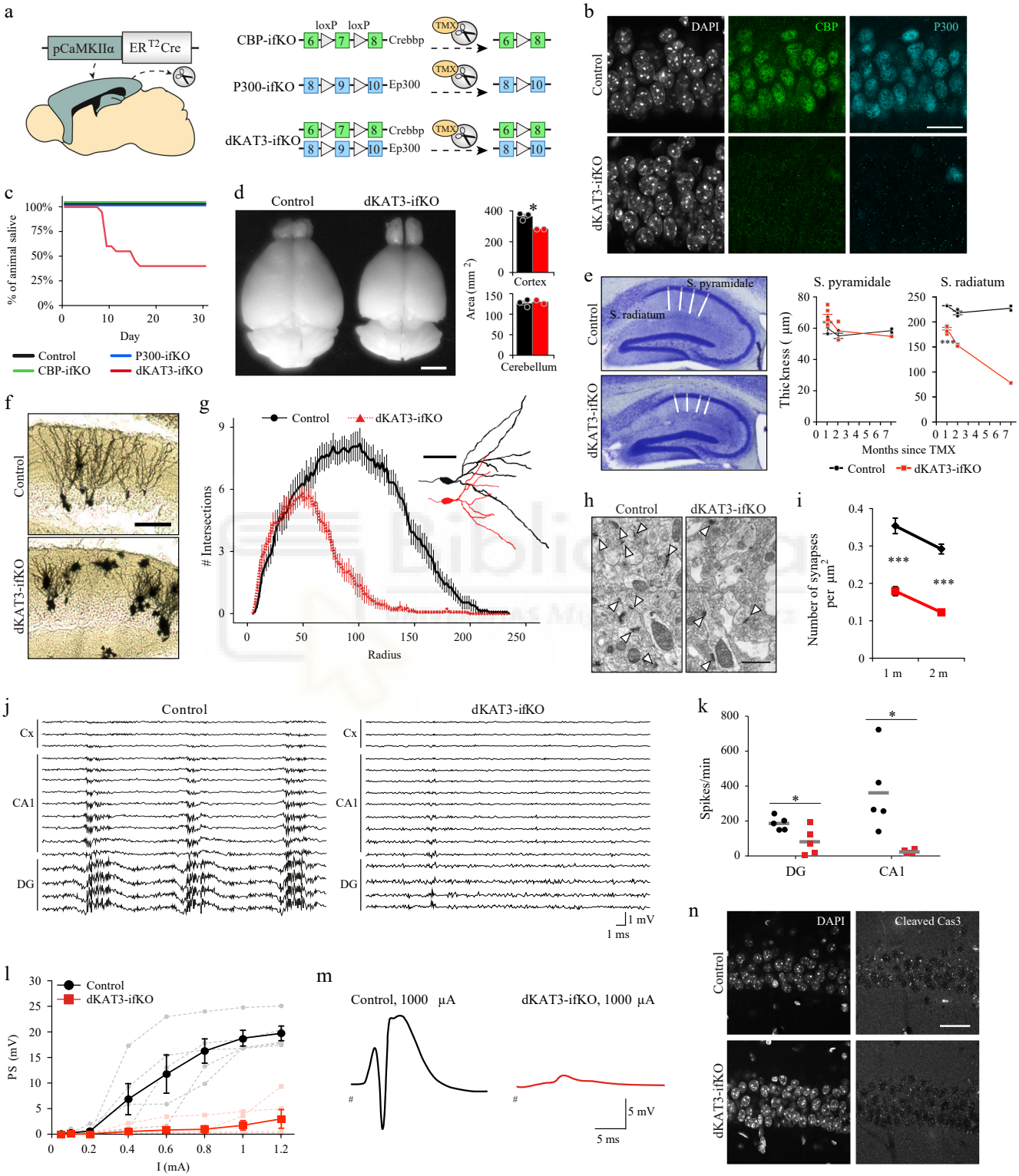
a
pCaMKIIα
ER T2 Cre
CBP-ifKO
P300-ifKO
dKAT3-ifKO
loxP
Crebbp
Ep300
TMX
b
DAPI
CBP
P300
Control
dKAT3-ifKO
c
% of animal salive
Day
Control
CBP-ifKO
P300-ifKO
dKAT3-ifKO
d
Control
dKAT3-ifKO
Area (mm 2)
Cortex
Cerebellum
e
S. pyramidale
S. radiatum
Thickness (µm)
Months since TMX
f
g
Intersections
Radius
h
i
Number of synapses per µm2
1 m
2 m
j
Cx
CA1
DG
1 mV
1 ms
k
Spikes/min
l
PS (mV)
I (mA)
m
Control, 1000 µA
dKAT3-ifKO, 1000 µA
5 mV
5 ms
n
Cleaved Cas3

Fig. 1 Loss of both KAT3 proteins causes severe neurological alterations. a Genetic strategy for the production of inducible, forebrain-specific CBP, p300, and double KAT3 knockouts. b Double immunostaining against CBP and p300 in the CA1 region. The analysis was performed twice with different sets of animals. Scale: 10 µm. c Survival of the three ifKO lines after TMX administration (control, n = 14; dKAT3-ifKO, n = 20). d Left: representative images of control and dKAT3-ifKO brains 2 months after TMX. Scale: 5 mm. Right: quantification of cortical and cerebellar sizes (control, black bars, n= 3; dKAT3- ifKO, red bars, n= 2). Two-tailed t-test: *p-value=0.024. e Left: Nissl staining of hippocampi 2 months after TMX. Right: quantification of the thickness of the strata pyramidale and radiatum of control (1 m, n = 3; 2m, n = 3; 7m, n = 2) and dKAT3-ifKO mice (1 m, n = 6; 2m, n = 2; 7m, n= 1) at different time points after TMX. Points show separate observations. Two-way ANOVA; st. radiatum: ***p-valgenot =1.09e−09, p-valtime =2.26e−05, **p-valgenot:time= 0.006; st.pyramidale: *p-valgenot = 0.036. Post-hoc Tukey HSD comparison st. radiatum 1 month control—1 month dKAT3-ifKO; ***p-value= 1.7e–06. F Representative images of Golgi staining in the dentate gyrus 1 month after TMX (n =4). Scale: 100 µm. g Sholl analysis of DG neurons 1 month after TMX (32 neurons from 4 control mice; 38 neurons from 4 dKAT3-ifKOs). The right inset shows representative Neurolucida-reconstructed neurons. Scale: 50 µm. H Electron microscopy images showing the stratum radiatum 1 month after TMX. Arrowheads indicate positions of the synapses (n = 3). Scale: 1 µm. i Number of synapses per µm2 in the stratum radiatum (average of 30 areas from 3 mice per condition). Two-tailed t-test; ***p-val1 month < 0.0001; **p-val2 months < 0.001. j Representative in vivo electrophysiological recordings of spontaneous activity across cortical and hippocampal layers. k Firing frequency (spikes per minute) recorded in CA1 and DG. SUA: single unit analysis (n = 5). Gray lines represent the mean values. Two-tailed t-test: *p-valCA1 = 0.022, p-valDG = 0.028. l Population spike (PS) amplitude in DG after the application of increasing intensities in the perforant pathway (n = 5). Lighter-colored elements show the results for each animal separately. Two-tailed t-test. m Representative evoked potentials waveforms (PS) to 1 mA stimulation. n Immunohistochemistry for cleaved Cas3 shows no sign of apoptosis in the CA1 subfield 1 month after TMX. The analysis was performed twice with different sets of animals. Scale: 30 µm. In panels (d), (e), (g), (i), and (l), data are presented as mean values ± SEM. Source data for graphs in panels (c), (d), (e), (g), (l), (k), and (l) are provided as a Source data file.

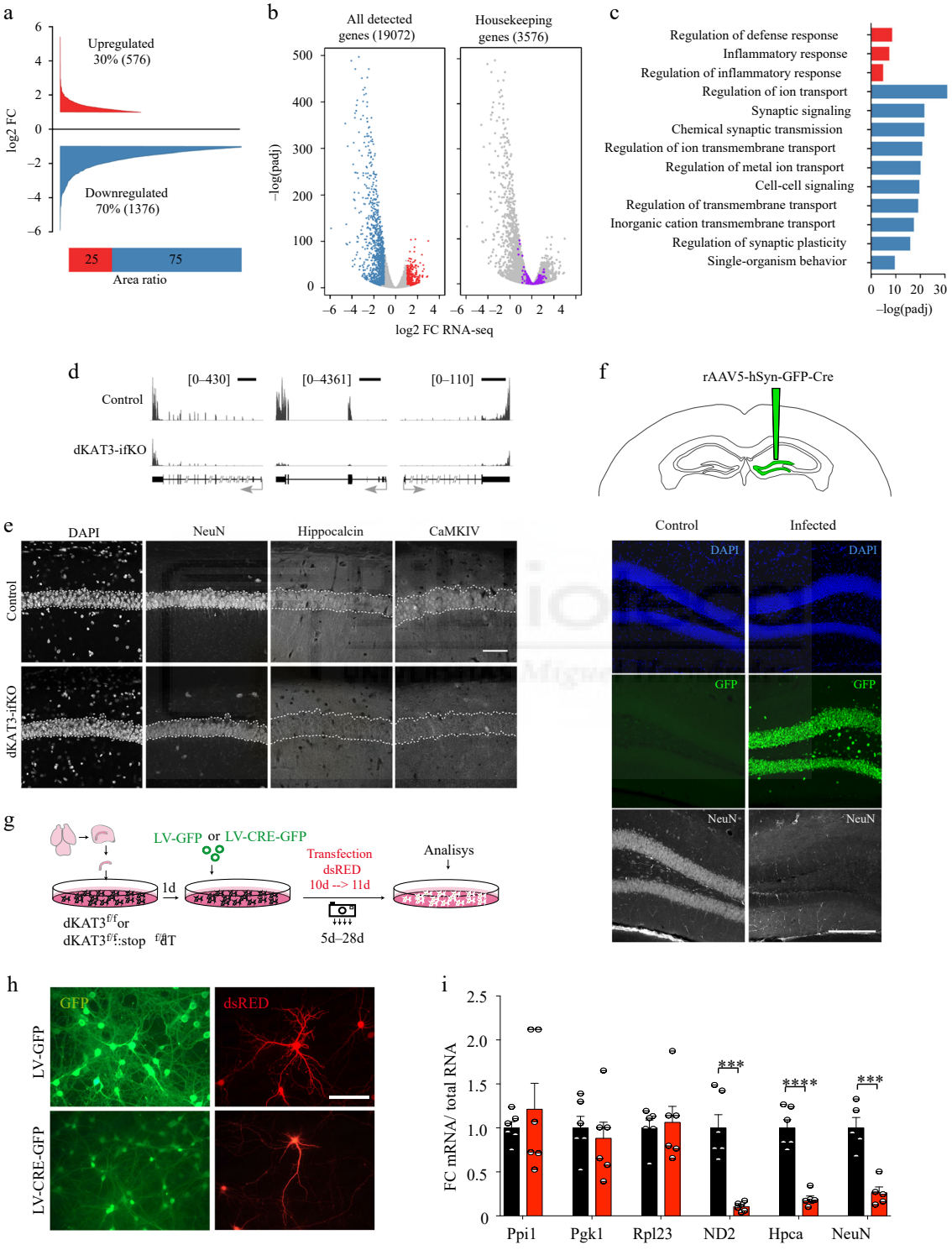
a
Upregulated
30% (576)
Downregulated
70% (1376)
log2 FC
25
75
Area ratio
b
All detected
genes (19072)
Housekeeping
genes (3576)
–log(padj)
log2 FC RNA-seq
c
Regulation of defense response
Inflammatory response
Regulation of inflammatory response
Regulation of ion transport
Synaptic signaling
Chemical synaptic transmission
Regulation of ion transmembrane transport
Regulation of metal ion transport
Cell-cell signaling
Regulation of transmembrane transport
Inorganic cation transmembrane transport
Regulation of synaptic plasticity
Single-organism behavior
–log(padj)
d
Control
dKAT3-ifKO
[0–430]
[0–4361]
[0–110]
e
DAPI
NeuN
Hippocalcin
CaMKIV
Control
dKAT3-ifKO
f
rAAV5-hSyn-GFP-Cre
Control
Infected
DAPI
GFP
NeuN
g
LV-GFP or LV-CRE-GFP
1d
Transfection
dsRED
10d --> 11d
Analisys
5d–28d
h
LV-GFP
LV-CRE-GFP
GFP
dsRED
i
FC mRNA/ total RNA
Ppi1
Pgk1
Rpl23
ND2
Hpca
NeuN
***
****
***

Fig. 2 Hippocampal cells lacking KAT3 fail to express neuronal-specific genes. a Cumulative graph showing the log2 fold-change value of DEGs in dKAT3 ifKOs (mRNA-seq, 1 month after TMX, n = 3 per genotype). Upregulated genes are presented in red and downregulated genes in blue (p.adj < 0.05 and |log2FC| ≥ 1). The bottom bar graph compares the area in each set. b Volcano plots of RNA-seq analysis. From left to right, we present all genes (left) and the subset of housekeeping genes listed in ref. 76 (right). Gray: genes that are not significantly deregulated; red: upregulated genes; blue: downregulated genes; purple: housekeeping genes. c The 10 most enriched categories identified by Gene Ontology (GO) analysis on up- (red) and downregulated (blue) genes with a p.adj < 0.05 and |log2FC| ≥ 1. The upregulated gene set only retrieved three categories. d RNA-seq profiles for three representative neuronal-specific genes: Rbfox3 (NeuN), Hpca, and Camk4. Scale: 2 kb. e Immunohistochemistry against the neuronal protein encoded by Camk4, Rbfox3 (NeuN), and Hpca. Dashed line labels the position of the stratum pyramidale based on DAPI images (n = 3). Scale: 60 µm. f Loss of NeuN immunoreactivity in DG neurons infected with a cre recombinase-expressing AAV (GFP+). The experiment was performed 3 times with different sets of mice. The virus was injected unilaterally into the DG of adult Crebbpf/f::Ep300f/f mice and the mice were perfused 1 month later (Supplementary Fig. 3e). See Supplementary Fig. 3f for immunostaining against CBP in the same brain slide. Scale: 200 µm. g Scheme representing the strategy to eliminate both KAT3 proteins in hippocampal PNCs from E17 dKAT3f/f embryos. h Representative images showing morphological changes in Crebbpf/f::Ep300f/f hippocampal neurons infected with LV-CRE compared with LV-GFP control (n =6 in both groups). i RT-PCR demonstrates decreased levels of Neurod2 (ND2), Hpca (hippocalcin), and Rbfox3 (NeuN) transcripts in dKAT3-KO PNCs. In contrast, several housekeeping genes (Ppl1, Pgk1, Rpl23) are unaffected (n = 5–6 in both groups). Data are presented as mean values ± SEM. Two-tailed t-test: ****p < 0.0001, ***p < 0.001, **p < 0.01. Source data for graphs in panel (i) are provided as a Source data file.

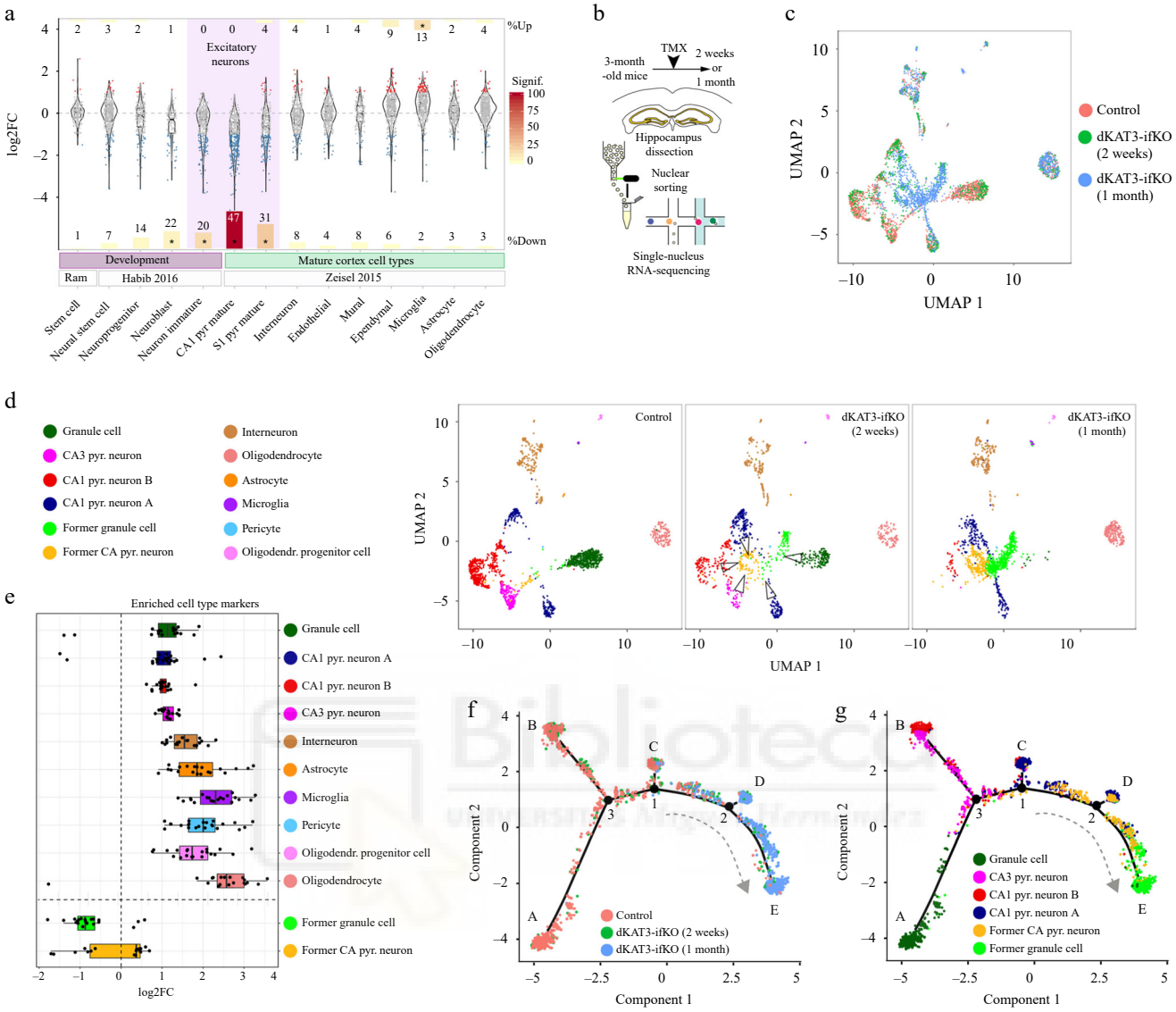

Fig. 3 Cells lacking KAT3 proteins do not die or dedifferentiate, but acquire a novel, molecularly undefined fate. a Violin plots show the change in expression of gene sets associated with stemness19 and different neuronal differentiation stages20 during development (purple bar) or with different cell types in the adult mouse cortex18 (green bar). Each dot represents a single gene. Number of genes tested per cell type: stem cell = 195, neural stem cell = 365, neuroprogenitor = 200, neuroblast = 109, immature neuron = 353, CA1_pyr mature =371, S1_pyr mature = 251, interneuron = 337, endothelial= 337, mural= 141, ependymal = 420, microglia= 387, astrocyte = 223, oligodendrocyte = 418. Bar sizes are proportional to the percentage of up- or downregulated genes in each gene set as indicated by the number in each bar. Bar colors indicate the significance of the enrichment (−log10) in a hypergeometric test for the number of regulated genes. Enrichments with p-values < 5e–10 are labelled with an asterisk (p-valInmature_neuron= 4.82e–17; p-valCA1_Pyramidal= 2.59e–101; p-valS1_Pyramidal =4.69e–25; p-valMicroglia = 3.49e–15). B Scheme of the single-nucleus RNA-seq experiment. c UMAP plot of integrated analysis of snRNA-seq datasets from the dorsal hippocampus of dKAT3-fKOs and control littermates. d UMAP plots showing identified populations in the hippocampus of control littermates (left) and dKAT3-ifKO mice 2 (center) and 4 (right) weeks after TMX treatment. Nuclei are colored by their classification label as indicated. e Boxplots showing the expression of the top 20 markers for the 10 cell types detected in the hippocampus of control mice and the two new clusters detected in dKAT3-ifKO mice 1 month after TMX (Supplementary Data 2). Whiskers lengths are 1.5 the interquartile range from the box. Abbreviations: Pyr, pyramidal; Oligodendr, oligodendrocyte. f, g Single-nucleus trajectory analysis of hippocampal excitatory neurons reveals cell state-transitions toward a non-functional interstate deadlock. Nuclei are colored by experimental condition (f) or cluster subpopulation (g) as indicated in the legends. Loss of dKAT3s caused the progressive relocation of the cells from the root in the branches A, B, and C (expressing markers for different types of excitatory neurons) towards the outcome in branches D and E that are populated by the type of cells described in (e) that do not express distinctive markers. Source data for graphs in panels (a) and (e) are provided as a Source data file.

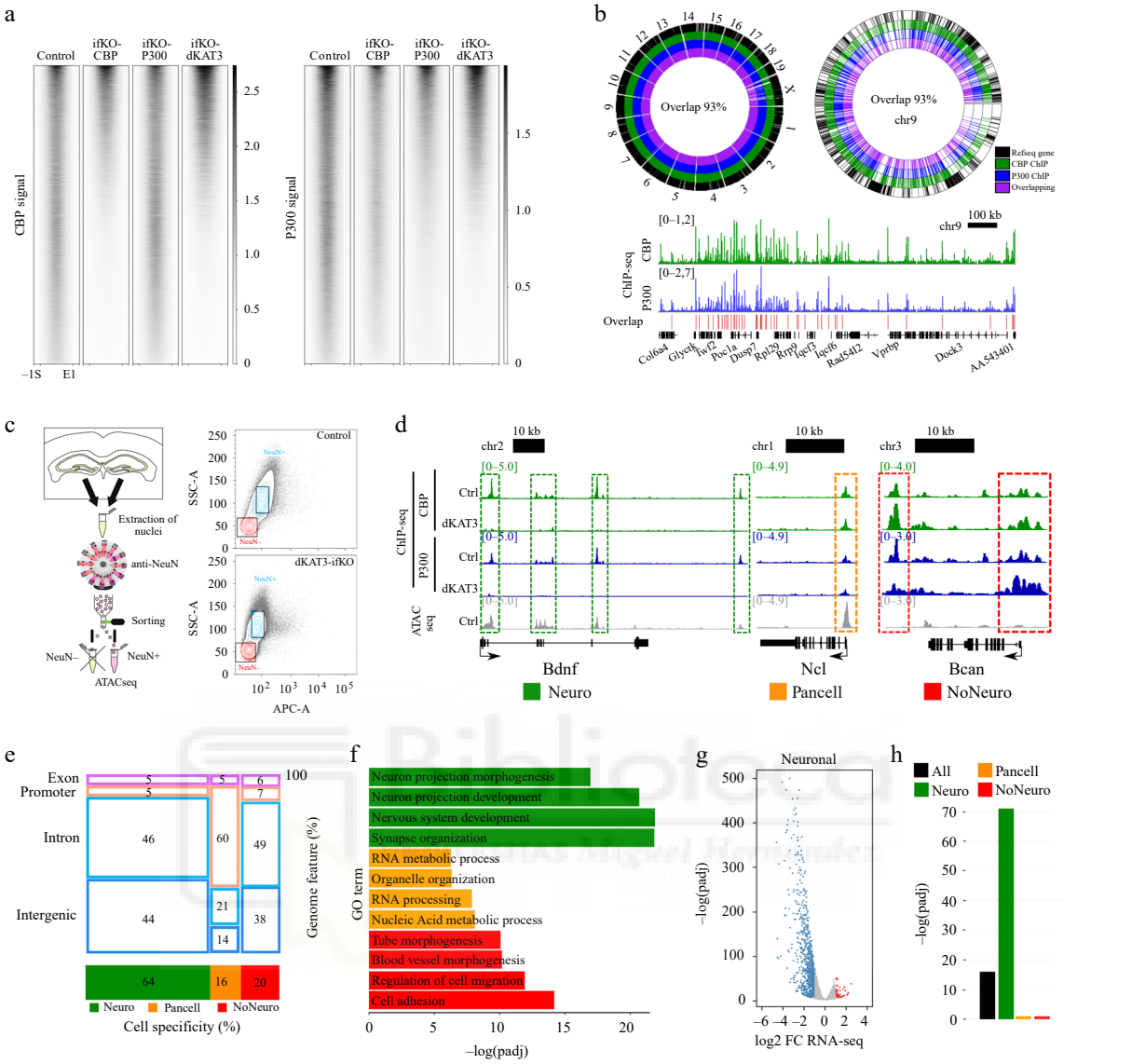

Fig. 4 CBP and p300 bind to the same genomic sites. a Heat maps showing the control CBP/P300 KAT3 ChIP-seq peaks and the signal in the corresponding locations of CBP-, p300-, and KAT3-ifKO. Intensity ranges from strong (black) to weak (white). S: peak start, E: peak end, ±1 kb. b Circos plots of the entire genome (left) and chromosome 9 (right). Below: a snapshot of a gene-rich region in chromosome 9. Colors indicate CBP and p300 binding in hippocampal chromatin and their overlap. Refseq genes in black. c Left: scheme of the FANS/ATAC-seq experiment. Right: flow cytometry sorting plots for control and dKAT3-fKO samples. Boxes indicate the gates used for sorting NeuN+ nuclei (blue). APC-A is the signal of anti-NeuN staining. d Snapshot illustrating the classification of KAT3 peaks in neuronal (green), non-neuronal (red), and pancellular (orange). Representative peaks classified as neuronal, non-neuronal, and pancellular are marked with a green, red, and orange dashed rectangle, respectively. e Classification of KAT3 peaks according to cell specificity (neuronal, pancellular, and non-neuronal) and genomic features (promoter, exon, intron, intergenic). The numbers within each sector represent percentages. f GO enrichment analysis performed on the gene sets associated with neuronal (green), non-neuronal (red), and pancellular (orange) KAT3 peaks. g Volcano plots of RNA-seq analysis for the subset of genes classified as neuronal. Red: upregulated genes; blue: downregulated genes. h BETA analysis of the association between all, neuronal, non-neuronal, and pancellular KAT3 peaks, and transcriptome changes.Neuronal peaks show the strongest association with gene downregulation. p-Values in Kolmogorov–Smirnov test using BETA-cistrome software: p-valAll = 6.24e−17; p-valNeuro = 3.34e−72; p valNoNeuro = 0.3; p-valPancell = 0.3.

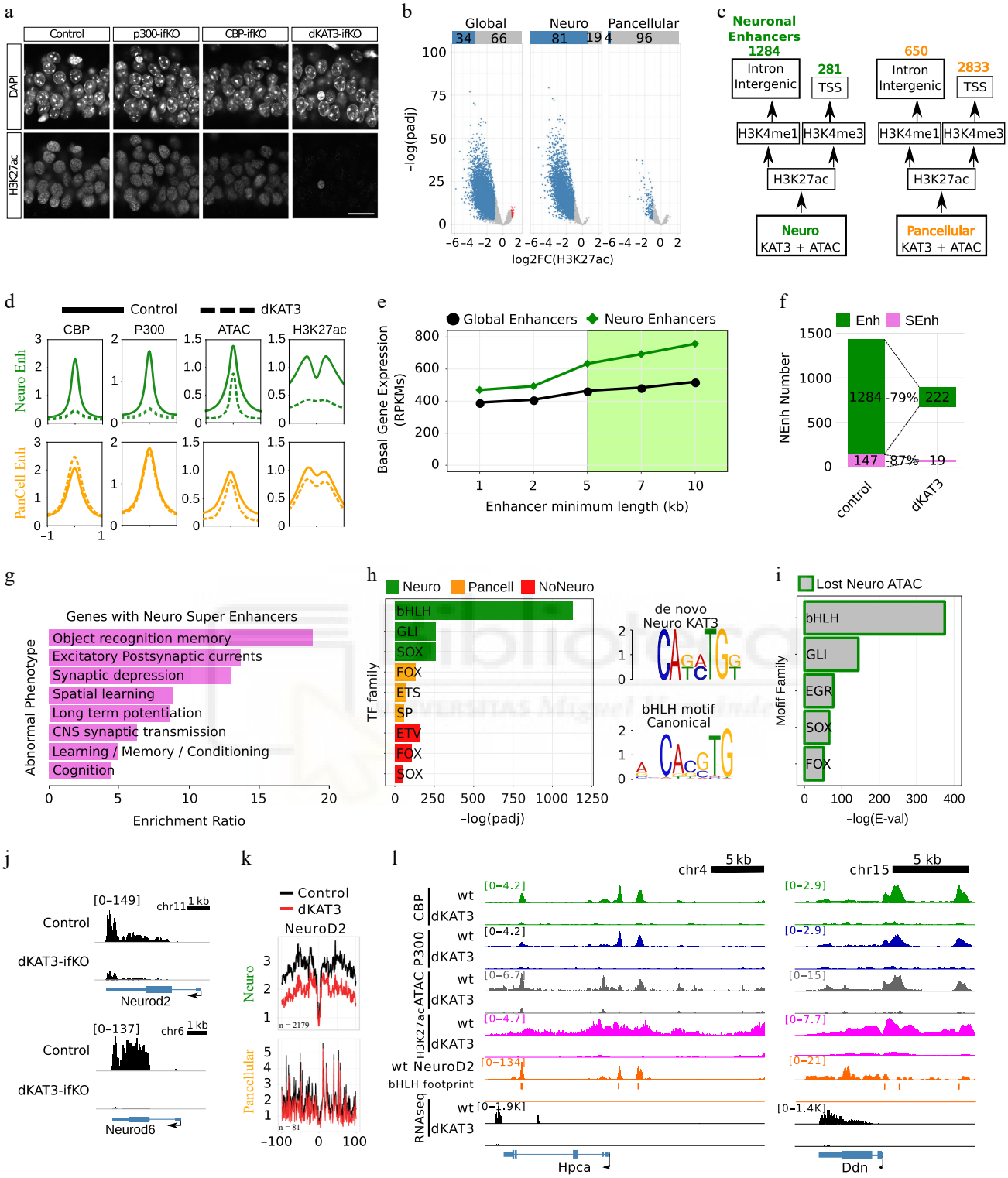

Fig. 5 H3K27ac is strongly decreased in neuro-specific locations and correlates with gene downregulation. a Immunostaining against H3K27ac in the CA1 subfield of single and dKAT3 ifKOs (IF signal control: 21.62 ± 2.24, dKAT3 ifKOs: 4.94 ± 1.03, $p < 0.0001$, unpaired t-test); the single ifKOs show nonsignificantdifference compared to controls. The experiment was repeated 3 times. Scale: 10 µm. b Genome-wide analysis of H3K27ac changes in dKAT3 ifKOs. Volcano plots show the fold change and significance values for all peaks (Global) and for the subsets of neuron-specific (Neuro) and pancellular peaks. c Classification of regulatory regions categorized by genomic features. D Metaplots of ATAC-seq, KAT3, and H3K27ac ChIP-seq signals in neuronal and pancellular enhancers in controls and dKAT3-ifKOs. Plots are centered in the peak center and expanded ±1 kb. e Correlation between length of the enhancer and expression level of the proximal gene. f Number of downregulated genes that contain enhancers or super-enhancers in control mice and percentage that lose acetylation in dKAT3-ifKOs. g Barplot showing the top 10 enriched categories from the Phenotype analysis for genes harboring neuronal enhancers. h TFBS analysis of neuronal (green), non-

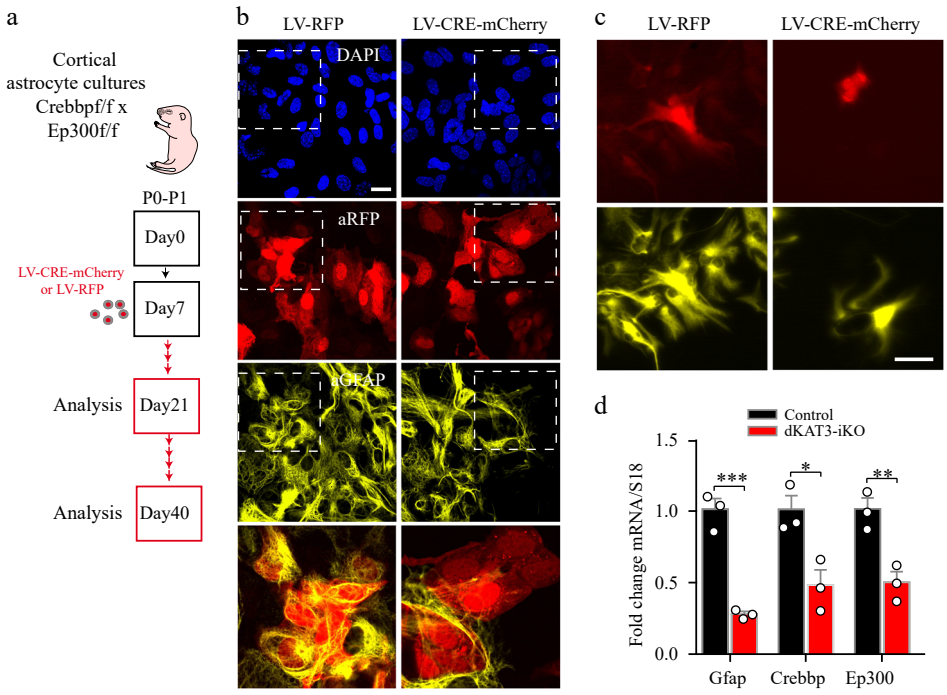

Fig. 6 CBP and p300 are needed to maintain the fate of other cellular types. A Generation of dKAT3-KO astrocytes. Cortical astrocytes from Crebbpf/f:: Ep300f/f pups were infected with a cre recombinase-expressing LV. b Cultured dKAT3f/f astrocytes show a downregulation of astrocyte marker GFAP 2 weeks after infection with a cre recombinase-expressing LV (n= 3 for both groups). Scale bar: 20 µm. c The loss of astrocyte morphology is more evident 4 weeks after infection (n =3 for both groups). Scale bar: 50 µm. d RT-PCR quantification of the Gfap (GFAP), Crebbp (CBP), and Ep300 (p300) transcript levels in cultured dKAT3f/f astrocytes (n= 3). Data are presented as mean values ± SEM. Two-tailed t-test: ****p < 0.0001, ***p < 0.001, **p < 0.01; *p < 0.05. Source data are provided as a Source data file.

neuronal (red), and pancellular (orange) KAT3 peaks. Each motif family name is a usercurated approximation to the results provided by the MEME-suite algorithm. The most enriched de novo-identified binding motif in neuronal KAT3 (upper right motif) is very similar to the NeuroD2 motif (bottom right). Log E-values obtained with the expectation maximization algorithm (MEME-ChIP suite): Neuro: bHLH =1130, GLI = 258, SOX = 257; Pancell: FOX = 130, ETS =67, SP = 57; NoNeuro: ETV = 157, FOX = 105, SOX= 49. i TFBS analysis of neuronal regions with a reduced ATAC-seq signal in dKAT3-ifKOs. j RNA-seq profiles for Neurod2 and NeuroD6. Scale: 1 kb. k Digital footprinting of NeuroD2 at neuronal and pancellular KAT3-bound regions. Values correspond to normalized Tn5 insertions. l Representative snapshots of KAT3, ATAC, and H3K27ac depletion with bHLH footprint and NeuroD2 overlaps, at two genes that are strongly downregulated in dKAT3-ifKOs. Source data for graphs in panels (e) and (h) are provided as a Source data file.

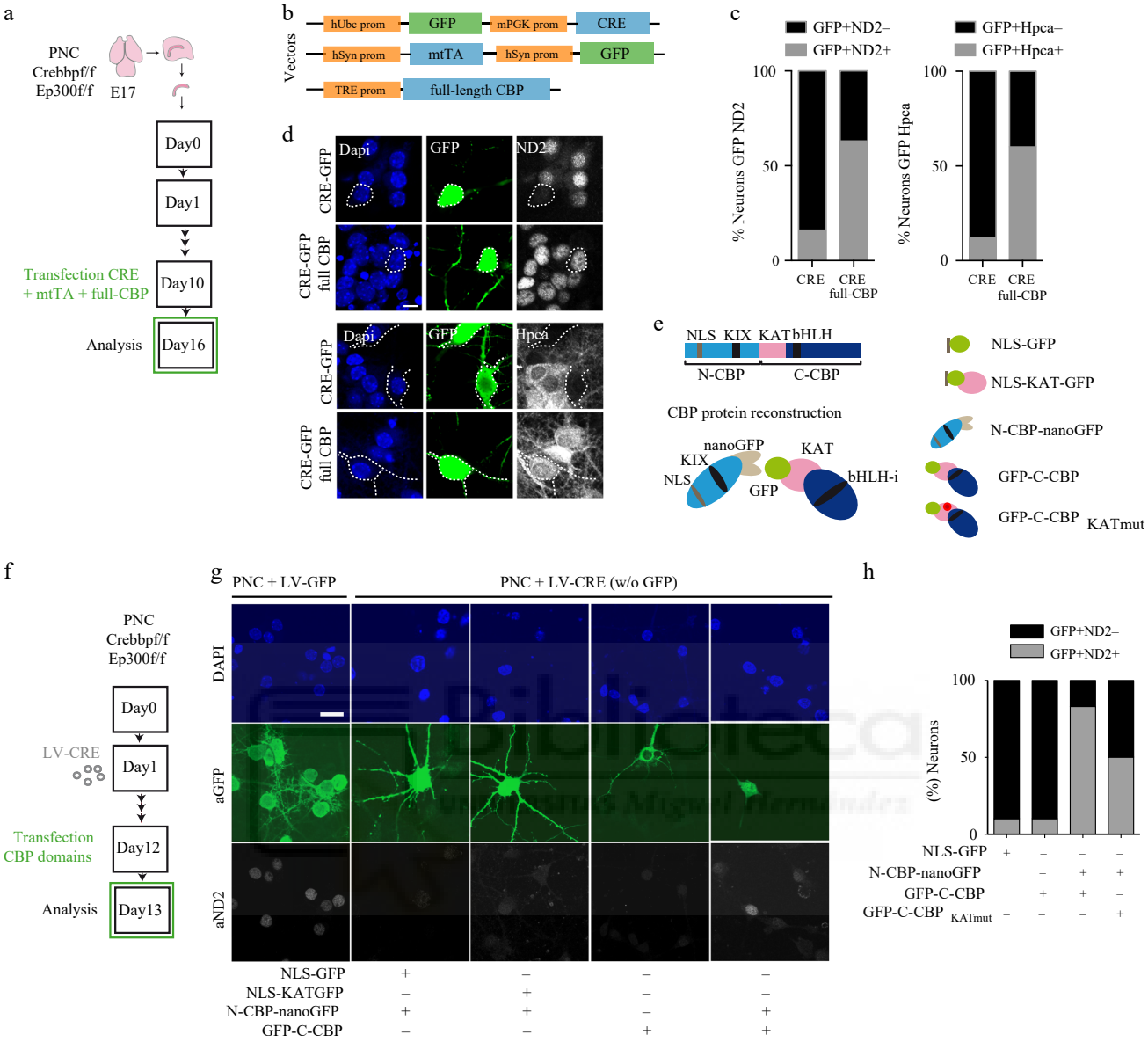

Fig. 7 Full-length CBP is required to restore neuronal-specific transcription. A Hippocampal PNCs from E17 Crebbpf/f::Ep300f/f embryos were cotransfected with constructs that drive the expression of the Cre recombinase and full-length CBP. b Plasmid combination to express recombinant CBP simultaneously to endogenous CBP and p300 ablation. c Representative images of NeuroD2 and hippocalcin staining in PNC transfected with the constructs shown in (b). Note the reduced expression in the GFP+ cells in the absence of heterologous full length CBP (experiments in two independent PNCs). Scale: 10 μm. D Quantification of the percentage of NeuroD2-positive or -negative cells and hippocalcin-positive or -negative cells among all GFPpositive cells (n = 60 neurons per condition). e Scheme of the CBP fragments used for rescuing NeuroD2 expression (see Methods for additional details). NLS: nuclear localization domain; KAT: acetyltransferase domain; KIX: kinase-inducible domain interacting domain; bHLH-i: region of interaction with bHLH transcription factors. f Hippocampal PNCs from E17 Crebbpf/f::Ep300f/f embryos were transfected with constructs that drive the expression of the Cre recombinase and the different CBP fragments and the KAT domain shown in panel (e). g Representative images of NeuroD2 staining in PNCs infected withLV CREw/oGFP and transfected with the different domains of CBP shown in panel (e). PNCs infected with LV-GFP (i.e. with wild type phenotype) were used as a control for baseline NeuroD2 level (2 independent PNCs). Scale: 20 μm. H Quantification of the percentage of NeuroD2-positive or -negative cells among all GFP-positive neurons (n = 30–80 neurons per condition). Source data for graphs in panels (d) and (h) are provided as a Source data file.

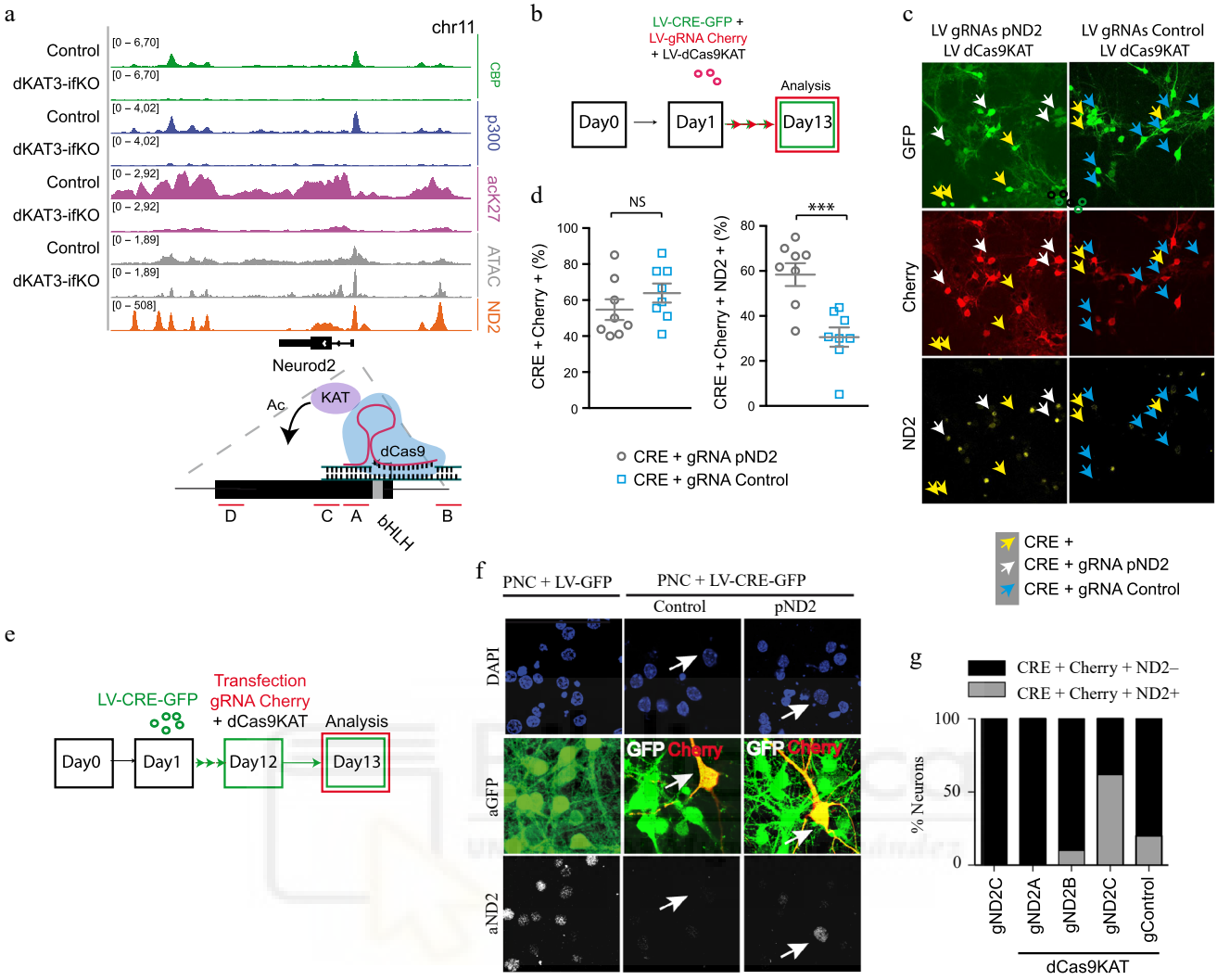

Fig. 8 Locus-specific acetylation restores NeuroD2 transcription. a Snap view of the Neurod2 locus. The profiles for CBP and p300 binding, H3K27 acetylation and ATAC-seq signal are shown. The bottom orange track corresponds to the NeuroD2 ChIP-seq data generated in ref. 29. A scheme presenting the strategy used to drive the KAT activity of p300 to the Neurod2 promoter using a fusion protein with dCas9 is also shown. The positions targeted by the gRNAs (red lines, gND2 A-D) are indicated. Note that the target regions are in the proximity of bHLH sites. b Scheme of the co-infection of LVs expressing cre recombinase, dCas9-KAT, and the Neurod2 gRNAs (A-D mix). c Representative image of NeuroD2 protein levels in the cells coinfected with LV-CRE-GFP and the lentiviruses LV-gRNA-mCherry specific for Neurod2 (white arrows). As a specificity control, we conducted the same experiment using a gRNA targeted to Hpca (blue arrows) (n = 4 wells per condition in 2 PNCs). As a comparison, cells infected with LV-CRE-GFP alone (yellow arrows) show strongly diminished NeuroD2 levels as well. Scale bar: 50 µm. d Quantification of different cell subpopulations observed in the experiment shown in panel (c) (n =4 wells per condition in 2 PNCs). Two-tailed t-test: ****p < 0.0001, ***p < 0.001, **p < 0.01; *p < 0.05. Data are presented as mean values ± SEM. e Scheme of rescue experiment with plasmids carrying dCas9-KAT and the Neurod2 gRNA in dKAT3-KO cells that had already lost Neurod2 expression. f Representative image of NeuroD2 expression in control (PNC + LV-GFP) and dKAT3-depleted (PNC + LV-CRE-GFP) neurons after transfection with dCas9-KAT and gND2-C targeting the NeuroD2 promoter. Arrows indicate LV-CRE-GFP infected cells transfected with the gRNA-carrying vector. A gRNA targeting the hippocalcin promoter was used as a specificity control. Scale: 20 µm. g Quantification of the percentage of transfected cells showing normal NeuroD2 expression after transfection with gND2-C alone and dCas9-KAT co-transfected with gND2-C, gND2-A, gND2-B, or gRNA control independently (experiments in three independent PNCs; n = 30–40 neurons per condition). Source data for graphs in panels (d) and (g) are provided as a Source data file.

ACKNOWLEDGEMENTS

La presente tesis doctoral no hubiera sido posible sin el apoyo y contribución de todos los compañeros y compañeras, familiares, amigos y amigas que me han acompañado desde septiembre de 2016 que comenzó este viaje.

Me gustaría comenzar agradeciendo a mi director de tesis, Jose, por la oportunidad y la confianza depositada en mí para realizar esta tesis doctoral, como primer miembro y doctoranda de su laboratorio. Durante estos años he podido ver de primera mano la dificultad de empezar un proyecto desde cero, y como hemos ido construyendo poco a poco esta historia que hoy es mi tesis doctoral. Gracias por transmitirme tu rigurosidad científica y, sobre todo, tu entusiasmo por la ciencia en cada resultado que obteníamos.

En segundo lugar, quiero hacer especial mención a mis compañeros de laboratorio: Ángel Márquez, Alejandro Expósito y Aysha Bhojwani. Gracias por vuestro apoyo y amistad. Me gustaría continuar agradeciendo al que ha sido mi segundo laboratorio durante todos estos años. Gracias a Ángel Barco, investigador principal del mismo, por acogerme en su laboratorio como un miembro más y darme la oportunidad de aprender y formarme científicamente en el campo de la neurociencia. Especial mención a todos los amigos y compañeros de este laboratorio y del Instituto de Neurociencias sin los cuales no estaría donde estoy ahora mismo: Juan Medrano, Ana Martín, Michal Lipinski, Alejandro Medrano, Nuria Cascales, Marilyn Scandaglia, Bea del Blanco, Marta Alaiz, Miguel Fuentes, Sergio Niñerola, Mayte, Paula, Carina, Jordi, Javier Rodríguez, Irene Huerga, y Sergio Valbuena. Gracias a todos por vuestra contribución directa o indirectamente a este trabajo.

Agradecer también a Amanda Sierra por darme la oportunidad de realizar una estancia de investigación en su laboratorio y formarme científicamente en el campo de la microglía e inflamación al inicio de mi tesis doctoral, y a todos los miembros de su laboratorio y del Achucarro Basque Centre for Neuroscience por la gran acogida: Irune, Sol, Virginia, Jorge, Iñaki, Victor, e Irene.

Thanks to Paul Whiting and Lorenza Magno for giving me the opportunity to carry out my international research stay in the Drug Discovery Institute (DDI) at the University College of London. I am very thankful for your support and scientific training essential for the culmination of this PhD thesis. I would like to thank all the people that have enriched this research stay. First, to Soyon Hong, thank you for getting me involved in your laboratory scientific meetings and discussion, it has been really fulfilling. Second,thanks to all the people from the DDI and the Dementia Research Institute (DRI): Stefano, Dominic, Dimi, Seppe, Ludovica, Gerard, Judy, Tom and Sang-Eun.

Sin olvidarme de agradecer a todo el personal a cargo de los servicios del Instituto de Neurociencias sin los cuales este trabajo no hubiera sido posible. Me gustaría agradecer especialmente a Antonio Caler, técnico de citometría; Alejandro y Selene, técnicos del animalario; Trinidad y Eva a cargo del servicio de genotipado; Trinidad a cargo del servicio de autoclave; y Virtudes a cargo de la gestión del doctorado.

Me gustaría terminar agradeciendo a mi familia porque sin su apoyo no estaría donde estoy ahora y, sin duda, esta tesis no habría sido posible: a mi padre, a mi madre y a mis hermanos, Luis y Miguel, a mis abuelos y a todas mis tías y tíos. Gracias.

Por último, agradecer a la persona que siempre está ahí, no solo a nivel personal, sino que tengo la suerte de que también es un gran científico, del que he podido aprender durante estos 4 años. A mi pareja, Javier, gracias por tu apoyo incondicional.

Carmen María Navarrón Izquierdo

Alicante, 19 de abril de 2021.